



Dielectrophoresis Control of Semiconductor Nanowires for Sensing Technology

Thesis submitted in accordance with the requirements of the University of Liverpool for the degree
of Doctor in Philosophy by

Siriny Laumier

April 2023

Abstract

Semiconductor nanowires (NWs) synthesis successes have given keys to unprecedented nano-scale sensitivity opening up new opportunities in device applications. NWs' potential relies upon the possibility of engineering and modifying properties such as sensitivity and carrier transport, by tailoring the NWs' morphology and conductivity. New challenges have taken place with the downscaling of electronics for NWs integration and assembly techniques. Amongst a large variety of integration techniques, dielectrophoresis (DEP) is a powerful tool for the precise manipulation of NWs of different compositions and sizes. However, experimental implementation and analysis with DEP often lack depth regarding the optimisation of the technique and the effects of the parameters on the performances of the final devices, crucial for the understanding of NWs' electric transport properties and technology improvement.

Consequently, this thesis presents a comprehensive study of the experimental implementation of DEP which is of paramount importance to obtaining optimum conditions for NWs alignment. With this aim in mind, the presented work demonstrates a detailed investigation of the electrical and optical properties of germanium (Ge) and gallium-arsenide-bismuth (GaAsBi) NWs-based devices by DEP as a function of the collection frequency. The Ge and GaAsBi NWs were obtained by MOVPE and MBE respectively as a collaborative work with the Institute of Material for Electronic and Magnet (Italy) for the Ge NWs, and with the research team of Dr Robert Richard at the University of Sheffield (Department of Electrical Engineering and Electronics) for the GaAsBi NWs.

Firstly, to maximise NWs alignment precision, optimum DEP parameters are for the first time thoroughly extracted by testing the effects of different mediums (chemical inertia, volatility and contact angle) and electrode designs (gradients and electric field).

Secondly, fabricated with a DEP frequency range of 500 kHz to 10 MHz the devices were electrically characterised using voltage-current response. An asymmetric diode-like behaviour was found to be originating from heterostructured Ge NWs specifically orientated by electrophoresis combined with DEP. This result is particularly promising for orientation control demonstrated for the first time, tuning and altering current response from chemically heterostructured nanowires.

A particular focus was given to the effect of increasing frequency on the device performances such as carrier transport. Despite a decrease of aligned NWs corroborating theoretical analysis, increasing frequency collected higher conductivity Ge NWs with carrier mobility improving from 20 at 500 kHz to 4.380 at 10 MHz demonstrated using Mott-Gurney, and GaAsBi NWs with carrier mobility increasing from 5.29 ± 0.027 to $100 \pm 0.70 \text{ cm}^2 \text{ V}^{-1} \cdot \text{s}^{-1}$ at 500 kHz and 10 MHz demonstrated using the Fermi-velocity law. Such selectivity is of great potential to improve sensing technology transduction.

Using optimum parameters previously found, a low-cost and simple voltage divider system joined to DEP is demonstrated for the first time to improve the alignment technique of a single Ge nanowire. The resulting spectral response was consistent with optical characterisations found in the literature for a single Ge nanowire and demonstrated high sensitivity near-infrared and communication wavelength as confirmed with a high responsivity of $6.2 \times 10^5 \text{ A/W}$ at 1550 nm. Such high resistivity is amongst the highest ever obtained for NWs.

Furthermore, a NWs-based biosensor for the spike protein of the SARS-CoV-2 was fabricated by multilayered surface functionalisation evidenced by Raman spectroscopy. Upon exposure to increasing concentration of the protein, the biosensors transduced increasing current response with a working range of at least 1 aM to 100 fM. Selectivity to the spike protein was testified using bovine serum albumin as a negative control reference.

The GaAsBi NWs were for the first time fully characterised and implemented as devices by DEP. The NWs surface roughness showcased the importance of surface properties that influenced DEP collection and carrier transport. Spectral responses from the devices brought to light the different bismuth content at the origin of reduced band-gap energy shown by the cut-off energies of the spectrum. With a Bi content increase of roughly 1% in GaAs the photodetectors presented high responsivity from $1.3 \times 10^4 \text{ A/W}$ to $5.6 \times 10^4 \text{ A/W}$.

Effective NWs-based biosensors and photodetectors were proof of concept devices that corroborate NWs and dielectrophoresis functionality paving the way to future nanotechnology improvement.

List of publications and conferences

Accepted manuscripts

- **Siriny Laumier**, Thomas Farrow, Harm van Zalinge, Luca Seravalli, Matteo Bosi, and Ian Sandall. *Selection and Functionalization of Germanium Nanowires for Bio-Sensing*. ACS Omega, 7(39):35288–35296, 2022
- Thomas Farrow, **Siriny Laumier**, Ian Sandall, and Harm van Zalinge. *An Aptamer-Functionalised Schottky-Field Effect Transistor for the Detection of Proteins*. Biosensors, 12(5), 2022

Manuscripts in preparation

- **Siriny Laumier**, Luca Seravalli, Matteo Bosi, and Ian Sandall. *Rapid low-cost fabrication of single nanowire devices utilising dielectrophoresis*.
- **Siriny Laumier**, Ian Sandall, Robert Richard. *GaAsBi Nanowire-based Photodetectors by dielectrophoresis*.

Conferences presentation

- **Poster:** Fabrication of MSM Ge Nanowire Photodetector Utilizing Dielectrophoresis. *UK-Semiconductor*. (2019)
- **Poster:** Selection and functionalization of germanium nanowires for bio-sensing. *BioMED-Eng21*. (2021)
- **Oral:** A New Method for Rapid, Low-Cost Fabrication of Single Nanowire Devices. *UK-Semiconductor*. (2022)

Acknowledgements

"One shouldn't work on semiconductors, that is a filthy mess; who knows if they really exist" Wolfgang Pauli (of Pauli's exclusion principle) said in 1931.

There are so many people that I would like to thank, that supported and helped me through the PhD journey but more importantly made it fun, enjoyable, and thriving. Science is and has to be fun and my supervisor Ian Sandall made sure of that through trust and guidance throughout the past four years. You have helped me develop as a scientific researcher and also helped me to trust myself whenever I just saw clouds and worries. I also want to thank Kai Hoettges as well, for his insightful knowledge and guidance, offering me sound advice and teaching me about dielectrophoresis and electronics I look forward to working with you in the future on more exciting projects. Thank you both for your professionalism and friendliness. Many thanks to Harm van Zalinge for his resourceful knowledge of biology as I had no clue about biosensing and proteins and yet I managed to publish work on COVID-Sars-2 biosensing. A special thanks to David Donaghy for his work and expertise.

It is important to note that this thesis would not have been possible without my collaborators in Parma Italy at the Institute of Materials for Electronic and Magnet for growing my germanium nanowires samples. Thank you to Robert Richard, my other collaborator in Sheffield for growing my GaAsBi nanowires samples. Moreover, I wanted to thank the Department of Microscopy; the Albert Crewe Centre for electron microscopy of the University of Liverpool for their trust and for letting me use their equipment (SEM, EDX, and TEM). The Material Innovation factory on the campus of the university was also kind enough to trust me and let me use their equipment with initial training on; the optical microscope, Raman spectroscopy, infra-red microscopy, and zeta sizer.

Thanks to all women in my life, my cousins, my mum, and my friends those are the best beings I could have ever imagined, I love you all. More than four years in a foreign country doing a PhD can feel long but my best friend and flatmate Michael Mueller made it feel like a couple of months and helped me be a scientist, researcher, and engineer but also helped me be a good person and friend. The world has better watch out when we work together again. Thank you to Adeem Alshamari was his open mind and friendship always gave me courage in times of doubt. It is always good to have a French fella, and mon cher Stéphane Simon thanks for your friendship and courage.

Contents

Abstract	i
List of publications and conferences	iii
Acknowledgements	iv
Contents	v
List of Figures	ix
List of Tables	xvii
1 Introduction	1
1.1 Significance of nanomaterials for sensing technology	1
1.2 Significance of Dielectrophoresis.....	3
1.3 Motivation and thesis overview.....	4
1.4 Semiconductors nanowires, fundamentals and previous work.....	6
1.5 Nanowires.....	8
1.6 Nanowires growth and implementation in technologies.....	10
1.6.1 Top-down integration techniques.....	11
1.6.2 Bottom-up integration techniques.....	11
1.7 Towards nano-manipulation.....	13

1.7.1	Chemical or electrostatic interaction	14
1.7.2	Shear force interaction.....	14
1.7.3	Blown bubble film.....	15
1.7.4	Microfluidic force.....	16
1.7.5	Langmuir Blodgett.....	17
1.7.6	Dielectrophoresis technique.....	18
1.7.7	Comparison.....	19
1.8	Dielectrophoresis control.....	21
1.8.1	Dielectrophoresis for nanowires geometry	22
1.9	Electrophoresis.....	28
1.10	Nanowires sensor devices.....	30
1.10.1	FET building blocks for nanosensor.....	30
1.10.2	Conduction, transport mechanism in nanowires.....	33
1.11	Bio-Sensor devices and previous work	44
1.12	Previous work on germanium nanowires	46
1.13	Previous work on GaAs and GaAsBi.....	48
2	Fabrication and characterisation	51
2.1	Germanium nanowires growth by Metalorganic Vapour-Phase Epitaxy.....	51
2.2	GaAsBi growth by Molecular Beam Epitaxy.....	52
2.3	Electrodes fabrication	54
2.4	Bio-functionalisation of the nanowires	57
2.5	Characterisation and analysis tools.....	58
2.5.1	Electron Microscopy.....	58
2.5.2	Optical microscopy.....	62
2.5.3	Raman Spectroscopy.....	63
2.5.4	Contact angle, wettability.....	64
2.5.5	Zeta potential	65
2.5.6	Photocurrent Spectroscopy	66
2.5.7	Current response characteristic	68
3	Dielectrophoresis implementation for germanium nanowires-based device	68
3.1	Characterisation of the nanowires.....	69
3.1.1	Morphological and chemical characterisation of the nanowires	69
3.1.2	Characterisation of the nanowires in different mediums for DEP	72
3.1.3	DEP force and Clausius-Mossotti factor calculations.....	79
3.2	Dielectrophoresis platform	82
3.2.1	Design of the electrodes	82
3.2.2	Simulation and dielectrophoresis set-up	84

3.2.3	Real-time resistance monitoring	92
3.3	Influence of the dielectrophoresis frequency	96
3.3.1	Establishment	96
3.3.2	Electrical properties; IV response	96
	Conclusion	109
4	Fabrication and characterisation of a single nanowire-based device	111
4.1	Voltage divider set up	112
4.2	Current response	116
4.3	Optical properties; photocurrent spectroscopy	119
	Conclusion	125
5	Germanium nanowires-based biosensor device	126
5.1	Characterisation of the functionalisation layers by Raman spectroscopy	127
5.2	I(V) with increasing spike protein concentration	131
	Conclusion	135
6	Dielectrophoresis implementation for GaAsBi nanowires-based device	137
6.1	Characterisation of the nanowires	138
6.1.1	Morphological and chemical characterisation of the nanowires	138
6.2	Characterisation of the nanowires in different mediums for dielectrophoresis	142
6.2.1	Characterisation of the nanowires in anisole	162
6.2.2	Dielectrophoresis force and Clausius-Mossotti factor calculations	143
6.2.3	Real-time resistance monitoring	145
6.3	Influence of the dielectrophoresis frequency	151
6.3.1	Electrical properties; IV response	151
6.4	Optical properties; photocurrent spectroscopy	160
	Conclusion	165
	Conclusions and further work	166
	Bibliography	170
	Appendix A	232
A.1	Semiconductor nanowires, fundamentals and previous work	232
A.2	Fabrication and characterisation	234
A.3	Fabrication and characterisation of single Ge NW alignment	249

A.4	Germanium nanowires-based biosensor device.....	253
A.5	DEP implementation technique for GaAsBi nanowires-based device	255

List of Figures

1.1	More than Moore's status roadmap.....	2
1.2	Energy band diagrams semiconductor in metal, and insulator.....	6
1.3	Energy band structure of (a) Ge, (b) Si and (c) GaAs.....	8
1.4	SEM images of top-down NWs fabricated by electron beam etching (EBL).....	11
1.5	Vapor-Liquid-Solid method; A) Binary phase diagram of gold and silicon B) Si crystallisation mechanism C) Heated reactor with inert gas flow D) SEM image of a Si NW grown using an Au nanocluster of 150 nm in diameter; scale bar 150 nm.....	12
1.6	Assembly by shear forces.....	15
1.7	Blown bubble film technique.....	16
1.8	SEM images of layer-by-layer assembly of NWs by microfluidic and functionalisation deposition. The black arrows show the flow direction.....	17
1.9	Network of crossed NWs aligned by Langmuir Blodgett.....	18
1.10	First DEP applied on gold NWs by Mayer <i>et al.</i> in 2000.....	18
1.11	DEP coupled with microfluidic channels. a) schematic of the DEP/microfluidic set-up b) Aligned NWs obtained by coupling DEP and microfluidic.....	19
1.12	DEP principle; a) in a uniform electric field, b) in a non-uniform electric field.....	22
1.13	Geometrical drawings of a prolate ellipsoid (a) and classic spheroid particle shape (b).	24
1.14	Nanowire (red) in an AC electric field subjected to DEP force influenced by the anisotropic nanowire a) top view b) side view.....	27
1.15	Images obtained by Brown <i>et al.</i> showing the difference between a) EP and b) DEP at 15 s of the experiment. Scale bar 100 μm	29
1.16	Cross section of a floating gate FET.....	31
1.17	SEM images of five bending modes of a ZnO nanowire (left) and the corresponding current response I(V) showing the piezoelectric FET sensor curves.....	31
1.18	Schematic of the p-type Si NW FET sensor (left) and its electrical measurement for every functionalisation layer (right).	32
1.19	Schottky barrier contact between metal and p-type semiconductor.....	35

1.20	Typical I–V characteristic curve for p-type nanorod Schottky diodes (left) and a scanning electron microscopy (SEM) image (right).....	36
1.21	Functionalised Schottky Si NW with b) antibodies and its c) current response when exposed to increasing concentration of antigens (1) 0 fM in black, (2) 5 fM in blue, (3) 10 fM in red.	37
1.22	Semiconductor (p-type) band diagram with defect state levels shallow and/or deep traps.....	41
1.23	Current–voltage behaviour of NWs with SCLC.....	42
1.24	Schematic illustration of a) NNH mechanism and b) VRH mechanism. K_B is Boltzmann’s constant and T is temperature.....	43
1.25	SEM images of GaAs/GaAsBi NWs obtained by MBE by Ishikawa <i>et al.</i>	49
2.1	Schematic representing the MOVPE main chamber.....	52
2.2	Schematic representing an MBE chamber.....	53
2.3	Schematic of a) Thermal evaporation and b) resulting deposited layers of Cr and Au on a glass substrate.....	55
2.4	Schematic of the fabrication of the device electrodes by photolithography and etching. Not to scale.	56
2.5	Schematic of the functionalisation steps a) bare device, b) device after silanisation terminated with an amine group NH_2 , c) device after Glutaraldehyde treatment acting as a linker between amine of b) and aptamer, d) final functionalised device with attached aptamer, e) functionalised device in the presence of spike protein.....	58
2.6	Schematics of optical microscope, Transmitted Electron Microscope and Scanning Electron Microscope.....	60
2.7	Diffraction pattern of different structures of Aluminium a) monocrystalline, b) polycrystalline, and c) amorphous.	61
2.8	Images obtained by Energy Dispersive X-ray Spectroscopy of a) GasAsBi NWs and b) composite nanoparticles.....	62
2.9	Drop fitted contour and determination of the angle θ by drop shape analysis.....	64
2.10	Schematic of contact angle principle.....	64
2.11	Surface Zeta Potential of a particle in a medium.....	65

2.12 Schematic of the photocurrent spectrometry measurement set-up.....67

2.13 Current-voltage characteristics in a linear and semilog scale of a practical heterojunction Ge diode at room temperature. The inset shows the same I(V) with a semilog scale.....68

3.1 SEM images of the germanium nanowires on the silicon substrate. Top magnification is 4.53 k and bottom magnification is 26.26 k.72

3.2 TEM images of the germanium nanowires surface. Left; nanowire surface after growth. The bottom left inset is the diffraction pattern of the nanowires. Right; nanowire surface after two months.....72

3.3 Raman spectra of Ge NWs on glass. The glass background has been removed and the signals smoothed.....73

3.4 Wettability contact angle images of the Ge NWs droplet solution prepared with different mediums. With wettability angles of a) DIW = $55.83 \pm 1.30^\circ$, b) DMF = $50.9 \pm 0.20^\circ$, c) Toluene = $7.94 \pm 2.18^\circ$, d) DMF/Toluene 50:1 = $32.15 \pm 1.07^\circ$, e) anisole = $46.57 \pm 1.42^\circ$ and f) IPA = $4.68 \pm 0.38^\circ$ 76

3.5 TEM images of the influence of deionised water on Ge nanowires after two days...77

3.6 Dark field TEM images of the influence of DMF/Toluene on Ge NWs after two days..... 78

3.7 TEM images in bright field showing the influence of anisole on Ge NWs after two months. On both images, the NWs are demonstrated to be intact in anisole after two months..... 79

3.8 TEM images in bright field images of the influence of anisole on Ge NWs after two months..... 80

3.9 Simulated real part of the CMF along the long axis as a function of the frequency for Ge NWs aligned at a voltage of $8V_{peak-to-peak}$ on a $20\mu\text{m}$ electrode gap in anisole..... 82

3.10 Simulated real part of the CMF along the short axis as a function of the frequency for Ge NWs aligned at a voltage of $8V_{peak-to-peak}$ on a $20\mu\text{m}$ electrode gap in anisole..... 82

3.11 Simulated real part of the Clausius Mossotti factor as a function of the frequency for Ge NWs aligned at a voltage of $8V_{peak-to-peak}$ on a $20\mu\text{m}$ electrode gap in anisole..... 83

3.12 Simulated DEP force as a function of the frequency for Ge NWs aligned at a voltage of $8V_{peak-to-peak}$ on a $20\mu\text{m}$ electrode gap in anisole..... 83

3.13 Schematics of common electrode design. A) parallel or interdigitated, B) castellated, C) oblique, D) curved, E) quadrupole, F) microwell, G) matrix, H) extruded, I) and J) wall-patterned, K) side-wall, L) isolating obstacles based, M) Medium contact-less..... 85

3.14	Circuit topology for DEP. The dotted box contains a photograph of the DUT and below is shown close-up photography of the electrodes deposited on glass.....	87
3.15	Schematic image of the interdigitated electrode design with gaps from 5 to 25 μm . a) Overview of the interdigitated electrodes, b) Enlargement of the left side of the electrodes.....	88
3.16	Electric field and gradient distribution simulation using COMSOL MULTIPHYSICS. A voltage of 8 $V_{\text{peak-to-peak}}$ and frequency of 500 kHz was applied on the interdigitated electrodes. a) top-view of the electrodes, b) region of the big gaps, c) region of the small gaps. The scale barre on the left indicates the strength of the gradient.....	88
3.17	SEM images of resulting DEP at 8 $V_{\text{peak-to-peak}}$ and 500 kHz on interdigitated electrodes.....	89
3.18	Schematic image of the parallel electrode design with 20 μm gap.....	91
3.19	Simulation of the electric field and gradient distribution along the surface using COMSOL MULTIPHYSICS. A voltage of 8 $V_{\text{peak-to-peak}}$ and frequency of 500 kHz was applied on the round and rectangular tips. The scale on the left indicates the strength of the gradient. Gradient distribution A) and B) and electric field lines A') and B').	92
3.20	Optical microscopy images of geometry A (round tip) a) and b) and geometry B (rectangular tip) c) and d) after DEP at low and high frequencies.	93
3.21	Calculated resistance as a function of time of DEP at a voltage of 8 $V_{\text{peak-to-peak}}$ and frequency of 500 kHz. Graph obtain by resistance calculation approximation using a Matlab code.....	95
3.22	Inverse of time constant τ , indicating the magnitude of the DEP force as a the function of DEP signal frequency	96
3.23	Schematic of a floating gate Ge NWs device with the idealised alignment of NWs between source and drain electrodes.....	98
3.24	IV characteristics of fabricated Ge nanowire devices at differing DEP frequencies with floating gate potential.....	99
3.25	Combination of Dielectrophoresis and Electrophoresis forces; not to scale. Alternating DEP voltage (red arrows and signs) of 8 $V_{\text{peak-to-peak}}$ and fixed EP voltage (black arrows and signs) of 100 mV.....	102
3.26	Schematics of (a) representation of contacted NW and (b) schematic of the resulting band alignment.....	103
3.27	Forward IV characteristics of as fabricated Ge NWs devices fabricated at DEP frequencies of (a) 500 Hz, (b) 1 MHz and (c) 10 MHz all fabricated with a peak-to-peak DEP voltage of 8 $V_{\text{peak-to-peak}}$	104

3.28	Reverse IV characteristics and gradient fitting lines of as fabricated Ge NWs devices fabricated at DEP frequencies of (a) 500 Hz, (b) 1 MHz and (c) 10 MHz all fabricated with a peak-to-peak DEP voltage of 8 V _{peak-to-peak}	106
3.29	(a) Forward Turn on Voltage and (b) Rectification Ratio (at +/- 1.5 V) as a function of DEP frequency.....	107
3.30	Theoretical band alignment of the Ge NWs-based devices. At low frequencies, the devices exhibit SCLC shallow trap states present in the collected NWs. Energy levels are relative for illustration purposes and are not absolute values.....	108
3.31	$\theta\mu$ as extrapolated by fitting the Mott-Gurney law to the IV curves as a function of DEP frequency.....	110
3.32	IV Characteristics of multiple Ge Nanowire devices fabricated with a DEP frequency of 10 MHz and a peak-to-peak DEP voltage of 8 V _{peak-to-peak}	111
4.2	Voltage divider system with DEP circuit topology.....	128
4.2	Images obtained by optical microscopy of devices fabricated at a DEP voltage of 8 V _{peak-to-peak} and frequency of 10 MHz. The voltage divider system was set with Rd = a) 0 k Ω , b) 16 k Ω , c) 22 k Ω and d) 33 k Ω	116
4.3	SEM images of ≈ 1 NW in devices fabricated at a DEP voltage of 8 V _{peak-to-peak} , frequency of 10 MHz and with a voltage divider resistor of 33 k Ω	117
4.4	I(V) characteristics of the aligned NWs at 1 MHz and AC field of 8 V _{peak-to-peak} , with a voltage divider resistor Rd=0 k Ω and 16 k Ω	118
4.5	I(V) characteristics of the aligned NWs at 10 MHz and AC field of 8 V _{peak-to-peak} , with a voltage divider resistor Rd=0 k Ω , 16 k Ω , 22 k Ω and 33 k Ω	119
4.6	Resistance of the device's measured between 10-11 V as a function of the voltage divider set-up resistor Rd.....	120
4.7	Spectral response spectroscopy at room temperature of an array (black curve) and single (red curve) Ge NW. At a DEP frequency of 10 MHz with a resistor of 0 k Ω (black curve) and 33 k Ω (red curve).....	122
4.8	Spectral response spectroscopy at room temperature of ≈ 1 Ge NW. The device is fabricated with NWs aligned at a DEP frequency of 10 MHz with a resistor of 33 k Ω	123
4.9	Optical responsivity of an array of Ge NWs (in black) and 1 NW (in red). Both devices have NWs aligned by DEP at 10 MHz with no resistor and with a resistor of 33 k Ω in the voltage divider system.	125

5.1	Raman spectra of the aligned Ge NWs after silanisation and a chemical representation of the 3-aminopropyl-triethoxysilane molecule.....	130
5.2	Raman spectra of the aligned Ge NWs after silanisation and glutaraldehyde monolayer. On the right is a chemical representation of the glutaraldehyde molecule.....	131
5.3	Raman spectra of the aligned Ge NWs after complete functionalisation; silanisation, glutaraldehyde and aptamerisation final monolayer. On the right are the chemical representations of protein molecules and their bases.....	132
5.4	(a) IV characteristics of as fabricated Ge Nanowire FETs, after functionalisation and exposure to increasing concentrations of the spike protein from 1 μ M to 1 nM. All devices were fabricated with a DEP frequency of 10 MHz. (b) shows the relative increase in the source-drain current, relative to a functionalised device at a bias of $V_{DS} = 2$ V.....	135
5.5	Control reference devices showing the relative variation in the source-drain current to a functionalised device with a) no NWs at a bias of $V_{DS} = 2$ V and b) functionalised NWs and increasing concentration of BSA protein at a bias of $V_{DS} = 2$ V.....	136
6.1	SEM images of the three different GaAsBi NWs.....	140
6.2	EDX chemical mapping of the three different batches of GaAsBi NWs.....	141
6.3	Raman Spectroscopy of the GaAsBi NWs.....	142
6.4	Bright field TEM images of the three different GaAsBi NWs batches in anisole after two months in solution.....	144
6.5	Calculated DEP force as a function of the frequency for GaAsBi NWs aligned at a voltage of 8 V _{peak-to-peak} on a 5 μ m electrode gap in anisole.....	146
6.6	Resistance as a function of time during DEP at a signal of 8 V _{peak-to-peak} and frequency of 500 kHz. The graphs are obtained by resistance approximation using a Matlab code calculation. The insets are SEM images of the respective NWs on the substrate.....	148
6.7	Example of DEP collection of GaAsBi nanowires; a) 500 kHz, b) 1MHz, c) 5 MHz, d) 10 MHz. This typical example is obtained from batch A.....	150
6.8	Inverse of time constant τ , describing the magnitude of the DEP force as a function of DEP signal frequency.....	151
6.9	IV characteristics of as fabricated GaAsBi nanowire devices at differing DEP frequencies and differing Bi % with a floating gate potential.	154
6.10	Reverse (top) and forward (bottom) voltage IV characteristics of GaAsBi NWs with Bi % 0.54 (batch A 140). DEP frequencies of 500 kHz, 1 MHz and 10 MHz with a voltage of 8 V _{peak-to-peak} . Below is a table of the gradients in reverse and forward voltage at differing frequencies.....	155

6.11 Reverse (top) and forward (bottom) IV characteristics of GaAsBi NWs with Bi % 1.74 (batch C 118). DEP frequencies of 500 kHz and 1 MHz fabricated with a voltage of 8 V_{peak-to-peak}. Below is a table of the gradients in reverse and forward voltage at differing frequencies.....156

6.12 Forward and reverse IV characteristics of GaAsBi NWs with Bi % 0.79 (batch B 136). DEP frequency of 500 kHz fabricated with a voltage of 8 V_{peak-to-peak}. Below is a table of the gradients in reverse and forward voltage at differing frequencies.....158

6.13 Fitting mobility on forward IV response of batch A. The table below summarises the obtained fitting mobility.....160

6.14 Fitting mobility on forward IV response of batch C. The table below summarizes the obtained the fitting mobility.....161

6.15 Normalised spectral responses as a function of the energy measured at room temperature. Devices fabricated with NWs aligned at a DEP frequency of 1 MHz. The pink line shows the GaAs band gap at 1.42 eV.....163

6.16 Optical responsivity of an array of GaAsBi NWs aligned at 1 MHz with a Bi % of 2.5 % in A (red curve) and **1.5 % in C (black curve)**.....166

Appendix

A.1.1 Schematic of Ohmic contact with p-type semiconductor. 232

A.1.2 Schematic of Schottky contact with n-type semiconductor. 233

A.2.1 Responsivity of commercial Silicon photodiode from Thorlabs..... 234

A.2.2 Responsivity of commercial InGaAs photodiode from Thorlabs. 234

A.2.3 Bright field image of clustered Ge nanowires and its EDX analysis..... 235

A.2.4 DEP force and CMF; Matlab calculation.....236

A.2.5 Calculated DEP force along the long axis as a function of the frequency for Ge NWs aligned at a voltage of 8 V_{peak-to-peak} on a 20 μm electrode gap in anisole. 239

A.2.6 Calculated DEP force along the short axis as a function of the frequency for Ge NWs aligned at a voltage of 8 V_{peak-to-peak} on a 20 μm electrode gap in anisole. 239

A.2.7 SEM images of collected Ge NWs at a voltage of 8 V_{peak-to-peak} and frequency .. of 500 kHz a)-c) and b)-d) are groups from the same device..... 240

A.2.8 Images obtained by optical microscopy of burned-off Ge NWs aligned at a) 10 V_{peak-to-peak} and b) 16 V_{peak-to-peak}.....241

A.2.9 Images obtained by SEM of aligned Ge NWs in a) rectangular and b) round end tip gap electrodes.....	242
A.2.10 TIA circuit topology, with the main DEP set in the brown box and TIA in the dashed box.....	243
A.2.11 Real-time resistance monitoring code; Matlab computataion.....	244
A.2.12 Images obtained by optical microscopy; a) 500 kHz, b) 1 MHz, c) 5 MHz.....	249
A.4.1 3-Aminopropyl-triethoxysilane (APTES) molecule with amine (NH ₂) group.....	251
A.4.2 Glutaraldehyde molecule.....	251
A.4.3 Protein Molecule; Oligomeres and their Amino acids (Bases).....	252
A.4.5 Control test current-voltage curves from a functionalised device fabricated with a DEP frequency of 10 MHz, after multiple exposures to PBS solution (with no spike protein), the sample was rinsed and dried between each exposure.....	254
A.4.6 a) is the I(V) response of the Ge NWs device before and after functionalisation, b) is a schematic of the underlying mechanism before the aptamer layer with holes carriers in the p-type Ge NWs (represented in red dots) and c) after deposition of the positively charged aptamer layer and depletion of holes.....	255
A.5.1 Dark field SEM image of the NWs from batch A 140.....	256
A.5.2 Dark field SEM image of the NWs from batch B 136.....	257
A.5.3 Dark field SEM image of the NWs from batch C 118.....	258
A.5.4 Bright-field images obtained by TEM of the oxide layer measured to be 3 nm thick on the GaAsBi NWs after two months in anisole.....	259
A.5.5 Diffraction pattern of the GaAsBi NWs.....	259
A.5.6 Calculated real part of the CMF along the long axis as a function of the frequency for. GaAsBi NWs aligned at a voltage of 8V _{peak-to-peak} on a 5µm electrode gap in anisole.....	260
A.5.7 Calculated real part of the CMF along the short axis as a function of the frequency for GaAsBi NWs aligned at a voltage of 8V _{peak-to-peak} on a 5µm electrode gap in anisole.....	260
A.5.8 Calculated real part of the Clausius Mossotti factor as a function of the frequency for GaAsBi NWs aligned at a voltage of 8 V _{peak-to-peak} on 5 µm electrode gap in anisole.....	261

A.5.9 Optical microscopy images of dielectrophoresis alignment of GaAsBi NWs
aligned at a voltage of 8 V_{peak-to-peak} and frequency of 5 MHz on 5 μm electrode
gap..... 262

A.5.10 Normalised spectral response as a function of the wavelength at room temperature.
Devices fabricated with NWs aligned at a DEP frequency of 1 MHz. 263

List of Tables

1	Materials properties	9
2	Table summing and comparing the different alignment techniques.	21
3	Materials characteristics.	75
4	Summary table of the mediums' characteristics.	80
5	Photodetector nanowire-based responsivities found in the literature	126
6	Raman vibrational peaks from the literature cited above and from the present work.	143
7	Materials characteristics.	145
8	Measured cut-off energies and corresponding incorporated Bi %.. . . .	164
A.3.1	Table of single NWs resistivity found in the literature.	250
A.4.4	Comparison of bulk and semiconductor nanowires mobility as a function of the apparent surface morphology.....	253

Chapter 1

Introduction

With Moore's law progression, integrated circuit technologies have seen significant growth of interest in generating electronic and optoelectronic devices with increased sensitivity, speed, and reduced power consumption. Wildly described by Moore's Law, the down-scaling technology has its limits, principally the top-down fabrication approach [1]. In this respect, bottom-up material fabrication control at the atomic scale (controlled size, composition, and doping) of one-dimensional (1D) nanostructures are the key. Semiconductors being the backbone of previous and upcoming technologies, semiconductor nanowires are showing the way to lead next-generation of sensing technology.

1.1 Significance of nanomaterials for sensing technology

Sensing devices can detect optical, physical, or chemical properties changing in the surrounding environment. Changes that are transferred as a signal to be read by users. The original Moore's prediction stipulates that around 2030, down-scaling technology will reach its limit for Complementary Metal Oxide Semiconductor (CMOS) and other Field-Effect Transistors (FETs). Sensing technology is capable of detecting changes in chemical species concentration [2], pH [3], pressure [4], temperature [5] and optical properties [6]. Beyond detection, most of the sensing technology is a combination of functional diversification. Known as "More than Moore", that recent trend is the product of research with the original aim of technology miniaturisation. To overcome Moore's law, growing innovation borrowed from silicon technology is not anymore exactly on the same line and scale as Moore's predictions. The following schematic Figure 1.1 illustrates the diversification of innovation originally based on Moore's law. This trend has accelerated the semiconductor industry production and research, especially on non-silicon materials like germanium and III-V semiconductors ("Life after Silicon" [8]).

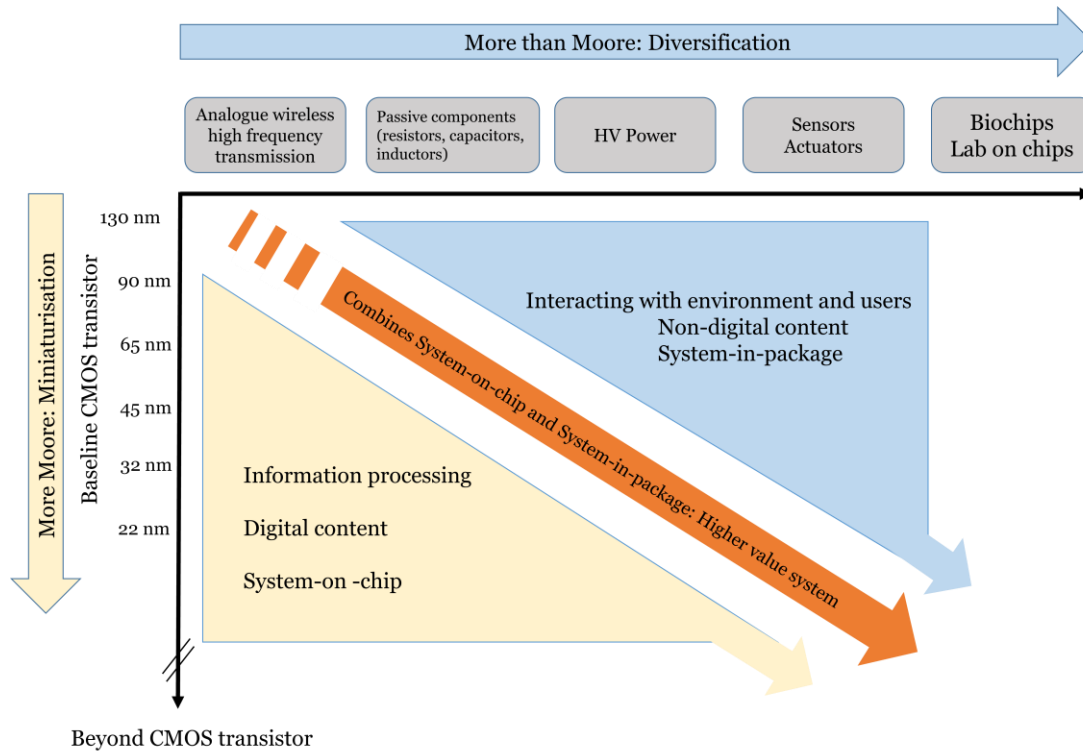


Figure 1.1: More than Moore's status roadmap.

Extracted from [7]. *Note; System-on-chip is a system that contains other chips on a single chip (more than one CPU, micro-controllers, digital signal processors, etc.). System-in-package combines different functionalities in a single unit (passives + MEMS + optical devices, etc.).*

Moreover, that diversification leads to technology like CMOS combined with Micro Electronic Mechanical Systems (Sensors and actuators system-in-package) and with FETs [7]. This thesis is focused on sensing and actuator technology at the heart of the "More than Moore" trend and within miniaturisation objectives. Together with miniaturisation, sensing nanotechnology opens up a large variety of possibilities in particular due to the high surface-to-volume ratio making nanomaterial very sensitive with low power consumption and fast response. Nanomaterials can allow the detection of small amounts of molecules, photons and mechanical displacements that are used for medical screening and diagnosis [9] and photodetection for solar cells for example [10]. For those applications, sensitivity, nanometer-scale size, robustness, low power, ease to use, low cost and versatility are desirable. However, those requirements have not yet been reached by the present nanotechnology [11]. To realise the integration of nanoscale technology, nanomaterials have to be of optimum good quality to reach the desired performances. Semiconductor nanowires are the main topic of this thesis. Nanowires have quasi-one-dimensional nature and can be grown axially or radially and/or directly onto existing silicon device systems.

Moreover, they have the ability to adapt to strains during growth and present fewer dislocations than for bulk or thin film materials beyond the fact that nanowires are monocrystals [12].

Hence, because of their dimensions, nanowires also enable control of the density of states, band-gap and electronic transitions that are determined by material chemistry and geometry. Fundamentally, they can provide a sensing platform that is not possible with conventional planar and bulk semiconductors but also they offer considerably reduced cost and material utilisation [13]. Similarly to a transistor, semiconductor nanowires are the sensing channel detecting changes in the environment [14]. Nanowires have already shown their potential notably in Field-Effect-Transistors applications [15] and sensing devices [16]. Despite significant knowledge refinement, properties like; charge carriers transport, surface dynamics, environment and size effect of the NWs are still rising redundant questioning. Besides, their manipulation and integration into devices are also remaining challenges.

1.2 Significance of Dielectrophoresis

With "More than Moore" progression and down-scaling, nanomaterial implementation brought new challenges. As outlined, nanowires already started to show the way for future nanotechnology. To keep up with miniaturisation, new techniques and equipment development were necessary for nanomaterial manipulation. The methods used for implementation will affect and determine the final device performances as much as the synthesis of the materials.

Implementation of nanowires in devices can be either vertical or horizontal, as an array of nanowires and even individually. The nanowires can also either be used attached to the growth substrate [17] or detached post-synthesis and transferred onto another system [18]. Several techniques have been developed for controlling the placement of nanowires, each has its specificity depending on the final channel connection and device structure. Sensing performances will require the semiconductor to be of high quality (crystallinity, low defects, purity, conductivity, compatibility) and so the implementation technique will have to be optimal to avoid damage. Effectually, manipulation and assembling of the nanoparticles in precise locations and orientations are critical stages and are still very challenging concerning repeatability and quality. Only then can practical applications of the device progress and probing or bio-functionalisation can be performed so that the nanowires can interact with a system and its surface can interact with the environment. Part of the challenge is first to locate the nanowires; either with the help of a medium (particles in liquid) or in dry environments. Existing methods of "pick and place" such as lasers (optical tweezers) [19] or scanning probe microscopy/atomic force microscopy [20] can accurately locate nanoparticles with the help of powerful microscopes even scanning electron microscopy [21]. On a large-scale production and low-cost scheme, the need for initial localisation is not ideal.

To address this issue, indirect contact for moving particles with precision can be done by means of dielectric properties, fluid dynamics, chemical properties or electrostatic [22]. Amongst the existing reported techniques that respond to low-cost, accuracy, low damage, label-free, and large-scale feasibility, dielectrophoresis is the most suitable and is extensively investigated in this thesis.

Intending to improve electrical engineering and electronics in line with miniaturisation and diversification, dielectrophoresis control exploits simultaneously the dielectric properties of the nanoparticles for placement and selection. More than that, the dielectric parameters and interactions between particles and dielectrophoresis allow the technique to "scan", sort and select nanowires of different lengths, conductivity, and morphology from a batch of many nanowires (say $\approx 36 \times 10^3 \text{NWs/mL}$ in $4 \mu\text{l}$ of solution). Such possibilities have tremendous potential for nanoparticle manipulation, combining direct analysing/selection and placement ("pick and place") without the help of a microscope. Such selection ability received a lot of attention for nanowires-based devices and a lot of efforts have been made to optimise further this assembly technique that differs with liquid mediums, particles, electrodes and dielectrophoresis parameters (voltage, frequency).

1.3 Motivation and thesis overview

The overarching ambition of this thesis is to investigate germanium and gallium-arsenide- bismuth nanowires-based device performances fabricated by dielectrophoresis. With the aim of pushing the intricacies of dielectrophoresis further from optimum preparation to final sensing properties and by tailoring electrical and optical properties. **Chapter 2** presents the central core of the fundamental principles of sensing technology based on semiconductor nanowires. It presents semiconductor nanowires including nanowire growth and implementation techniques. With a focus on dielectrophoresis principles and theory, are also proposed adjustments and refinement of dielectrophoresis equations for nanowires. Previous work on semiconductor devices such as transistors and sensor building blocks technology is exhaustively described in addition to the conduction mechanisms and carrier transport keys to technology improvements. A description of the materials' fabrication and characterisation is detailed further. The nanowires growth techniques for germanium and gallium-arsenide-bismuth are explained as well as the procedure for the electrode platform fabrication. All the equipment and methods are described for surface, chemistry, morphology, optical and electrical analysis performed in this work. In **Chapter 3**, the germanium nanowires are characterised and the dielectrophoresis parameters are investigated. To do so, different mediums, electrode designs, electric field lines and gradients are inspected for the optimum conditions of nanowires alignment.

Moreover, dielectrophoresis refined calculations are used to pre-estimate further the nanowires' collection behaviour. At the centre of **Chapter 3** also lies a complete scientific and experimental study of the influence of dielectrophoresis parameters (voltage and frequency) on the carrier transport and performances of the final high-quality and reproducible diode devices. Part of this work resulted in a publication [2] and was presented at UK-semiconductor-2019 and Bio-Med-Eng-2021 Conferences in Sheffield. Through a fabricated resistance monitoring set-up and electrical characterisation, **Chapter 3** additionally highlights dielectrophoresis selectivity and crucial surface chemistry as well as the possibility of combining other electrokinetic mechanisms for further alignment control and device characteristics. From **Chapter 3 to Chapter 5**, the presented work is focused on germanium nanowires. **Chapter 5** reports the first demonstration of one single germanium nanowire aligned between two electrodes using dielectrophoresis coupled with a simple and innovative voltage divider system. Using the dielectrophoresis parameters studied in Chapter 3, the voltage divider system is evaluated for single nanowire alignment. Afterwards, the obtained single germanium nanowire devices are analysed for their electrical and photo-detection properties. **Chapter 5** blends scientific and experimental research on optimum dielectrophoresis parameters for the fabrication of a nano-scale biosensor for the detection of the protein of the SARS-Corona Virus-2 using surface bio-functionalisation. The first part shows the characterisation of the functionalisation layers on the nanowires' surface and the second part demonstrated the selectivity and sensitivity of the devices with exposition to different concentrations of protein. This work was published [2] and presented at the Bio-Med-Eng2021 Conference.

For the first time, synthesised gallium-arsenide-bismuth nanowires-based devices are analysed using dielectrophoresis in **Chapter 6**. The nanowires are characterised and dielectrophoresis optimum parameters are investigated for this semiconductor. Electrical experiments demonstrate further the importance of surface morphology and the importance of nanowires synthesis and its impact on future devices. Furthermore, bismuth content in gallium-arsenide, the length, surface roughness and morphology of the nanowires are considered to be dielectrophoresis sensitive and to influence carriers' mobility. In addition, the photodetection characteristic of the nanowires device is investigated by means of spectral response measurements allowing simultaneous analyses of bismuth content and its importance on the responsivity and band-gap engineering. Finally, **Chapter 7** provides a closing conclusion and outlook on possible work and research for further improvement towards nanowires sensing technology using dielectrophoresis control.

1.4 Semiconductors Nanowires, fundamentals and previous work

Regarding electrical conductivity properties, semiconductors are a group of material intermediate between metals and insulators. In an atom, electrons occupy discrete energy levels (different levels of an atom's "shells"). Atoms brought together to form a solid will have their energy level split into energy bands instead of discrete energies like for free atoms. In a simplified description, electrons close to the nucleus (electrons in the valence band) and bound to their atoms are not able to participate in conduction and electrons far from the nucleus (electrons in the conduction band) have more freedom between atoms and available electrons bounding with other atoms and travelling through the material. The band theory models the behaviour of electrons in a solid with the energy bands represented in the following Figure 1.2

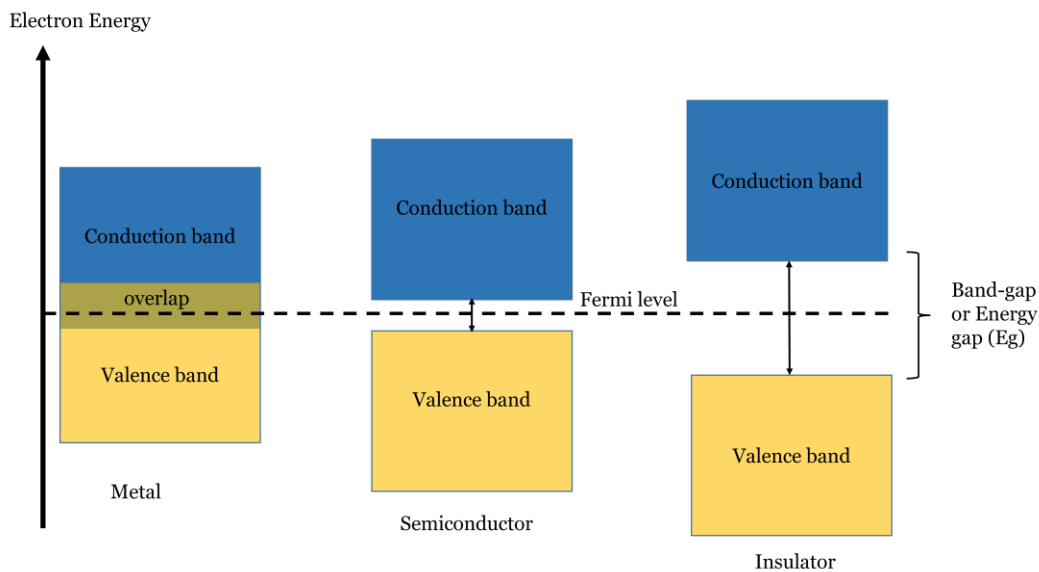


Figure 1.2: Energy band diagrams in metal, semiconductor and insulator.

At absolute zero temperature (0 K) the valence band is separated from the conduction band by the energy gap (E_g) and semiconductors or insulators cannot conduct. The Fermi level (as represented in Figure 1.2) is the highest energy level that an electron can possibly occupy at 0 K . From positive temperature, say room temperature, electrical conduction is possible through a variety of stimulation that enables electrons to be excited and go to the empty states in the conduction band. Nevertheless, at room temperature, for instance, the energy gap still dictates the semiconductor properties. Electron allocations in the energy bands are dominated by the energisation stimulation rate (heat, light, electromagnetic waves, strains, etc.).

In intrinsic semiconductors, atoms linked together by their orbital valence electrons form a covalent bond that provides cohesiveness of the matter. Atoms and bonds form the repeating structural unit, the regular geometric network of the material. Solid materials such as semiconductors can be of different structures, amorphous or crystalline depending on the atom arrangement expressing the degree of order of the repeating structural unit. The number of free electrons (high energy level \approx one in 10^{12} valence electrons in Si for example) have similar behaviour to those found in metal. When the material undergoes an electric field (at room temperature RT), valence electrons display mobility as well as a drift velocity that creates a conduction current. That conduction current is much lower than in metal that has more free valence electrons. In semiconductor crystals, energy bands broaden due to interactions of consecutive overlapping atomic orbitals creating a separation gap between the low energy band (valence E_v) and the high energy band (conduction E_c). As mentioned, enough applied energy will allow valence electrons to move to the conduction band and to be free and create conduction within the material. At the macro-scale, the crystal semiconductor can be a monocrystal or made of polycrystals. In an ideal mono-crystalline semiconductor (compared to polycrystalline or amorphous) there is no electronic states between the valence edge and conduction edge band. A free electron from its valence band will leave behind a hole of opposite polarity; an applied electric field will cause both carriers, electrons and holes to drift in opposite directions creating conduction. The III-V semiconductor groups like Ga, As and Ge, as well as compounds like InP and GaAs have been studied as a replacement for Si. Crystalline Si and Ge differ from elements of group III-V (except for AlSb) because of their indirect band-gap where at the smallest band separation, electrons transition is not vertical and needs more energy and momentum to transit [23]. Hence, with an indirect band gap a photon cannot be emitted as it transfers momentum to the crystal. Direct band gaps for compound materials like GaAs or InAs have electrons that can be directly excited to the upper band. Figure 1.3 shows the energy band structure of Ge, Si, and GaAs and Table 1 shows more details on the materials' properties.

This is where the interest in semiconductors lies; band gaps and the possibility to tune and alter them by engineering can create desirable electrical and optical properties. Carriers, electrons and holes in materials have different effective masses that depend on the nature of the semiconductor, band and crystal structure. Holes are heavier than electrons and tend to move slower in the material than electrons, hence their masses influence their mobility. By extension, the different carriers' mobility of semiconductors can be limited by the material's lattice crystal structure (defects, doping).

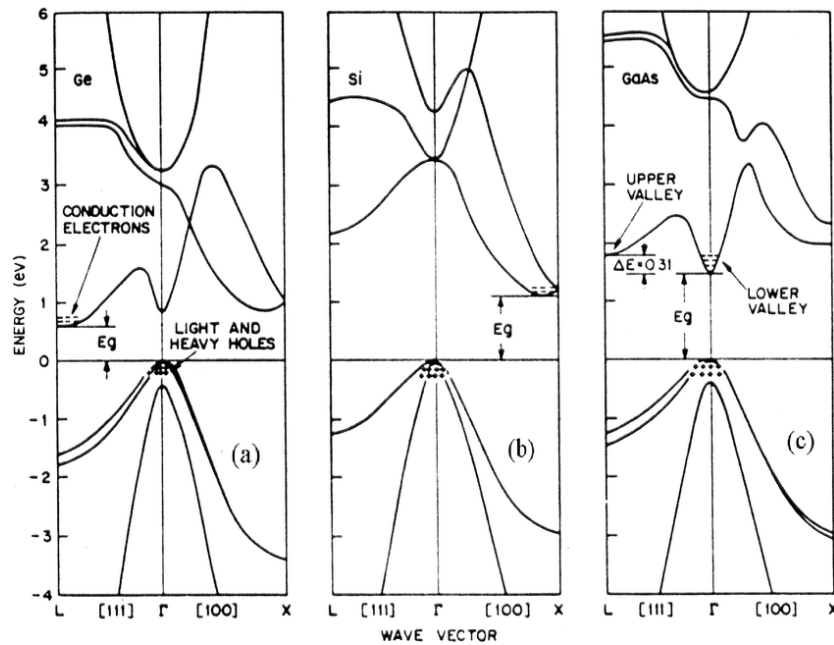


Figure 1.3: Energy band structure of (a) Ge, (b) Si and (c) GaAs.

From [23].

1.5 Nanowires

Nanowires (NWs) are quasi-one-dimensional single crystalline structures, they are defined as materials with at least one dimension between 1 and 1000 nm and are usually described as having 1 to 100 nm of diameter. By extension, compared to bulk and 3D material their electrons movement is only along the x - y -axis. Nanowire growth presents remarkable established properties during synthesis. In particular, the relaxation of the lattice from strains at the region of interfaces (on mismatched substrates) allows the crystal to be dislocation free while thin films or bulk are prone to defects and dislocations during growth [24]. Such crystal fabrication provides control on key properties; electronic properties like the density of states and carrier transport and hence it can be directly integrated with already existing Si technology [25]. From a physical point of view and compared to 2D (thin film) and 3D (bulk) the fundamental asset of NWs is their 1D nature where carriers flow directly from one point to another. Carriers in matter move in a random direction and change direction if they collide with an atom of the lattice. Compared to their bulk counterpart, in NWs, carriers' movement is confined at the nanoscale along the x - y axis and is even described as "quasi" one dimension along the long axis [26]. Because of the reduction of the transport path at the scale of the NW core, the chances of collision are reduced for well-structured NWs crystals with an optimal mean-free path. Semiconductor NWs have the unique potential of band gap engineering by tailoring their size, shape and doping, to respond to any demand of application function.

For instance, the optical and electronic properties of semiconductors greatly depend on the crystal size at the nanoscale [27]. Moreover, advantages of NWs for sensing properties emerge from their surface, where atoms undergo different environments than bulk material. Reactions at the surface of bulk material are mostly not influencing the properties of the whole material. Surface to volume ratio is higher for nanomaterial and surface events are critical making NWs interesting for sensing as they greatly increase the limit of detection. Nanomaterials size also provides reduced reflection and excellent light trapping providing photovoltaic less total cost [28].

Moreover, the diminution of electrical components by using NWs allows a higher integration density with more devices, functions and improvements. After growth, most of the semiconductors have a surface oxide layer that provides a natural gate (field effect transistor structure) that combined with the channel core controls the channel conductivity. These interesting properties make NWs promising nanosensors because of their sensitivity and tunable channel conductivity. They have proved their value in FET applications [15], photodetectors [29], light-emitters [30], solar cells [28] and sensing devices [16] and diodes [31]. NWs with dimensions lower than the Bohr radius have been used for their quantum confinement effect and implemented for resonant tunnelling diodes [32] and single electron transistors [33]. Quantum confinement modifies the nanocrystal band-gap structure and density of states because of degenerated split bands affecting occupancy level, electron transitions, mobility and density of the carriers. In such dimensions, NWs electrons behave differently where they are not considered like particles and the energy band becomes dependent on the size. In general NWs dimensions that are $\approx 30\text{-}200$ nm do not exhibit quantum effect [34], Table 1 shows examples of materials' Bohr radius.

Table 1: Materials properties.

	Germanium (Ge)	Silicon (Si)	Gallium Arsenide (GaAs)	Bismuth	Gold (Au)
Direct Band Gap (eV)	0.88	1.17	1.42	0.15	NA
Indirect Band Gap (eV)	0.66	1.12	1.71	0.38	NA
Fermi level (eV)	0.72	0.56	0.77	0.1	5-53
n/h mobility ($\text{cm}^2\text{V}^{-1}\text{s}^{-1}$ at RT in bulk)	$\mu_n=3800,$ $\mu_h=1800$	$\mu_n=1500,$ $\mu_h=450$	$\mu_n=8500,$ $\mu_h=400$	NA	$\mu_{n-h} \approx 30\text{-}50$ (Au, Cu, Ag)
Bohr Radius (nm)	50 (longitudinal) 400 (transverse)	40 (longitudinal) 90 (transverse)	12	NA	0.174

NWs surface is a crucial factor; roughness, morphology, and chemical nature (dangling bound) have an impact on NWs sensitivity, transport characteristics and by extension exchange of information with the environment that is part of the future sensing performances. To a point where surface passivation treatment is usually done (if not natural in the air) to protect or modify the NWs and their intrinsic electrical properties. NWs synthesis is able to fabricate nanoparticles and NWs of many different chemical elements, structures, sizes, and shapes, even with a protective shell of another material to avoid surface oxidation and tailor new properties. This is why synthesis is a very important step for the fabrication of sensing technology.

1.6 Nanowires growth and implementation in technologies

Integration of NWs in devices has an advantage over common planar devices (like thin films FET); it can be done in many different approaches that will depend on the NWs fabrication method categorised as "bottom-up" or "top-down". The "top-down" way is a subtractive model where the material is removed from bulk, using etching or electron beam lithography (EBL) for instance. Inversely, the "bottom-up" approach can be described as an additive mode where the material is scaled-up (like a tree growing from seeds) from a reactive precursor. NWs synthesis methods are described in the following sections.

1.6.1 Top-down integration techniques

To create increasingly smaller structures down to the nanoscale, conventional lithography techniques have evolved. Top-down NWs fabrication can be done by chemical lithography, using a resist stencil material or physical lithography using an electron beam. Chemical lithography is one of the main techniques currently used in the microelectronics industry. A photoresist film (polymers like SU8 or poly-methylmethacrylate (PMMA)) is deposited on a single crystal wafer or bulk surface and by photoreaction, develops a pattern designed from exposure of a stencil or a mask. As the NWs are fabricated at specifically defined locations, the top-down approach allows simultaneous integration of the circuit parts at a chosen area and assembling of the device. The wavelength of light used in the photolithography technique limits NWs' resolution generally not suitable for small NWs (below 100 nm standard limitation) [35]. Although in development, shorter wavelengths like extreme ultraviolet and X-ray allow resolution down to 10 nm allowing higher resolution for high-quality lithography.

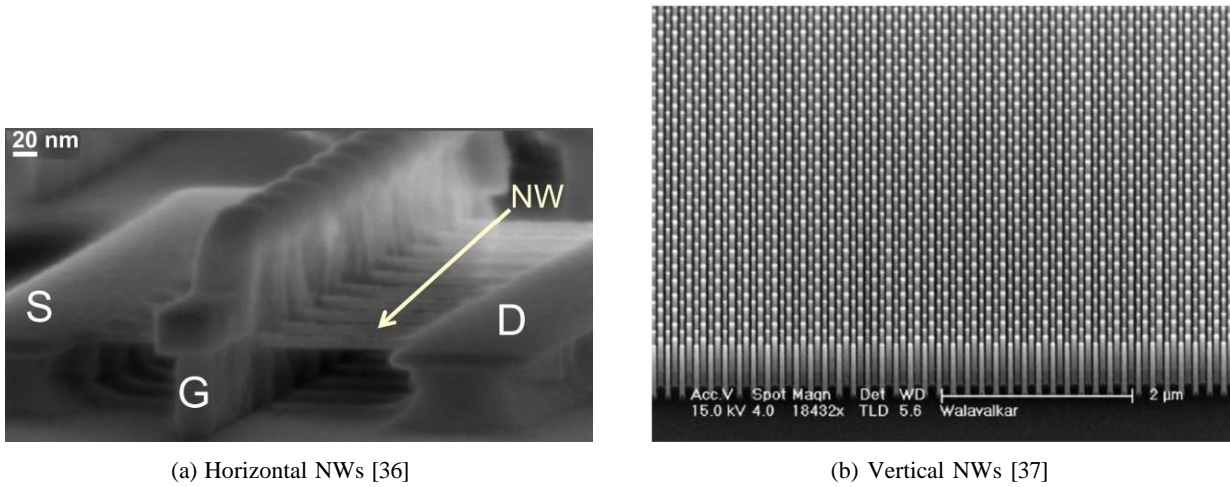


Figure 1.4: SEM images of top-down NWs fabricated by electron beam etching (EBL).

High resolution of lithography is usually achieved using EBL with possible patterns down to 20 nm. EBL is a direct writing method that does not require a shadow mask and where a beam of electrons is used as a "chisel" to carve down bulk material. It offers the possibility to obtain highly organised NWs horizontally or vertically as shown in Figure 1.4.

The top-down method has been found to have resolution limitations, yielding surface roughness to the detriment of sensing properties as well as an increasing cost associated with increasing time of fabrication [38]. In addition, synthesis by top-down limits the final NWs chemical structure to the fixed starting material. The bottom-up method represents an alternative to the top-down fabrication. It enables more accessible possibilities and imagination for new device ideas.

1.6.2 Bottom-up integration techniques

In comparison with the top-down method, NWs fabricated via bottom-up are chemically grown by absorbed atoms of chosen nature offering more control over their dimensions, shapes and chemistry.

The most used technique for NWs synthesis via bottom-up is Chemical Vapour Deposition (CVD); CVD gathers a well-known group of methods used in microelectronics such as laser-assisted catalytic growth, Metalorganic Vapour-Phase Epitaxy (MOVPE) and Molecular Beam Epitaxy (MBE). The first NWs growth has been elaborated in 1964 by Ellis and Wagner [39] and was named the vapour-liquid-solid (VLS) mechanism standing for the three different states of the deposited material. It uses metal particles or nanoclusters that act as a catalyst or seeds and form a liquid alloy with the growing material. In the example of growing Si NWs those nanoclusters act as advantageous energetic sites for the volatile gaseous precursor (SiCl_4 or SiH_4 precursors) absorption and decomposition.

The precursor is transported in a heated reactor by an inert gas flow (Ar or H₂) to the seed particles (or nanocluster). As the precursor vapour blends with the nanocluster, it changes to a liquid phase and diffuses toward the liquid-solid interface by a concentration gradient. In the nanocluster, the material precursor concentration increases up to a solubility threshold point established by the binary phase diagram. Figure 1.5 A) shows the Au/Si nanocluster precursor binary phase diagram. At 500 °C, the Au/Si mixing containing more than ≈ 20 % of Si will have Si crystallising (also called nucleation) at the interface nanocluster/substrate. At the base of the nanocluster, a NW starts to grow by epitaxy layer after layer concentrated on the nanocluster. Cui *et al.* have shown that Si NWs grown by VLS were having a diameter dependent on the Au nanocluster size [40] giving control on the NWs' final diameter.

Nanoclusters on the substrate can be obtained in different ways;

- By lift-off nano-structuration
- By thin film dewetting
- By the use of a colloidal solution

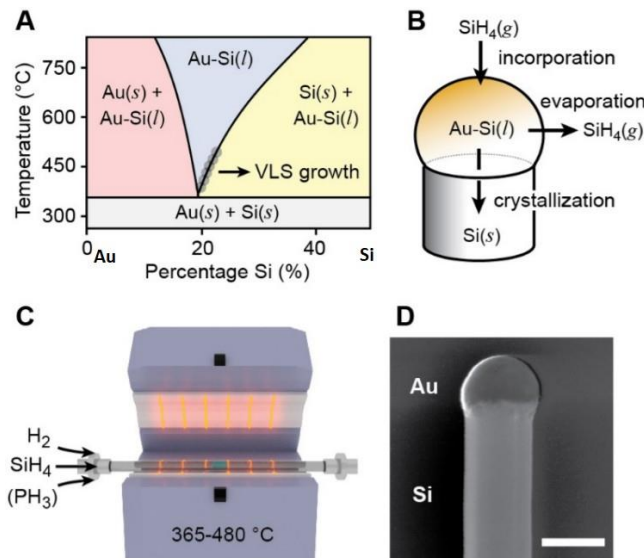


Figure 1.5: Vapor-Liquid-Solid method; A) Binary phase diagram of gold and silicon B) Si crystallisation mechanism C) Heated reactor with inert gas flow D) SEM image of a Si NW grown using an Au nanocluster of 150 nm in diameter; scale bar, 150 nm.

From [41].

Nanostructuring by lift-off is an expensive and time-consuming process as it also requires EBL to generate a lift-off mask. Thin film dewetting on the other hand is a rather fast and cheap method. It consists of a thin film on a substrate that dewets and agglomerates into islands when heated. The issue with that technique is the increasing size of the nanocluster island during the growth of the NWs with annealing. A possible way to overcome tapering morphology is a pre-treatment of the substrate surface which inconveniently add more steps [42]. Colloidal solutions for NWs growth are mixture solutions of insoluble nanoparticles showing good control over the diameter size of the nanoparticles during growth [43]. The nanoparticle solution is usually drop-casted on the substrate and placed in the synthesis chamber. In this work, the Ge NWs were grown by using gold nanoparticles in solution as nanoclusters deposited on a Ge substrate. M. Bosi *et al.* demonstrated the advantage of growing germanium NWs by using nanoparticles colloidal solution over dewetting technique [44]. In addition to Ge, GaAsBi NWs were grown using Molecular Beam Epitaxy using Ga nanoclusters deposited on an unknown substrate. The laboratory where the GaAsBi NWs were grown kept the synthesis protocol confidential and hence only the basics on the growth are explained.

1.7 Towards nano-manipulation

It is possible to create either a single nanowire or a NWs network-based device. Unlike polyhedral and spherical nanoparticles, NWs are long enough to be relatively easily integrated into microstructures due to their wire shape. In order to fabricate NWs devices, one of the most important and challenging steps is the NWs manipulation and implementation. It is possible to grow NWs directly on a functional surface and avoid the assembly step, or isolate NWs synthesis from their assembly. As seen in the previous section and Figure 1.4, top-down NWs fabrication is highly time and cost-consuming. Usually, a couple of NWs are fabricated with specific placement and electrical contact is deposited on the top. The top-down technique for NWs implementation lacks versatility and accessibility.

After growth, NWs have to be found, selected and manipulated. Once removed from the substrate they have a random orientation and alignment. Implementation techniques via a bottom-up approach have been already developed to direct assembly into a chosen configuration. Separation of NWs growth from the assembly step has the benefit that the growth conditions are preserved and the NWs can be manipulated afterwards. There are different methods for NWs assembly by a bottom-up approach, either by direct contact using atomic force microscopy (AFM), optical tweezers or indirect-contact like microfluidics (electrokinetics) with which most of the time uses NWs solution that is cast on substrate or electrodes.

Using different kinds of electrokinetic forces interaction between NWs and the surface one can direct the NWs to final orientation without "touching" them avoiding risks of damage. Methods like Langmuir Blodgett [45], electric or magnetic field-assisted assembly [46, 47], contact printing [48], blown bubble film [49, 50], optical trapping [51], microfluidic assembly [46], chemically driven assembly [52] are widely used and have proven to be promising alignment techniques. Those techniques are described in more detail in the following subsections.

1.7.1 Chemical or electrostatic interaction

NWs in solution deposited on a substrate will have a random orientation. Their placement will depend on their interactions (hydrogen bond, van der Waals, electrostatic) with the surface. Precise placement and selection can be obtained by initial chemical or biological surface treatment resulting in engineered interaction without using external forces. Biological or molecular ligand binding is attached to the NWs surface by functionalisation and can interact with a surface treated with a complementary bond. In this way, it is possible to tailor specific contact and orientation by using hydrophobic or hydrophilic interaction for instance. By extension, using a variety of antibodies and their targeted proteins it is possible to have specific collection and binding, and even create complex structures. This technique is helpful for recognition, combination and placement. The team of Lee *et al.* used functionalised NWs to assemble them on pre-patterned electrodes using DNA hybridisation [53]. They functionalised NWs and the substrate surface by complementary DNA strands creating a selection and recognition mechanism. The limitation of that technique is the necessity to use pre-treatment and functionalisation of both NWs and host surface resulting in possible undesired reactions and inaccurate alignment.

1.7.2 Shear force interaction

Shear force interaction also called "contact printing" is a rather simple assembly technique that consists of putting into contact directly as-synthesised NWs on the substrate with another surface. NWs on the substrate (ideally forest-like growth) are slid onto a receiver surface that is pre-structured defining "sticky" and "non-sticky" areas (van der Waals interactions). The sliding contact is very slow (20 mm min^{-1}) and has a well-defined and controlled pressure. The NWs are aligned with the sliding direction and are collected on the receiver substrate. Its main limitation is the contact that has to be very well controlled to not damage the NWs that in addition have to be long enough to fit the contact equipment settings. The technique is illustrated in the following Figure 1.6.

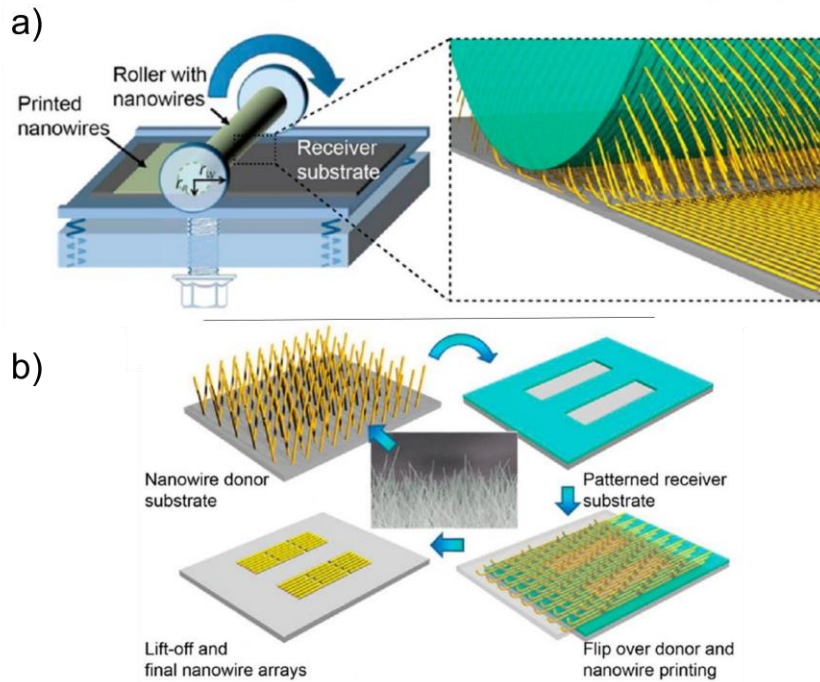


Figure 1.6: Assembly by shear forces. a) Roller placing NWs on a substrate, b) placement of NWs by contact printing. Extracted from [54].

1.7.3 Blown bubble film

Blown bubble film is a technique mainly used in the plastic film industry. From that, Yu *et al.* [49] got inspiration and applied blown bubble film to nanotechnology. NWs are dispersed in a polymer that can be shaped as a bubble using nitrogen with controlled gas pressure. As a consequence, the blown film (usually ≈ 100 nm thick) contains aligned and oriented NWs. It is possible to obtain large sheets of NWs film of 35 cm diameter and 50 cm large. The NWs films can be later used to be transferred on another large rigid, plastic or curved surface which makes it its main potential. However, that same potential is also a drawback as the NWs are enclosed within the polymer and it is possibly altering their properties and chemical nature. Reactive ion etching could potentially free the NWs from the polymer matrix which would add more steps and risk of damage.

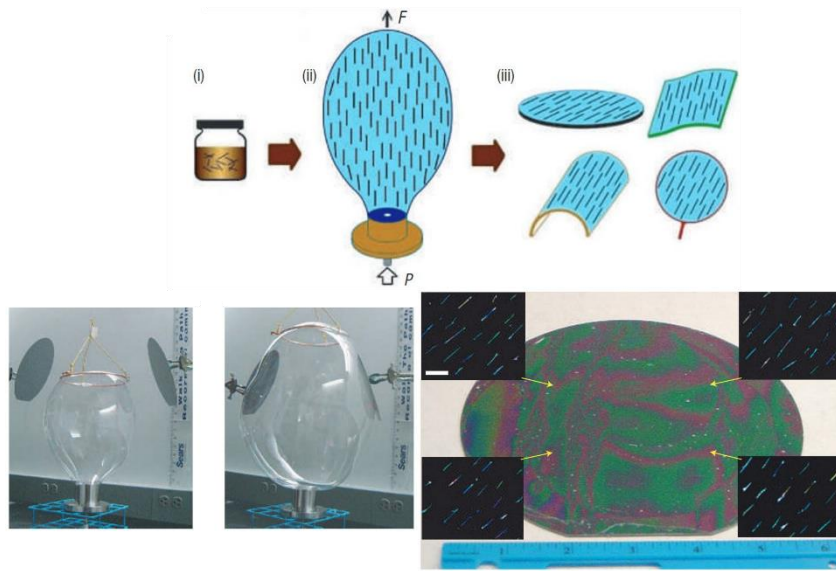


Figure 1.7: Blown bubble film technique. Top; NWs in bubble schematic, bottom images of the formation of the bubble with the NWs and placement on substrate by contact.

Extracted from [49].

1.7.4 Microfluidic force

Laminar flow from microfluidic channels can also be used to align NWs. In a solution, NWs undergo a stream flow in a channel, and to minimise the fluid drag they align in parallel to the flux direction [55]. Microfluidic channels are usually easy to fabricate using polymers like polydimethylsiloxane (PDMS) or polymethylmethacrylate (PMMA). The microfluidic channels determine the aligned NWs area (generally 100 nm). However, the bigger the channels the less uniform the fluid drag force will be.

According to the micro-channels design, it is possible to obtain different structures of aligned NWs by using a layer-after-layer method demanding good control of interactions between NWs and receiver substrate [56]. Huang *et al.* [46] found a way to control NWs and substrate interactions in the channel flow by combining it with functionalisation resulting in NWs network. The following Figure 1.8 shows aligned NWs obtained by microfluidic force and functionalisation.

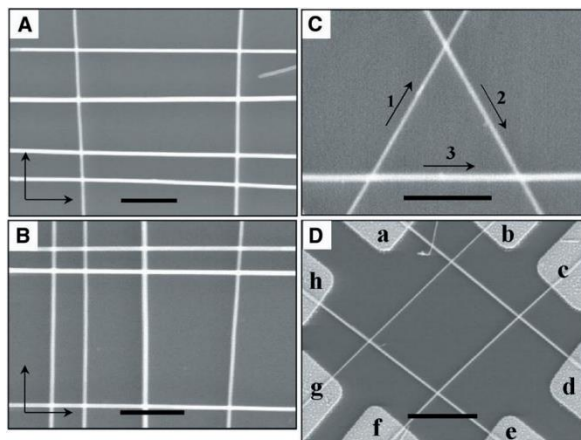


Figure 1.8: SEM images of layer-by-layer assembly of NWs by microfluidic and functionalisation deposition. The black arrows show the flow direction.

Extract from [46].

The microfluidic assembly process has great potential for geometrical integration in future devices especially if it is coupled with functionalisation and is compatible with flexible substrates.

1.7.5 Langmuir Blodgett

Langmuir Blodgett assembly method combines capillary forces followed by the removal of extra NWs. NWs, rendered hydrophilic are placed on the surface of a water-based solution described as a “microscopic version of logs-on-a-river” [57]. The solution undergoes a controlled uniaxial pressure aligning the NWs on the surface and forming a well-organised monolayer. By means of capillary force and surface tensions between the receiver substrate and the liquid, the NWs settle on the substrate. Similarly to microfluidic force, this method is versatile and can be used to form structures of NWs. This method asset relies on the fact that it is simple and can be used for large-scale deposition. In the following example Figure 1.9, the NWs networks are obtained by combining Langmuir Blodgett, surface functionalisation and photolithography [58].

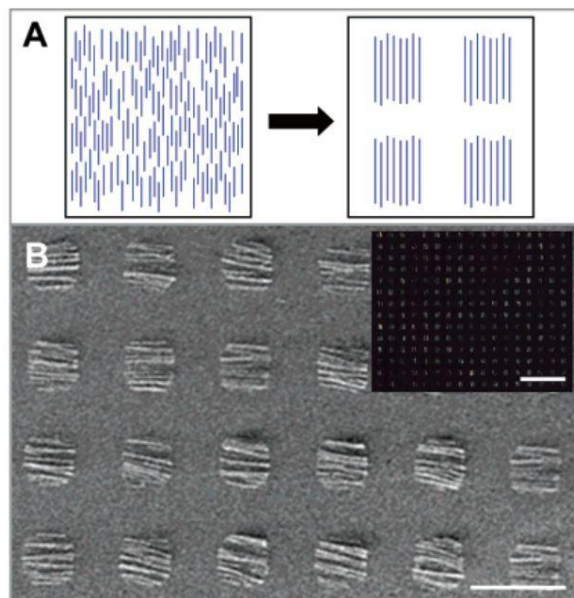


Figure 1.9: Network of crossed NWs aligned by Langmuir Blodgett.
Extracted from [58].

1.7.6 Dielectrophoresis technique

Dielectrophoresis (DEP) is based on the polarisation of particles through an electric field where induced charges move at the surface creating a dipole that aligns with the electric field. Aligned for the first time by DEP, gold NWs were assembled between electrodes forming a parallel network of NWs and are shown in Figure 1.10.

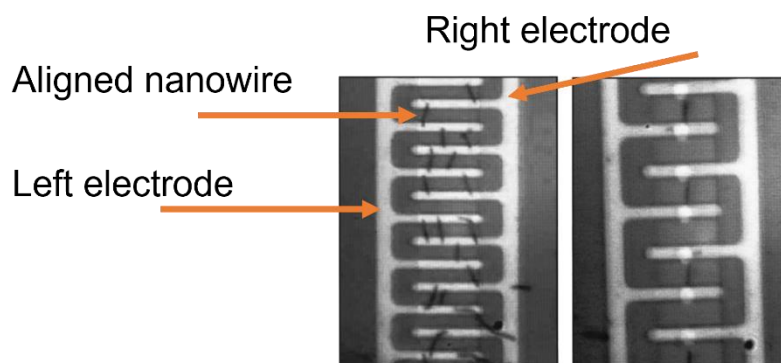


Figure 1.10: First DEP applied on gold NWs by Mayer *et al.* in 2000.
From [59].

DEP depends on the dielectric properties of the particles in relation to the dielectric properties of the medium within which the NWs are transported and deposited. By contrast, electrophoresis (EP) depends on the net charge over the size ratio of the particles.

There are two different ways to put the NWs solution and the electrodes together; either by simple drop-casting on the top of the electrodes or employing microfluidic channels integrated into the DEP electrodes. Using micro-channels fabricated on the top of electrodes it is possible to obtain 100 % alignment efficiency (100 % of the NWs in the solution are collected) [60]. The following Figure 1.11 shows an example of DEP coupled with microfluidic.

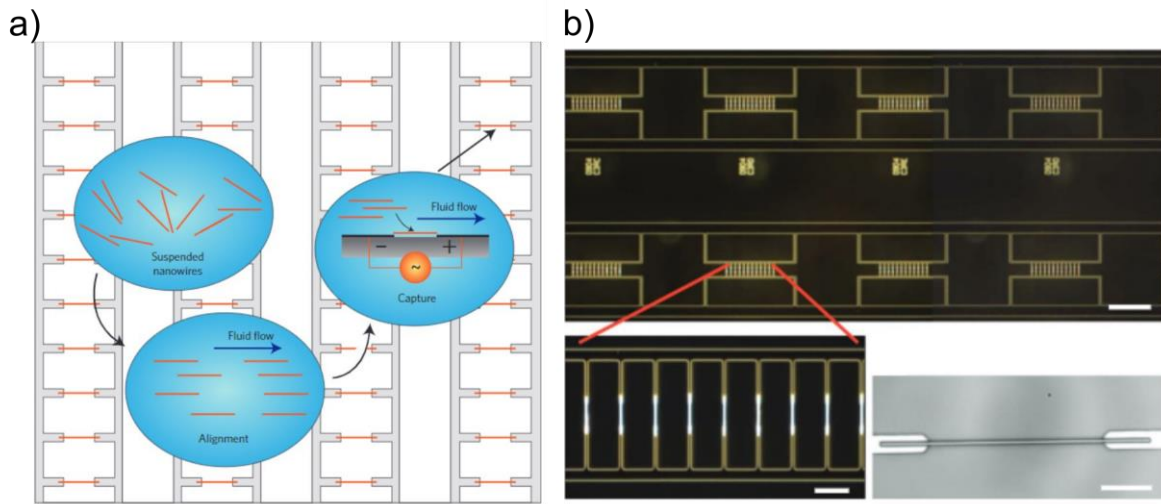


Figure 1.11: DEP coupled with microfluidic channels. a) schematic of the DEP/microfluidic set-up b) Aligned NWs obtained by coupling DEP and microfluidic.

From [60].

Overall, for any apparatus, the use of DEP is designed so that the DEP force overcomes others such as gravity, Brownian motion, and viscous force. Similarly to microfluidic, DEP alignment direction can be changed by changing the electric field direction but also by changing the medium or nanoparticles' dielectric properties.

1.7.7 Comparison

For potential manufacturing, control over the placement and alignment of NWs is essential. The differing alignment technique used will require specific conditions such as; low cost for manufacturing, versatility and easy integration.

- Manufacturing:
 - Easily installed to be suitable for large-scale fabrication.
 - Performance and efficiency.
- Versatility:
 - Possible differing assembly (NWs or connection structure).
 - Possible selectivity (material nature and size).
- Easy integration :
 - Device integration substrate is ideally possible on a flexible or rigid substrate.
 - Possible post-processing external to the assembly step.
 - Ideally without the need for surface functionalisation avoiding extra steps and possible damage and degradation.

So far, NWs in solution guided by an electric field like dielectrophoresis (DEP) show convenience and precise alignment across electrodes [61]. Besides, this technique offers ease, low cost and fast fabrication time. Depending on the future application, the alignment technique has to be under three main prerequisites; **large-scale fabrication potential, low cost, versatility and easy integration**. The following table outlines the different existing techniques along with their advantages and drawbacks. Manipulation of nanoparticles by DEP appears as a preferable technique according to Table 2. Its possibility for large-scale fabrication coupled with easy integration and the fact that the working surface does not require functionalisation put DEP control at the centre of this thesis.

Table 2: Table summing and comparing the different alignment techniques.

	Technique → Criteria ↓	Assembly by Chemical or electrostatic interaction	Shear force	Blown bubble films	Microfluidic force channel	Langmuir- Blodgett	Dielectrophoresis
Large scale Manufacturing	Easy installation	✗ Interaction to be defined	✓	✗	✗ Channels to structure Flow to control	✗ Process control	✗ Electrodes to structure
	Performance	✗ Specificity	✗ Difficult to manage	✗	✗	✗	✓ Specificity Rapidly
Versatility	Alignment precision	✗ Inaccurate	✗ Inaccurate	✗	✗	✗	✓ Precise alignment
	Connection	✗ Dense NWs network only	✗ Long NW Dense network	✗ Oneness very challenging	✗ Limited by microchannel size	✗ Dense NWs network only	✓ - Single - Network
	Particle sorting possibility	✗ Only responding to binding element	✗	✗	✓ By size	✗	✓ - Size - Dielectric properties
Integration	Device integration	✓	✗ Rigid substrate	✗ By reactive ion etching	✓	✗ Rigid substrate	✓
	Post-processing	✗	✓	✗ NWs dispersed in polymer	✓	✓	✓ If grounded electrodes
	Needless surface functionalisation	✗	✗	✗	✗	✗	✓

1.8 Dielectrophoresis control

Dielectrophoresis has been first observed in 1924 for the separation of different minerals achieved by Hatfield. Only in 1951, DEP reappeared and the term "dielectrophoresis" started to be known from the work of Herbert Pohl which used to describe the translational motion of an electrically polarised particle in a non-uniform electric field. Later, DEP gained more and more recognition, so well that it is now integrated into at least six commercial products. For instance, the Apo-Stream technology separates target tumour cells from blood using DEP [62], whilst the Panasonic bacteria counter uses electrical impedance changes of bacteria captured between DEP microelectrodes to measure their concentration [63] or the Shimadzy IG-1000 that collects nanoparticles by DEP to create an optical grating [64]. In that respect, and in the last ten years, DEP has mostly been exploited for its interaction with biological cells and for clinical applications.

Non-biological particles handled with DEP only started to grow considerably in the late 1980s, especially with the trend of lab-on-chip and miniaturisation technology [65].

Towards nanowires (NWs), the first experiments on such shapes were with the separation and orientation of carbon nanotubes (CNT) in 1992 [66] and gold NWs alignment in 2000 by Mayer *et al.* [59]. It was followed by more research on the new generation of NWs-based devices that demonstrated strong and innovative characteristics for applications like a light-emitting diode (LED), nano-electronic and nano-optic [59], [67]. The possibility to control NWs or any non-biological nanoparticle in general without direct contact is of great interest for nano-device fabrication. It was previously explained that DEP is a suitable method for NWs control to fabricate nanodevices for possible manufacturing. Although considerable work has been done to understand the complexity of DEP, research on the latter has been mostly focused on biological cells and only a little on non-biological particles.

1.8.1 Dielectrophoresis for nanowires geometry

Suspended in a liquid medium, and in a uniform DC electric field E (example a) Figure 1.12) each side of the particle is under the same generated Coulomb force strength, as they compensate each other in zero force the particle does not move.

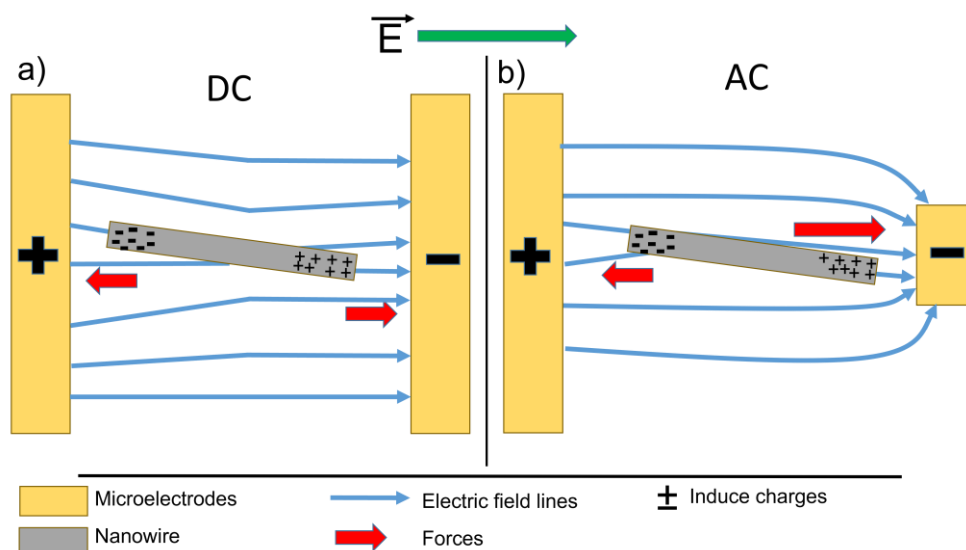


Figure 1.12: DEP principle; a) in a uniform electric field, b) in a nonuniform electric field. Inspired from [68].

A particle in an AC electric field E (example b) Figure 1.12) experiences an electric dipole moment (per unit volume) by charges separation at its surface. If the polarisability of the particle is greater than the polarisability of the medium the electric field lines pass through the particle forming the surface polarisation. The dipole moment and AC field result in an uneven force strength that leads the particle to move and to direct towards high field density regions (called positive DEP). The electric dipole interacts with the applied electric field and to minimise their potential energy the particles move along the electric field resulting in particles like NWs to self-assemble in the electrode gap.

The DEP force applied on a spherical particle having a radius R follows equation 1.1 described by Jones [69] where $\tilde{\epsilon}_m$ is the permittivity of the medium that surrounds the particles, \Re_e is the real part of the Clausius-Mossotti factor (CMF) and \vec{E} is the electric field (with ∇E as gradient).

$$\vec{F}_{\text{DEP}} = 2\pi\epsilon_m R^3 \Re_e(K_{\text{spheroid}}(\omega)) \overrightarrow{\nabla E^2} \quad (1.1)$$

The term "dielectrophoresis" is associated with the Coulomb responses of an electrically polarised particle in a non-uniform electric field where DEP force is the result of the differing Coulomb forces illustrated in red arrows Figure 1.12. The dipole moment magnitude and polarity are influenced by the dielectric properties of the particle and are proportional to the CMF. For a particle more polarisable than the medium the particle movement dominates over the medium, the CMF will be positive and the net force will move the particle towards high electric field regions (positive DEP). Likewise, for a particle that is less polarizable than the surrounding medium, the particle movement is dominated by the medium, the CMF will be negative and the particle will move towards the region of low electric field (negative DEP). The CMF $K(\omega)$, can be described as the strength of the dipole and has no unit. For NWs, contrary to spherical particles, the CMF is anisotropic and so DEP depends on the orientation of the NWs to the electric field gradient [70]. The CMF is an essential element of the dielectrophoresis force (direction and magnitude) and relies on the applied frequency (ω is the angular frequency ($\omega = 2 \times \pi \times$ frequency)).

For a spherical particle, the CMF $K(\omega)$ is defined by;

$$K_{\text{spheroid}}(\omega) = \frac{\tilde{\epsilon}_p - \tilde{\epsilon}_m}{\tilde{\epsilon}_p + 2\tilde{\epsilon}_m} \quad (1.2)$$

In which $\tilde{\epsilon}_p$ and $\tilde{\epsilon}_m$ are respectively the complex permittivity of the particle and the medium and are detailed as followed in equation (1.3), where σ is the conductivity of the medium or the particle and ϵ the relative permittivity of the medium or the particle. \mathbf{j} is the imaginary vector with $\mathbf{j} = \sqrt{-1}$.

$$\tilde{\epsilon} = \epsilon - \mathbf{j} \frac{\sigma}{\omega} \quad (1.3)$$

As previously shown the CMF equation 1.2 is written for spherical particles that are isotropic systems. However, NWs have a cylindrical shape assimilated to a prolate ellipsoid shape that is an anisotropic system. Figure 1.13 shows a prolate ellipsoid 1.13a shape used for the NWs and spheroid shape 1.13b geometries commonly used in literature for the calculation of DEP forces and CMF on NWs.

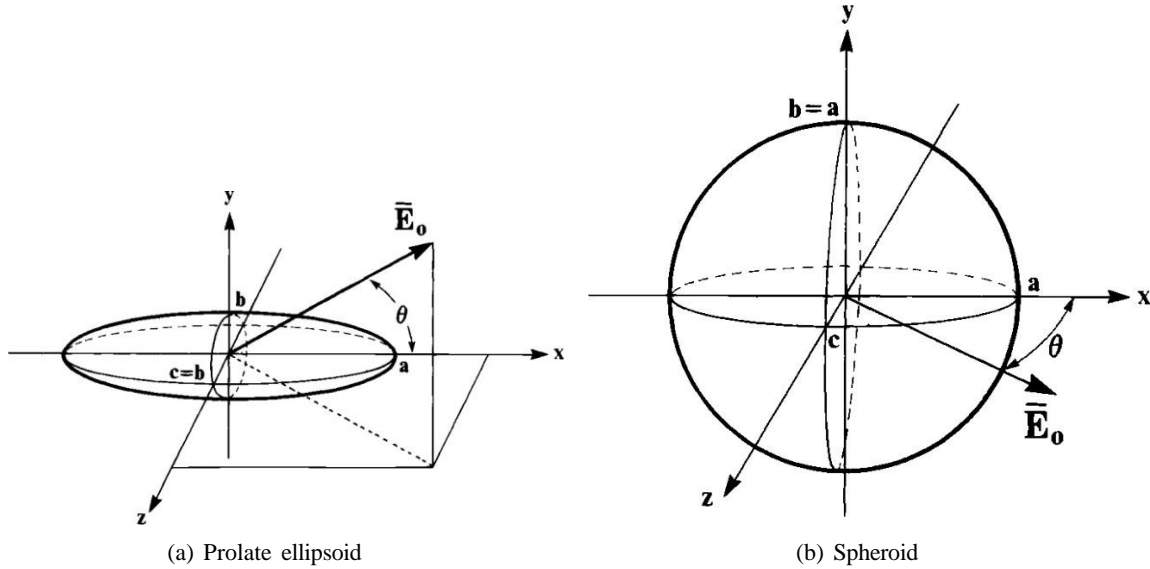


Figure 1.13: Geometrical drawings of a prolate ellipsoid (a) and a classic spheroid particle shape (b).

It has been demonstrated that the prolate ellipsoid shape was a valid substitute for cylindrical shape NWs to be included in the equations originally for spherical particles [71]. The prolate ellipsoid expresses the major and minor axes from the NW length (a) and diameter (b=c).

DEP on NWs is a relatively recent method, their corresponding equations are very often found without taking into account their ellipsoidal shape and resulting anisotropy which potentially leads to incomplete analysis.

In this work, to take into account the anisotropy of NWs, the depolarisation ratio and eccentricity factor have necessarily been included for equation 1.2 for the study of DEP for ellipsoidal shapes.

For a particle more polarisable than the medium (positive DEP), the depolarisation ratio A_a evaluates, as a result of the induced polarisation charges at the surface, how reduced (depolarised) is the electric field inside the particle compared to the external applied electric field [72]. This gives information on the influence of the particle on the electric field and resulting changes. Its equation is written as followed (1.4) and (1.5).

$$Aa = \frac{1-e^2}{2e^3} \left[\log \left(\frac{1+e}{1-e} \right) - 2e \right] \quad (1.4)$$

$$A_b = \frac{1-Aa}{2} \quad (1.5)$$

Where a is the a -long-axis depolarisation ratio of a prolate ellipsoid and b -short-axis ($a > b$) and the eccentricity e is the geometrical factor for the prolate ellipsoid shape and is described in equation (1.6).

$$e = \sqrt{1 - \frac{b^2}{a^2}} \quad (1.6)$$

As a result and conforming to Jones [69] the DEP force and the Clausius-Mossotti factor are described by two mathematical components. Equation 1.2 is therefore now written using the two axes, as follows;

$$K_{\text{ellipsoid}}(\omega) = \frac{1}{3} \frac{\tilde{\epsilon}_p - \tilde{\epsilon}_m}{\tilde{\epsilon}_m + A_i^*(\tilde{\epsilon}_p - \tilde{\epsilon}_m)} \quad (1.7)$$

$$K_{a\text{-long-axis}}(\omega) = \frac{1}{3} \frac{\tilde{\epsilon}_p - \tilde{\epsilon}_m}{\tilde{\epsilon}_m + A_a^*(\tilde{\epsilon}_p - \tilde{\epsilon}_m)} \quad (1.8)$$

$$K_{b\text{-short-axis}}(\omega) = \frac{1}{3} \frac{\tilde{\epsilon}_p - \tilde{\epsilon}_m}{\tilde{\epsilon}_m + A_b^*(\tilde{\epsilon}_p - \tilde{\epsilon}_m)} \quad (1.9)$$

Thus, for prolate ellipsoid, there is a polarisation variation within the NWs according to their orientation to the electric field gradient. When the electric field gradient is parallel to the NWs, the DEP force will be directed along the long axis of the NWs. In the opposite case, when the NWs are perpendicular to the electric field gradient, the DEP force will be directed along the short axis.

For NWs randomly oriented to the electric field gradient, the DEP force will be related to both axes with a stronger force along the long axis. Figure 1.14 illustrates the assembly and polarisation of a NW parallel to the electric field lines. After polarization of the NWs each pole is attracted to the electrode by DEP force and will depend on several parameters such as magnitude (electric field magnitude in newton per coulomb), frequency, NWs material and electrode shape.

The device conduction is related to the number of aligned NWs where more NWs should lead to a higher current [73]. The collection rate can be influenced either by NWs solution concentration or by the AC applied voltage (frequency and amplitude). However, given the size of the NWs the applied voltage is limited by the possible voltage overload in the dielectric leading to destruction [74]. One of the most underrated and understudied features of DEP manipulation is its capacity to simultaneously align NWs and select quality NWs with enhanced electrical conductivity. Only a couple of publications have highlighted this unique characteristic including results obtained in this work [2, 75, 76]. Polarisability being related to conductivity, it was found that increasing the frequency parameter of DEP led to aligned NWs with increased conductivity properties. Hence, low-frequency collections present NWs of mixed qualities together with low quality (purity, conductivity, crystallinity defects, traps, etc.) whereas high frequencies cause only high-quality NWs to align. More details will be given in this work over the next chapters. DEP motion can also be influenced by the electronic double layer caused by the interaction between the NWs surface and the aqueous medium [77]. Particles like NWs have an electronic layer forming at the surface when they are immersed in a medium. Even in "pure" non-polar solvents, like anisole, dimethylformamide (DMF) or ethanol possible traces of ions can create an electrical double layer at the surface of the particles forming a low net charge. That net charge can be determined by zeta potential measurement equipment. The zeta potential (net charge) at the surface of the NWs can be either positive or negative depending on the polarity of the medium and NWs surface chemistry. For a non-polar solvent (ethanol, anisole, toluene, etc.) the zeta potential is rather negative. On germanium NWs for instance O⁻ from the thin oxide layer if in a polar solvent (like water, acetone, etc.) the zeta potential will be rather positive, as counterions of O⁻ will surround the NWs surface [78]. In this work, the DEP forces and Clausius-Mossotti factor equations after refinement for prolate ellipsoid have been investigated through a computational code written using Matlab. They are addressed later in the next chapters.

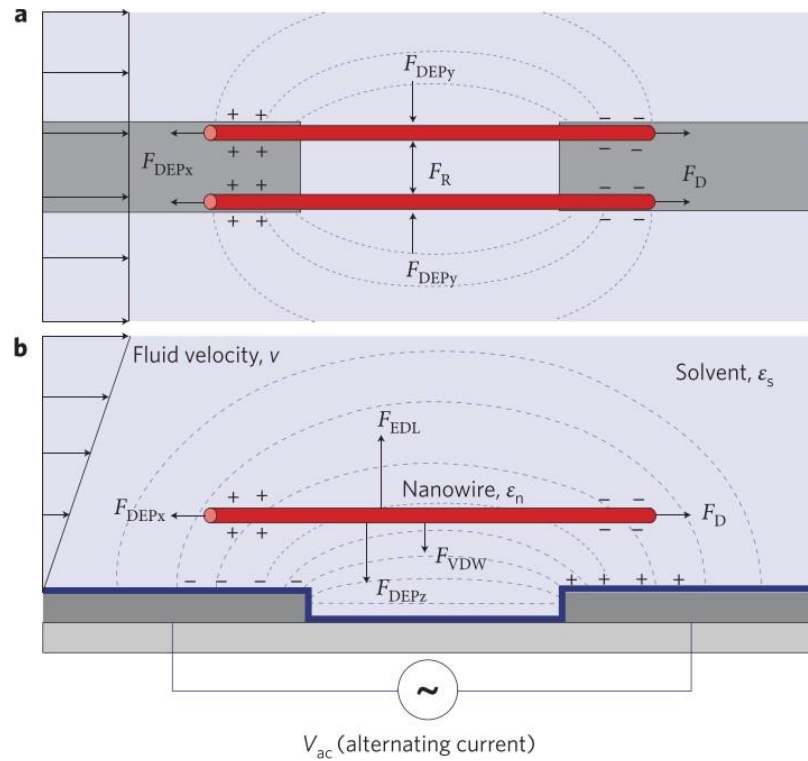


Figure 1.14: Nanowire (red) in an AC electric field subjected to DEP force influenced by the anisotropic nanowire a) top view b) side view.

From [60].

As expressed in equation 1.7 the CMF (describe the strength of the NWs dipole) is a function of influencing parameters:

- Dielectric properties of the particle are expressed by conductivity σ_p and permittivity ϵ_p .
- The shape of the particle, length and diameter.
- Structure of the particle (morphology, homogeneity, defects, doping).
- Dielectric properties of the medium are expressed by conductivity σ_m and permittivity ϵ_m .
- and lastly voltage and frequency of the AC electric field.

1.9 Electrophoresis

Similarly to DEP, Electrophoresis (EP) is used to manipulate nanoparticles with the interaction of an electric field. In a medium, EP acts primarily on fixed charged particles ("pure" electrostatic force) while DEP acts on unfixed charges (polarisation). The motion of particles via EP requires a DC voltage that interacts with the electrical net charge of particles and so the movement of the particles is unidirectional and proportional to the electrical field and polarity strength. Charged particles are most likely organic and/or they can be found in polar mediums with an electrical double layer. A simple Coulombic force system will move a charged particle with a force $F \propto QE$ (Q =charge, E =electric field) towards one single electrode of opposite polarity. The moving force and thus the mobility will be determined by the medium properties and electrical double layer formed on the dielectric particles. EP is thus proportional to the electrokinetic potential (determined by the net charge zeta-potential) and the electric field strength (Coulombic force) [79].

Derived from the Coulomb equation, the electrophoresis force equation is presented as follows [80];

$$\vec{F}_{12} = \frac{Q_1 Q_2}{4 \pi \epsilon_0 r^2} * \vec{r}_{12} \quad (1.10)$$

\vec{F}_{12} is the force acting on particle 2 of net charge Q_2 exerted by particle 1 of net charge Q_1 , ϵ_0 is the permittivity of the vacuum, r is the distance between particle 1 and 2 and \vec{r}_{12} is the vector from Q_1 to Q_2 . For a prolate ellipsoid shape like NWs as illustrated in Figure 1.13 a) the EP force has been adapted as follows by [81];

$$\vec{F}_{EP} = \frac{-8\pi\mu cv}{\left[\left(\frac{a}{b}\right)^2 + 1\right] \coth^{-1}\left(\frac{a}{b}\right) - \left(\frac{a}{b}\right)} = -6\pi\mu b v R \quad (1.11)$$

With μ the dynamic viscosity of the medium, v the relative viscosity of fluid-particle, a is the major axis and $b = c$ is the radius and with \mathbf{R} ;

$$R = \frac{4}{3\sqrt{\left(\frac{a}{b}\right)^2 - 1} \left[\left(\frac{a}{b}\right)^2 + 1\right] \coth^{-1}\left(\frac{a}{b}\right) - \left(\frac{a}{b}\right)} \quad (1.12)$$

For a NW parallel to the electric field E with a thin electrical double layer in the case of a non-polar solvent the EP force can be written with E (DC electric field), ζ zeta potential of the particle in the medium with $\mu_e = \varepsilon_m \zeta / \mu$ as follows;

$$\vec{F}_{\text{DEP}} = 6\pi\mu b\mu_e RE = 6\pi b\varepsilon_m \zeta RE \quad (1.13)$$

Where ε_m is the electric permittivity of the medium. EP is mostly used to sort out and separate particles and very few applications used EP for NWs implementation where EP is used as a trajectory force [82]. The following Figure 1.15 shows the difference between EP (DC electric field) and DEP (AC field) both in equal conditions. Si NWs of 15 μm long and 300 nm diameter were manipulated by EP and DEP. For EP a) Figure 1.15, the DC applied voltage is 1.5 V in dimethylformamide (DMF). For DEP b) Figure 1.15, the AC applied voltage is 10 V at 5 MHz in both situation conductivity and permittivity of the particles are higher than the medium DMF [83].

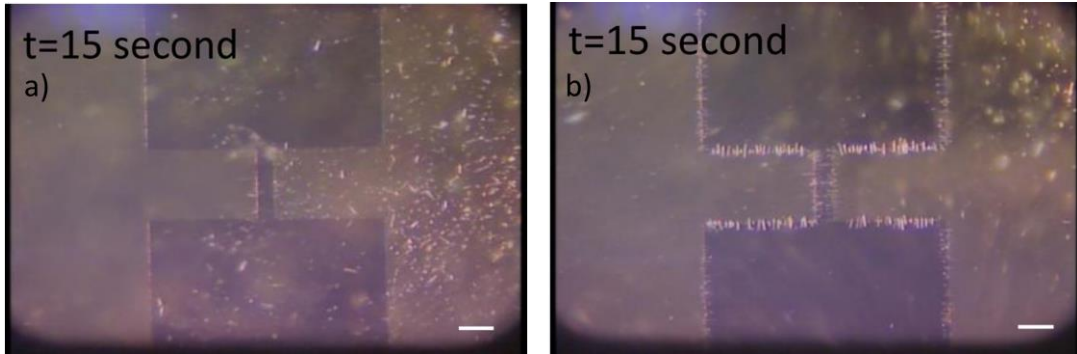


Figure 1.15: Images obtained by Brown *et al.* showing the difference between a) EP and b) DEP at 15 s of the experiment. Scale bar 100 μm .

From [83].

For a fixed same time, the Figures show well the different collection features obtained either with EP or with DEP. The NWs collection with EP a) is principally on the right electrode (on the whole electrode surface) while collection using DEP b) is mutual attraction (strong gradient at the gap) leading to NWs aligned at the edge gap between the electrodes.

1.10 Nanowires sensor devices

It has been explained that the potential integration of nanoparticles in devices has great potential because of their enhanced sensitivity and electrical properties like band gap engineering and density of states modification [84]. NWs have already been largely exploited in many forms of devices and sensors that will be reviewed in the following sections. Being at the centre of research for modern technology, it is important to understand the electronic properties of NWs. The probing of particles at the nanoscale is not as straightforward as for bulk material due to spatial localisation for example. A variety of measurement techniques have been developed either for single NW or arrays of NWs mostly performed using microscopy probing like AFM or electrical contact I(V). NWs implementation in devices is a challenge, such as making electrical contact with the nanostructure. I(V) curves can be obtained using two probes contact that can influence the contact and the device performance.

1.10.1 FET building blocks for nanosensor

Field Effect Transistor (FET) is the most fundamental electronic device along with diodes for high-density circuit integration. In traditional planar bulk material FETs, the device's structure has three terminals; metal source/drain electrodes and a gate. Current is injected and collected through the source and drain electrodes that have opposite doping. The gate is capacitively joined to the channel with an insulating layer (usually silicon oxide). For a p-type semiconductor channel (with n-type source and drain), a reverse bias applied at the gate will deplete the carriers (p-holes) and reduce the conduction channel (depletion), while a forward bias will create an accumulation of carriers and increase conduction in the channel. By modulating the potential at the gate voltage it is possible to control "on" and "off" states and change the channel conduction. A n-type channel works inversely the same way.

Unlike standard FETs where source/drain contacts are formed with doped material, simple metal contacts are often used for source/drain material in NWs FET [85]. Semiconductor NWs, play the role of the conduction channel between source and drain electrodes as shown Figure 1.16.

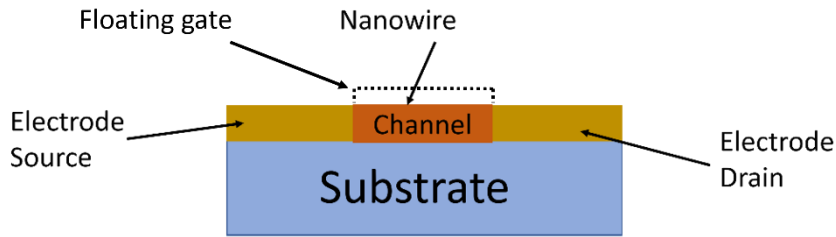


Figure 1.16: Cross section of a floating gate FET.

NWs' sensitivity to the environment (light, biomolecules, gas...) leads to alteration of the channel conductance. In this configuration of FET the floating gate can be played by the oxide layer of the semiconductor channel and or by the surrounding environment and showed in dashed lines Figure 1.16. Upstream, any changes in the electric field are quantifiable and transduced into electronic signals making a sensor device.

Hence, gateless FET sensors are considered a new type of sensor, where the gate is replaced by the NWs' surface interactions that intimately change the electrical conductivity. In this fashion, NWs from the sensor devices are either more exposed to their environment and/or the device fabrication is more straightforward, especially by using DEP alignment [14]. The two following examples show NWs FET sensor devices fabricated without a gate for two different types of detection; a mechanical sensor through piezoelectric properties and biosensing through electrical interaction properties.

Wang *et al.* [86], measured the piezoelectric properties of a single ZnO NW capable of detecting nano-Newton force range. The NW was randomly chosen and detected in a SEM chamber followed by needle probing measurement on two silver contacts. Figure 1.17 shows the obtained results.

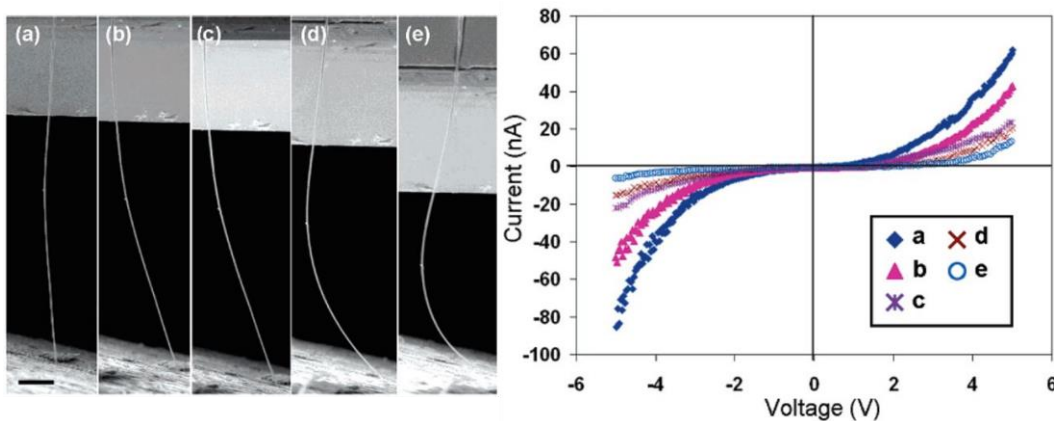


Figure 1.17: SEM images of five bending modes of a ZnO nanowire (left) and the corresponding current response $I(V)$ showing the piezoelectric FET sensor curves.

Extracted from [86].

From the current response on the right Figure 1.17, they observed a good symmetric signal with ohmic contact at both ends of the NW. For an increasing bending force, the current response decreases. Conversely, the NW was able to retrieve its "normal" electrical properties with an increasing current response as the strain force was released back to a straight shape. The bending of the NW and its core structure alteration was detected by the needle probes thanks to the piezoelectric properties of the ZnO NW.

The basic design of an immuno-FET is a transistor in which the gate is replaced by a layer of antibodies specific to a target protein. In the case of functionalised p-type Si NWs, receptors like antibodies attached to the NWs surface will react with a corresponding target molecule in its environment. It creates an increase or a decrease in the NWs current response depending on whether the binding target molecule is negatively charged (accumulation of holes) or positively charged (holes depletion) [87, 88]. In the following example of bio-FET Figure 1.18, Rahman *et al.* [3] functionalised a p-type Si NW connected between two gold electrodes fabricated by a top-down approach.

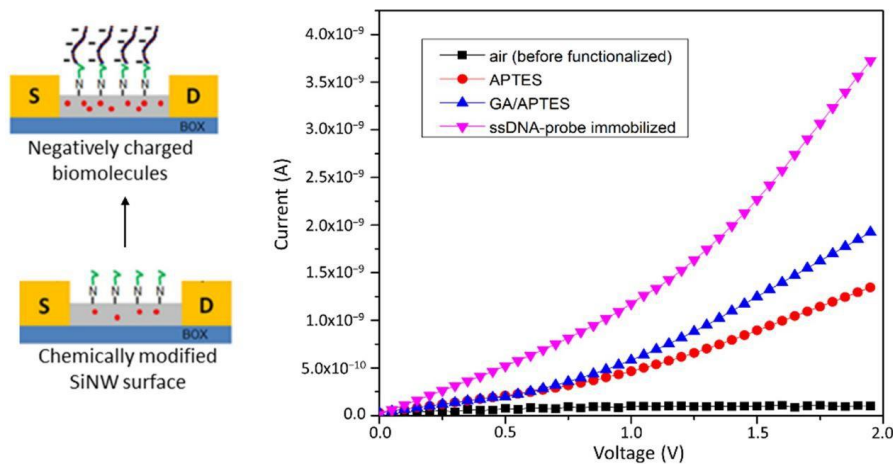


Figure 1.18: Schematic of the p-type Si NW FET sensor (left) and its electrical measurement for every functionalisation layer (right). From [3].

The Si NW was functionalised with a layer of 3-aminopropyl-triethoxysilane (APTES red curve) followed by a layer of glutaraldehyde (GA/APTES blue curve) both presenting negative net-charge as well as for the final probing receptor (ssDNA-probe in a pink curve) [89]. On the Si NW surface, the functionalisation layers and probing receptor attachment lead to the accumulation of holes (red dots in the left-handed schematic) in the p-type NW. As a result, they observed an increase in the current response as seen in the I(V) measurement in forward bias Figure 1.18.

Conversely, if the net charge of the probing receptors was positive, a decreasing current response (recombination) would be measured [3]. Those NWs-based sensors are quasi-real-time interactions/interpretations of events. NWs characteristics and low size-scale integration are showing the way to modern nanosensors and surpassing standard detection limits without the need for labelling offering possibilities for many applications.

The current flow translates the NWs channel electrical characteristic as a response to an applied voltage. The electrical resistances are at the contacts where electrons enter and leave the NWs, and are involved with the functioning properties of the device.

1.10.2 Conduction, transport mechanism in nanowires

The conventional way to fabricate NWs diodes by the bottom-up approach starts with a random distribution of NWs properties followed by the fabrication of the contact electrodes. It was explained earlier in this chapter that DEP enables specific selection and manipulation of NWs to collect them between pre-patterned electrodes. Although mainly used for FET NWs fabrication, DEP has shown successful diodes [90, 91]. DEP has mainly been used for simple collection alignment without exploiting selection properties that have been only scarcely studied for the fabrication of FET and diodes often due to the lack of previous reports. This thesis aims to compile DEP collection and selection properties to investigate their impact on device performances as an additional building block to nanotechnology research.

Schottky diodes like p-n junction diodes are the simplest type of diodes. Because of their properties at the nanoscale, NWs implementation as diodes has been at the centre of many research projects and has proven its potential for solar cells because of their light trapping properties [92] but also similarly to FET for their transducing properties for sensing technology [16]. It has been demonstrated that Schottky diode sensors were exponentially sensitive to conduction changes on the NWs because of the Schottky contact band bending alteration and the surface interaction supporting NWs integration in nano-sensing future technology [93]. Conduction mechanisms (or injection-limited conduction mechanisms) have been particularly studied. Analysis of devices' conduction mechanism is largely done via $I(V)$ s current-voltage response measurements. Four main conduction mechanisms are frequently observed in nanostructure devices; **Schottky emission (or thermionic emission), tunnelling, surface roughness scattering (SRS), space charge limited current (SCLC) and hopping conduction**. These conduction mechanisms are described in the following part and are illustrated with examples from previous research.

Schottky conduction mechanism

NWs devices often use metal contact electrodes in contrast to common bulk or planar diodes that have doped contacts. Depending on the channel and contact material nature, the junction metal/semiconductor M(-S) NWs will be either Schottky with rectifying behaviour and non-linear current-voltage response or ohmic, non-rectifying and linear current-voltage response. Schottky barriers are due to band bending at the junction M-S; electrode-NWs and NWs surface states combined where electrical current flowing across is non-linear (discontinuity of energy). This results in diode device performances influenced by the contact properties. The current transport is mostly due to the majority of carriers, holes in p-type and electrons in n-type.

For rectifying contact, the basic process with a p-type semiconductor is the transport of holes over the Schottky potential barrier where holes are the majority carriers mostly resulting in conduction. For a classic p-type Schottky contact, the rectifying contact is formed when a metal has a lower work function (energy to remove an electron to vacuum) than the semiconductor which results in barrier height at the middle of the metal and semiconductor work function. As known, NWs have at the surface incomplete chemical bonds called dangling bonds. Dangling bonds and impurities produce energy levels located within the band gap. Those surface states, either donor or with acceptor character are generally not well known and there are different varieties of states depending on the surface morphology [94]. At the interface M-S, semiconductor NWs energy state levels will be physically located at the interface. Those state levels result in the pinning of the Fermi level so that work functions are independent of the metal contacts. Germanium NWs have presented Fermi-level pinning for Schottky contact as it is well known that Ge has energy state-level from surface dangling bonds [95]. For a p-type semiconductor such as the Ge NWs used in this study, metal contact like gold and band bending at the junction can be illustrated as follows. When contact is made, electrons from the metal flow to the empty states of the valence band (of the semiconductor) resulting in an upward bending to reach equilibrium (a) Figure 1.19).

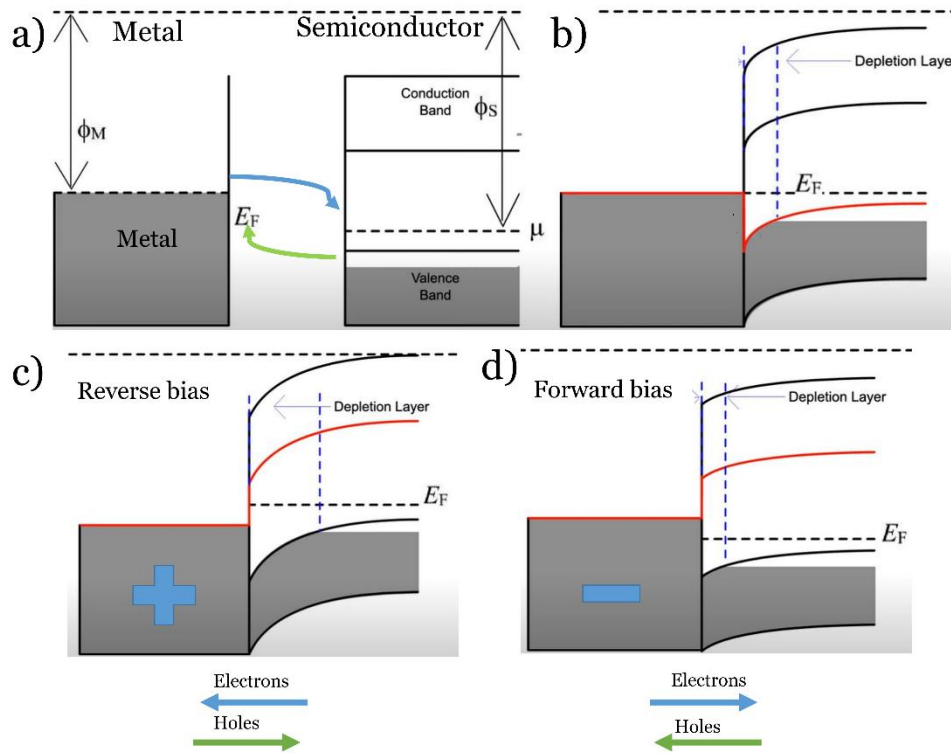


Figure 1.19: Schottky barrier contact between metal and p-type semiconductor.

As a comparative example band banding of ohmic contact and n-type Schottky barrier type illustrations have been put in appendix Figures A.1.1 and A.1.2.

At equilibrium after contact (Figure 1.19 b)), a region called the space charge region has been depleted of electrons creating a potential barrier for holes (abrupt interface red line) to reach the metal interface and recombine with electrons in the semiconductor. The metal connected to the positive electrode in reverse bias results in holes repelled by the interface as illustrated c) Figure 1.19. The potential barrier is increased (as well as the depletion zone) ensuing in a low current response in reverse bias. If the metal is connected to the negative electrode forward biasing results in holes attracted towards the interface illustrated d) Figure 1.19. The potential barrier is reduced, giving a larger current in forward bias. Electrons' emission from metal to the semiconductor channel is called Schottky or thermionic emission. On the metal contact side, if electrons can gain enough energy (from thermal activation), the electrons overcome the energy barrier to go towards the semiconductor channel. Thermal activation will lead to the lowering of the energy barrier due to the Schottky effect. Schottky diodes exhibit specific rectification behaviour where forward bias conducts the current response and reverse bias displays a smaller current response and can result in reverse leakage.

The performance of a Schottky diode is measured by the rectification ratio given by the ratio between forward bias current response and reverse bias current response. As an example, commercial Si (bulk) based diodes have a rectification ratio of $\approx 10^5$ to 10^8 . A higher rectification ratio gives more control over the current.

In photodetection technology, Schottky devices with a p-type channel rely precisely on the junction metal-semiconductor of the Schottky barrier effect that involves the generation and collection of photo-generated carriers. Incident light (photons) with enough energy will be absorbed by the semiconductor channel generating electron-hole pairs. The Schottky barrier separates the photogenerated carriers with electrons moving toward the metal contact and holes moving rather towards the semiconductor. The opposite movement of the carriers results in the flow of a photocurrent that is enhanced by the application of an external bias voltage which also enhances the device sensitivity and response.

Nanowires-based Schottky devices

As a standard Schottky device example using NW, Park *et al.* [96] fabricated a ZnO p-type NW-based diode (randomly chosen) in contact with a Au/Ti (ohmic) electrode and a Au (Schottky) electrode deposited by EBL. They obtained the following I(V) current response (at RT) presented in Figure 1.20.

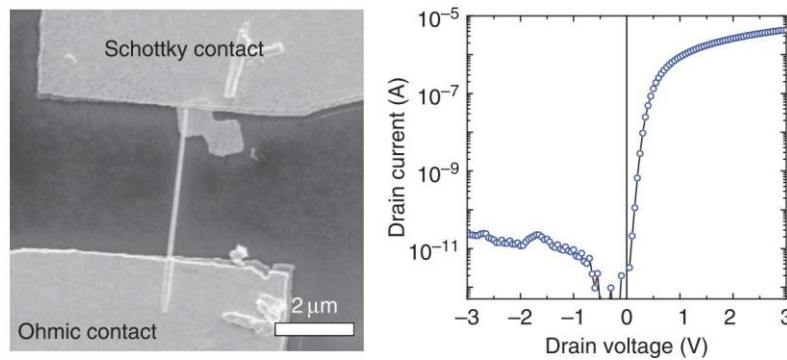


Figure 1.20: Typical I–V characteristic curve for p-type nanorod Schottky diodes (left) and a scanning electron microscopy (SEM) image (right).

Extracted from [96].

The current response to the applied voltage highlights nonlinear and asymmetric behaviour originating from the ZnO contacts. The ohmic contact has low resistance with the ZnO NW so that charge carriers can travel without obstacles. They observed no significant break-down voltage in

reverse bias with good rectifying behaviour and turn-on voltage around 0.5 V.

Similarly to the FET sensors presented in Figure 1.18, NWs-based Schottky sensors sensitivity also leads to the possible detection of bio-molecules. Schottky sensors have been improved with NWs implementation and have been widely studied for mechanical strains, biomolecules, and gas detection [93]. Carrara *et al.* [97] fabricated a Schottky Si NW for the detection of antigens. The Si NW was fabricated by top-down approach (etching) and contacted between Ni/Ti electrodes deposited by thermal evaporation using a mask. The Si NW surface was functionalised with rabbit antibodies called AB-NW binding sites (red dots Figure b) 1.21. Figure 1.21 illustrates the functionalised NW and its current response to increasing concentrations of antigens (AB).

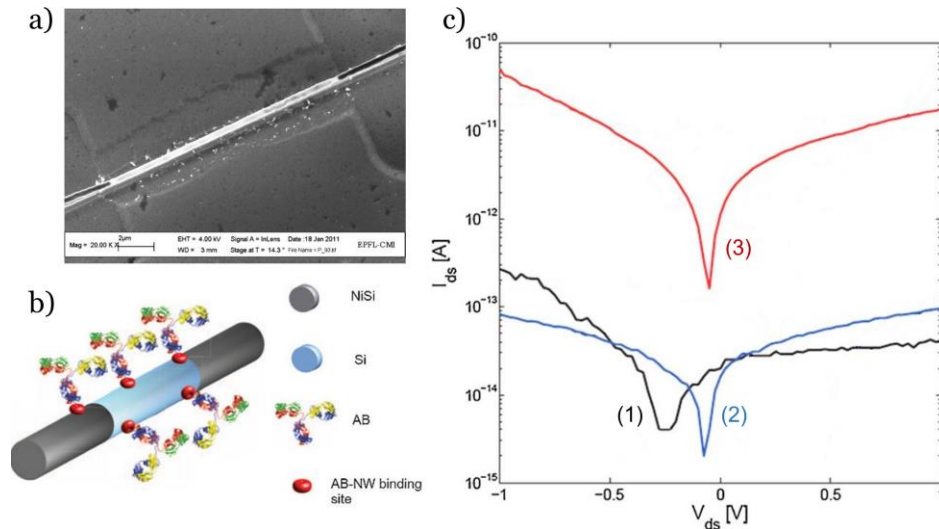


Figure 1.21: Functionalised Schottky Si NW with b) antibodies and its c) current response when exposed to increasing concentration of antigens (1) 0 fM in black, (2) 5 fM in blue, (3) 10 fM in red.

Extracted from [97].

Before the antigens exposure, they observed after functionalisation, a decrease in the current response due to the positive net charge of the rabbit antibodies on the surface of the NW (shown in ref [97]). Moreover the author proposes that the voltage shift observed on the IV responses is due to the presence of the functionalisation layer. Upon antigens exposure b) and c) Figure 1.21, the sensor is detecting the molecule at a concentration superior to 5 fM otherwise the signal is similar to 0 fM. The surface detection by the NWs is related to the electrical charges of the antibodies, the amount of injected charges and the carrier mobility of the NW. In that example, a concentration of 5 fM was not enough to modify the channel conductivity and/or change the Schottky barrier height.

The sensitivity and ultimate Limit of Detection (LoD) of such devices are largely determined by the surface area of the sensing element (i.e. thin film or NW). The smaller the surface area the fewer entities are required to bind to the aptamer/antibody and result in a measurable change in the current. Additionally, carriers' mobility and crystal quality of the channel will play a crucial role in the LoD and sensitivity of the sensor. For the detection of viruses, biosensors can be found in the literature with a variety of LoD performances such as 0.20 mM using In_2O_3 thin film [98], 1 pM using AlGaIn/GaN thin film layers [99], 10 to 1 fM using graphene [100] while NWs biosensors have shown possibilities to detect one single virus using Si NW [101] or 0.1 fM also using Si NW [102] and 2.5 pM using InN microtubes [103]. Thus, NWs are an attractive possible platform for sensors, given their innate small size, with the ultimate sensitivity potentially being offered if a single nanowire can be utilized as opposed to an array.

The precise detection mechanisms of NWs sensing devices are not yet well-understood [104] although the sensitivity to the environment is clear, studies have highlighted detection mechanisms only due to the metal-semiconductor contact junction over the channel implications [105, 106] while others have shown the clear influence of the conduction channel for detection [87, 107] and even participation of both have been proposed [93], [108].

Nanowires Heterojunction

Heterojunction devices are traditionally p-n diodes with p-type and n-type doped materials. As known, NWs devices' electrode contacts are intrinsic (undoped) metal. Instead, the NWs channel itself can also be doped either intentionally or unintentionally. With the improvement of NW synthesis, it is possible to control the growth process allowing a large panel of compositions, doping, dimensions and shapes (corrugated, straight, kinked, etc.). Only possible by a bottom-up approach, even radial and/or axial chemical heterostructures have been achieved [109]. Control and multiple possibilities on NWs synthesis enable most of all development of functionalities and modification of their electronic properties.

In his Nobel Lecture about the modern role of semiconductors in electronic devices, Kroemer Herbert pointed out "The interface is the device". Indeed as for Schottky devices, heterojunction is achievable with differing metal contact (as seen in the previous paragraph), but also achievable with different materials within the conduction channel. There are two distinct heterojunctions; axial and radial, and this thesis is involved with axial heterojunction. Axial heterostructures have shown interest in the domain of electron transport because of the possible insertion of different sharp band structures that can operate as resonant tunnelling diodes [110], barriers [111] and single electron transistors [112].

During growth, the axial chemical nature of NWs can be obtained by changing precursors and/or catalysts seeds or by using generated laser ablation enabling block-by-block NWs of different materials [113]. In NWs crystal structure, a disruption of the lattice symmetry can lead to electrostatic potential (like the barrier illustrated by the red line in Figure 1.19) from new states leading to charge barriers. Similarly to metal contact with semiconductors for Schottky and p-n junction different band bending can occur in heterostructured NWs. Heterostructured NWs device properties will depend on the junctions that can be abrupt or graded (graded by several times the NW diameter). In a graded junction, the barrier is by definition less abrupt than illustrated in Figure 1.19. Graded junctions have been shown to avoid leakage current pathways [114] because of a more stable lattice mismatch from one material to the other. For most catalysts/seeds used for NWs growth by VLS, gold has been shown to produce graded heterojunction for Si and Ge because of their alloying good solubility [114]. Hence research on heterostructured NWs devices has obtained low barriers Schottky diodes by simply using Au nanoparticles as seeds for the growth of ZnO [115], GaAs [111], and Ge NWs [116].

Heterojunctions in NWs and entailing electronic properties are considerably lacking knowledge mainly because of the difficulty to get lattice and dislocation images in the device, as well as the intricacies of electrostatic potential and interface state properties [117].

Tunnelling

Tunnelling is a quantum mechanical conduction mechanism. It occurs when electrons can penetrate directly through an energy barrier due to their wave nature. This effect is particularly observed with nanoscale materials. In a FET the tunnelling is modulated through the gate, and in a diode, the tunnelling is modulated through the bias across the channel. In FETs or diodes, band-to-band tunnelling can be from the metal to the semiconductor conduction band often resulting in high leakage current. Similarly to the Schottky barrier for the p-type channel in forward bias (illustrated Figure d) 1.19) the potential barrier narrows increasing the possibility of tunnelling from the metal to the semiconductor conduction band. Electron tunnelling is a possible explanation for high current response at low forward bias. Tunnelling is also possible from the valence band of the semiconductor to the metal in reverse bias where the potential barrier is high enough with the space charge region still extending on a small distance at the interface M-S. The energy distribution of the carriers is influenced by the temperature as well as the doping of the material and so can generate tunnelling [118].

Surface Roughness Scattering (SRS)

It was explained in the previous sections that FETs and diode fabrication were the keys to understanding transport mechanisms and electrical features. An applied voltage allows probing NWs carriers' transport giving information later interpreted. Contacts between NWs and electrodes or structure and morphology of the NWs or even chemical interactions can lead to different transport and conduction mechanism. The transport mechanism within NWs and devices is very different from thin films and bulk as carriers travel mostly along the long axis and their mobility is also determined by scattering. Within NWs, carriers not only scatter with other carriers and atoms but also from impurities decreasing the mean free path (ballistic transport). It is clear that NWs' electrical properties are most of all ruled by their sensitivity to their environment and interaction with other materials. It was also explained that NWs' electrical properties can be influenced by their morphology and physical strain in the case of piezoelectric material. Depending on the synthesis parameters like for heterostructured NWs, NWs surface can present different morphology from rough to corrugated, smooth and even star shape. Surface roughness (SR) can be obtained during synthesis with variations in temperature or nanoclusters' chemistry and stability [119]. It is also possible to use post-growth techniques to shape NWs and their surface, mostly done via etching [120].

Surface roughness act as elastic scattering (no loss of energy) of charge carriers and is associated with potentials that displace the charge density and can increase scattering, this scattering of charges is called Surface Roughness Scattering (SRS). SRS has been shown to increase optical efficiency by 17 % for NWs-based solar cells compared to smoothed NWs surfaces [121]. SRS produces light scattering between the surface walls increasing light absorption. Star shape surface NWs have also featured multiple light scattering between NWs placed in arrays increasing resulting light absorption and solar cells performances [122]. In Si NWs, SRS has also reduced the density of states (below the Fermi level) resulting in an increase in the threshold voltage [123]. However, as a consequence, the downside of SRS is that it also decreases electron mobility with increasing roughness and as a consequence could potentially decrease NWs sensitivity despite an increasing surface-to-volume ratio [124]. A greater roughness will increase the scattering effect and deteriorate electronic properties as roughness enters deeper into NWs. Hence, SRS induces local changes in electronic band structure that become less effective as the NWs have a bigger diameter, letting more volume for the carriers and decreasing in turn carriers scattering by SRS. The majority of the work on SRS properties has been obtained using simulations and only a few experimental reports are estimating the effect of SRS on electrical properties. SR, morphology and size of NWs are crucial parameters of electronic properties that are important for future applications of NWs-based devices.

Space Charge Limited Current (SCLC) mechanism

Electron space charge is a characteristic commonly observed in dielectric or in insulator materials and Schottky contact devices. It is particularly sensitive to the presence of electronic state level and carriers trap often due to defects like surface oxide, interface, lattice defect, impurities, etc. [125]. Those defects are the source of intermediary states level with traps (shallow and deep traps) or without trap levels in the band gap [126]. In a NW-based device, when the applied voltage is increased the injection level follows specific regimes within the channels; i) first ohmic conduction then ii) shallow traps SCLC regime, iii) trap-filled limited conduction and finally iv) trap-free SCLC. At low voltage applied to the device, the conduction mechanism is ohmic i), in that regime, the intrinsic electrons are in higher concentration than injected ones and the Ohm's law is valid. In SCLC regimes, the injected charge carriers dominate the current that displays a quadratic response $I(V^2)$ as illustrated by the blue curves in Figure 1.22. For such a regime, the current response depends on the mobility (in contrast to ohmic conduction) and not on the charge carrier density anymore which is why mobility can be obtained based on a simple $I(V)$ measurement. ii) SCLC is a conduction mechanism that can be of two types; either trap-free (trap-free state level) SCLC or with traps of the extended states (shallow and deep traps) with trapping and possible de-trapping events in NWs. Figure 1.23 shows a schematic of the state level with shallow and deep traps.

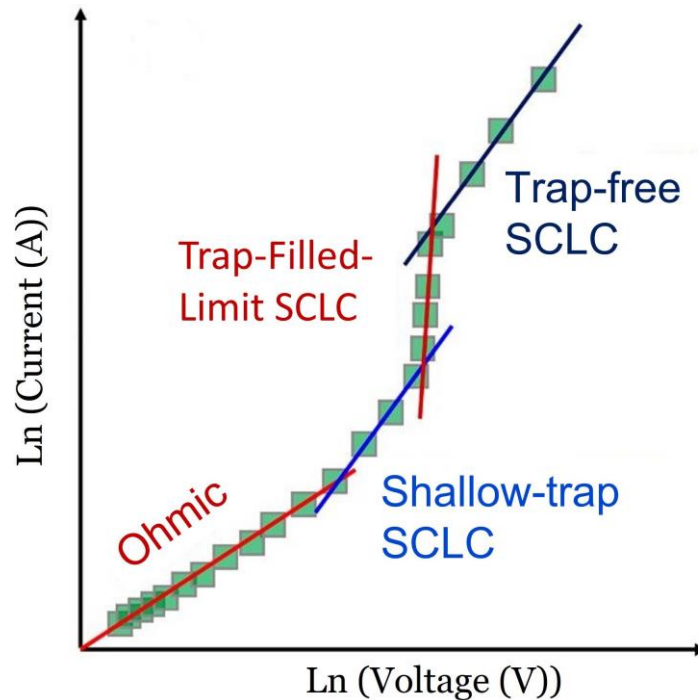


Figure 1.22: Current–voltage behaviour of NWs with SCLC.

Extracted from [126].

iii) Shallow traps have a small energy difference from valence and conduction bands and so those traps can be overcome by thermal energy or high voltage. By voltage energy, they appear as SCLC in $I(V)$ s. Deep traps are generally in the middle of the band gap with energy levels well separated from the bands. They are not easily filled and are likely to promote recombination under thermal excitation. For a trap-free regime iv), the SCLC is governed by the V^2 relationship first derived by Mott [127]. The trap-free regime does not always necessarily imply that the material is trap-free but is also valid for iii) trap-filled states. The injected current density in the SCLC regime is then given by the Mott-Gurney law shown in equation 1.14 [128].

$$J = \frac{9}{8} \epsilon_0 \epsilon_r \mu_{NWs} \frac{V^2}{L^3} \quad (1.14)$$

Where ϵ_r is the relative permittivity and μ is the electron mobility. It has been well demonstrated that for SCLC indicating $I(V^\alpha) \alpha > 2$ state level or shallow traps were distributed in energy between conduction and valence band as illustrated in Figure 1.22 [126], [129].

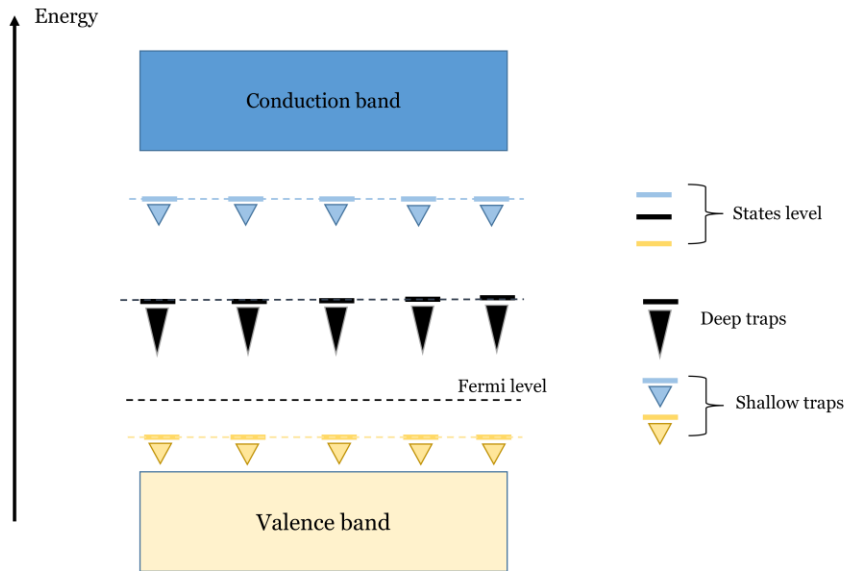


Figure 1.23: Semiconductor (p-type) band diagram with defect state levels shallow and/or deep traps.

At low voltage and in the traps filled SCLC regime, current response results from injected free electrons that gradually fill the traps (shallow traps below Fermi level) until other empty traps are limiting the ensuing increase of current. This is often observed in low intrinsic doping materials [130]. As the voltage is increased, as well as the injection level, injected free electrons now overtake injected trapped electrons (filled traps) and a quadratic dependence is again observed. In the case where deep-level traps are in the band gap (usually around the Fermi level) it is possible to have again $I(V^\alpha) \alpha > 2$ at high applied voltage [131].

So far in the literature, there is no relation for the full range of the applied voltage for all the kinds of energy level traps. As SCLC is sensitive to defect-trapping carriers it is often used to highlight the energy distribution of defect states and density.

Hopping transport

The hopping transport mechanism arises from disordered systems where the bandgap of the semiconductor channel presents intermediate defect state levels and shallow or deep traps. The hopping conduction can be at the nearest neighbour state (nearest neighbour hopping (NNH)) or variable range state (variable range hopping (VRH)) [132].

- In the NNH conduction, electrons with enough energy from high-temperature input ($T \approx 580$ K for example [133]), can hop to the nearest empty site. The conductivity equations following the hopping event at a temperature T are well described in the reference [134].
- In the case of VRH, electrons rather hop to a site using minimal energy and occur at a lower temperature than for NNH (wide range of $10 \text{ K} < T < 120 \text{ K}$ [135]). VRH is the most studied mechanism of hopping conduction and was first shown by Mott who described the conductivity at a certain temperature T as follows;

$$\sigma \propto \exp\left(\frac{-T^*}{T}\right)^{\frac{1}{2}} \quad (1.15)$$

and,

$$T^* = \frac{2.8e^2}{\kappa\alpha K_B} \quad (1.16)$$

with κ dielectric constant, α energy of the original hopping site and K_B is the Boltzmann constant [136]. The SCLC conduction regime explained in the section above is similar to hopping transport. The difference is that hopping conduction from one state to another arises thanks to temperature-dependent energy input while SCLC is dependent on charge injection. A schematic illustration of the hopping conduction mechanism is shown in the following Figure 1.24.

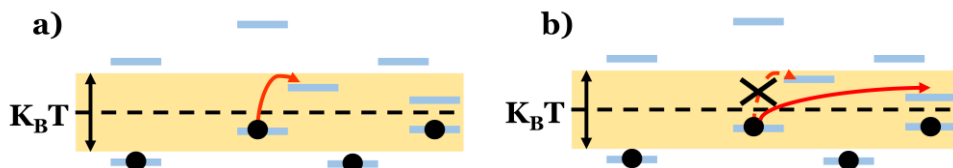


Figure 1.24: Schematic illustration of a) NNH mechanism and b) VRH mechanism. K_B is Boltzmann's constant and T is temperature.

1.11 Bio-Sensor devices and previous work

Sensor devices, either bulk, thin films or nanowires are associated with relevant chemical or physical interactions to be transduced as signals. Four main types of bio-transducers can be found;

- Chemiresistive (also called capacitive transducers) are common for the detection of gases where the sensing element or targeted molecule transfer charges to the channel. For instance, upon absorption, NH_3 or alcohols like methanol and ethanol (that are acceptors) oxide the semiconductor channel. Upon oxidation, MoS_2 or p-type carbon-based materials undergo a decrease of the hole concentration which increases resistivity and reduces transduced signal. Conversely, NO_2 gas by injection of holes increases p-doping and conductivity [137].
- Optical transducers are the most common in nanosensing technology where optical waves changing (UV to IR) are measured after interacting with the sensing material. Changes like polarisation, frequency, phase and intensity are used in spectroscopy to characterise analytes [138].
- In Electrochemical or Amperometric transducers, chemical species affect the carriers' concentration. In those sensors, often in liquids, a constant potential is applied and any charge transfer with the measurands marks a change in current [139].
- Solid state or FET transducers are mostly made of metal, semiconductor or isolating junction materials and are based on electric field modification in the presence of the detected targets. Electric field modifications are monitored by means of impedance, capacitance, current properties and other electrical properties (carrier concentration, resistance, barriers, etc.). Semiconductor devices (transistors or diodes) are sensitive to changes in their environment and external stimuli where any changes in the electric field or the number of holes and electrons can be measured. As shown in a previous example negatively charged DNA that binds to a receptor on an n-type NW will increase the resistivity of the channel [140].

This type of bio-transducer is the main topic of this thesis and has resulted in published material [2]. For biosensors, semiconductor-based devices on protein functionalisation is the research trend for the last ten years [141].

Those devices rely on solid states and FET transduction. The semiconductor has the role of reliable, fast signal acquisition and transmission while proteins enable specificity, sensitivity and a wide genetic field of detection. The covalent attachment of receptors on semiconductors provides docking sites for the specific binding of the targeted molecules. For the group III-IV semiconductors, three main routes for surface functionalisation are well reviewed in reference [142]. Although cycloaddition is the most investigated route it requires specific conditions like ultra-high vacuum [143]. Besides, surface oxides, impurities and structural defects have a negative impact on the attachment of receptors by cycloaddition which does not suit with NWs surface. The most adapted functionalisation route for possible manufacturing of NWs biosensors is silanisation by 3-aminopropyl-triethoxysilane (APTES) widely used with oxides, quartz and Si/SiO₂ biosensor devices [144]. Often, pre-oxidation by H₂O₂ is necessary to obtain O⁻ or OH-terminated surface to react with the APTES, in the case of Ge the natural oxide layer of Ge acts already as a suitable surface. Most studies have shown that a stable layer of APTES on semiconductors can provide protective surface passivation without electronic drawbacks for up to several weeks in ambient conditions [145]. Only a few experiments have been done on Ge and polytypes semiconductors like SiC or SiGe although Ge has been shortly studied, it has never been functionalised with APTES [146]. Being of similar sizes, NWs with atomic or molecular contact on their surface can lead to accumulation or depletion of carriers that are measurable via NWs device fabrication and measurements. Like in this thesis, the working principle of semiconductor NWs sensor devices is via field effect electrical transduction.

Si NWs and carbon nanotubes have been used for sensing devices due to their known sensing properties and simultaneously as conduction channels within the device [141]. NWs being sensitive to their environment, electrical transport is mostly depending on the nature of the NWs and their surface. Detection for biosensing technology is mostly achieved by using labels attached to the DNA targets like redox indicators, isotopic and fluorophores that are only later detected by corresponding equipment (radioisotope, fluorescent probe, chemiluminescent probes, etc.) [3]. Those labels require expensive measurement techniques and label attachment is time-consuming. In 2001, Lieber's group demonstrated for the first time the idea of functionalisation on Si NWs using diverse classes of targets/receptors with selective detection of proteins, ions, nucleic acids and viruses [147].

From that Si NWs and other semiconductors have been a platform for NWs implementation and functionalisation for sensing devices. Later, biosensing using NWs-based devices has been shown to be applicable for the characterisation of a large range of molecules with fast response and working as label-free detectors [147].

As mentioned most of the sensor devices found in the literature have been using top-down and other better-known bottom-up approaches and the DEP technique has been only scarcely used because of the lack of knowledge. Silicon NWs have been used for the detection of a couple of times via bottom-up integration for biosensing technology, where mostly p-type NWs of 20 to 60 nm of diameter were functionalised for antigen and virus detection with LoD ranging from 7 nM to 0.5 fM [148].

Using DEP with Si NWs, research groups used a simple set-up to align single or arrays of NWs between electrodes and highlight a robust nanomanufacturing process [60], [149]. Only gold NWs have been reported for their manipulation via DEP followed by biofunctionalization [150]. The research team of Kumar *et al.* [151] functionalised gold NWs post-alignment using biotin-streptavidin for the detection of two types of cortisol with a detection range of 10–80 μM and 5–30 μM . Those devices used a microfluidic channel pattern on the top of the electrode and showed great potential for manufacturing.

1.12 Previous work on germanium nanowires

Germanium is slowly getting more interest as its properties have the potential for enhanced functionalities compared to Si. As known Ge has higher intrinsic carrier concentration and mobility promising a faster response than Si. Table 1 shows a couple of material properties as well as the Bohr exciton radius larger in Ge enabling more control over the bandgap and possible quantum effect. Hence, at the nanoscale, Ge NWs have been recognised for optoelectronic and field effect transistors [152]. For instance, it was found that at room temperature, the Schottky barrier is less important for Ge NWs than observed with bulk Ge [153] but also compared to planar Si and NW devices' performance [154]. Most results obtained from FET Ge NWs feature current responses from nano to micro amp highlighting Ge NWs as an ideal candidate for nanoscale technology with some patents that already demonstrated its interest in sensing elements in detection devices [155].

For implementation, NWs have to be crystalline with a minimum of defects (to avoid state level and recombination) for optimised conductivity and the response of the device. Currently, the little research on Ge NWs for sensing is due to a lack of control and understanding of the interface oxide layer. Wang *et al.* [156] studied p-type Ge NW (boron doped and passivated by chemical etching) devices contacted with palladium.

They obtained carrier mobility of $\approx 600 \text{ cm}^2\text{V}^{-1}\text{s}^{-1}$. In other studies, passivation of Ge with Si coating and alloy has shown unchanged carrier mobility [157].

Ge natural oxide layer can indeed be a source of surface traps that reduces mobility, however for intrinsic Ge NWs (with [111] ideal crystal orientation [158]) with a natural oxide layer, a mean carrier mobility of $3000 - 12000 \text{ cm}^2\text{V}^{-1}\cdot\text{s}^{-1}$ has been reported, the latter hasn't been reached by Si NWs performance [159]. In fact, more studies have demonstrated that surface oxide may be the origin of high conductivity [160]. Similarly to Ge coated with Si [161], the work of Hanrath *et al.* [162] on Ge grown using Au gold catalyst/seeds presented that Ge NWs conductivity was due to trapped surface charge rather than the presence of Au from the Au seeds. The location of electron traps energy level from surface or core defects has been determined to be located at $\approx 0.15 \text{ eV}$ close to the valence gap and below the Fermi level (0.72 eV) in the work presented references [163, 164]. Now, a couple of research groups have already functionalised Ge NWs without using chemical etchant or treatment for passivation before functionalisation and found that biofunctionalisation layers on intrinsic Ge NWs provided better stability than untreated bulk Ge [165].

Functionalised with isoprene Ge NWs have even shown improved carrier mobility compared to non-functionalised NWs [166]. Using a suitable biofunctionalisation route it is possible to functionalised and simultaneously protect and passivate Ge NWs from oxidation and degradation as the organic monolayer is attached at the surface [165]. Most of the studies found on semiconductor NWs and Ge NWs manipulated by DEP feature pure NWs characterisation with a superficial usage of the DEP properties [167, 168]. Afterwards, the NWs are probed to investigate their microstructure and response to diverse stimulation and rarely DEP involvements are questioned.

As a sensor, Ge NWs have been mostly exploited for their optical advantages thanks to the properties already mentioned. Most of the time, their implementation is made directly through a transparent polymer membrane within which they are grown from. The advantage of the supercritical-fluid-inclusion technique is the combination of growing NWs directly in a transparent matrix forming the final channel ideal for optical technology. Moreover, this technique has demonstrated NWs of similar electrical quality when characterised individually [169]. This is where DEP is an important asset; for biosensing, this technique is not adapted as the NWs are enclosed in a polymer keeping them from chemical interaction with the environment and hindering surface functionalisation. While DEP has demonstrated unprecedented selection properties and alignment characteristics without direct contact and damage to the crystal structure, manipulation of Ge NWs has never been thoroughly studied. In order to achieve good alignment control and optimum selection of NWs, DEP parameters have to be analysed in depth offering the opportunity to manipulate a large range of Ge NWs to be embedded in a wide variety of device sensors.

1.13 Previous work on GaAs and GaAsBi

GaAs is well known for its piezoelectric properties, which is why it has been used for resonant sensors and actuators [170]. Hence, GaAs has been used for piezotronic and pressure sensors as potential crystal quartz microbalance [4]. Moreover, because of its high electron mobility (as seen in Table 1) GaAs has been investigated for its fast response features in high-speed transistor and integration in optoelectronic devices in the visible and UV range, especially in photovoltaic application coupled with its thermal resistivity due to its wide band gap [171]. GaAs with Ge are at the centre of interest as a replacement for Si because of their properties already mentioned.

GaAs NWs have been synthesised in high quality either by MBE or by MOCVD using GaAs or Au catalysts/seeds [172]. Like Ge, because of the intrinsic instability of GaAs oxide layer in an aqueous environment, functionalisation studies have been limited. Nevertheless, a couple of alternative solutions have been found using protective layers compatible with further functionalisation [173, 174]. At the nanoscale, GaAs NWs have mainly been used for their optoelectronic properties. Effective photoresponse has been achieved in a vertical array of GaAs NWs that provides increased photoactive area and photoconductive response [175]. NWs in photosensors and optoelectronics have improved photocurrent due to enhanced light absorption, conversion efficiencies and lower cost compared to thin films [176, 177].

Li *et al.* [178] studied the photoresponse of a single GaAs NW synthesised by MBE and implemented by EBL for electrical contact. They observed for a NW of 15 μm long and diameter of 160 nm a sensitive peak response at 1.40 eV compared to a conventional peak response at 1.42 eV from the GaAs band-gap. In thin films, the most sensitive peak is also found at 1.42 eV [179]. Using DEP, the integration of GaAs NWs has been particularly investigated by the group of Nunez *et al.* [91], [180]. The studies principally demonstrated ideal collection rate parameters. By chemical beam epitaxy they obtained GaAs NWs of 5 μm long and 50 nm in diameter with hexagonal morphology. They showed that using DEP, the ideal collection rate is dictated by an AC voltage of 5.66 V applied between the electrodes with a frequency of 100 kHz in ethanol. DEP studies, in the vast majority of the literature lack analysis of the influence of parameters on the quality of the collected NWs and electrical properties. Instead, DEP is widely used as a quantitative tool rather than a qualitative one. This work hopes to fill the gaps of information about the influence of frequency collection on the properties of the NWs to improve implementation for future technology using DEP.

One essential interest of GaAs relies on its compatibility for ternary to quaternary compound mixing. Indeed, GaAs has been synthesised as numerous alloys such as SbGaAs [181], InGaAs [182], AlGaAs [183], GaAsBi [184, 185] and often with a surface layer of different chemistry [186, 187]. As a function of the Bi % content, GaAsBi alloy has shown encouraging results in the field of electronic [188] and photovoltaic [189]. Bulk GaAsBi has been successfully grown by MOVPE, MBE and Liquid Phase Epitaxy (LPE) [190, 191]. Most of all, research has mainly been pointing towards MBE growth because of its flexibility and the possibility to reach stable high content of Bi [192]. The growth of GaAsBi NWs is very scarce with only a couple of publications [193, 194, 195]. The team of Ishikawa *et al.* [193] synthesised GaAs NWs with a GaAsBi shell (%Bi 0.5-2 %) by MBE.

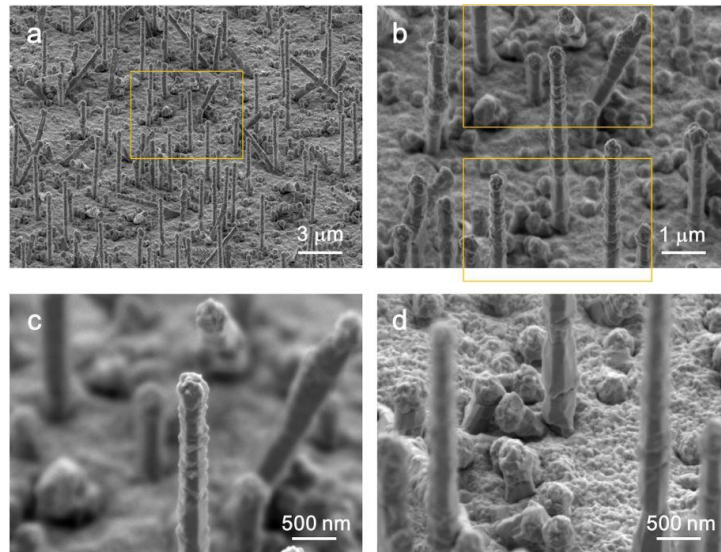


Figure 1.25: SEM images of GaAs/GaAsBi NWs obtained by MBE by Ishikawa *et al.*.
Extracted from [193].

They showed NWs morphological features close to the NWs investigated in that study. Their NWs had strong surface roughness morphology and an inhomogeneous distribution of Bi revealed by EDX. SEM images of the obtained NWs have been put in the following Figure 1.25. It was demonstrated that small incorporation of Bi content of less than a few per cent can shrink the band gap with the valence band moving towards a higher energy range and the conduction band moving towards a lower energy range [196]. Hence, the possibility of absorbed or emitted photons wavelength can be increased with the potential for increased sensitivity and high-speed photoresponse that are leading features for photosensing. The introduction of Bi in the GaAs host creates perturbation in the band structure.

The valence orbitals of Ga, As and Bi suggest that their core orbitals and electrons are unchanged during the formation of bonds GaAs with Bi. GaAs valence band and Bi atomic orbitals follow a resonance theory resulting in the GaAs valence band energy rising with Bi incorporation [197]. A decrease of band gap by a rate of 83 meV/ Bi % has been demonstrated [188], which is much larger than for incorporation of In with 10 meV/ In % in InGaAs [198] and Sb with 16 meV/ Sb % in SbGaAs [196], and N with 150 meV/ N % in NGaAs [199]. However, if the incorporation of N in GaAs decreases the band gap, it also leads to a deterioration of electron mobility [200]. The incorporation of Bi in GaAs offers interesting band gap engineering with possibilities of improving hole mobility [201]. There have been several DEP studies with the objective of device fabrication for future sensors and nanotechnology analysing how NWs chemical nature and structure can be used to increase their performances. However, although valuable progress has been made in the field and DEP has been recognised as a leading tool for precisely aligning NWs forming a nanodevice, in-depth DEP research towards improvement of the quality of the aligned NWs and the impact of these key parameters is lacking.

The research carried out in this thesis aims to address this issue by demonstrating control and key transport parameters of germanium and gallium arsenide bismuth, as well as analysing the use of the resulting NWs as diodes and biosensors.

In the next parts of the thesis, the key objectives are therefore the following;

- To explore the key steps involved in the fabrication process, including nanowire synthesis, device design for dielectrophoretic manipulation, and characterisation, emphasising their significance in achieving high-performance sensor devices.
- Discuss dielectrophoresis as a fabrication technique for precise positioning and alignment of nanowires onto target substrates, enabling the realisation of functional sensor devices.
- To explore electrical, biological and optical properties of the fabricated sensor devices, ensuring their quality and performance
- To highlight the importance of germanium and GaAsBi nanowires as promising materials for sensor devices, considering their unique electrical, optical, and mechanical properties
- To summarise the key findings and insights obtained from the discussed techniques and equipment, and to identify future prospects and challenges in the field of sensor devices fabricated using germanium and GaAsBi nanowires via dielectrophoresis.

Chapter 2

Fabrication and characterisation

Introduction

In order to investigate nanowires' manipulation, implementation in sensor devices and electrical properties, accurate measurements of the nanowires morphology, placement and electrical response are essential.

The following Chapter 2 discuss the key steps involved in the fabrication process, including nanowire synthesis, first elements of device design, biofunctionalisation and characterisation methods. Additionally, the chapter will highlight the importance of specific equipment and instrumentation employed at each stage, providing insights into their functionalities and capabilities.

2.1 Germanium nanowires growth by Metalorganic Vapour-Phase Epitaxy

Amongst the growing techniques involved with the VLS mechanism, Metalorganic Vapour Phase Epitaxy (MOVPE) (also named Metal Organic Chemical Vapour Deposition (MOCVD)) is largely commercialised for semiconductor epitaxially grown. From blue laser or light emitting diodes to high-speed solar cells, the production of a wide range of semiconductors and its versatility make MOVPE a leading technique for semiconductor optoelectronic and electronic devices. The term "metalorganic" stands for the nature of the precursor gas and "vapour phase epitaxy" for the low-defect-density and lattice-matched epitaxy with the substrate. MOVPE allows control and high-quality material synthesis from semiconductor thin films to heterostructure and nanowires. That is why in collaboration with the IMEM-CNR: Institute of Material for Electronic and Magnet which is part of the Italian National Research Council in Parma (Italy) the studied Germanium nanowires in this thesis were grown at the IMEM by MOVPE [202]. As similarly described previously and following the VLS mechanism; in the hot wall MOVPE system, a single liquid metal organic precursor, isobutyl germane (iBuGe), is mixed with a pure gas carrier (500 sccm palladium purified H₂).

In the case of Ge growth NWs, Ge-hydride (GeH_4) is generally used as a precursor. However here, due to its higher toxicity, iBuGe is used instead as it is safer and has shown conclusive success [44], [203]. In the growth chamber, the iBuGe precursor was kept at a constant temperature of 10°C within a thermostatic bath [44]. Gold nanoclusters were used as seeds (from a gold-nanoparticles-based solution) which allow control over the diameters of the NWs. The Au nanoclusters were drop-casted on a $\text{Si}(111)$ substrate and placed in the chamber.

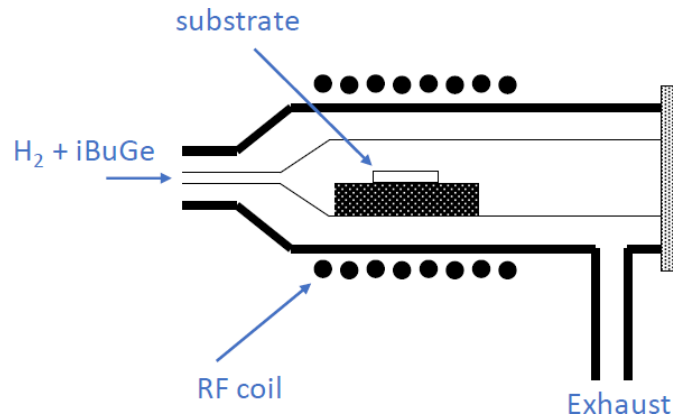


Figure 2.1: Schematic representing the MOVPE main chamber.

MOVPE occurs either at low (commonly 100 mbar) or high pressure. The vaporised precursor is transported in the main chamber that is heated at 430°C (for the Ge NWs) towards the substrate followed by nucleation mechanism and growth, and the remaining reagents evaporate from the system. The NWs were grown over a period of 1 hour at a pressure of 100 mbar and using iBuGe as a precursor [202]. The length of the NWs can be modulated by the growth time. The process explanation has been simplified and is more complicated than stated as a number of reactions take part in the growth during gas phases and surface processes. More details are well presented in references [44] and [202].

2.2 GaAsBi growth by Molecular Beam Epitaxy

Curiously, bulk GaAsBi was one of the first materials to be synthesised by MOVPE [204]. While most elements of the III-V group (Al, Ga, As, Sb, Bi, In..) have been well established for their growth via MBE, GaAsBi has mostly been reported for its growth via MOVPE [204, 205] and MBE [206]. With the successful work of Tixier *et al.* [207] investigation of GaAsBi growth by MBE has seen increasing interest because of the possibility to push Bi content up to 20 % unachievable by MOVPE [208].

MBE, similar to VLS and MOVPE techniques of crystal growth is also a successive atomic layer deposition, based on reactions of source element in contact with a heated crystalline substrate. MBE is however performed in ultra-high-vacuum (UHV) (typically 10^{-7} Torr by MOVPE VS 10^{-11} Torr by MBE). UHV conditions avoid contamination and the main reactions involve an atomic or molecular beam which gives this technique advantage of purity. MBE process is a strong asset compared to MOVPE.

Reflection High-Energy Electron Diffraction (RHEED) is a setup technique implemented to MBE that allows real-time in-situ measurement and control of growth and composition (stoichiometry, epitaxy, temperature) [208]. Such purity and monitoring have led to promising band-gap engineering [208]. MBE growth also revealed its enormous potential with the discovery of the quantum Hall effect at the origin of the 1998 Nobel Prize in Physics [209]. To the best of our knowledge, GaAsBi NWs have been only scarcely explored by a couple of groups' work resulting in publications [193, 194, 195]. Two of them present either multi-shell GaAs/GaAsBi shell NWs by MBE, or GaAsBi NWs by MOVPE while the other introduces the first principal simulation on electrical and optical properties, GaAsBi NWs have never been synthesised by MBE before. As mentioned and as represented in the following Figure 2.2 within a UHV chamber, epitaxy growth occurs between one or more beams (K-cells) of atoms or molecules thermally evaporated from sources passing through the cells orifices towards the heated crystalline substrate (controlled temperatures).

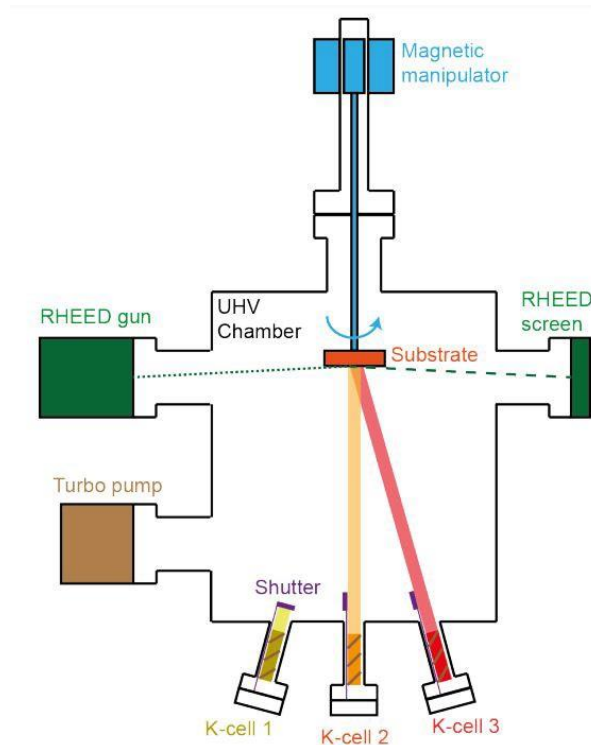


Figure 2.2: Schematic representing an MBE chamber.

In the deposition chamber, the most important part of the MBE system, a substrate is placed to host the NWs growth. Atoms from the beam, As, Bi and Ga are generated by the beams generator K-cell as illustrated in Figure 2.2. The beams of atoms hit the heated substrate surface and nanoclusters are evaporated or sublimed allowing chemical interaction. The growth mechanism is a formation of a thin crystal layer after layer. Although the details of the growth mechanisms are not well known a series of models have been proposed for GaAsBi thin film [191]. Beams atoms flux rate and substrate temperature are critical and have to be precisely controlled. Usually, for Bi incorporation, As:Ga flux is stoichiometric and the substrate temperature is heated below 400 ° C [210]. To grow NWs, nanoclusters of GaAs are used from (a colloidal solution) and deposited on the substrate. More details on the growth haven't been shared by the research team.

2.3 Electrodes fabrication

To fabricate the electrodes, a layer of 5 nm of chromium (Cr) followed by 50 nm of gold (Au) was deposited by metal thermal evaporation on corning glass. All electrodes have been designed using *KLayout* Software and later printed on a chromium mask to perform photolithography. Photolithography was used to define the electrode geometry via the designed electrode, undeveloped resist was then removed before the samples were placed in Au and Cr etchant to take out the unwanted metal. The photoresist on the samples was subsequently washed out by immersing them in acetone.

Thermal evaporation

A Moorfield minilab 60 thermal evaporator was used to deposit the metal layers. The equipment is located within the facilities of the Department of Electrical Engineering and Electronics of the University of Liverpool and all the metal depositions originate from the author's interaction with the equipment.

All chemicals and metals used in this part were obtained from Merck and used as received unless otherwise stated. A first layer of Cr followed by a layer of Au was deposited. The principle of deposition relies on the heating of the solid source material (Au or Cr) that vaporises in a vacuum chamber and is transported to the clean substrate where the metal particles condensate to form a thin film. In the Moorfield minilab 60, the target substrate is fixed on a rotating plate above the metal source for an upward deposition.

A shutter between the metal vapour and the target substrate allows protection against unwanted particles and can intercept the vapour to control the deposition rate. The pressure, usually kept under 10^6 mbar minimises collision between gas and metal vapour particles. Moreover, such pressure creates a mean free path for the vapour particles to reach the above target substrate. On the substrate surface, the particles form a nucleus and generate growing islands until a film is formed. The uniformity of the film is achieved by the rotating plate. Both metal layers of Cr followed by Au are deposited after the other without breaking the vacuum avoiding contamination in layers. The final glass substrate with the metal layers is simplified in the following Figure 2.3 b).

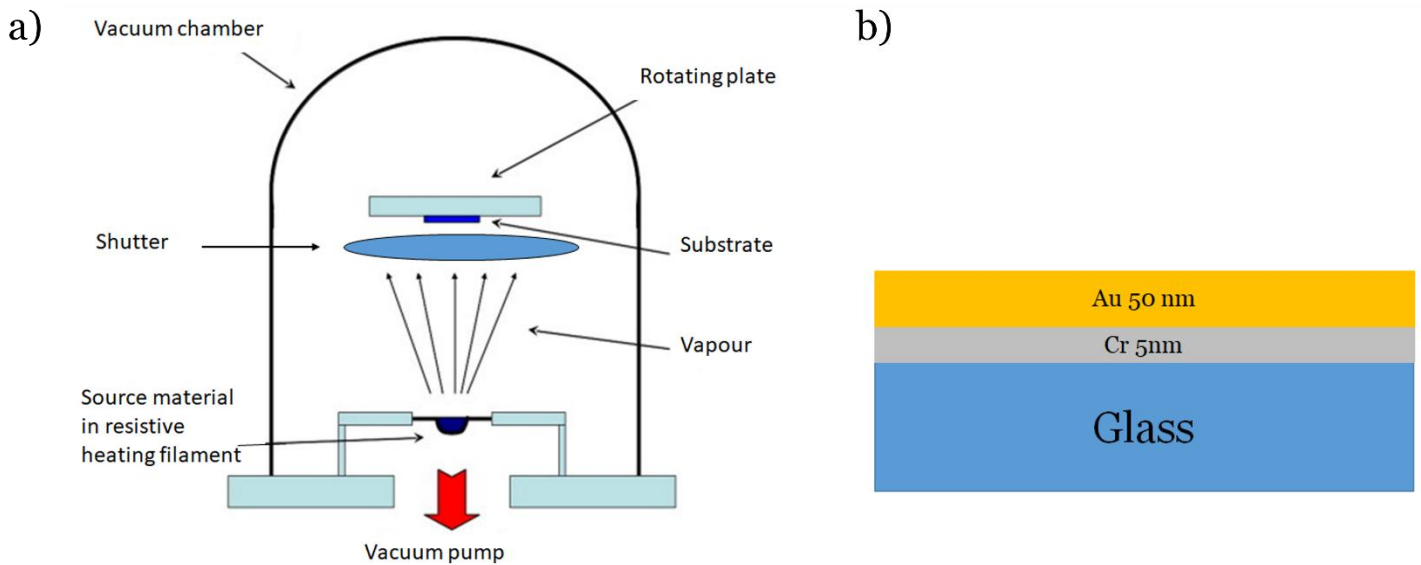


Figure 2.3: Schematic of a) Thermal evaporation and b) resulting deposited layers of Cr and Au on a glass substrate.

Photolithography

The technic of photolithography for micro-fabrication is widely spread in the electronic industry and research. It is based on a pre-designed pattern mask transferred onto a photo-sensitive polymer deposited on the top metal layer. The schematic Figure 2.4 is the step-by-step process for photolithography. Once the metal layers have been deposited onto the glass substrate, the surface is covered by a layer of cordovan photosensitive polymer (MICROPOSIT S1813 reacting to UV light illustrated Figure 2.4 a) 1)) using spin coating. The mask pattern is placed on the cordovan photoresist (a) (2)) and UV light is shone on the top (a) (3)).

The UV light that comes through the mask reacts with the exposed part of the photosensitive polymer b) (1). The photoresist is then baked in order to harden the unexposed part and sensitise further the exposed part. The exposed parts are thus easily removed by chemical reaction using a photo-developer. In this example, the positive photoresist is removed by the developer that reacts with the exposed part while a negative photoresist is removed by the developer that reacts with the unexposed part. As a result, the left photoresist layer has the pattern of the future electrodes (as seen in c)).

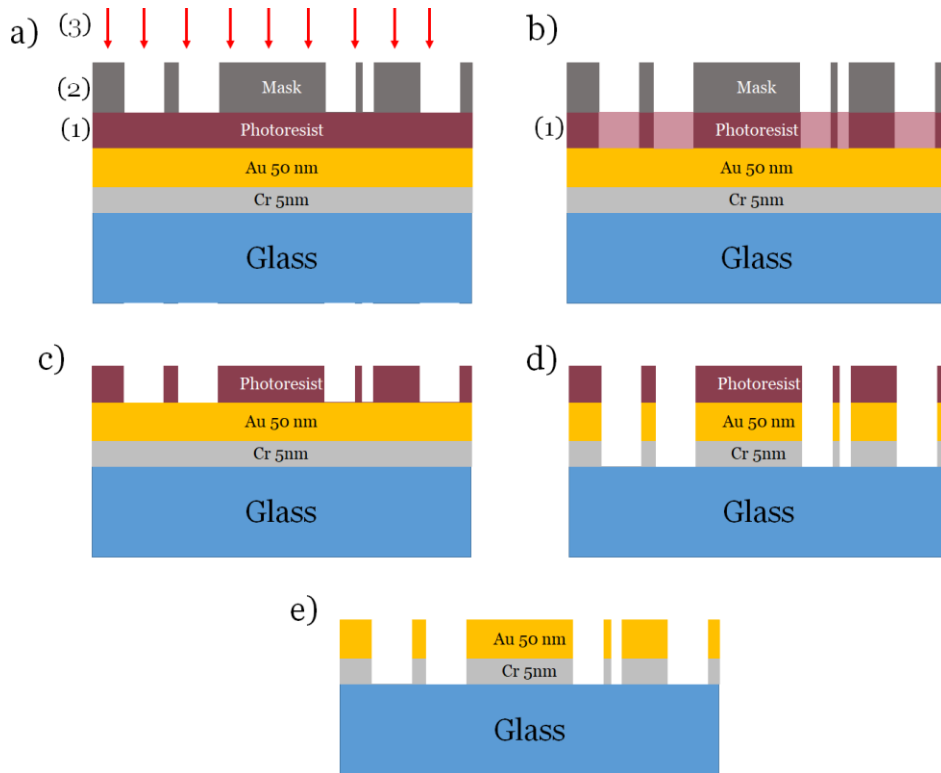


Figure 2.4: Schematic of the fabrication of the device electrodes by photolithography and etching. Not to scale.

To form the final metal electrodes, chemical etchants that do not react with the photoresist are used to remove the parts unprotected by the polymer. Specific Au etchant followed by Cr etchant removes the layer of unwanted metal (see d)) [211]. Finally, the remaining photoresist is washed away using acetone and the samples are dried using N_2 gun step e).

2.4 Bio-functionalisation of the nanowires

The NWs in this work are being studied as potential sensor channels for biotechnology. The Ge NWs are thus functionalised using the silanisation method described below and also detailed in reference [212]. The devices were immersed in an ethanol solution containing 3% of (v/v) 3-aminopropyl-triethoxysilane ((APTES) chemical molecule represented in appendix Figure A.4.1) at 80 °C. After 2 hours the samples were removed from the solution and washed four times with ethanol to remove any excess material. This step was completed by drying the samples under nitrogen and a curing step of 1 hour at 110 °C. The Si–OH groups of the silane react with the OH and O[−] dangling groups of the oxide surface [213]. This leads to the formation of a stable bond on the surface. The surface at this point is terminated with an amine group (NH–2) that can be used for further functionalisation as pictured in the schematic Figure 2.5 b).

The samples were then immersed in an aqueous solution containing 2% of (v/v) glutaraldehyde at room temperature (25 ± 2 °C) for 1 hour. The glutaraldehyde (GA) acts as a linker that binds with the amine-terminated silane and provides an aldehyde binding group for the amine-terminated aptamer sequence. After rinsing, the samples were dried under N₂. The functionalised devices were subsequently immersed in a solution containing amine-terminated aptamers (200 μL, 100 nM), Eurogentec, Belgium. The devices and aptamer solution were incubated at 37 °C for 2 hours and then rinsed with 1× Phosphate-Buffered Saline (PBS) and deionised water to remove the excess aptamers and subsequently dried under N₂ resulting in the device shown in Figure 2.5 d). That aptamer was previously reported to bind to the spike protein of the SARS-CoV2 virus [214]. The specific sequence is

5'CAGCACCGACCTTGTGCTTTGGGAGTGCTGGTCCAAGGGCGTTAATGGACA-3'

with an amine group attached to the 5' end. There is a possibility that not all aldehyde groups (R-CH=O) provided by the GA will have bound to an aptamer and as such, they would provide sites that potentially can bind non-specifically to any amine group present in the proteins. To prevent this, following the aptamer functionalisation, the samples were immersed in a PBS solution containing 80 mM of glycine for 1 hour at room temperature. They were subsequently rinsed in PBS and dried in an N₂ atmosphere to remove excess material as well as any water, Figure 2.5 e) provides a schematic overview of the functionalisation steps and final device in the presence of the spike protein reacting with the attached aptamer.

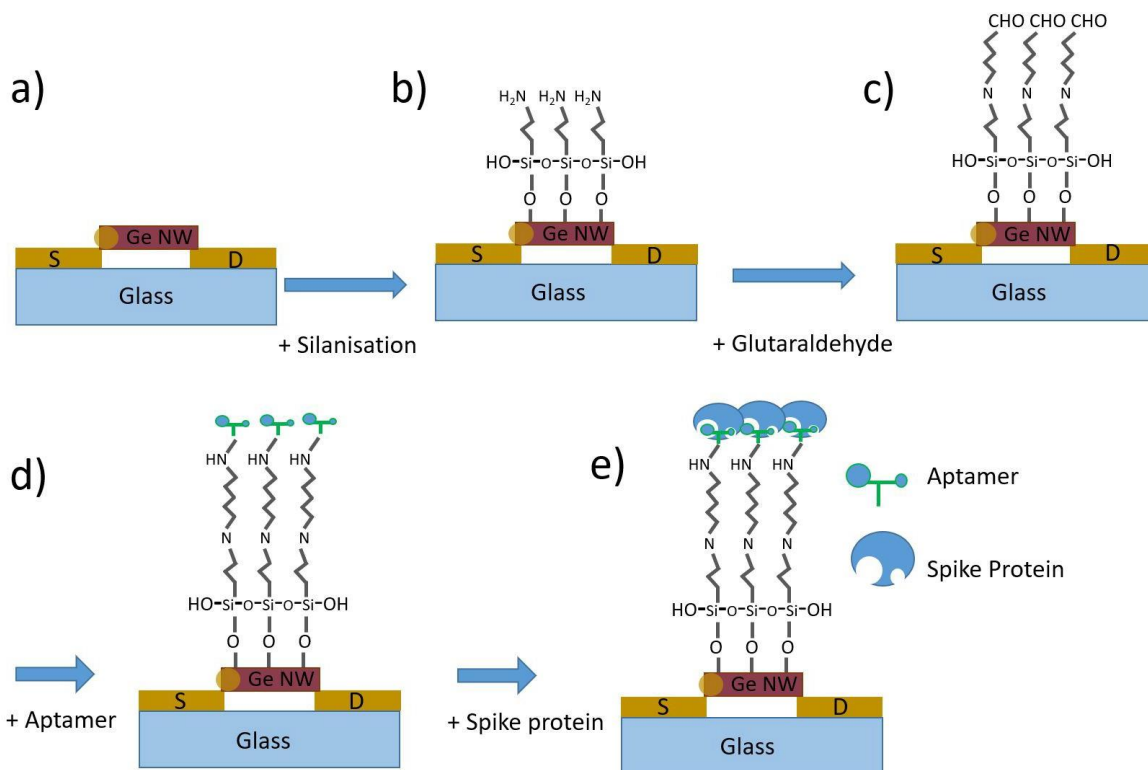


Figure 2.5: Schematic of the functionalisation steps a) bare device, b) device after silanisation terminated with an amine group NH_2 , c) device after Glutaraldehyde treatment acting as a linker between amine of b) and aptamer, d) final functionalised device with attached aptamer, e) functionalised device in the presence of spike protein.

2.5 Characterisation and analysis tools

In order to characterise the NWs and the resulting final devices through their journey starting from synthesis, DEP manipulation and finishing by functionalisation and biosensor fabrication or photodetector properties analyses, accurate measurement techniques are employed. Chemical nature, physical shapes, orientation in space, electrical properties and surface are analysed thanks to specific pieces of equipment that have been used throughout this study and are explained in this section.

2.5.1 Electron Microscopy

Scanning Electron Microscopy (SEM)

In this work Scanning Electron Microscopy (SEM) images and analysis were obtained using a JEOL 7001F from the Albert Crewe microscopy Department of the University of Liverpool where most of the obtained images are from the author's interactions with the equipment.

A SEM is composed from top to bottom of an electron gun, a system of electromagnetic condenser lenses, scanning coils, an objective aperture lens, two detectors and the sample on stage in a vacuum chamber. Figure 2.6 (right) shows details of the SEM equipment. The electron microscope is a powerful technic to analyse the morphology, atomic structure and chemical nature of small elements from micro to nanoscale.

Traditional optical microscopes use light while SEM uses electrons to form an image allowing higher magnification and structural depth. This technique can probe chemical species by Electron Dispersive X-Ray Spectroscopy (EDS or EDX) also used with Transmitted Electron Microscopy (TEM). From the source, electrons are generated by a heated tungsten filament and beamed through the gun. A voltage is used to improve the electrons' kinetic energy enough to hit the sample and interact with the matter. In the case of SEM there will be two different types of interaction with the matter, resulting in the detection of Backscattered Electrons (BSE) and Secondary Electrons (SE). Many other energetic interactions occur like X-ray emission or cathodoluminescence [215]. It is the choice of the user which signals to capture for adapted analysis as each signal carries information.

BSE and SE detectors are respectively placed above the sample concentric with the beam and placed at an angle.

- BSE have elastic interaction with the matter in the depth of the sample where electron energy from the beam is conserved. They transfer momentum to the sample atomic nucleus because of the mass difference. Large atoms (high atomic number) will result in more electrons being scattered and able to reach the detector producing higher signals and ensuing brighter images giving contrast. The BSE will provide information on the sample's chemical nature as well as the topography and crystallography.
- SE have inelastic interaction, they are electrons from the sample's surface where electron energy is lost compared to the initial electrons. Electrons from the source collide with electrons from the sample's atoms and come out with a loss of energy, a secondary electron is emitted ionising the atom. Detection of SE gives information on the topography of the sample's surface up to 10 nm depth. It provides an image of the surface, profile observation and morphology.

For SEM analysis samples can be of any thickness although they must have a conductive path for the electrons to scatter and probe the matter. Hence for insulating material, surface treatments are done to cover the sample using plasma deposition of chromium for example.

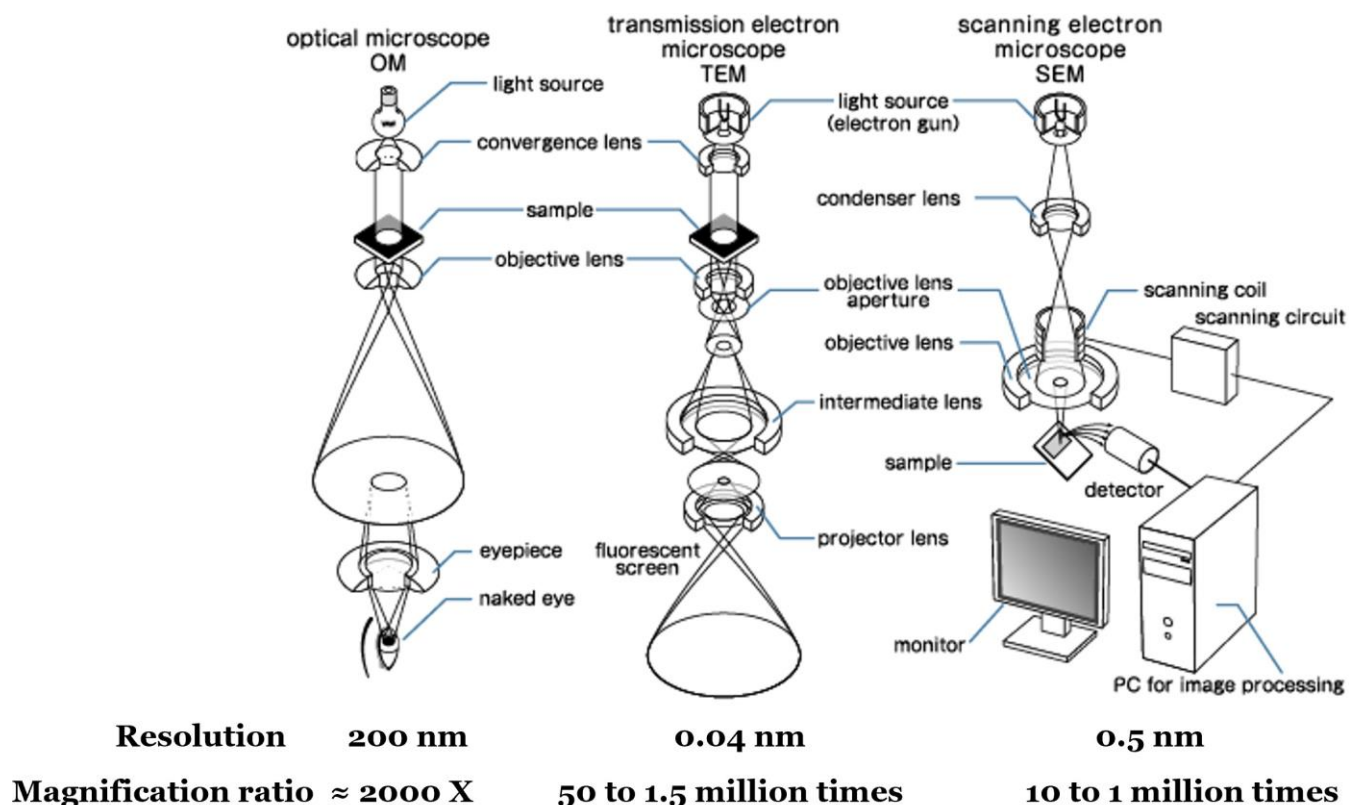


Figure 2.6: Schematics of an optical microscope, Transmitted Electron Microscope and Scanning Electron Microscope.

Transmitted Electron Microscopy (TEM)

In this work Transmitted Electron Microscopy (TEM) images were obtained from a JEOL 2100 Cs Corrected STEM also available at the Albert Crewe Microscopy Department of the University of Liverpool, most of the obtained images are from the author's interactions with the equipment.

TEM follows a similar principle to SEM although with higher magnification and more advanced options. For this technique, samples have to be thin enough (< 150 nm) so that, as the name suggests, electrons from the gun are transmitted through. Compared to SEM the sample stage is situated in the middle of the column and transmitted electrons go through objective, aperture, intermediate and projector lenses finally diffraction pattern and image are converted on a fluorescent screen or by a charge-coupled device camera (CCD) as illustrated Figure 2.6 in the middle schematic. As electrons pass through they are transmitted in the same direction or diffracted and they have either elastic or inelastic interaction with the sample. Further below in the machine after the sample, the electrons pass through the objective lenses and form a diffraction pattern on the focus plane of the objective lens system as well as an image on the image plane.

Electrons scatter in the sample (elastic scattering) or rather they diffract waves from one point of the sample atomic structure.

Focused by the objective lens that energy is converted and forms one spot on the focus plane resulting in the diffraction pattern. The diffraction pattern is a good asset to investigate the crystal nature of the sample. It gives information about the crystallinity of the sample. For a monocrystalline area hit by a parallel or tilted beam, the diffraction pattern will show one single spot for one single crystallographic plane.

By extension, this enables analysis of the interplane distances and symmetry. For a structure less oriented or for polycrystalline areas the diffraction pattern will exhibit spots that appear more like dashes and for an even less oriented structure like amorphous phases, it will appear with lines and rings as the diffraction pattern translates more random structural orientation. Figure 2.7 shows an example of diffraction patterns obtained from three different structures of Aluminium (Al) with a) showing well organise and clear spots of crystallographic planes.

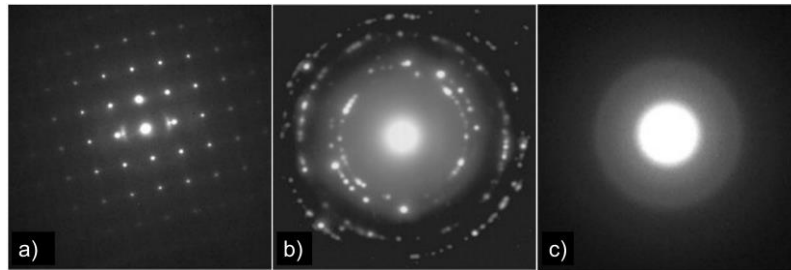


Figure 2.7: Diffraction pattern of different structures of Aluminium a) monocrystalline, b) polycrystalline, and c) amorphous.

Extracted from [216].

Similarly to SEM, the transmitted beam is sensitive to the density and thickness of the sample where thicker regions scatter more electrons appearing darker on the image and conversely for thinner regions giving contrast to the image. The interest in using TEM is the possibility of observing the same region of the sample and obtaining the diffraction pattern and the magnified image. It is also very useful for analysing the chemical nature and defects in semiconductors. With TEM a high resolution down to 0.04 nm has been achieved recently [217, 218] although traditionally TEM resolution reaches 0.08 nm [216]. As explained TEM samples have to be very thin (< 150 nm) and they sometimes need to be processed to be very flat which can be tedious [215]. For surface morphology, 3D projection analysis by SEM is a better choice but for crystal structure analysis as well as lattice defects and impurities TEM has to be used.

Energy Dispersive X-Ray Spectroscopy analysis (EDX)

Energy Dispersive X-Ray Spectroscopy (EDX or EDS) is a widespread technique for chemical investigation. Available within SEM and TEM equipment it gives qualitative and quantitative information on the chemical nature of the selected area with the possibility to get a chemical map of a few cubic micrometres. As mentioned when the sample is hit by the electron beam X-rays can originate from the beam and matter interaction.

Those X-rays are detected using an energy-dispersive spectrometer [219]. The energy of the detected X-ray is interpreted by a lithium drifted silicon detector and gives information on the chemical composition. A very interesting and common tool used for sample analysis is chemical mapping. As an example the following Figure 2.8 shows two different examples of individual elemental mapping a) obtained from this work and combined chemical mapping b) obtained from the work presented reference [220].

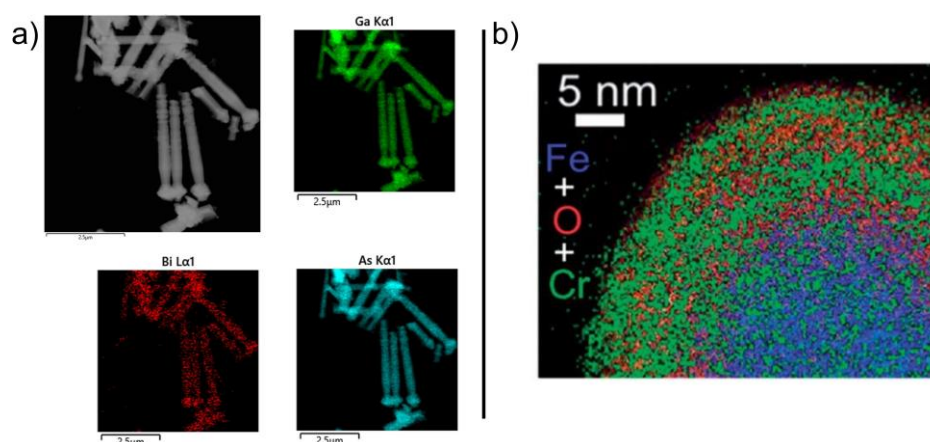


Figure 2.8: Images obtained by Energy Dispersive X-ray Spectroscopy of a) GaAsBi NWs and b) composite nanoparticles.

Extracted from [220].

2.5.2 Optical microscopy

In this work, the optical microscope images were obtained using an Olympus BX53 available at the Material Innovation Factory (MIF) of the University of Liverpool. All images are from the author's interactions with the equipment.

Compared to SEM and TEM the optical microscope is rather used for quick analysis with low magnification. The sample installation is extremely easy compared to SEM and TEM and does not require any preparation. An optical microscope uses light instead of electrons and can magnify ≈ 2000 times.

As shown in Figure 2.6 optical microscopy is simpler equipment with a system of lenses and the image obtained is the "real" magnified image of the sample. The Olympus BX53 was equipped with a Brace-Koehler compensator allowing the use of polarising light and resolution up to 20 nm.

2.5.3 Raman Spectroscopy

In this study, the Raman spectroscope used for surface analysis was a Renishaw InVia Qontor available at the MIF of the University of Liverpool. All results and analyses obtained were performed by the author.

Raman spectroscopy is based on the inelastic scattering of light photons from their interaction with matter. When a monochromatic light source shines on a material surface the majority of the scattered light energy is elastic and is called Rayleigh scattering, another part (≈ 1 part in 10^6) is inelastic and called Raman scattering [221]. Rayleigh scattering, having no change of energy can not be used. Raman scattering is composed of two subcategories of scattering called Stokes for loss of energy and Antistokes for a gain of energy. Antistokes scattering is rarely used and the Renishaw equipment only analyses Stokes scattering [222]. Inelastic Stokes scattering originates from the exchange of photons with atomic bond vibration in the material. The Raman spectrum is obtained from the detection of those Stokes scattered photons. The vibration of the atomic and molecular bond by the incident photons implies polarisability and bond modifications. Vibration modes can be symmetrical or asymmetrical, stretched and in-plane or out-of-plane bending (rotational, stretching, scissoring, rocking, etc.) [223]. The resulting Raman spectrum can be composed of a multitude of peaks translating one specific type of vibration from specific atoms and molecules giving information on the sample molecular arrangement. From a rich database and vibrational tables, spectrum vibrational peaks are assigned to corresponding atomic and molecular bonds [224]. The Renishaw InVia is equipped with two wavelengths in the visible region at 532 nm and near IR in the 785 nm regions. The spectrums obtained in this work were obtained from a laser source wavelength of 532 nm.

2.5.4 Contact angle, wettability

Contact angle measurements are performed using a KRUSS Drop Shape Analysis System (DSA 10 Mk2) to measure the wettability angle of liquids. All collected results are from the interaction of the author with the equipment available within the Electrical Engineer and Electronics building. The drop shape analysis system allows measuring the contact angle from the image of the drop and the surface tension of the support solid.

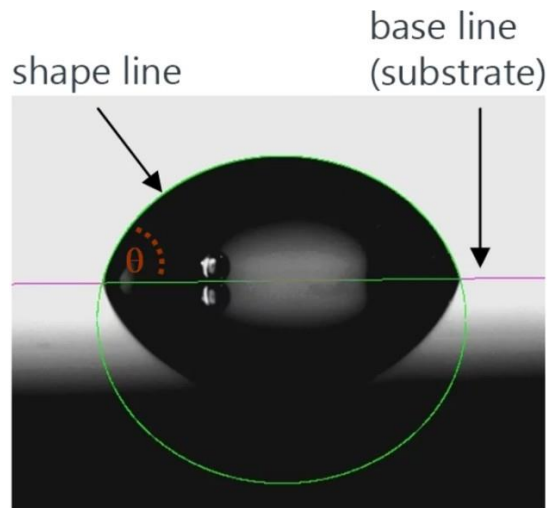


Figure 2.9: Drop fitted contour and determination of the angle θ by drop shape analysis. Extracted from KRUSS [225].

The wettability of a solid by a liquid is quantified by the contact angle. It is the angle formed by a liquid at the three-phase boundary between air, liquid and solid surface. The following Figure 2.10 shows the different contact angles for two types of liquid on a surface.

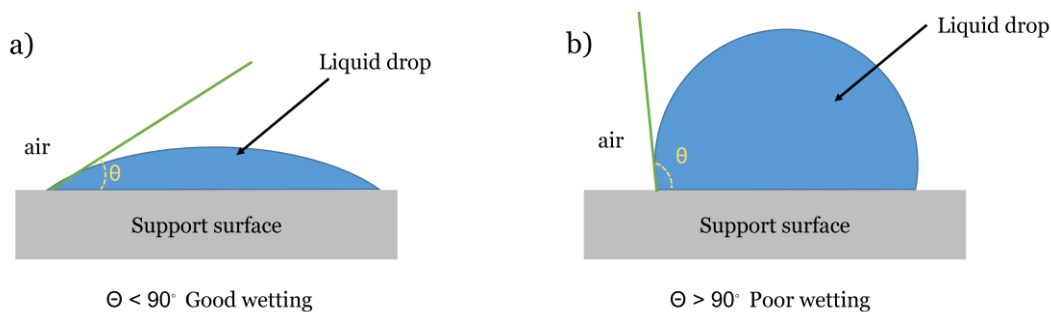


Figure 2.10: Schematic of contact angle principle.

In the case of a complete wetting like shown a) Figure 2.10 the liquid spreads over the surface with a large area of covering and the contact angle is considered as $< 90^\circ$. Above $> 90^\circ$ angle the liquid is considered as not wettable and does not spread over a large area on the surface.

2.5.5 Zeta potential

In this thesis zeta potential analysis was obtained from a Malvern DLS ZETASIZER ZS available at the MIF of the University of Liverpool. All data obtained originated from the author's interaction with the equipment.

Zeta potential is experienced by any particle in suspension similar to a surface electrokinetic potential. It is the external layer net charge (as shown Figure 2.11) that forms at the particles' surface and the medium, it is the net charge of the particle surface in dissociation with the surrounding medium. The following figure illustrate the surface Zeta potential of particles in medium.

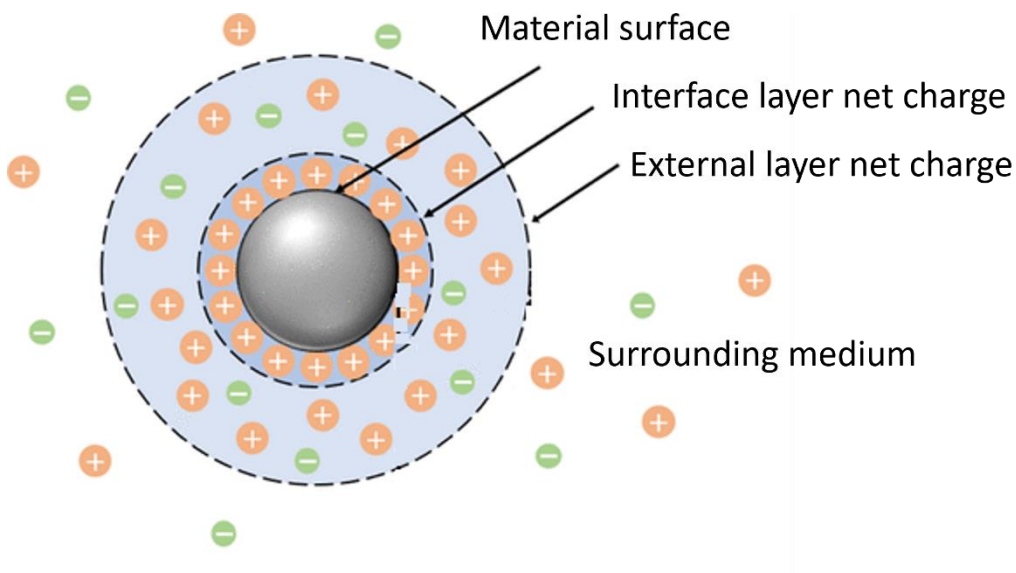


Figure 2.11: Surface zeta potential of a particle in a medium.

That surface potential is about millivolts and influences the ionic distribution from the medium by attracting counterions at the surface, especially for polar solvents like water. This forms most of the time an Electrical Double Layer (EDL). The overall potential surface charge is measured by means of electrophoresis (EP). Within a cuvette, with two facing electrodes, the zeta potential is measured by applying a DC electric field between the electrodes.

Laser Doppler is used to tracking the transport of the particles that moves toward the opposite electrode with a velocity proportional to the zeta potential [226].

By comparing medium dielectric permittivity and viscosity the mobility of the charged particles is converted to zeta potential.

2.5.6 Photocurrent Spectroscopy

Traditional photocurrent spectroscopy enables by means of wavelength light excitation to analyse material morphology and properties like photocurrent of electrically contacted NWs. Because of the NWs dimensions, photocurrent can be influenced by quantum confinement in the case of dimensions lower than the Bohr radius [227]. In that study, all the NWs have dimensions above the Bohr radius limitation and so no quantum confinement effect should be expected. An incident beam of photons with a larger energy $h\nu$ than a semiconductor band gap will excite the electrons escaping from the valence band to the conduction band. Hence, photocurrent gives information on the NWs band structure [228]. Photocurrent spectroscopy measures the resulting current generated by photons wavelength and bias voltage stimulation of a material, in this study case, semiconductor NWs electrically contacted by DEP.

A laser light from a monochromator system ([Horiba iHR320](#)) modulated by an optical chopper passes through a lens and focuses onto the NWs device. A voltage is applied to one electrode of the device using a Stanford Research 570 ([SR570](#)) low-noise current pre-amplifier. The [SR570](#) amplifier also allows the application of a bias voltage to the device and collects back the current response from the other electrode to amplify it. Afterwards, the signal goes to a Stanford Research 850 ([SR850](#)) digital signal processing lock-in amplifier.

As working with nanoscale material sensitive to its environment that is a potential source of noise, the optical rotating disc chopper (placed after the light source) at a programmable frequency is used as a reference signal. The [pre-amplifier \(SR570\)](#) enhances the measured weak signal from the device and the [lock-in amplifier \(SR850\)](#) rejects the overwhelming noise at a given reference frequency and phase of the expected signal set by the optical chopper. Any large variations of the input signal that is out of tune with the chopper for instance sources of noise are being suppressed.

In this work, the NWs devices are mounted onto a customised printed circuit board and the electrodes are connected to the photocurrent set-up as illustrated in Figure 2.12.

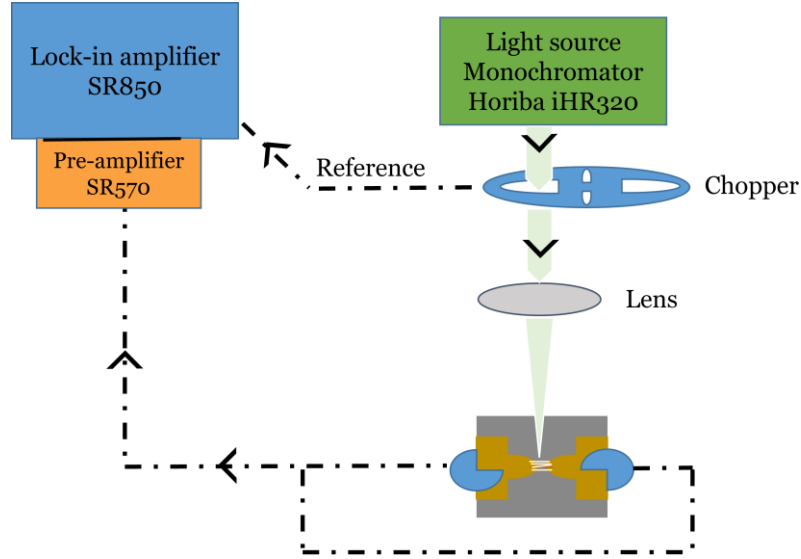


Figure 2.12: Schematic of the photocurrent spectrometry measurement set-up.

Responsivity

The performance of photodetectors is measured by their responsivity, bandwidth and spectral range. It quantifies the conversion efficiency of a device; photons are converted to electron-hole pairs in other words photocurrent produced by a photodetector when illuminated. The responsivity (R) is in amperes per watt ($R_{device} = A_{device}/W$) and is the electrical current divided by the incident optical power in watts ($W = A/R$). The incident optical power is determined using commercial diodes of known responsivity [229]. In this work, Si and InGaAs diodes photocurrent $A_{Si-InGaAs}$ (measured) and responsivity $R_{Si-InGaAs}$ (extracted from the commercial manual) are used and placed in appendix Figures A.2.1 and A.2.2.

The incident optical power W takes into consideration the area of the device $Area_{device}$ (aligned NWs in a rectangle area) and the surface of the illuminating spot $Area_{Light.spot}$ and can be written as follow;

$$W = \frac{A_{Si-InGaAs}}{R_{Si-InGaAs}} * \frac{Area_{device}}{Area_{spot-light}} \quad (2.1)$$

And,

$$R_{device} = \frac{A_{device}}{W} \quad (2.2)$$

2.5.7 Current response characteristic

The current responses are measured using a semiconductor parameter analyser (Hewlett-Packard 4155C) probe station at room temperature with no potential applied to the gate (floating gate). The equipment is located within the Department of Electrical Engineering and Electronics building of the University of Liverpool and all the data obtained originate from the author's interaction with the equipment.

A DC voltage was swept on the electrodes through the aligned NWs by connecting tungsten probe needles on the contacts and the current flowing through the devices was recorded. The current curve response defines the operating characteristic of the electronic device and by extension the characteristic of the channel material. Most of the diodes and transistors are fabricated using semiconductor P-N junctions. Diodes have non-linear I(V) characteristics where the current passes in forward bias and is blocked in reverse except for leakage current. Figure 2.13 shows a characteristic example of a practical I(V) Ge diode at room temperature. Contrary to ideal diodes, real diodes have a small reverse current response for small reverse bias until it reaches the "breakdown" where the reverse current increases in a constant way. Some diodes called Zener diodes are used as regulators for their constant output specifically designed to operate in the breakdown region. In forward voltage, the current response is small and gradual until the voltage reaches the internal barrier of the material (0.3 V for Ge and 0.7 V for Si) and features an avalanche in which forward current response increases rapidly for small voltage increases.

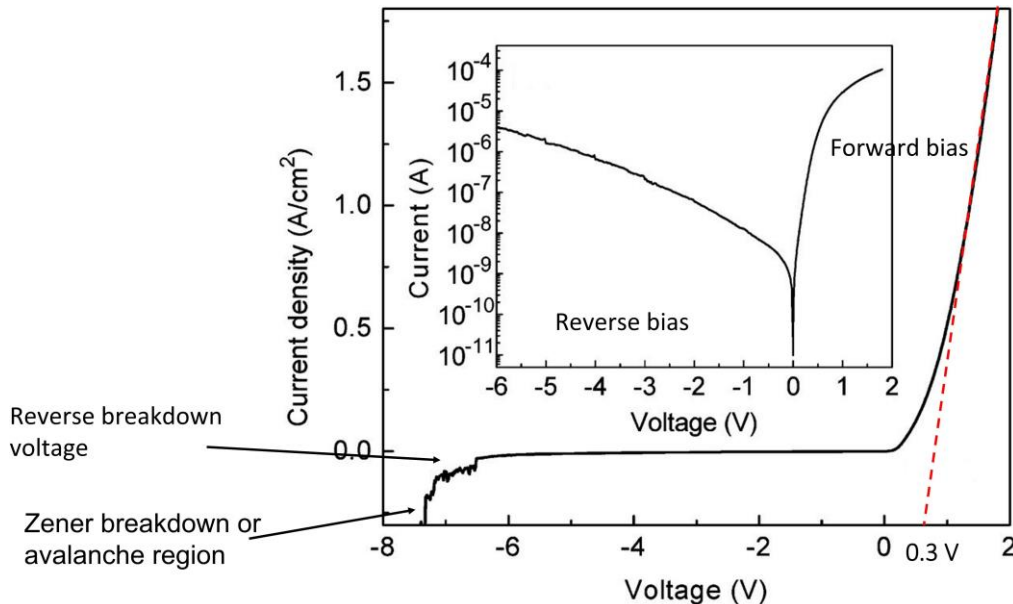


Figure 2.13: Current-voltage characteristics in a linear and semilog scale of a practical heterojunction Ge diode at room temperature. The inset shows the same I(V) with a semilog scale.

Extracted from [230].

Using I(V) measurement, analysis of the curves and calculation are good indicators of the device characteristic and its conduction mechanism previously explained.

This chapter introduced the synthesis and fabrication of the very basic elements necessary to the NWs and the resulting device analysis. It is a transition between the theory of the presented work and the experiments and results presented later in the next chapter.

Chapter 3

Dielectrophoresis implementation for germanium nanowires-based device

Introduction

This chapter introduces the NWs material characterisation after synthesis by the IMEM-CRN Institute. The technical methods for dielectrophoresis as well as its background theory concerning the Ge nanowires are presented. The Ge NWs dimensions and surface were evaluated via Scanning Electron microscopy (SEM) and Transmission Electron Microscopy (TEM). Different mediums were tested for the preparation of the Ge NWs solution matrices for the DEP process and device fabrication. Thus, wettability, volatility and chemical inertia of the NWs within different mediums were investigated to have optimum conditions for DEP experimental instalment and nanowires collection. Electrode platform designs and the influence of shapes on electric field lines and gradients were also investigated. Predictions over NWs collection were performed using resistance calculations code and experimental results. By means of a second computational code, equations for Clausius Mossotti Factor (CMF) and DEP force were formulated and simulated in accordance with the prolate ellipsoid shape of the wires. Finally, the electrical properties of the resulting devices were analysed. This chapter is a transition between a literature review on NWs for sensing devices and the fabrication by DEP for the main experimental part of that thesis. It poses the first building block that establish the core of the thesis by demonstrating the principles of DEP on Ge NWs and the properties of the resulting devices.

3.1 Characterisation of the nanowires

3.1.1 Morphological and chemical characterisation of the nanowires

Scanning and Transmitted Electron microscopy analysis

The Ge NWs are grown by Metalorganic Phase Vapor Epitaxy (MOVPE) in partnership with the IMEM-CNR [202]. Chapter 2 describes the MOVPE technic and NWs growth process for the Ge NWs. As discussed in reference [44], the length of these NWs can also be controlled by changing the growth time, while maintaining a reduced degree of tapering (which is the increase of nanowire diameter over the length ensuing conical shapes). The NWs have been characterised by Scanning Electron Microscopy (SEM) and by Transmitted Electron Microscopy (TEM) in order to define their growth direction, dimensions, and detailed morphology. Prior to TEM analysis, the NWs were transferred to a carbon-coated copper grid by applying gentle scrubbing. For SEM small pieces of the substrate directly out of the synthesis chamber were placed in the SEM. The NWs growth axis is along the $\langle 111 \rangle$ direction (epitaxial to the substrate) as observed from the diffraction pattern in the left image Figure 3.1. The NWs have a smooth needle shape. Their dimensions were measured and are; $20\text{-}25 \pm 0.5 \mu\text{m}$ long with a diameter of $60 \pm 5 \text{ nm}$. The following Figure 3.2 shows images of the NWs obtained by SEM. The amorphous oxide layer (observed by TEM) in Figure 3.1 at the nanowire surface has a thickness of 0.5 nm just after growth and is $\approx 2.0 \text{ nm}$ after 2 months in the air. The bottom left inset Figure 3.1 shows the diffraction pattern of the NWs and indicates the NWs' crystallinity in zinc blende structure of $[111]$. The NW tip composition has been analysed by energy dispersive X-ray spectroscopy (EDX) by [202], and it was determined that the tip contains Ge and Au alloy with a composition of $27 \pm 3 \text{ atomic \% Ge}$ and $73 \pm 3 \text{ atomic \% Au}$.

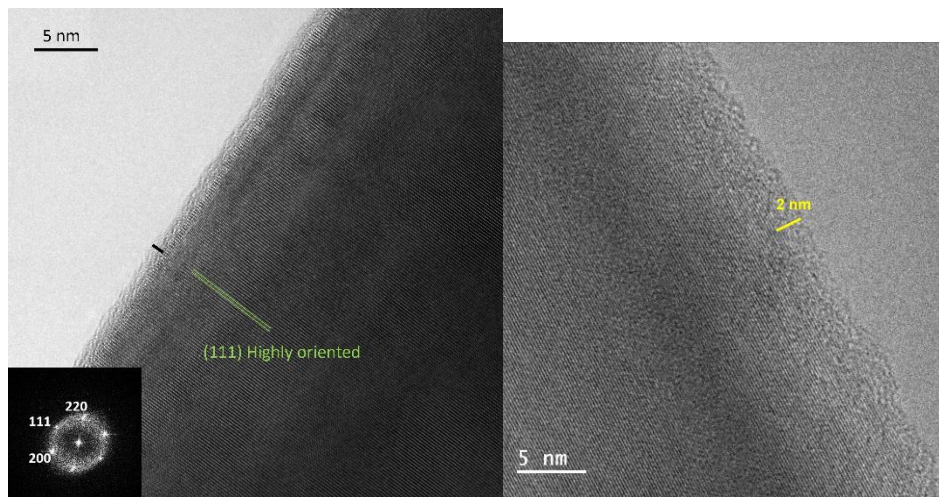


Figure 3.1: TEM images of the germanium nanowires surface. Left; nanowire surface after growth. The bottom left inset is the diffraction pattern of the nanowires indicating good crystallinity of the nanowires in $\langle 111 \rangle$ orientation for diamond cubic structure. Right; nanowire surface after two months.

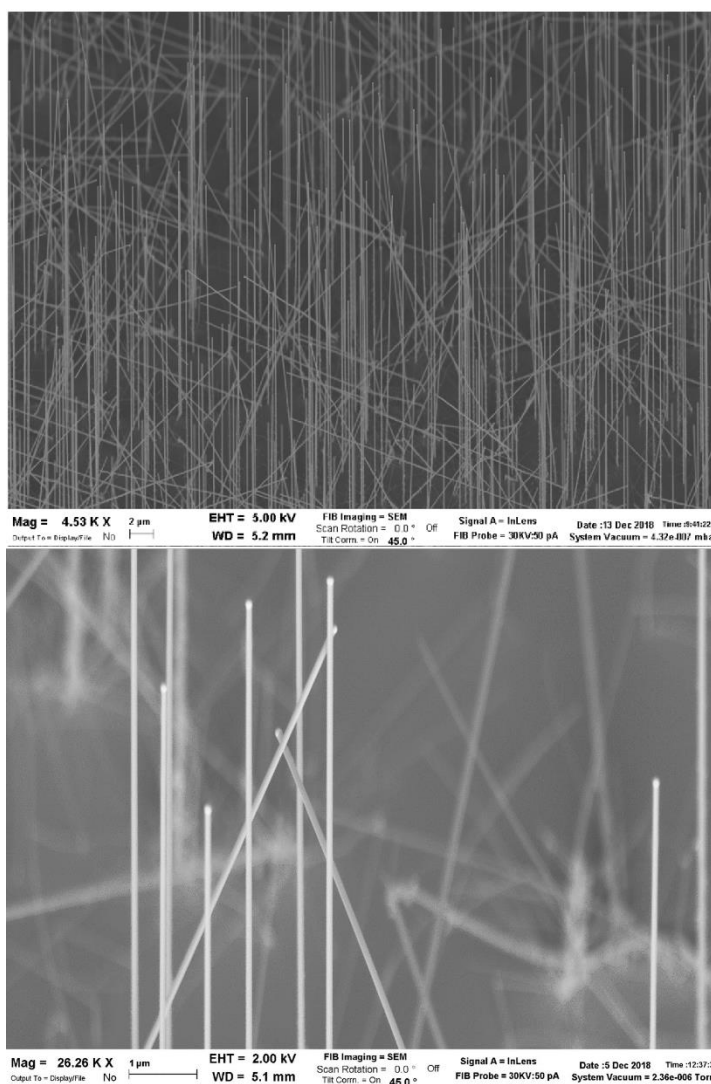


Figure 3.2: SEM images of the germanium nanowires on the silicon substrate. Top magnification is 4.53 k and bottom magnification is 26.26 k.

Raman Spectroscopy Characterisation

The chemical nature of the NWs was analysed further by Raman spectroscopy. The sample consisted of the as-grown Ge NWs transferred on a glass substrate by gentle scrubbing. The experiment was carried out using the inVia Reflex Qontor Confocal Raman Spectroscope (Renishaw, UK). The analysis of the NWs was performed using a 532 nm laser with 3 mW power and 10 s exposure time with a 100X objective. The 532 nm laser provides a circular analysing spotlight of 0.8 μm diameter. Each spectrum consisted of a series of 7 scans in the range of 150 to 3500 cm^{-1} . The glass signal was automatically removed using the WIRE-5 software (Renishaw, UK).

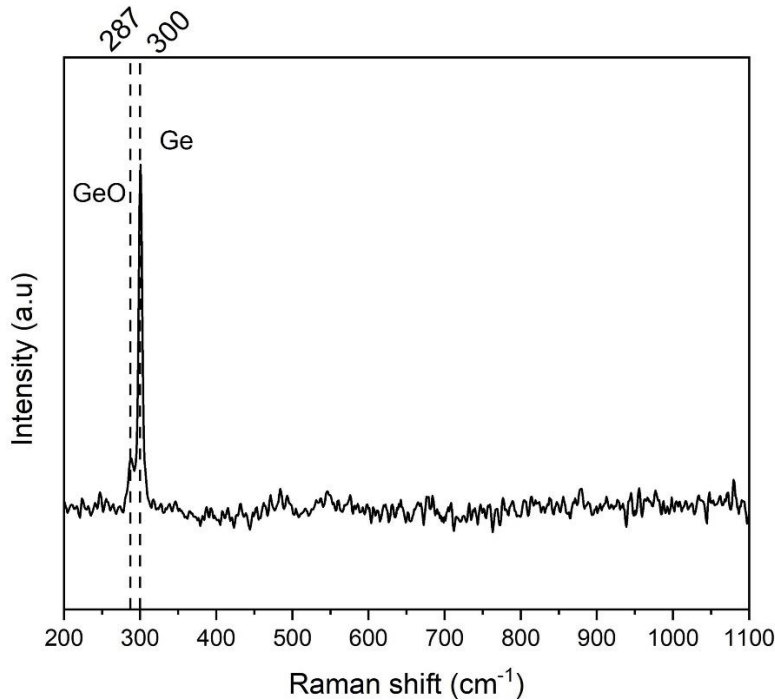


Figure 3.3: Raman spectra of Ge NWs on glass. The glass background has been removed and the signal smoothed.

The obtained spectra showed Figure 3.3 has one single peak centred at 300 cm^{-1} , that peak is attributed to crystalline Ge. The presence of germanium oxide observed in the previous SEM analysis is shown in the Raman spectra at 287 cm^{-1} (also usually observed at 450 cm^{-1} [231]). This is most likely due to a lack of material for the detector to get enough signal from the Ge oxide molecular vibration. The sharp signal obtained at 300 cm^{-1} from the Ge indicates that the NWs are rather crystalline supporting observations from TEM diffraction pattern. From the diffraction pattern itself it was not possible to determine if either the structure was Zinc blende or Wurtzite.

3.1.2 Characterisation of the nanowires in different mediums for dielectrophoresis

The medium used for the NWs solution is the NWs conduit, it allows them to have a matrix to circulate within during DEP but it is also a practical way to carry and manipulate them. As explained in Chapter 1, the way the NWs are going to move, either attracted or repulsed by the electrodes depends on the nature of the electrical interactions between the particles and the medium. Equation 1.7 in Chapter 1 shows that for an effective attractive force on the NWs (positive DEP), the dielectric constant of the NWs (ϵ_p) has to be higher than the dielectric constant of the medium (ϵ_m) (likewise for the conductivity ($\sigma_{p,m}$)). Four types of mediums have been considered; Deionised Water (DIW), anisole, and Isopropanol (IPA). They have been selected first for their easy access and handling along with low toxicity. A formulation of Dimethylformamide (DMF) and toluene has also been tested with a 50:1 ratio respectively, chosen for its previous successful use in Si NWs manipulation using DEP and for storage [232]. Dielectric constant ϵ , wettability angle ($^\circ$), volatility (T $^\circ$ C) and chemical inertia are the parameters that are going to dictate the choice of the medium. The following Table 3 gathers the materials' electric and chemical characteristics. All mediums information has been taken from the literature except for the wettability angles which have been measured as shown later in this section. Sarah Beretta *et al.* from the IMEM-CNR institute [233] used Focused Ion Beam Induced Deposition (FIBID) to randomly select Ge NW (NWs used in this study and fabricated by MOVPE and previously mentioned parameters) and connect them to platinum and gold electrodes. From I(V) measurements, they found resistivity values of 0.18 - 0.21 Ωcm (476.19 - 555.56 S m^{-1}) for a single Ge NW randomly selected. Those results are being used for the following work and later be investigated further. To remove the NWs from the substrate and prepare the solution, a substrate slide of 1 cm^2 of as-grown Ge NWs is used and then put with 300 μL of medium and sonicated at low power (≈ 100 W) for a duration of 60 s. If the amount of NWs on a slide of 1 cm^2 is considered generally the same from batch to batch, the concentration of NWs for a droplet of 4 μL is $\approx 36 \times 10^3$ NWs.mL^{-1} as determined by using a cell counter grid.

Table 3: Materials characteristics.

Materials	Dielectric constant ϵ	Electrical Conductivity (Sm^{-1})	Boiling Temperature ($^{\circ}\text{C}$)	Viscosity (cP)	Wettability Angle ($^{\circ}$)
Germanium	16	476.19 - 555.56	NA	NA	NA
DIW	29.3	5.5E-6	100	1	55.83
DMF	66.7	2.5E-4	153	0.79	50.9
Toluene	2.38	5E-12	110.6	0.55	7.94
DMF/Toluene 50:1	NA	NA	NA	NA	32.57
Anisole	4.33	2E-6	153.8	0.77	46.57
IPA	19.92	6E-6	82	1.92	4.68

Wettability

Gravity, viscosity and wettability of the medium used simultaneously have considerable advantages for DEP. The higher the viscosity the higher the DEP force will have to be for the NWs to move through and reach the electrodes before complete evaporation of the medium. Moreover, a medium that has low wettability can cover a small area with a maximum of NWs in a maximum volume of a droplet. If the medium has a high wettability (small wettability angle) the droplet on the glass surface and electrodes will spread over and the solution will go further away from the electrode gap reducing NWs concentration in the vicinity of the electric field and reducing the space for the NWs to circulate within.

Hence, the wettability of the mediums on the electrodes has been measured using the method and equipment described in Chapter 2. A 4 μL of NWs solution was dropped on the electrodes, the KRUSS camera analyser was focused on the drop shape and the surface of the substrate aligned with the red baseline. The wettability angles were measured by Shape Analysis System on the electrodes at room temperature. The following Figure 3.4 shows the resulting images of a 4 μL Ge NWs droplet prepared with each medium and cast on the electrode's surface.

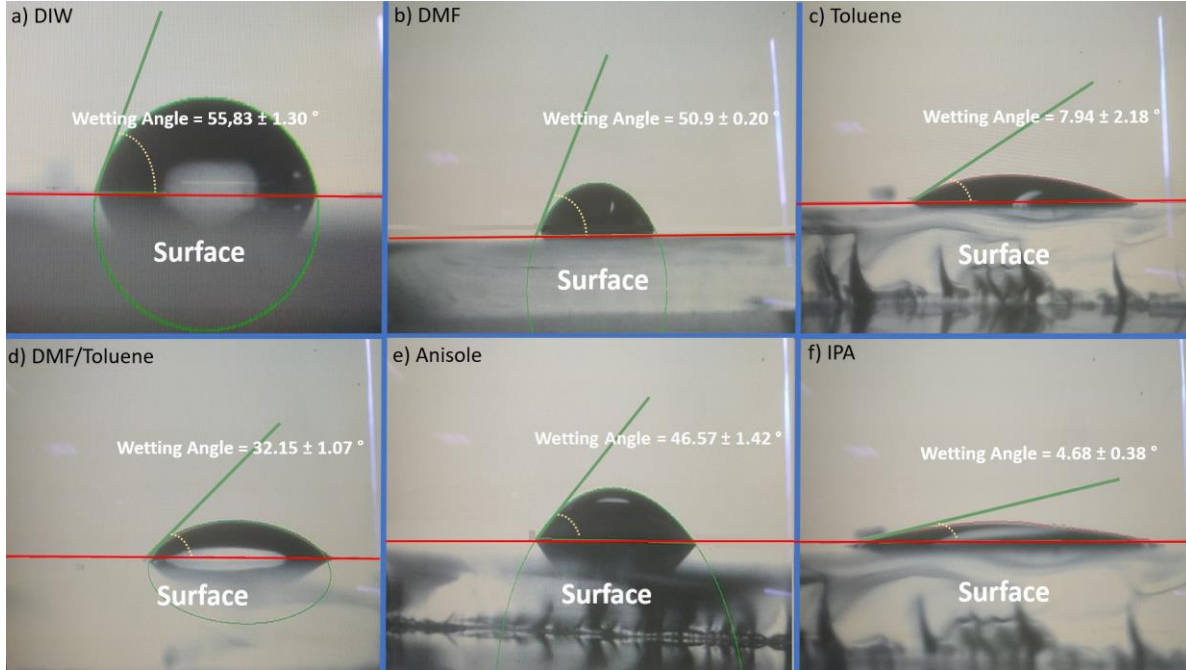


Figure 3.4: Wettability contact angle images of the Ge NWs droplet solution prepared with different mediums. With wettability angles of a) DIW = $55.83 \pm 1.30^\circ$, b) DMF = $50.9 \pm 0.20^\circ$, c) Toluene = $7.94 \pm 2.18^\circ$, d) DMF/Toluene 50:1 = $32.15 \pm 1.07^\circ$, e) anisole = $46.57 \pm 1.42^\circ$ and f) IPA = $4.68 \pm 0.38^\circ$.

As shown in Figure 3.4 and reported in Table 3 the largest wettability angle is given by DIW $55.83 \pm 1.30^\circ$, DMF $50.9 \pm 0.20^\circ$ and anisole $46.57 \pm 1.42^\circ$ while IPA (Figure 3.4 f) shows, on the other hand, the highest wettability with the smallest wettability angle of $4.68 \pm 0.38^\circ$. The error has been obtained automatically from the software system based on the comparison of four measurements. Another experiment was similarly conducted with a small tilt ($\approx 10^\circ$) of the substrate to enable a rolling flow of solvent and NWs towards the electrode gap, the results were analogue to the non-incline samples. IPA wettability and viscosity are not ideal to perform DEP as well as toluene and the formulation of DMF/Toluene that have high wettability. DIW solution shows a bigger volume of materials on a smaller surface leaving enough matrix for the NWs to be circulating within. However, DIW with IPA has higher relative viscosity.

Volatility

The NWs solution is drop-cast on electrodes and lets to dry during the DEP process, the solvent mustn't evaporate too quickly to let the NWs move through the medium for enough time and align. Mediums with low boiling temperatures have high volatility and will stay for ≈ 20 s on the surface during DEP.

Ideally, a time of a minimum of 30 to 60 seconds would avoid the rush and allow more than enough time for the NWs to align. Ge NWs solutions have been prepared with each medium and volatility tests were performed in DEP condition to record the length of time needed for a droplet of 4 μL to completely evaporate at room temperature (RT).

The Ge NWs solution prepared with IPA completely evaporated after a few seconds on the electrodes due to its low boiling temperature of 82 °C (see Table 3) which implies high volatility. All the other mediums, anisole, DMF/toluene, DIW were completely evaporated after at least **6 to 10 minutes**, leaving more time for the NWs to align at the electrodes. A 4 μL of solution dropped on electrodes stayed for \approx **12, 9 and 6 minutes for anisole, DMF/Toluene and DIW** respectively. With a short period on the electrodes, high wettability and viscosity IPA shows non-ideal characteristics for NWs solution to do DEP.

Chemical inertia

Besides their dielectric constant, medium and NWs material have to be in a condition of chemical inertia with each other. The Ge NWs have to be resistant to degradation from reactions that might be caused by the medium. Hence, the NWs' chemical and physical properties have to remain unchanged. Long-term chemical inertia (say a week) of medium and particles are seldom discussed for DEP. To resolve this, solutions of Ge NWs in diverse mediums have been prepared; DIW, DMF/Toluene and anisole have been used and the NWs were observed by TEM to evaluate their inertia with the medium and confirm their compatibility.

The following Figures 3.5 and 3.6 obtained by TEM show images of the state of the Ge NWs in solution with DIW and DMF/Toluene respectively after 2 days.

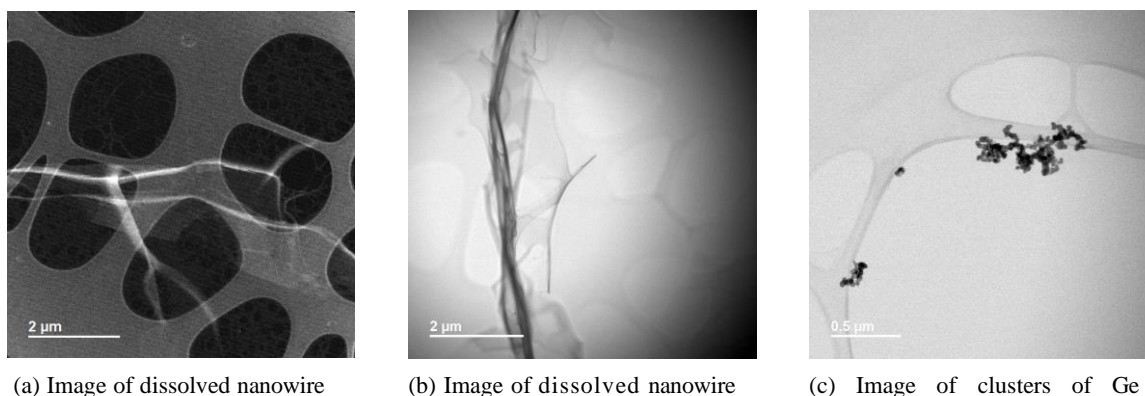


Figure 3.5: TEM images of the influence of deionised water on Ge nanowires after two days.

In DIW, it is observed that the NWs dissolve. O_2 being naturally present in the air and water reacts with the Ge to form GeO_2 that is soluble in water as explained in the chemical equation (3.1) [234].

Besides that, as shown in Figure 3.5 (c) the NWs in DIW tend to form clusters (chemical nature confirmed by EDX put in appendix Figure A.2.3) which is not ideal as their shape has completely changed.



GeO_2 is soluble in water and O_2 reacts with Ge to form GeO_2 again, there is therefore a continuous process of oxidation and dissolution leading to the degradation of the NWs. Because of the oxidation process, the Ge NWs are not able to stay in the solution for a maximum of two days, which leaves a very short time of usage from the moment they are being sonicated to prepare the solution. Resulting in unnecessary waste, water is not an ideal medium for Ge NWs besides having a high dielectric constant compared to Ge and high viscosity.

Figure 3.6 shows the behaviour of the Ge NWs in DMF/Toluene. It appears that DMF/Toluene has a similar effect on the Ge NWs than in water. Like in DIW, only a few intact NWs have been found, they have also formed clusters of NWs (chemical nature confirmed by EDX) instead of beads that also greatly hinder the movement of NWs during DEP. While DMF/toluene seemed to be a good match for Si NWs [232], Ge NWs cannot be prepared and used in that medium.

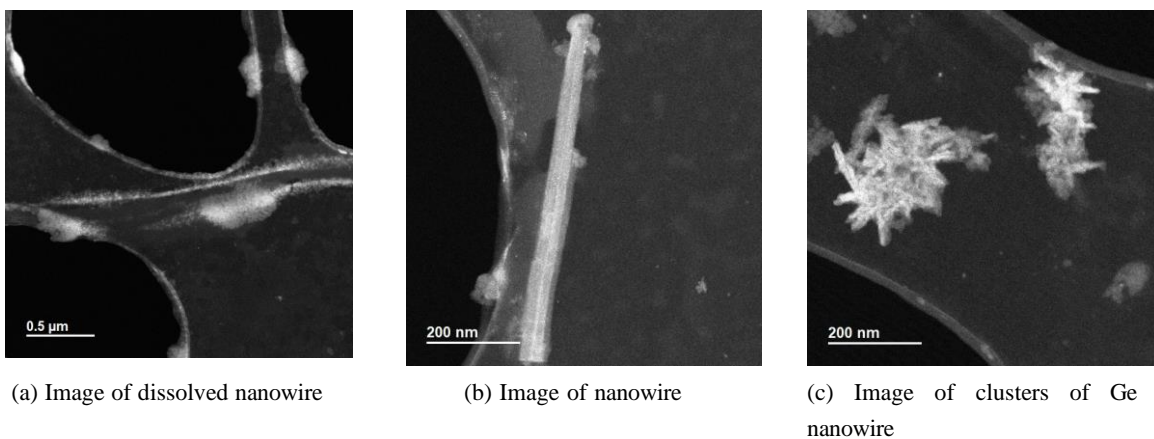


Figure 3.6: Dark field TEM images of the influence of DMF/Toluene on Ge nanowires after two days.

Anisole has previously shown ideal properties to be used as a medium for DEP. After 2 days and later 2 weeks, the Ge NWs showed no changes, the analysis has thus been pushed a little further in time to 2 months in anisole. Figure 3.7 shows how the Ge NWs react within an anisole solution after two months. After 2 months in anisole, and similar to air exposure the NWs haven't changed if only for a thicker oxide layer of ≈ 3 nm (as shown in Figure 3.8). The analysis showed no cluster formation and no NWs dissolution making anisole an ideal candidate for Ge NWs medium solution and DEP.

From all the mediums considered for the Ge NWs solution, anisole has shown the most suitable inertia allowing to keep the NWs for a long time in good condition in the medium. Besides, anisole has the lowest volatility (153.8 °C), the lowest dielectric constant ($\epsilon = 4.33$) and a low viscosity. Hence, with low viscosity and low dielectric constant, anisole doesn't polarise as easily as DIW or DMF/Toluene allowing more movement freedom of the Ge NWs. Finally, anisole has on electrodes and glass a large wettability angle of 46.57 ° which optimises simultaneously, a maximum amount of material within a small area of the electrode gap, gravity for NWs collection and enough matrix to undergo polarisation and attractive DEP force. In the following work, anisole is used as a solution medium to fabricate the devices. The following Table 4 summarises the characterised mediums and their compatibility with the DEP setup.

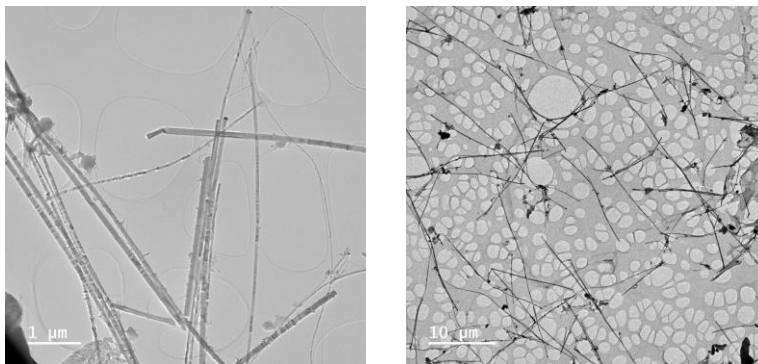


Figure 3.7: TEM images in bright field showing the influence of anisole on Ge nanowires after two months. On both images, the NWs are demonstrated to be intact in anisole after two months.

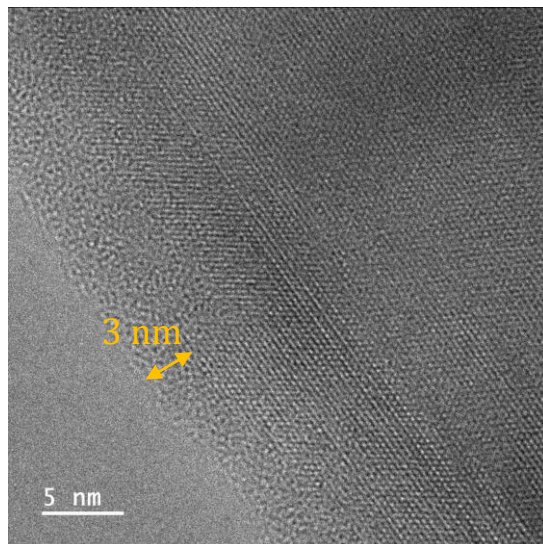


Figure 3.8: TEM images in bright field images of the influence of anisole on Ge nanowires after two months. The image shows the surface of a germanium nanowire showing an oxide layer of 3nm slightly larger than post-fabrication.

Table 4: Summary table of the mediums' characteristics.

Mediums	Viscosity (cP)	Wettability Angle (°)	Boiling temperature (°C)	Evaporation time 4 μ L droplet (time)	Chemical inertia	Usage for DEP
DIW	1	55.83 \pm 1.30	100	6 min	Dissolved	✗
DMF/Toluene 50:1	NA	32.57 \pm 1.07	NA	9 min	Dissolved	✗
Anisole	0.77	46.57 \pm 1.42	153.8	12 min	✓	✓
IPA	1.92	4.68 \pm 0.38	82	14 sec	NA	✗

Prior to more concrete experiences, DEP forces and Clausius Mossotti factor leading NWs alignment have been simulated as preliminary analyses of the parameters.

3.1.3 Dielectrophoresis force and Clausius-Mossotti factor calculations

As explained in Chapter 1, the DEP force is described by the following equation:

$$\vec{F}_{\text{DEP}} = 2\pi\epsilon_m R^3 \text{Re}(K_{\text{spheroid}}(\omega)) \overline{\nabla E^2} \quad (1.1)$$

With NWs of radius R , ϵ_m is the permittivity of the medium that surrounds the particles, Re is the real part of the CMF and $\overline{\nabla E^2}$ is the electric field (with ∇E as gradient) [235].

To analyse the DEP force equation and predict its behaviour with the frequency a computational Matlab code has been written. It is detailed in the appendix A.2.4 The equations have been adapted to take into account the prolate ellipsoidal geometry of the NWs by implementing in the CMF; the depolarisation factor A_x and A_y as well as the eccentricity e . In the simulations, preliminary parameters were used; AC electric field of 8 V_{peak-to-peak} applied on electrodes of 20 μm gap for Ge NWs of $\approx 20 \mu\text{m}$ long with non-intentional doping and in anisole solution. A specific gap of 20 μm has been chosen according to previous research from Liu et al. [236]. They determined that the ideal ratio gap size/NWs length was about $\approx 0.85 - 1$ for an optimised DEP force. Hence, with NWs measured at 20-25 μm long a gap size of 20 μm giving a ratio of 1-1.2 should be able to provide optimum DEP force (by considering the length of the NWs measured by SEM 20-25 $\pm 0.5 \mu\text{m}$).

Graphs from Figures 3.9 to 3.12 have been obtained. They all have a clear tendency; as the frequency increases the CMF decreases and so is the DEP force. Figures 3.9 to 3.10 present the influence of the frequency on the CMF according to the orientation of the NWs to the electric field.

The short-axis contribution is mostly independent of the frequency and 5 orders of magnitude lower than the contribution along the long axis for the CMF at low frequency as shown in Figure 3.10. This means that the DEP force along the short axis is weaker when the NWs are perpendicularly oriented to the electric field. This highlights the fact that the NWs tend to align where the force is the strongest, in parallel with the electric field and by extension to the electrode gap. In the case where a NW is randomly oriented to the electric field, the dominant force along the long axis will orientate the NW parallel to the electric field. In the interest of investigating the effect of frequencies on the Ge NWs, frequencies from 500 Hz, 500 kHz, 1 MHz, 5 MHz and 10 MHz have been selected. It was explained in Chapters 1 and 2 that increasing frequency has been demonstrated to attract NWs of better conductivity than NWs collected at low frequencies [2, 75]. Hence, the selected frequency range situated at the end of the plateau of the maximum DEP force (see Figures 3.11 and 3.12), should provide simultaneously maximum DEP force and improvement of the NWs conductivity with increasing frequencies.

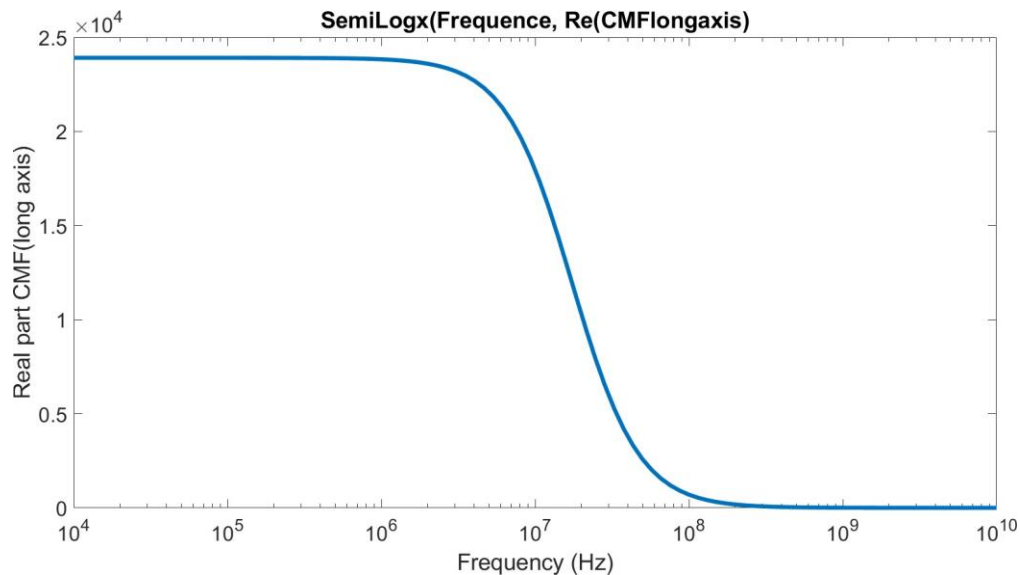


Figure 3.9: Simulated real part of the CMF along the long axis as a function of the frequency for Ge NWs aligned at a voltage of $8V_{peak-to-peak}$ on a $20\mu\text{m}$ electrode gap in anisole.

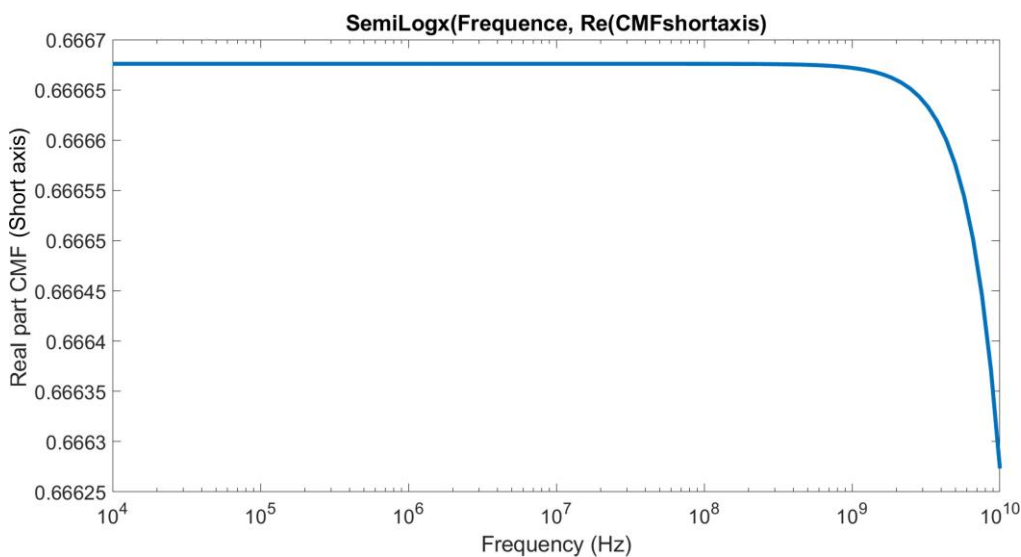


Figure 3.10: Simulated real part of the CMF along the short axis as a function of the frequency for Ge NWs aligned at a voltage of $8V_{peak-to-peak}$ on a $20\mu\text{m}$ electrode gap in anisole.

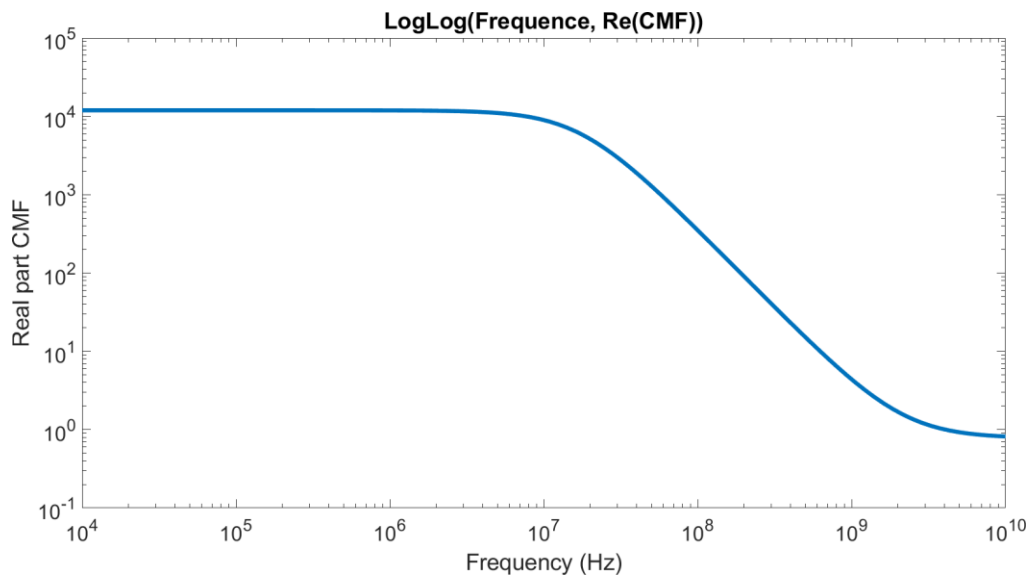


Figure 3.11: Simulated real part of the Clausius Mossotti factor as a function of the frequency for Ge NWs aligned at a voltage of $8 V_{peak-to-peak}$ on a $20 \mu\text{m}$ electrode gap in anisole.

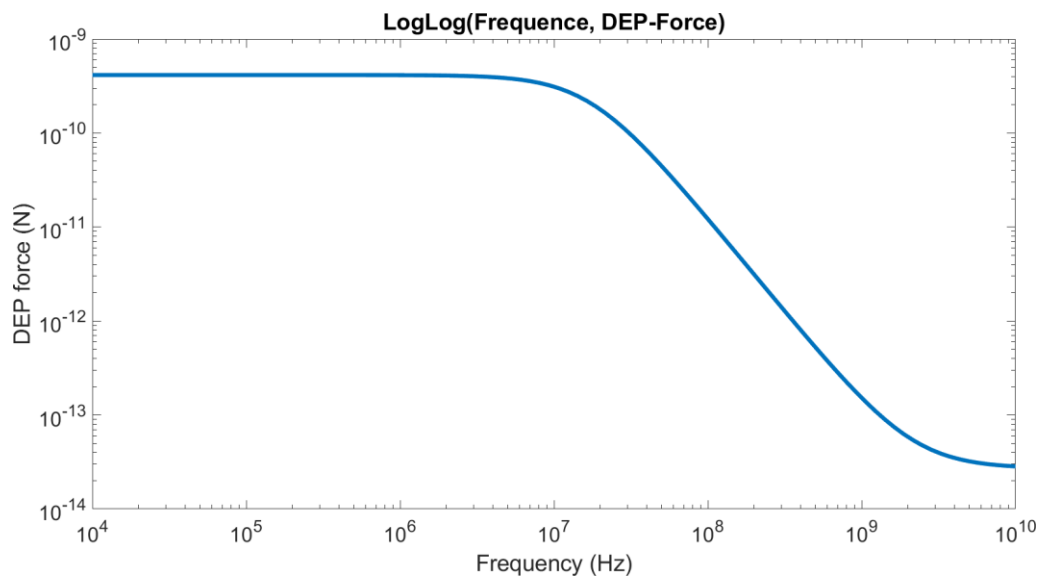


Figure 3.12: Simulated DEP force as a function of the frequency for Ge NWs aligned at a voltage of $8 V_{peak-to-peak}$ on a $20 \mu\text{m}$ electrode gap in anisole.

3.2 Dielectrophoresis platform

In this section, the essentials of DEP development, electrical set-up and background designs are presented with a study on the DEP platform used in this work. SEM and TEM images as well as COMSOL simulation and optical microscopy have been carried out in order to highlight the optimum parameters being used and electrode design characteristics to perform NWs collections.

3.2.1 Design of the electrodes

DEP either being used to attract or repel particles is found in the literature with a very wide range of different electrode designs. For instance, it is mainly found for bioparticle sorting by means of a channel flow where 2 different types of bioparticles are separated from each other according to their dielectric properties [237]. The design system can be integrated for DEP within a stream flow channel (bioparticle sorting) or a simple immobile droplet or a well of particle solution (particle collection). For any design, the DEP force has to overcome possible issues like electroosmosis or electrofluidic to move the particles effectively. For any specific goals of transport one can play with different parameters that influence the particle movement; varying the electric field lines by the electrode structure or varying the dielectric properties by selecting relevant medium permittivity and conductivity. AC electric field gradients can be generated by 2D or 3D electrode designs. 2D electrodes are usually fabricated by standard photolithography and metal evaporation methods on a chosen substrate. In 2D designs, the electric field mostly reaches particles that are in the vicinity of the electrodes. 3D designs are rather more complex to fabricate but they reach bigger volumes of particles in the solution. Common 2D designs have interdigitated or parallel electrode fingers [238], castellated [239], oblique [240], curved [241], quadrupole [242], microwell [243], or matrix designs [244], Figure 3.13 (A to J). And for 3D designs, extruded [245], wall pattern [246], insulator-based 2D design structure [247] but creating a 3D electric field gradient, and medium contactless [248], Figure 3.13 (K to M).

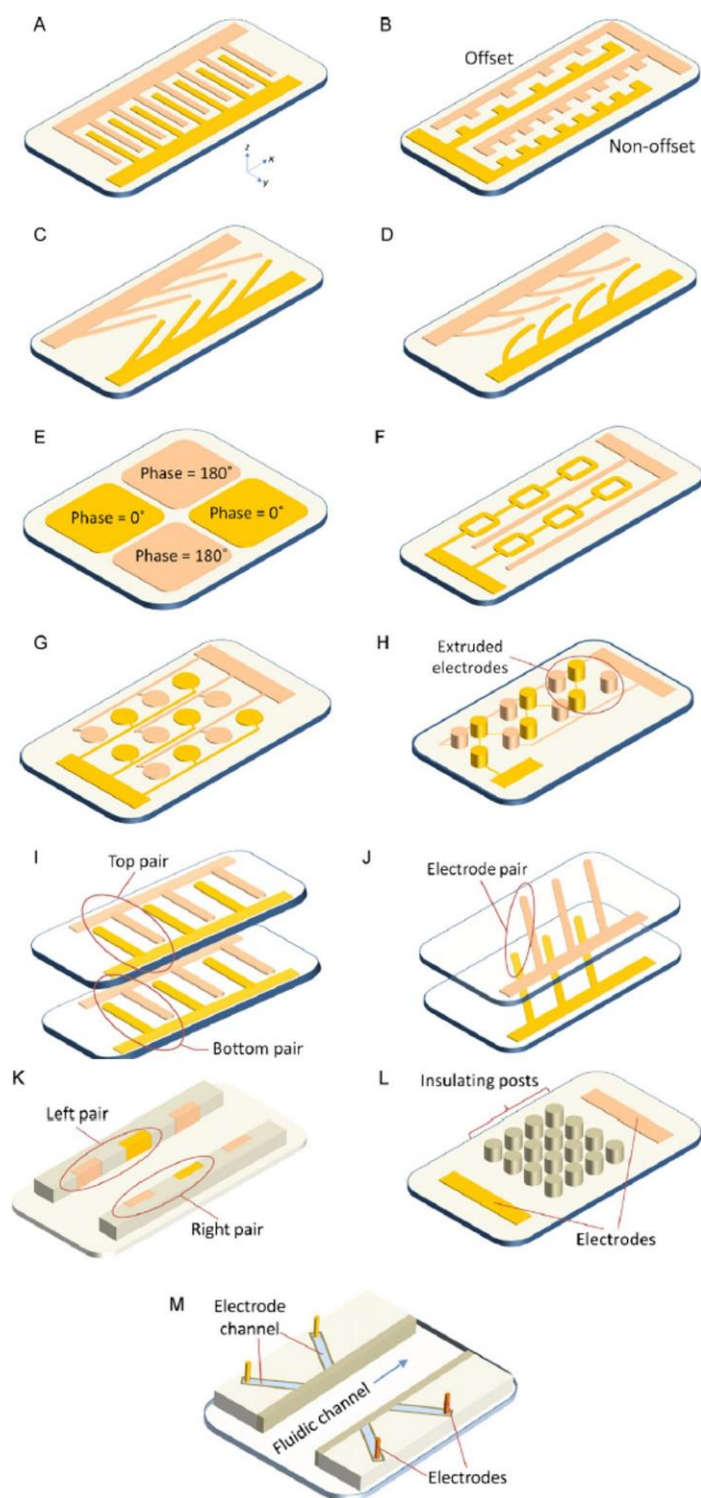


Figure 3.13: Schematics of common electrode design. A) parallel or interdigitated, B) castellated, C) oblique, D) curved, E) quadrupole, F) microwell, G) matrix, H) extruded, I) and J) wall-patterned, K) side-wall, L) isolating obstacles based, M) Medium contact-less.

Extracted from [68].

Each electrode configuration enables a specific localised or diffused electric field gradient to interact with the particles in the solution. In Figure 3.13, designs A to H are rather used for droplet mode while designs I to M are rather used for stream flow channels. As mentioned, alignment properties such as precision, yield and NWs density, can be controlled by tailoring several factors. In this work, the principle of the Ge NWs device fabrication is to obtain contact between NWs and electrodes, so that the NWs bridge the gap between the electrodes. Ideally, the design of the electrodes allows the NWs to be collected at specific locations easily analysed and treated.

3.2.2 Simulation and dielectrophoresis set-up

In the following part, two different electrode design geometry have been investigated; interdigitated and parallel electrodes. As a start of that PhD research, DEP was performed on interdigitated electrodes as an inherited project within our facilities. A simulation study using COMSOL MULTIPHYSICS was first done followed by experimental analysis to investigate and confirm the influence of the interdigitated electrodes on the NWs collection by DEP.

It has been explained that the gap size separating the electrodes is in close relationship with the NWs collection rate where gaps length collected NWs of similar dimensions [249]. The applied electric field is equally distributed in the gap and so NWs of shorter length than the gap "see" the DEP force decrease as the electric field around the NWs is less strong (the larger the space the lower the field "pressure") and for a smaller gap, DEP also decreases as the electric field is reduced at the entire NW length rather than the gap. According to that, the designed electrodes were predefined so that the gap size was between 5-25 μm for the interdigitated electrode design and 20 μm for the design of the parallel electrodes.

For all the future experiments of this work, electrode fabrication, as well as NWs solution preparation, are following the same experimental protocol.

In the COMSOL simulation with MULTIPHYSICS, an "electric potential study" was used and compiled with surface gradient and electric fields along the surface of the electrodes in an anisole environment. An AC voltage of 8 $V_{peak-to-peak}$ was used with a frequency of 500 kHz. This allows visualising the gradient generated by the electrodes and the electric field lines giving an idea of where and how the NWs can potentially align. Afterwards, for the DEP experiment on the interdigitated and parallel design, the electrodes (Device Under Test (DUT)) fabricated by metal evaporation (explained in Chapter 3) are electrically connected by a set-up that enables the connection to a Tektronix Digital oscilloscope, and Agilent function generator and later connected to a fabricated Trans-Impedance Amplifier (TIA).

The TIA features and fabrication are explained later in the chapter. Voltage and AC frequency signals are preset before the NWs solution drop-cast. Direct-time alignment across the electrodes was monitored by following the resistance changes held by the NWs forming electrical bridge contact between the electrodes. The details about resistivity monitoring are explained later in that section. The DEP process was carried out until the cast droplet dried (≈ 12 minutes for anisole). Figure 3.14 illustrates the electrical installation used for DEP.

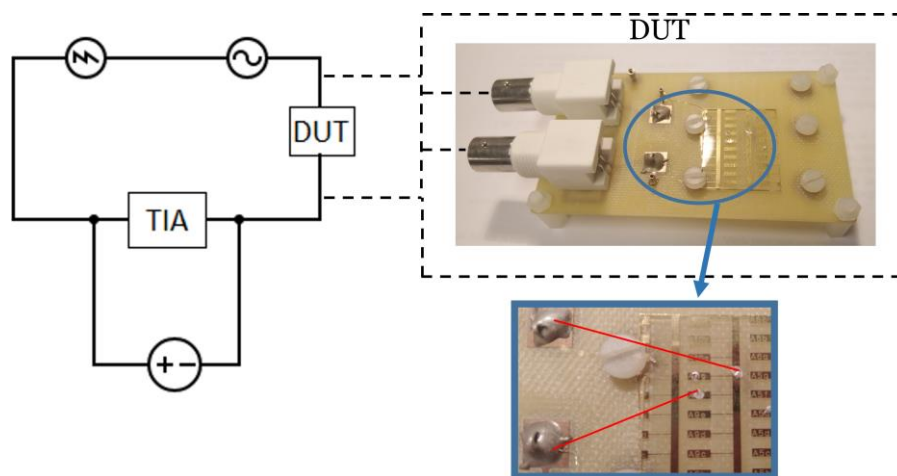


Figure 3.14: Circuit topology for DEP. The dotted box contains a photograph of the DUT and below is shown close-up photography of the electrodes deposited on glass.

The NWs were removed from the substrate slide (slide of 1 cm^2) of the as-grown NWs and put in $300 \mu\text{L}$ of anisole and sonicated at low power of 100 W for a duration of 60 s . The DEP assembly process is operated with the drop-cast method on an inclined substrate of $\approx 10^\circ$ angled to enable a rolling flow of solvent and NWs towards the electrode gap. Using a micropipette, a droplet of $4 \mu\text{L}$ was dropped cast on the electrodes, and an AC voltage of $8 V_{\text{peak-to-peak}}$ and a frequency of 500 kHz was applied. The AC voltage of $8 V_{\text{peak-to-peak}}$ was used from an inherited promising project investigation on those NWs. The droplet was left on the electrodes until it was completely dry, the electrodes were then gently rinsed with IPA and blow-dried with N_2 to wash out impurities and any non-attached NWs.

Interdigitated electrodes design

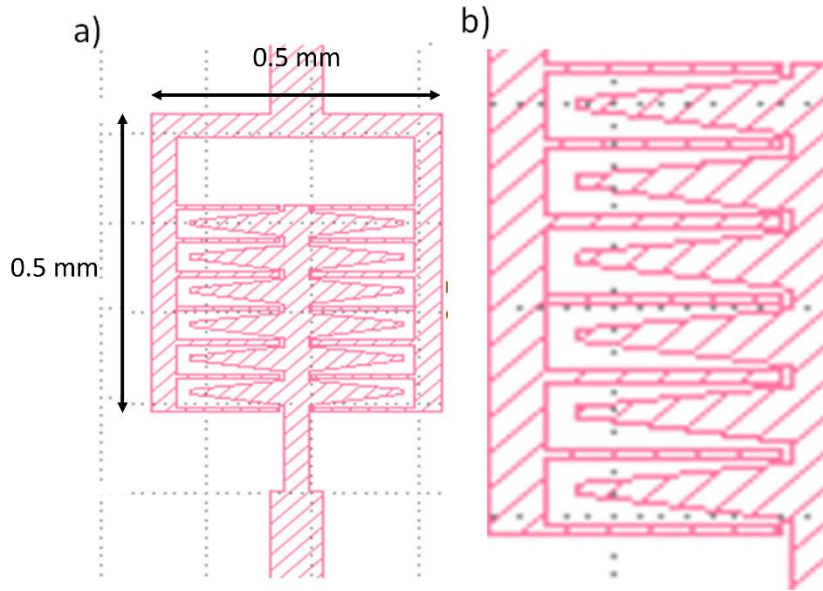


Figure 3.15: Schematic image of the interdigitated electrode design with gaps from 5 to 25 μm . a) Overview of the interdigitated electrodes, b) Enlargement of the left side of the electrodes. The striped parts are the metal of the electrodes.

The interdigitated electrodes are pictured above in Figure 3.15 where the red strips represent the electrode material. The electrodes were first simulated using COMSOL MULTIPHYSICS in order to analyse the electric field lines and gradients. Figure 3.16 shows the obtained simulation. For higher frequencies, the simulation showed a similar gradient and electric field lines pattern.

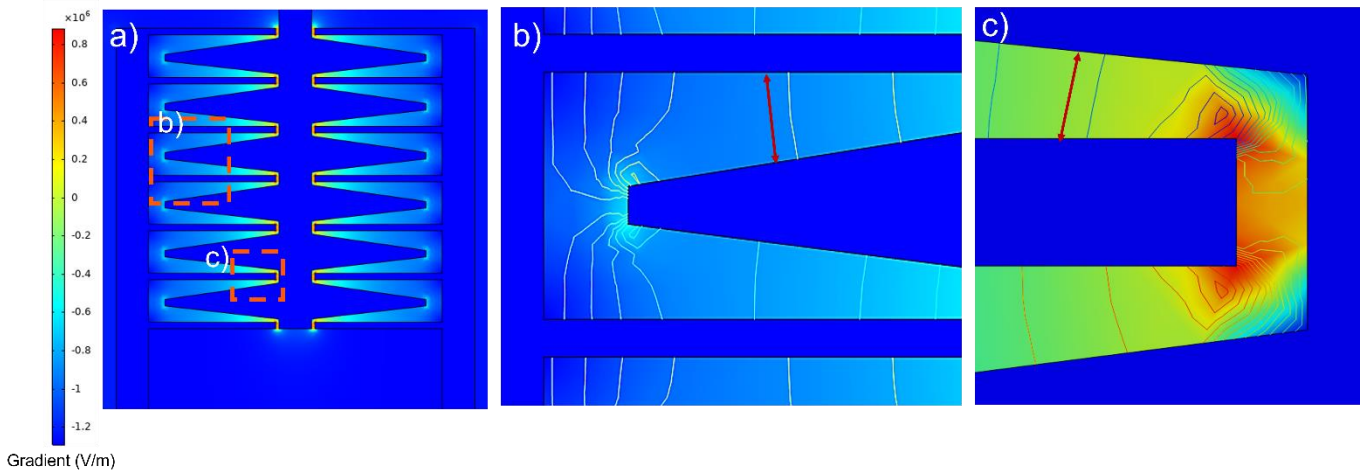


Figure 3.16: Electric field and gradient distribution simulation using COMSOL MULTIPHYSICS. A voltage of $8 V_{peak-to-peak}$ and frequency of 500 kHz was applied on the interdigitated electrodes. a) top-view of the electrodes, b) region of the big gaps, c) region of the small gaps. The scale barre on the left indicates the strength of the gradient.

The resulting simulation indicates a stronger gradient at the smallest gap of 5 μm as illustrated in c) Figure 3.16. The gradient is less intense in the regions with larger gaps. Moreover, the simulated electric field lines along the surface show that the NWs are more likely to bridge along the sides where the electric field lines are crossing and parallel to the red arrows. The following Figure 3.17 shows SEM images of the resulting DEP experiment on the interdigitated electrodes using the parameters mentioned.

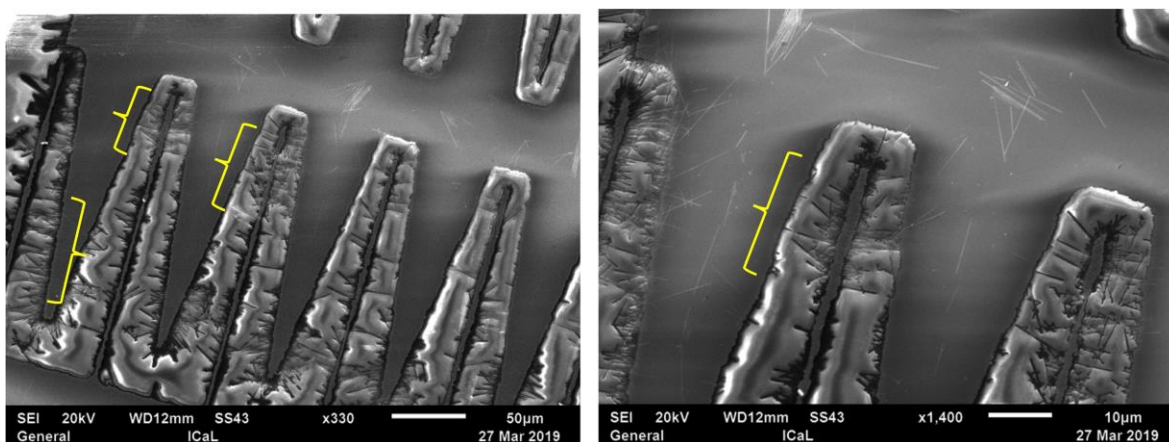


Figure 3.17: SEM images of resulting DEP at 8 $V_{peak-to-peak}$ and 500 kHz on interdigitated electrodes.

In this particular design, the saw tooth electrode shape allows a gap size range from 5 to 25 μm , in this way, it is possible to collect and "scan" a bigger range of NWs lengths. Figures 3.17 and A.2.6 in the appendix show images of aligned NWs. The SEM images reveal that the NWs are mainly attracted to the zones of 5-10 μm and between 20-25 μm (highlighted in yellow brackets in Figure 3.17 and bars in Appendix a) and c) Figure A.2.7). NWs between 5 to 12 μm were measured at the region of 5-10 μm gap (ratio of 0.4–2), and NWs between 24 to 27 μm long were measured at regions of 20-25 μm gap (ratio of 0.75–1). This is in correlation to what has been observed previously by Liu *et al.* [236] with a length collection ratio of 0.85-1, although it seems that for a small gap, the length collection distribution is larger. Moreover, the alignment regions match the regions indicated with the red arrows in Figure 3.16 where the NWs aligned parallel to the electric field lines. The collected NWs indicate that some NWs broke during the sonication process and as a consequence, the NWs solution after sonication contains batches of 5-10 and 20-25 μm long NWs. Although the sonication power was gentle, a lower power couldn't have removed the NWs from the substrate.

Dai *et al.* [250] have evidenced that breaking forces from sonication decrease with decreasing length and diameter and that NWs were also more susceptible to break at areas of lattice defects, leaving in the solution long intact Ge NWs that have fewer defects. The collected NWs of similar lengths to gap sizes coincide with the previous studies by Benjamin Smith *et al.* [249] and Liu *et al.* [236], where they show that DEP can be used as a selective length tool. Examples are given in Figure A.2.7 a)-c) and b)-d) in the appendix show the collection of a mixture of debris and some NWs at the smallest gap (5 μm) where the gradient is the strongest. Moreover, at regions of the electrodes pads instead of aligning by the gaps, NWs are collected in small packs as shown in the yellow and red dot circles Figure A.2.7). Those NWs and debris (in dot circles) on the side of the electrode are due to a phenomenon called electroosmosis; a combination of DEP forces and fluid flow in the medium [251]. It is a dynamic of charges in the electrical double layer at the surface of the electrodes. During DEP, vortexes of liquid form over the electrode edge and pull back the attracted NWs from the gaps in the middle of the electrode pads. The regions of the strongest gradient being at the smallest gap as depicted in the COMSOL simulation Figure 3.16 is also where the electroosmosis effect is the most prominent. Indeed at bigger gaps of 20-25 μm , smaller packs of NWs are visible (red dot circle) where the electric field and vortexes are less strong. Electroosmosis can be an advantage and has been used to separate medium or particles by vortexes or particles' dielectric properties [252] or by particle sizes [237]. Electroosmosis is frequency dependent and is the strongest at low frequencies where the vortexes have enough time to form whereas the electrode polarity changes are too fast to follow at high frequencies. In our case, electroosmosis can pose a problem as it pulls back the NWs resulting in a competitive force against attraction and collection of NWs in the gap. Although electroosmosis wasn't observed at a higher frequency a simpler design should avoid side-by-side vortexes resulting in less drifted NWs and less electric field and gradient discrepancy. The debris collected at the small gaps of 5 μm at the tip of the electrodes can also be avoided by using a bigger gap size that won't be able to attract those small particles.

Parallel electrodes design

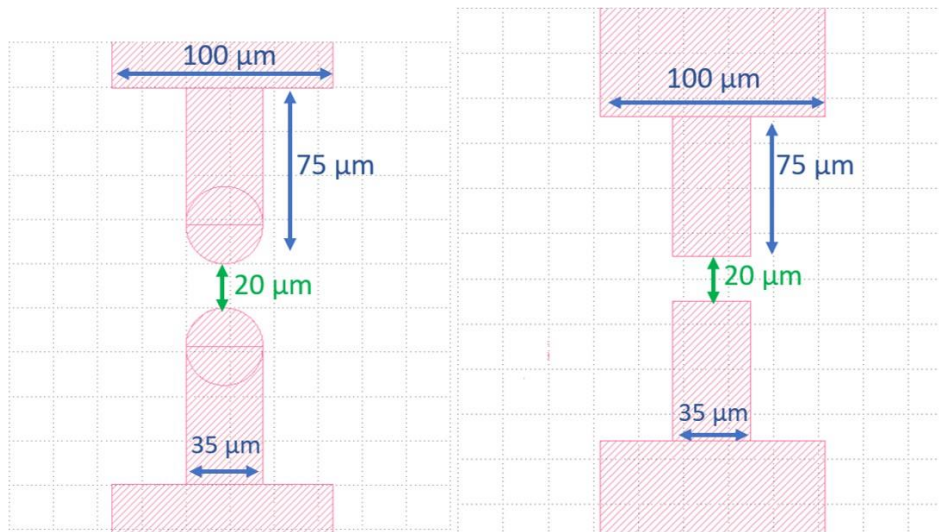


Figure 3.18: Schematic image of the parallel electrode design with 20 μm gap.

The interdigitated design is not ideal for the collection of the Ge NWs used in this work, and another design has been considered; parallel electrodes. In this section two different end tips have been analysed, round shape tip and square shape tip as depicted in Figure 3.18. As shown, this design is smaller and simpler than the interdigitated electrodes in terms of shapes and ease of development during the fabrication process as it has less intricate features and angles. That design has one single gap by device, although the coverage area is smaller than for the interdigitated design, the attractive force is focused on one single area giving one way for the NWs. The geometry of the electrode gap should enable easier analysis of the behaviour of the NWs collection.

To evaluate the influence of the geometry over the DEP collection on the two different shapes, the total gradient distribution and the electric field lines in the anisole at the gap were also simulated using the COMSOL MULTIPHYSICS simulation tool. The obtained simulation, pictured in Figure 3.19 shows that geometry **A** (round tips) has less gradient variation than geometry **B** (rectangular tips) which has a stronger gradient at the corners and then spreads over the surface at the gap. Although the trapping region is larger for geometry **B**, geometry **A** provides a gradient more focused at the centre of the gap.

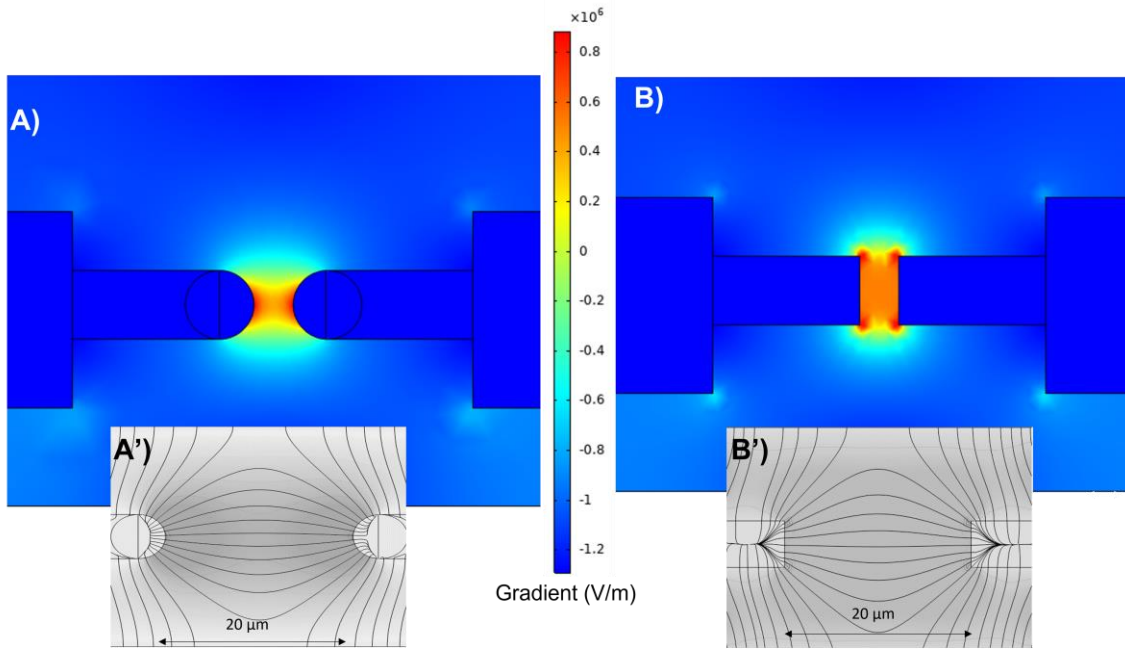


Figure 3.19: Simulation of the electric field and gradient distribution along the surface using COMSOL MULTIPHYSICS. A voltage of $8 V_{peak-to-peak}$ and frequency of 500 kHz was applied on the round and rectangular tips. The scale on the left indicates the strength of the gradient. Gradient distribution A) and B) and electric field lines A'') and B'').

Following the simulation, several devices were fabricated at 6, 8, 10, and 16 $V_{peak-to-peak}$ at a frequency of 500 kHz in order to study the influence of the applied voltage on the NWs collection. It was found that 8 $V_{peak-to-peak}$ was an ideal voltage, as the NWs were burned off the electrodes contact at a higher voltage. Figure A.2.8 in the appendix shows images of devices with NWs broken in the middle and aligned at 10 and 16 $V_{peak-to-peak}$. If the voltage is too high the NWs can break as soon as they connect between the electrodes while at the lower voltage, the NWs stay intact when aligning although with a reduced DEP force. Therefore, a voltage of 8 $V_{peak-to-peak}$ was selected to study the Ge NWs alignment and resultant devices fabricated in this work.

Another series of devices were made by DEP using the parameters previously mentioned i.e a droplet of 4 μL dropped cast on the parallel electrodes and a voltage of 8 $V_{peak-to-peak}$ and a low frequency of 500 kHz and a higher frequency of 5 MHz. The electrodes were subsequently analysed by SEM with images shown in appendix Figure A.2.9 and by optical microscopy (Olympus BX53 with a polarised light Brace-Koehler Compensator (U-CBR1)) shown in Figure 3.20. The aligned NWs were measured by SEM, both shapes showed a distribution of collected NWs of 18 to 27 μm along with a ratio of 0.75-1.1 (ideal ratio of 0.85-1 according to [236]).

Figure 3.20 shows that both round and rectangular shapes had no packs of NWs left on the sides at low and high frequencies indicating that electroosmosis did not occur and that DEP was the dominating force. In addition, only a few pieces of debris have been collected or dragged to the electrode gap (debris visible outside the gap), confirming precedent speculations.

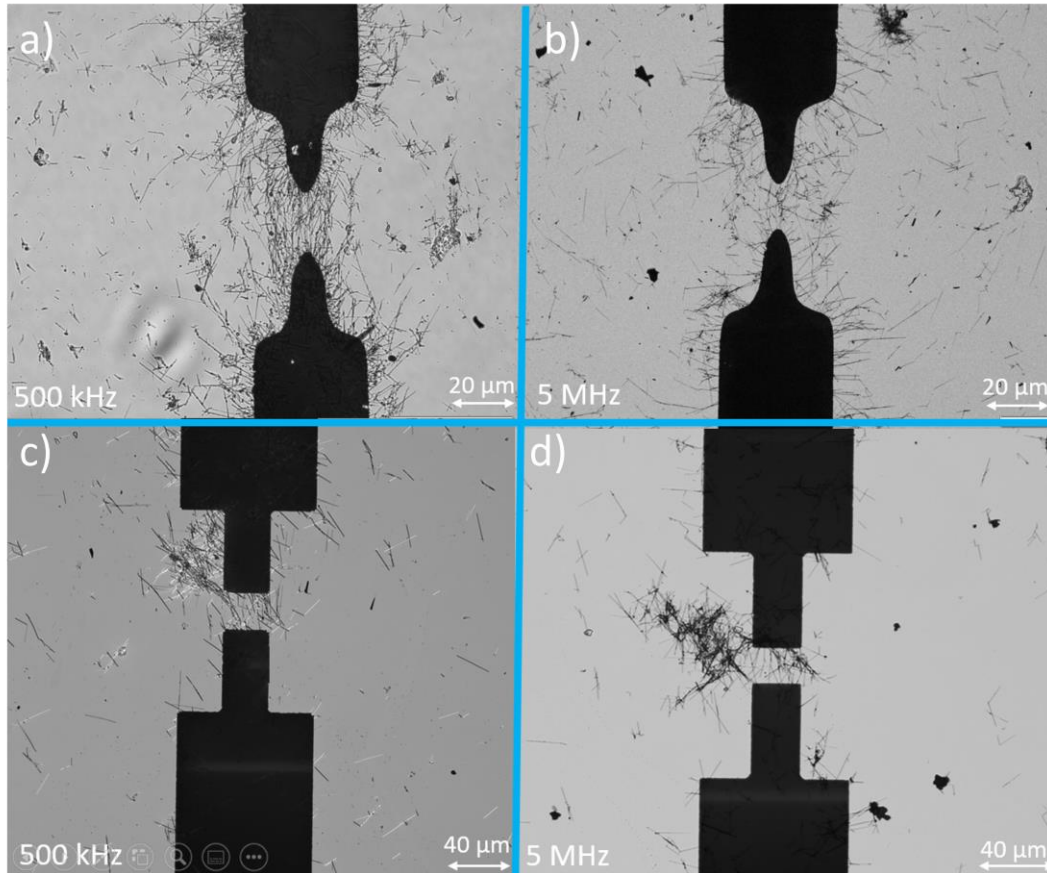


Figure 3.20: Optical microscopy images of geometry A (round tip) a) and b) and geometry B (rectangular tip) c) and d) after DEP at low and high frequencies.

Geometry **B** seems to collect fewer NWs than geometry **A** at low and high frequencies which is unexpected due to its generally larger strong gradient area as seen in the simulation. This could be explained by the gradient discrepancy being stronger at the corners of the tips of **B**, which also answers why small packs of NWs tend to be collected at the corners leaving NWs little freedom to connect at both ends. Furthermore, geometry **A** at low and high frequency (Figure 3.20 shows a better distribution of NWs aligned at the gap that follows the electric field pattern and strong gradient.

After considering two different designs and geometry, the round tip geometry of the parallel electrodes design appears to be the most suitable for NWs collection and investigation because of its simple features making it quick to fabricate and because of the gradient distribution it displays.

3.2.3 Real-time resistance monitoring

To detect NWs collection over time as the DEP process starts, the electrode gap was monitored by following the subsequent changes of resistance. A droplet of 4 μL was drop-casted on the electrodes on an inclined substrate $\approx 10^\circ$ angled to enable a rolling flow of solvent and NWs towards the electrode gap. The devices were then gently rinsed with isopropanol and blow-dried with nitrogen to wash out impurities and any non-attached NWs.

For the rest of the work presented in this thesis, the Ge NWs solutions are prepared following that protocol. DEP alignment and resistance monitoring was performed at the same time. Parallel electrodes with round tips as previously studied, a sinusoidal signal of 8 V_{peak-to-peak} and frequencies from 500 kHz to 10 MHz were applied to perform DEP.

Real-time resistance changes were recorded using a coded Matlab calculation command connected to the Tektronix Digital Oscilloscope, a function generator and the fabricated transimpedance amplifier (TIA). The TIA is generally used to convert and amplify (with high gain) current coming out of the DUT into voltage. They are very often used for the conversion of low-current sensors into voltage. It is the resistor R1 illustrated in Figure A.2.10 (in the appendix) that sets the gain of the amplifier but there are different configurations of TIA depending on the application. TIA provide high gain and low noise amplification. The recording of the resistance started prior to the Ge NWs solution placement on the Device Under Test (DUT: electrode gap) and was stopped after ≈ 12 minutes when the droplet completely dried. The samples are subsequently gently rinsed with ethanol and blow-dried with nitrogen. Finally, images of the aligned NWs were taken using optical microscopy and put in the appendix Figure A.2.12.

As DEP starts, both electrodes are affected by each other's electric field and behave like a capacitor (that intensifies at high frequency). This setup leads to an insufficient signal-to-noise ratio because of the parasitic capacitance that overlaps any changes in dropping resistance. The parasitic capacitance effect tends to increase with small electrode separation and becomes important especially when the devices are electrically characterised [253]. Hence, the use of a TIA will amplify the signal out of the DUT.

Figure A.2.10 in the appendix presents the circuit schematic of the TIA in two sections. Section 1 is the biasing of the electrodes and section 2 converts the current from the electrodes into a voltage and amplifies the signal. With the two sections, the total gain is found to be $1 \times 10^6 \text{ V}\cdot\text{A}^{-1}$.

Using the resistance monitoring system, the input/output signal relationship was approximated by using Ohm's law. The calculation code details are put in Appendix A.2.11.

Figure 3.21 shows a typical example of the obtained resistance plot over time at a voltage of $8 V_{peak-to-peak}$ and frequency of 500 kHz. Immediately following the placement of the solution, a fast drop of resistance is recorded followed by a small increase around 100 s and a linear decrease indicating alignment of NWs across the gap.

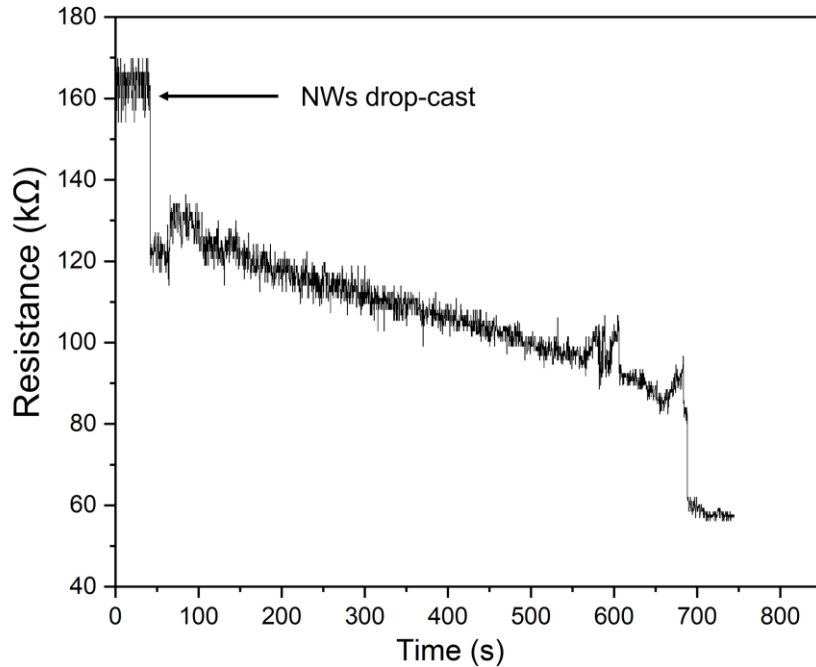


Figure 3.21: Calculated resistance as a function of time of DEP at a voltage of $8 V_{peak-to-peak}$ and frequency of 500 kHz. Graph obtain by resistance calculation approximation using a Matlab code.

The curves obtained from the Matlab code display two main characteristics; at first, a few seconds after the drop-casting of the NWs solution, the resistivity decreases sharply from $170 \text{ k}\Omega$ to $120 \text{ k}\Omega$ at any frequency either 500 kHz to 10 MHz. Then, the resistivity slowly decreases until the experiment is stopped when the droplet has completely dried. A verification test of anisole without NWs evidenced that the decrease of resistivity was not from the medium creating a conduction path between the electrodes. Indeed, the first sharp drop of resistivity originates from the NWs in the solution that comes to impact on the electrodes, the NWs being pushed by gravity to the electrodes create a quick bridge at the gap. That explains the small increase at $\approx 80 \text{ s}$ indicating that the pushed NWs were replacing themselves or moving away in accordance with the DEP force. Another sharp decrease in resistivity can be explained by several NWs aligning while slow decreases (between 100 to 600 s for example) are most probably due to a single NW connecting the gap.

At higher frequencies (from 5 to 10 MHz) sudden drops of resistivity were seldom observable, rather, a generally slow decrease of resistivity occurred. The electrodes behave even more like a capacitor at high frequency and so the parasitic capacitance effect takes over the TIA that cannot keep up with the decreasing signal-to-noise ratio and it becomes more difficult to detect any changes in resistivity. A way to overcome that issue could have been to refine the TIA circuitry, increase the gain, and reduce the noise at high frequency with the addition of an ultra-low noise operational amplifier.

Natasha Mureau *et al.* [254] suggested that the time for the resistance to drop during the NWs alignment is inversely proportional to the DEP force, hence the inverse of the time (given by time constant τ) expresses the DEP force magnitude. In order to analyse DEP force magnitude over the frequency dependence, τ presented equation 3.3 was extracted from the obtained resistivity curves from 500 kHz to 10 MHz.

$$\tau = \frac{-t}{\ln(Z(t)_{NWs})} \quad (3.3)$$

The time constant τ equation 3.3 is depending on time t at which the change of resistivity $Z(t)_{NWs}$ is obtained via the Matlab code. Figure 3.22 shows the resulting plot of the inverse of the time constant (DEP magnitude) over frequencies from 500 kHz to 10 MHz. The $Z(t)_{NWs}$ values were consistently chosen at the same time of 320 s generally where resistivity was already decreasing by bridging NWs. The same behaviour was observed for other batches of Ge NWs.

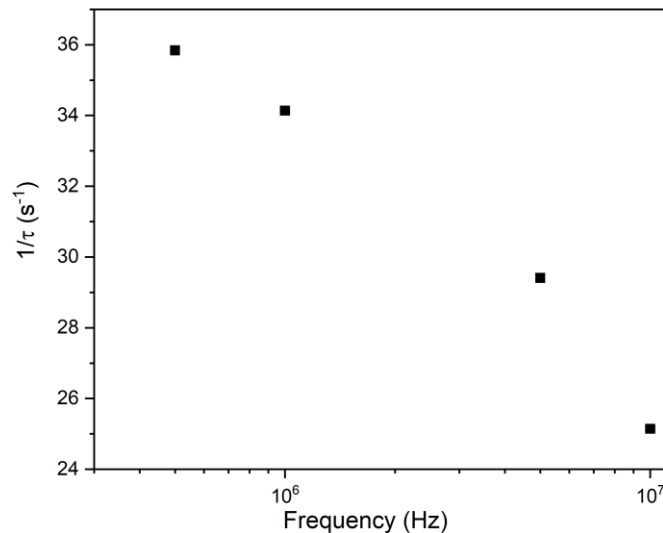


Figure 3.22: Inverse of time constant τ , indicating the magnitude of the DEP force as a function of DEP signal frequency.

Equation 3.3 expressing the DEP magnitude is an adequate approximation for NWs collection. For a given frequency, it is within a capture radius of the electrode gap that the NWs experience the strongest DEP force and gradient (as shown in simulations Figure 3.17 and Figure 3.19). At low frequency, and according to Figure 3.22 the DEP magnitude is the highest and as a consequence attracts more NWs than at high frequency. This is in conformity with the collection observed from optical microscopy analysis put in the appendix Figure A.2.12 where fewer NWs are collected as the frequency is increased. It is worth mentioning that for higher concentration than the one used in those experiments ($\approx 36 \times 10^3$ NWs mL⁻¹), the NWs collection showed more attracted NWs but also more debris and packs of NWs creating disordered structures. This indicates that an ideal concentration can also be considered to optimise NWs collection.

The experimental results obtained in Figure 3.22 have been also correlated to the theoretical DEP equations simulated via Matlab code Figures 3.11 and 3.12. In Figure 3.22, it would have been expected to see a plateau between 500 kHz and 1 MHz as calculated in Figures 3.11 and 3.12. Instead, experimentally the DEP magnitude already drops from 500 kHz to 10 MHz while theoretically, it features only a slight decrease from 10 MHz. The difference could be that the adapted DEP equation (3.2) needs to be further refined because of the difference between the approximated prolate ellipsoid and the real "needle" shape of the NWs. Besides, it could also be due to the thin oxide layer of GeO₂ often referred to as particle shell. A particle shell can have a very different electrical conductivity than the core and thus modify its transportation by the forces involved. Moreover, in the calculations, the Ge NWs are considered as unintentionally doped and as we have seen earlier in this chapter, the Ge NWs have a remaining gold tip that could change their surface polarisation compared to a "pure" Ge NW.

As a means to manipulate Ge NWs and fabricate devices, the first steps to determine the feasibility of the use of DEP were studied. In these experiments, analyses were performed for DEP platform basis like medium and particle inertia, simulations on electric field gradient of the electrodes and study of the CMF and DEP force to have primary insight on the relationship of DEP with the Ge NWs alignment. It was demonstrated, based on the mathematical plots and optical microscopy images, that, for an increasing frequency the CMF was decreasing and so the collection rate of NWs followed the theoretical trend. Optimal frequencies for a high yield of alignment have been already subjected to much research. However, if the NWs collection by DEP can be influenced by the dielectric properties of the particles, one could argue that the dielectric properties of all the NWs taken individually in fabrication batches out of the MOVPE chamber are not perfectly equal.

3.3 Influence of the dielectrophoresis frequency

3.3.1 Establishment

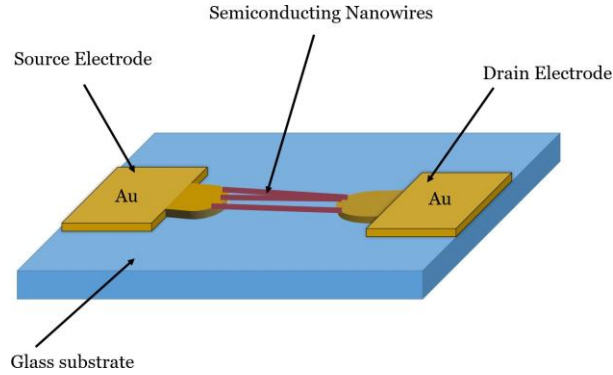


Figure 3.23: Schematic of a floating gate Ge NWs device with the idealised alignment of NWs between source and drain electrodes.

After alignment, the resulting devices are as shown in the schematic Figure 3.23 (and by optical microscopy Figure A.2.12 in the appendix). The electrical characteristics of the resulting devices were investigated with a focus on the influence of increasing frequency on their properties. This work allows more understanding of Ge semiconductor NWs-based devices fabricated by DEP manipulation as well as more understanding of their electrical properties performances and potential implementation.

Standard photolithography and metal etching were used to define the contact electrodes on glass. The devices were fabricated using the protocol and DEP parameters previously studied.

The Ge NWs alignment along the electrodes was performed using DEP with a sinusoidal signal of 8 $V_{peak-to-peak}$ at frequencies of 500 Hz, 500 kHz, 1 MHz, 5 MHz and 10 MHz (500 Hz was added out of curiosity).

3.3.2 Electrical properties; IV response

The resultant current-voltage (IV) response was measured for each device using the setup described in the previous Chapter 2. To evidence the electrical response characteristic, a reference control was fabricated where the NWs were drop-casted between the electrodes without applying any DEP signal. Once fabricated, the electrical properties of the NWs devices aligned at different frequencies were investigated. For each frequency, at least 6 devices were fabricated. Figure 3.24 shows the measured IV response for each DEP frequency.

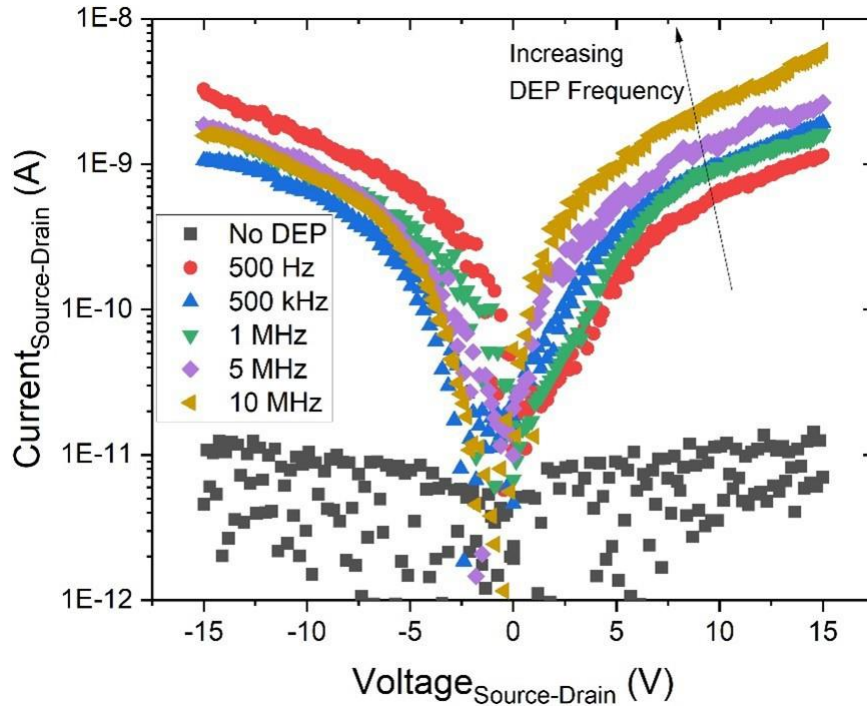


Figure 3.24: IV characteristics of fabricated Ge nanowire devices at differing DEP frequencies with floating gate potential.

Device IV in the black curve shows that without any DEP being applied, there is a slight, negligible increase in the current as the potential is increased. This is most likely due to residual surface contaminants, residing in the channel, from either drop casting the NWs or the subsequent isopropanol rinse forming a negligible conduction channel. Alternative possibilities may be a chain of overlapping or debris of NWs providing a conduction channel between the electrodes. However, the current without any DEP signal being applied is at least an order of magnitude smaller than that observed once a DEP voltage is applied, indicating that any NW alignment or current flow from just drop casting the NWs is insignificant.

When a DEP signal is applied, at 500 kHz (blue triangles curve), a clear IV response can be observed indicating that NWs have been aligned across the electrode gap. The response shows a slight asymmetry with a slightly larger current flow in the reverse voltage direction, no saturation in the current is observed up to the maximum voltage applied in either direction. For a fixed bias, in the forward direction, the current increases with the frequency, while the opposite occurs at reverse bias.

In both voltage directions, the increase and decrease in current is not a fixed shift with frequency, but with a degree of overlapping in the IV response from the devices fabricated at 500 kHz, 1 Mz and 5 MHz. The reason for this could be due to slight differences in the distribution of NWs used in each device. Looking across the entire frequency range, there is a clear change in the asymmetry at the highest frequencies. It was shown in this chapter (Figure 3.22 decreasing DEP magnitude) and in the literature that for positive DEP force the tendency was that above a certain frequency, the DEP force reduces for round particles [251] and ellipsoidal NWs [71] particles. Constantinou *et al.* [75] work on Si NWs devices demonstrated that DEP was, besides a length selection tool a quality selection tool that relied on the NWs conductivity. They noticed that with increasing frequency only the most conductive NWs can respond to the field and align in the electrodes gap. Considering only the IVs, it is not possible to determine whether more NWs are attracted or only highly conductive NWs.

The images put in appendix Figure A.2.12 show the Ge NWs alignment with increasing frequency. It is observable that fewer and fewer NWs are being attracted to the gap with increasing frequency which is in correlation with the results from the DEP magnitude calculation and simulation obtained in the previous chapter. The DEP force being affected by the NWs conductivity it is implied that NWs of mixed conductivity together with low quality are both being attracted at low frequency and thus only the highest conductive NWs with less defect are being attracted at a higher frequency. In FETs and diodes, it is intuitive speculation that more aligned NWs in the gap is related to increasing the conduction current. It has been demonstrated that this statement does not occur for the dense packing of ellipsoid particles. Indeed for FETs [255] and diodes [256] packs of NWs tend to induce screening effects and reduce device performances. As a consequence, the reduction of aligned NWs observed at increasing frequency Figure A.2.12 and the measured current response obtained from the IV plots Figure 3.24 should indicate that NWs attracted at high frequency are of better conductivity. In regards to the obtained IVs Figure 3.24, it would thus be expected to detect an increase in current across all biases. However, while we see this for positive bias with the opposite effect for negative bias potentials and the fact that this subset of NWs would be more conductive, this indicates that the behaviour observed here is more complex. It could also indicate that the aligned NWs are not yet dense enough at the gap for the screening effect to occur. No saturation of the current is observed for all DEP frequencies as the voltage is increased in both directions, as would be expected for a transistor-type behaviour. As mentioned, there is a degree of asymmetry in the IV responses. From these observations, one could argue that the devices are operating as diodes, rather than as transistors (with floating gate potential).

Orientation manipulation during DEP

While the device structure should be nominally symmetric, the Au nanoclusters used as seeds for NW growth remain on the tips of the NWs. TEM characterisation shows that Au diffuses inside the NW [44], resulting in NWs having an axial heterostructure with an alloyed Ge(Au) in contact with the Au electrode at one end, while the other end has an abrupt junction between the Ge NW and the Au electrode. Although intrinsically synthesised, Ge NWs are inevitably p-type as a consequence of surface traps at the interface Ge/GeO₂ oxide creating holes accumulation [257].

Therefore, the device is structured with two different junctions from one contact to the other. One contact is more ohmic (or "less Schottky") with a graded junction from Au electrode to Ge(Au)alloy/Ge(core), while the other is a Schottky contact with a more abrupt junction Ge(core)/Au(electrode) as shown in the schematic Figure 3.26 a). During device fabrication, the Ge NWs being different from one side to the other undergo nonetheless the same non-uniform electric field of DEP and so the Ge(Au)alloy or the Ge(core) side of the NWs should have no preferential alignment parameters or orientation. The asymmetric electrical properties of the devices from forward to reverse bias can be explained if the NWs have an orientation trend and orient a certain way i.e the Ge(Au)alloy sides connected on one electrode and Ge(core) sides connected on the opposite electrode. It was actually found that the function generator had a DC offset artefact of 100 mV. During DEP, that DC offset from the function generator created an additional electrokinetic force to DEP force; electrophoresis (EP). The DC offset generates an electrode with fixed poles "more positive" and "more negative" than the opposite electrode and hence two forces are determining the preferential orientation of the Ge NWs. The zeta potential of the Ge NWs was measured using a Malvern DLS ZETASIZER, and it was found that the NWs surface was negatively charged in anisole with $\zeta = -0.75$ mV. Indeed, with the thin oxide layer on the surface, the dangling bonds of oxygen form a layer of negatively charged O⁻. At the Ge(Au)alloy side, the surface is more likely to have no oxide layer or at least much less O⁻ bound due to the presence of gold and thus a more neutral net surface charge. Hence, the Ge(core) side of the NWs with its negative net charge in anisole, tends to orientate towards the "fixed" opposite polarity; the positive electrode of EP. EP is ruled by the fixed net surface charge of the NWs surface while DEP is ruled by polarisability, dielectric properties and moving carriers in the Ge NW.

The combined forces of DEP and EP, show an interesting assembly method to fabricate heterojunction diode-like devices. Indeed that serendipitous offset was enough to influence and direct the Ge(core) part of the NWs to one electrode. Hence, the Ge(core) side NWs are particularly attracted to the more positively charged electrode at a certain time under the AC field added with DC offset. Therefore, resulting in asymmetrical devices.

If the function generator is ideally set to 0 V offset, the aligned NWs have non-preferential orientation and the resulting device features more transistor-like behaviour with a symmetrical response. The following schematic 3.25 illustrates the combination of DEP and EP forces acting on Ge NWs with an oxide layer (green), rendering the net surface charge negative ($\zeta(-)$) and a Ge(Au) alloy sides neutrally charged ($\zeta(\emptyset)$) at the surface.

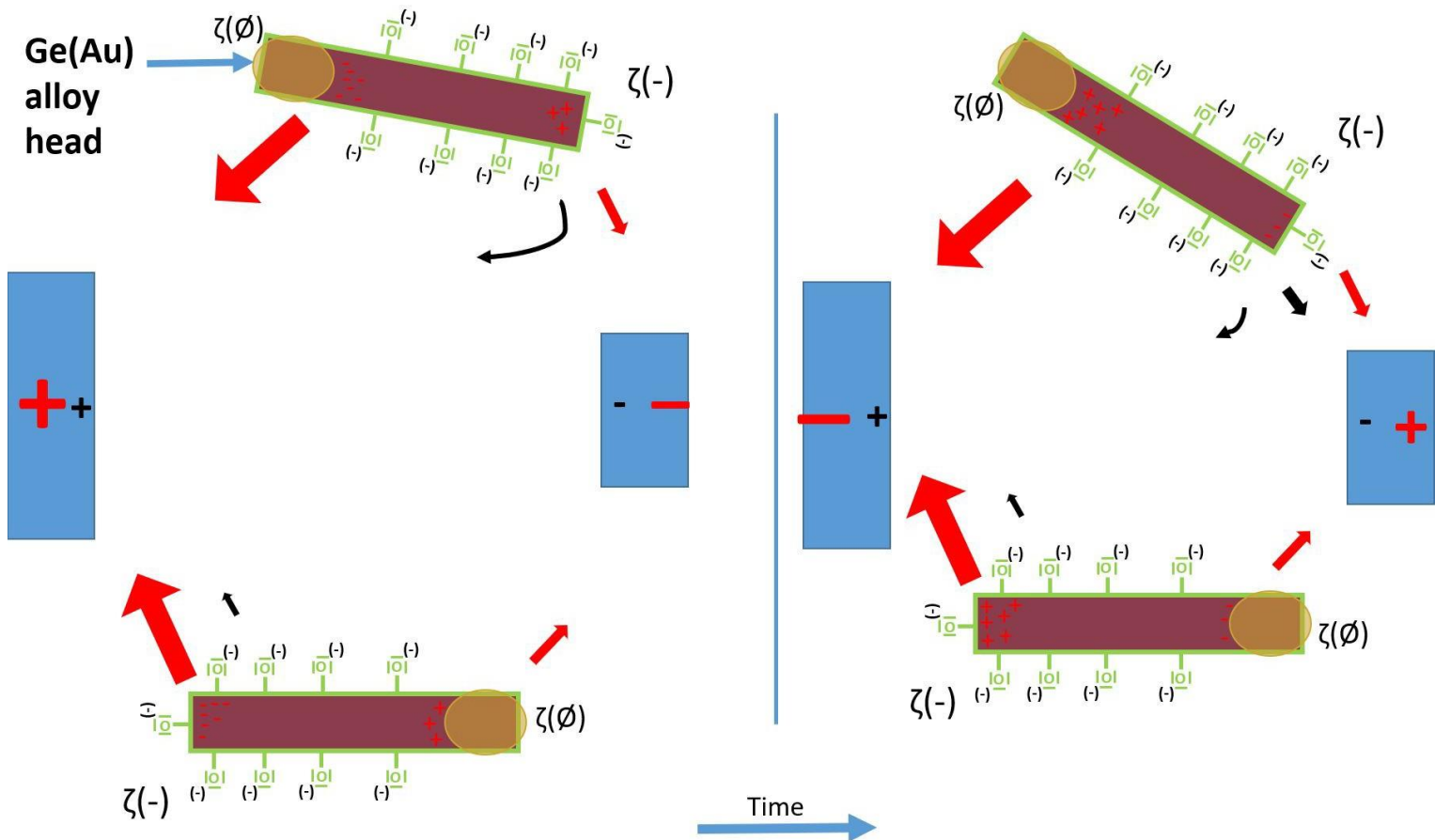


Figure 3.25: Combination of Dielectrophoresis and Electrophoresis forces; not to scale. Alternating DEP voltage (red arrows and signs) of $8 V_{peak-to-peak}$ and fixed EP voltage (black arrows and signs) of 100 mV.

Ge NWs heterojunction diode devices

After alignment and fabrication of the device by DEP, this hetero-junction Au(electrode)/Ge(Au)alloy-Ge(core)/Au(electrode) results in a band diagram illustrated in Figure 3.26 b). As input, known parameters were used for the band diagram reconstruction [95], [258]. On one end of the NW, the abrupt contact Ge(core)/Au(electrode) is considered a Schottky contact; the p-Ge NW band at the interface meta Ge bends upwards, and the holes are depleted close to the interface of the NW with the metal creating a potential barrier for holes to reach and recombine with electrons at the space charge region.

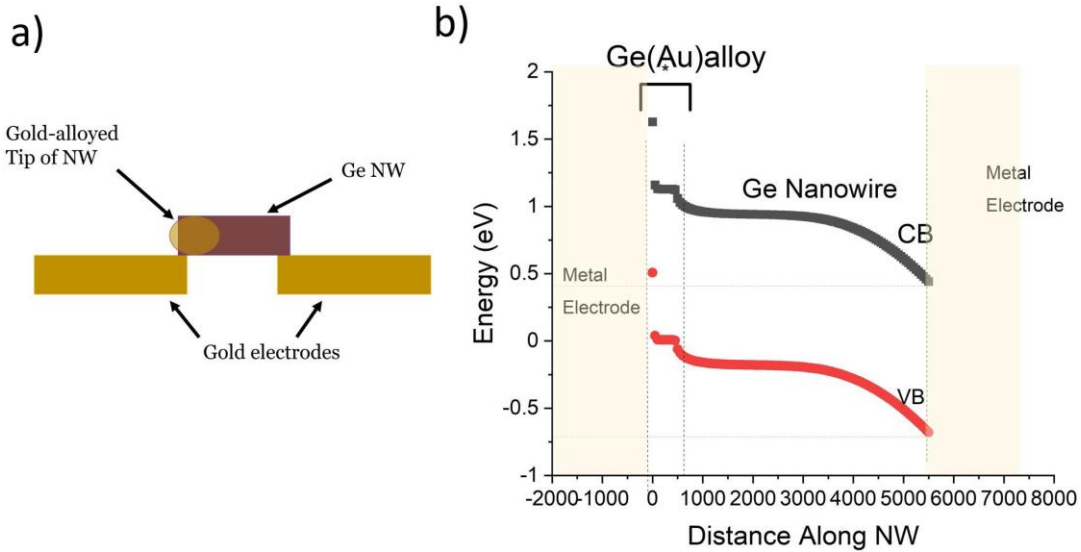


Figure 3.26: Schematics of (a) representation of contacted NW and (b) schematic of the resulting band alignment.

The contact Au(electrodes)/Ge(Au)alloy bends the energy band downwards and injects holes lowering the Fermi level in the Ge semiconductor [259]. The contacts Au(electrodes)/Ge(Au)alloy is gradually ohmic towards the electrode and gradually ohmic or "less Schottky" towards the chemical junction with the Ge(core). Recent work has shown very similar properties obtained with heterostructured NWs of In(Au)alloy/GaAs(core) and measured Schottky barrier lower than for traditional Au/GaAs Schottky contacts [111]. This reduction is caused by chemical bonds formed during the growth at the junction Ge(Au)alloy/Ge(core) that ease the junction from abrupt to graded and determine the carriers' transport. This is what can be observed during the annealing of semiconductors with metal contact where chemical bonding between these elements is improved leading to ohmic contact [260]. In the present case, one could argue that the band diagram actually shows lower bending at the junction Ge(Au)alloy/Ge(core) than at the abrupt contact Ge(core)/Au(electrodes).

To further investigate and understand the performance of the devices fabricated at different frequencies, the IV characteristics in Figure 3.24 are re-plotted on log-log scales in forward voltage Figure 3.27 and in reverse voltage Figure 3.28 for selected frequencies.

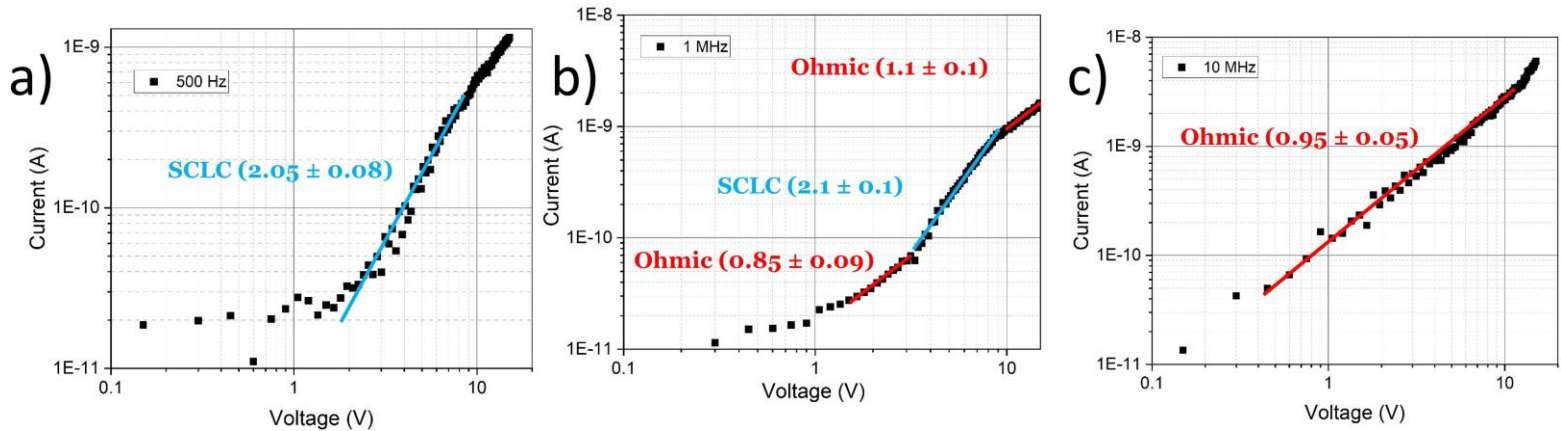


Figure 3.27: Forward IV characteristics of as fabricated Ge NWs devices fabricated at DEP frequencies of (a) 500 Hz, (b) 1 MHz and (c) 10 MHz all fabricated with a peak-to-peak DEP voltage of $8 V_{peak-to-peak}$.

- Looking first at the device fabricated at the lowest DEP frequency a) 500 Hz, the current response in forward bias voltage displays an initial region (between approximately 0 and 1.5 V) where a negligible current is able to flow, followed by an increase in the current as the voltage is further increased. The gradient of the increasing current is 2.05 ± 0.08 , which indicates that the device is dominated by space charge limited currents (SCLC) due to low carrier concentration from the depletion of injected electrons trapped by defect states [261]. Given that Ge has high electrons and holes mobility, it is most likely that the "pure" Ge NWs dielectric properties have little contribution to the conduction. That effect has been previously observed in nanowire-based diodes [262] where it is also demonstrated that SCLC is enhanced by dimensionality (high aspect ratio). At low voltage, the captured injected charges are not enough to overcome the SCLC, there is a coexistence of band carriers and trap states (shallow or deep traps). The slight tick-up at a high voltage of 10 V indicates an onset trap-free SCLC when the trap states are being filled.

At a DEP frequency of 1 MHz a noticeable change in the IV behaviour is observed, with the appearance of three distinct regimes. At voltages up to 1 V, there is no significant increase in the current, as similarly observed in the initial region at 500 Hz. The next region occurs between 1 and 3 V, where the current increases as the voltage is increased with a gradient of 0.85 ± 0.09 . In that region, the gradient is close to the value of 1 which is expected from **ohmic conduction**. The conductivity mechanism is slowly transitioning from SCLC to ohmic (from 500 Hz to 1 MHz and higher frequency) as trap states are less present in the NWs.

As the voltage is further increased >3 V at 1 MHz the current increases at a faster rate with a gradient of 2.1 ± 0.1 indicating SCLC as the dominant conduction mechanism in the device performance. SCLC that are most probably originating from shallow traps (low energy density of states either close to valence or conduction band) commonly observed in nanodiodes [126]. There is then a slight reduction in the gradient for the highest voltages ≈ 10 V (with a gradient of 1.1 ± 0.1) suggesting saturation of the SCLC and a return to ohmic behaviour supporting fewer trap state levels. As the voltage increases it becomes high enough to pull the Fermi level above the traps (in less amount than for lower frequency NWs) energy level and entails a device that features power dependence. For the device fabricated at the highest DEP frequency of 10 MHz, significantly different behaviour is observed with the current getting larger as the voltage is increased across the entire source-drain potential range. Furthermore, only a single ohmic gradient is observed for nearly the entire voltage range for this device with a value of 0.95 ± 0.05 , indicating true diode-like behaviour. One could assume that for NWs aligned at high frequency, the carrier concentration and mobility are higher than the trapped charge density and show fewer response differences. At the highest voltages, a slight uptick is observed in the gradient suggesting a potential onset of trap-free SCLC at voltages > 14 V when the trap states are filled and don't affect the carrier concentration anymore.

Firstly the initial region of no current flow becomes smaller as the frequency is increased, in other words, the threshold voltage required to turn the device ON reduces. Secondly, as the DEP frequency is increased an initial ohmic region is observed before the onset of SCLC, the upper threshold of this ohmic region then increases as the DEP frequency is increased along with fewer trap states leading to ohmic conduction dominating the performance of the device. Within the NWs, less SCLC and so fewer defects imply that the channel material quality heads toward a less disordered system and more ideal crystals.

- Conversely, looking at the IV behaviour for reverse bias Figure 3.28 a), b), c), it is observed that for the devices fabricated at 500 Hz and 1 MHz, a very similar feature is obtained with an approximate constant increase in the current being measured across the entire voltage range. For these devices, gradients of 1.15 ± 0.03 and 1.20 ± 0.04 were obtained. This suggests that the resultant diodes were suffering from high leakage currents. In reverse voltage, leakage are coming from crystal defects, dislocation, and lattice mismatch inducing trap states that reduce NWs quality and conduction [263].

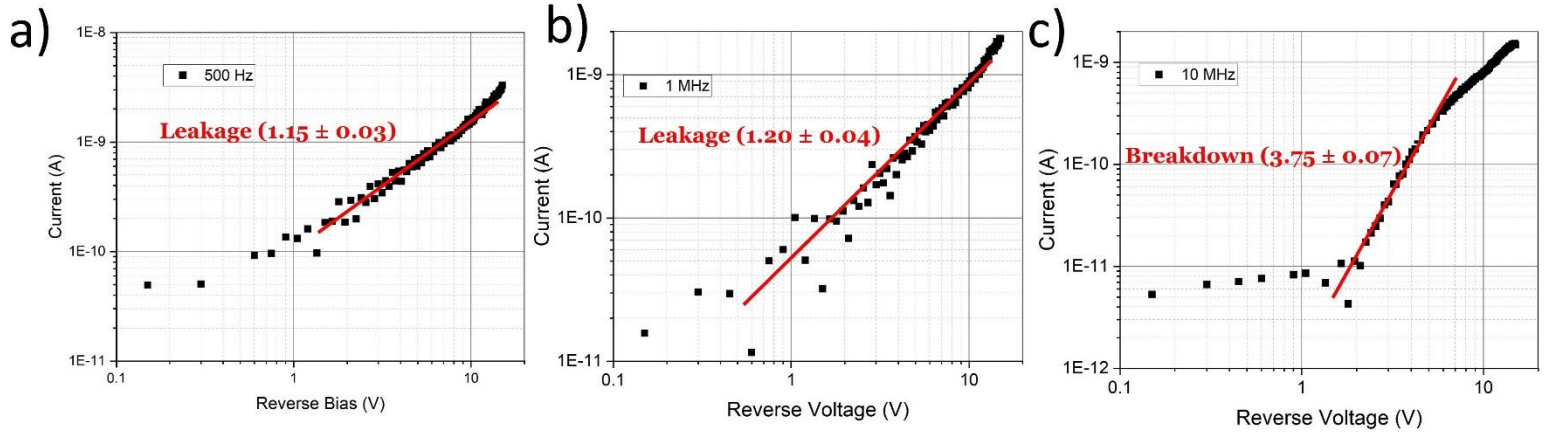


Figure 3.28: Reverse IV characteristics and gradient fitting lines of as fabricated Ge NWs devices fabricated at DEP frequencies of (a) 500 Hz, (b) 1 MHz and (c) 10 MHz all fabricated with a peak-to-peak DEP voltage of $8 V_{peak-to-peak}$.

For the 10 MHz devices, significantly different behaviour is observed; there is initially only a very small voltage dependence on the current that occurs up to a threshold of around 2 V. Above this value there is a sudden and sharp increase in the current (gradient of 3.75 ± 0.07) to a voltage of approximately 8 V after which the increase in current begins to reduce. This more closely resembles the one that would be expected from a diode in reverse operation with no current flow before a sudden breakdown occurs at ≈ 2 V, although the origin of the breakdown behaviour (i.e. Zener, impact ionisation, etc.) is not clear.

For the devices not shown, similar behaviour is observed in the 500 kHz and 5 MHz cases, with only the 10 MHz device exhibiting significant change to this.

To summarise the results and better help understand the performance of these devices as diodes, Figure 3.29 shows the measured forward “turn-on voltage” and the rectification ratio as a function of frequency. Figure 3.29 a) shows that as the DEP frequency increases, the turn-on-voltage decreases from 1.17 V to 0.2 V which is close to the expected turn-on for a Ge diode (0.3 V), while in Figure 3.29 b) the rectification ratio increases, reaching a value of over 500 at a voltage of 1.5 V at the highest frequency.

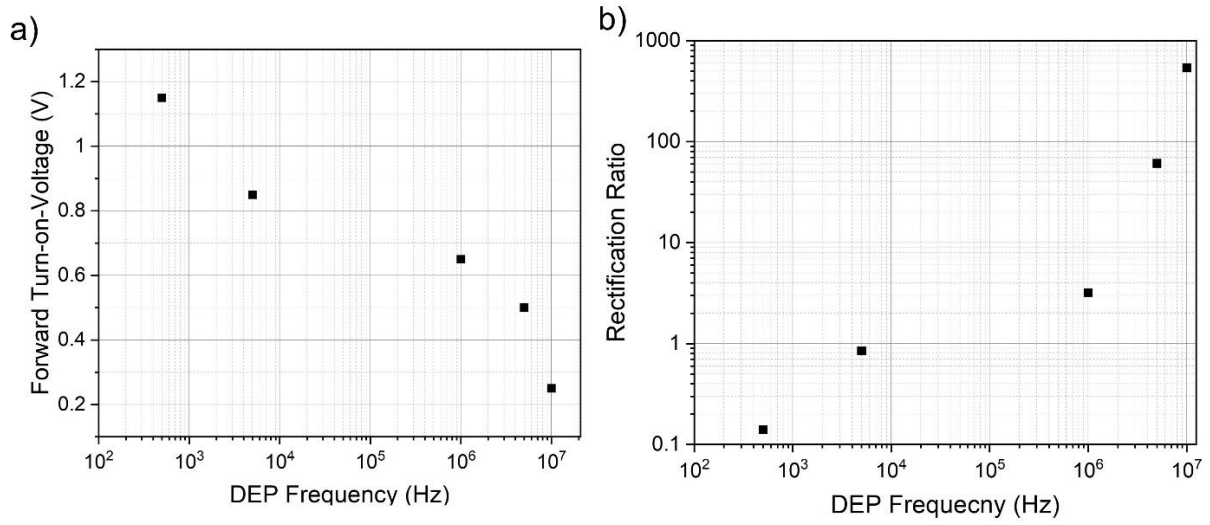


Figure 3.29: (a) Forward Turn on Voltage and (b) Rectification Ratio (at +/- 1.5 V) as a function of DEP frequency.

Other studies on the doped p-n junction of a single Ge NW diode showed a rectification ratio of 100 for NW of 60 nm of diameter on a device fabricated by VLS and E-beam contact [264]. A rectification ratio of 205 to 1430 for n and p doped array of Ge NWS of 150 nm diameter has also been measured [265]. Si NWs diodes have been reported with rectifying behaviour of 1.33 to 4.47 [266]. This rectification ratio is an important asset for semiconductor devices as it controls the flow by blocking undesirable leakage currents.

To understand the cause of these distinctly different regimes and device performance over increasing frequency, the NWs alignment by DEP force has to be considered, specifically the interactions between the AC field frequency and the NWs. At low frequencies, a similar force is experienced by all the NWs, regardless of conductivity or the number of defects in them. As such, for the most inferior frequency devices, any Ge NW will have been aligned and contribute to the observed current. SCLC occurring across all voltages above the turn-on, as well as leakage current, indicates that a significant percentage of the NWs have active traps and defects and subsequently these dominate the electrical performances seen in forward and reverse bias voltage. No significant SCLC has been observed at high voltage, one can assume that the majority of NWs have shallow traps rather than deep traps. A reconstructed schematic of the band alignment is shown in Figure 3.30.

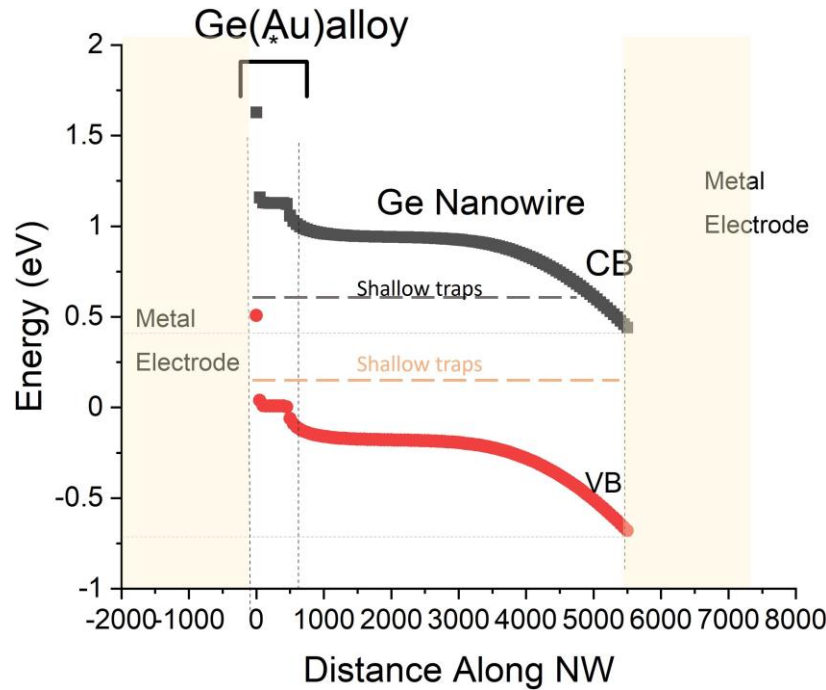


Figure 3.30: Theoretical band alignment of the Ge NWs-based devices. At low frequencies, the devices exhibit SCLC shallow trap states present in the collected NWs. Energy levels are relative for illustration purposes and are not absolute values.

The graph in Figure 3.30 shows shallow traps between the Valence Band (VB) and Conduction Band (CB). Shallow traps, close to the VB and CB are responsible for the observed SCLC of the NWs collected at low frequencies. Previous works estimated shallow traps from interface and surface defects in germanium NWs to be situated below the Fermi level at 0.13-0.15 eV [164]. Shallow traps above the Fermi level have been scarcely investigated, their defects type is unknown and they have been estimated to be situated at 13-17 meV above the Fermi level [267].

With increasing DEP frequency, the NWs require a higher conductivity (for the carriers to polarise the NW) and so fewer defect states to respond to the field and align; the most trap-rich NWs cannot respond to DEP during the fabrication, resulting in the appearance of SCLC regions in the IV characteristic. As the DEP frequency continues to increase, the device contains fewer selected NWs with fewer traps resulting in the ohmic region becoming larger until no SCLC is observed at the highest DEP frequency. Extrapolating this idea would eventually result in a reduction of the current as only a few NWs would be located inside the gap and contributing to the current flow. However, it would seem that from the results obtained in this work, we have not yet reached this critical frequency.

Increasing frequency aligns NWs that feature higher conductivity, and so the Mott-Gurney law was studied from the resultant IV curves. If a bulk semiconductor does not have any traps, the SCLC is governed by the V^2 relationship first derived by Mott [127]. For NWs that contain traps, the law is rewritten in the form as follows [268].

$$J = \frac{9}{8} \theta \varepsilon_{\text{Ge}} \mu_{\text{NWs}} \frac{V^2}{L^3} \quad (3.4)$$

In our case ε is the permittivity of Ge, μ_{NWs} is the NWs carrier mobility, V is the applied voltage, L is the distance between the electrodes and θ is a scaling constant that is inversely proportional to the density of traps in the NWs. As such, we have fitted the SCLC regions of the IV curves with equation 3.4 and extracted the product ($\theta\mu$) as a function of DEP frequency with the results shown in the plot Figure 3.31. Because no clear SCLC region was present in the IV response the analysis could not be performed at the highest frequency of 10 MHz. From the analysis, as the frequency is increased the product ($\theta\mu$) also increases. While it is not possible to decouple the terms using this approach, for the product to increase either the mobility is increasing or the trap concentration is decreasing or even both are occurring. An increase in carrier mobility can be seen as improving the quality of the NWs in the device. Similarly, a decrease in the trap concentration would be seen as signifying higher quality NWs. In that fashion, for NWs having higher conduction and carrier mobility, the carriers during DEP can follow the pace of high-frequency signal, transit within the NW and polarise it on both sides and finally align between the electrodes. This explains the hypothesis that increasing the DEP frequency results in better-quality NWs being selected and aligned.

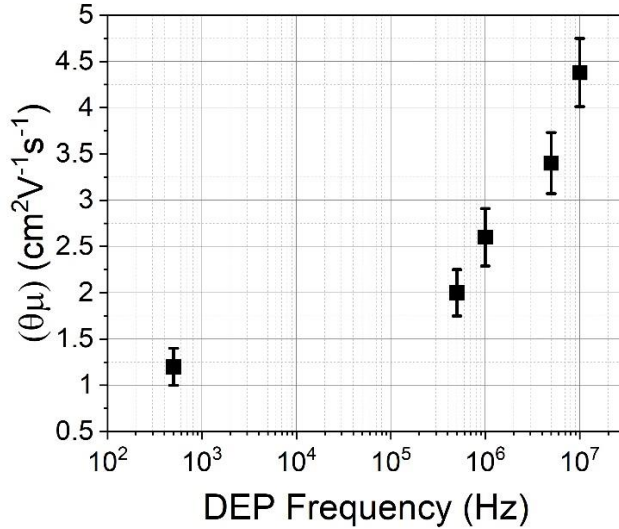


Figure 3.31: $\theta\mu$ as extrapolated by fitting the Mott-Gurney law to the IV curves as a function of DEP frequency.

The improved performance of the devices fabricated at higher DEP frequencies and their potential reproducibility were tested. Four repeat devices were made at the highest frequency of 10 MHz. Based on the analysis above we expect to only align the most conductive NWs and obtain the most diode-like behaviour. The resultant IVs are shown in Figure 3.32, each separately fabricated spanning a period of several months. Three of the devices show almost identical IV characteristics, with the fourth only showing a slight difference, primarily in the reverse voltage direction. All devices exhibit the same slight asymmetry as observed previously in Figure 3.24 and analysis of the forward bias response shows the same behaviour as observed in Figure 3.24, with identical gradients, turn-on voltages and rectification ratios (within the fitting uncertainty). This confirms that, despite the different oxide thicknesses observed in NWs of different ages, the Ge NWs are stable and suitable for device fabrication months after their growth, and DEP is a viable and attractive route to fabricate predictable devices utilising semiconductor NWs, resulting in a similar number of nanowires with the same mobility in the end device.

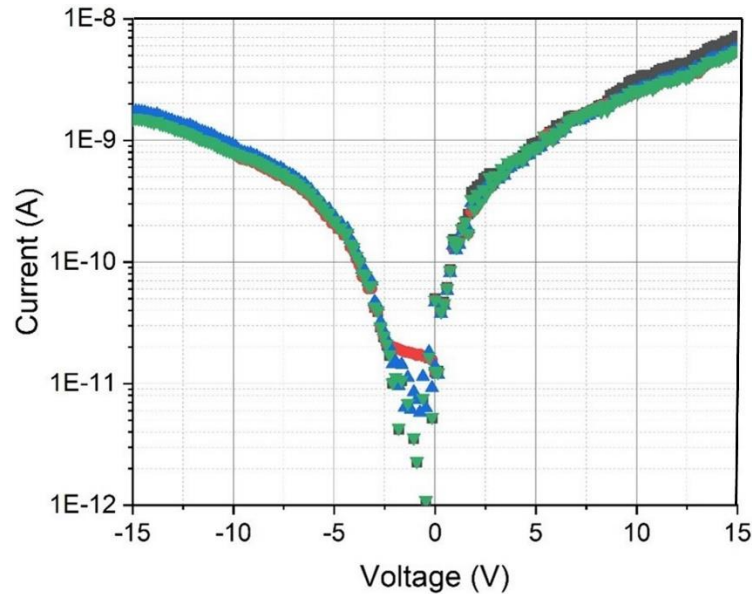


Figure 3.32: : IV Characteristics of multiple Ge Nanowire devices fabricated with a DEP frequency of 10 MHz and a peak-to-peak DEP voltage of $8 V_{peak-to-peak}$.

Conclusion

Choice of the medium according to its wettability with the platform surface, chemical inertia with the Ge NWs as well as the relevant design of the receiving electrodes have been identified as the most favourable parameters for DEP workability. With the aim of investigating DEP for Ge NWs, optimum fabrication parameters were found to be crucial. It was demonstrated by means of scientific experiments that DEP is an effective tool for the collection and selection (length and quality) of Ge NWs with different lengths and electrical properties.

NWs collected at high frequencies resulted in an alignment of NWs length similar to the gap, and high conductivity properties with the lowest level of defects confirmed by the absence of SCLC and increase of carriers' mobility. DEP collection at high frequency leads to the attraction of semiconductor NWs that tend towards ideal semiconductor crystals system. It was demonstrated that it was possible to manipulate and orientate heterostructured NWs by combining two electrokinetic mechanisms. Dielectrophoresis and Electrophoresis working together allow specific orientation and motion of electrical charges characterised by permittivity (DEP) and surface charge (EP) of particles in a medium in interaction with an applied electric field; AC and DC. This is the first time that such motion is performed on heterostructured semiconductor NWs, with the potential of orientating and aligning NWs to obtain heterojunction contact. DEP selections still occurred which means that it was dominating over EP.

To preserve the advantages provided by DEP, an applied AC voltage of 8 V_{peak-to-peak} and DC voltage of 100 mV were efficient parameters to electrically interact with the moving charges at the core of the Ge NWs and with the fixed negative net charge provided by the thin oxide layer at the surface of the NWs. SEM images and EDX chemical analysis were not possible to perform to have images of the preferential orientation alignment. SEM imaging has an interaction volume depth of electrons that is too big and too penetrating in the matter and thus was reaching the gold electrodes. A smaller excitation voltage would have not excited the gold enough for detection and therefore the detection of gold would have been hampered by the gold electrodes. However, analogous results have been obtained from previous electrical properties studies on heterostructured NWs supporting this reasoning [111, 260]. The obtained diode-based devices demonstrated to possess a Schottky contact at the Ge(core)/Au(electrode) junction and ohmic contact at the Au(electrode)/Ge(Au)alloy junction. The obtained diodes showed increasing performance characteristics, including carriers' mobility of 4.40 $\mu\text{m}^2/\text{Vs}$, a turn-on voltage of 0.2 V, a large reverse breakdown voltage, and a rectification ratio of 500 for characteristics obtained at the highest frequency of 10 MHz.

Lastly, from low to high frequencies, it is possible to control the features of the devices resulting in diode or transistor performance if one decides to align the NWs with heterojunctions (with electrophoresis) or homojunction (without electrophoresis). This is a promising technique for the next generation of nanotechnology for the manipulation of chemically structured nanoparticles.

Chapter 4

Fabrication and characterisation of a single nanowire-based device

Introduction

In Chapter 3 it was demonstrated that increasing frequency besides aligning superior electrical properties also collected fewer NWs because of decreasing DEP force and because of the unpredictable and limited amount of quality NWs by batch. As a consequence, it was observed that for frequencies higher than 10 MHz it was difficult to align NWs even with the aim of single NW alignment. As investigated in the previous Chapter and literature, despite the tremendous potential of DEP, manipulation, and placement of NWs is still a dominant challenge for nano-manipulation, especially for a single NW. By means of DEP, a possible way would be to have one single NW in the solution which would imply a randomly chosen NW without being pre-selected by DEP, adding manipulation that would risk damage. Another method would be to stop the DEP process as soon as a NW is aligned in the electrode gap, and the selection mechanism of DEP still occurs. Ideally, it could have been done by using the Matlab code and TIA set-up to stop the DEP process as soon as the calculation shows a drop in resistance. The issue is that at a frequency of 10 MHz the parasitic capacitance effect from the electrodes takes over the TIA that can not keep up with the decreasing signal-to-noise ratio and it becomes more difficult to detect any changes in resistance. Currently, most of the single NW alignment methods are by advanced lithography (top-down), electrophoresis, and tweezers manipulators used with a complex optical microscope (bottom-up). Those techniques have shown high precision placement but require direct contact with the particles which is a source of damage, time-consuming, and involves randomly chosen NW [269]. In the literature, single NW alignment by DEP relies on a very low critical voltage used together with a fluid flow channel system (electroosmosis from a conductive medium like water) which can be a problem regarding the chemical nature of the particles [60].

In the following Chapter, an experimental method is proposed to align one single NW by combining the advantages of DEP and a voltage divider set-up.

This system gives the possibility to use any frequency (and so variable NW properties) without additional constraint to the NWs' motion and environment. It is an easy and rapid method to have control over the density of NWs by keeping their properties provided by DEP at a selected frequency. Single NW alignment has great potential for analysis of fundamental properties of materials at the nanoscale as well as applications like a single molecule or photon sensors.

4.1 Voltage divider set up

The basic principle of a voltage divider is a simple series of resistor circuits allowing voltage division between two resistors and producing an output voltage divided by the input voltage. The voltage divider system can be implemented as presented in Figure 4.1 where the electrode gap is represented by the resistor R_{NW} . To simplify and avoid any additional electrical artefact, the alignment monitoring system with the TIA was removed for this experiment. Besides, as mentioned, at high frequencies the signal-to-noise ratio is too insufficient to detect any accurate changes in the resistance. Using the same protocol of fabrication and DEP parameters previously studied the system demonstrated in this chapter proposes an innovative way to have further control over nanoparticle manipulation. The voltage divider system is ruled by Ohm's law equation and the voltage passing through the electrode gap V_{gap} can be written as follow;

$$V_{gap} = V_{in} \frac{R_{NW}}{R_d + R_{NW}} \quad (4.1)$$

Before the start of DEP, the electrode gap R_{NW} can be considered as an "open circuit resistor" connected in series with a chosen resistor R_d . Therefore, before any NW starts to align $V_{in} = V_{gap} = 8 V_{peak-to-peak}$, and $R_{NW} \rightarrow \infty \Omega$. When the circuit is being closed by an aligning NW, the resistance R_{NW} ($R_{NW} \rightarrow 0 \Omega$) has to become considerably smaller than R_d so that the voltage passing through $V_{gap} \approx 0$ is negligible stopping the DEP process. For that purpose, R_d has to be low enough to allow $V_{gap} = 8 V_{peak-to-peak}$ at the start, but high enough for $V_{gap} \approx 0$ when $R_{NW} \ll R_d$. Ideally, in this way DEP allows one NW to align.

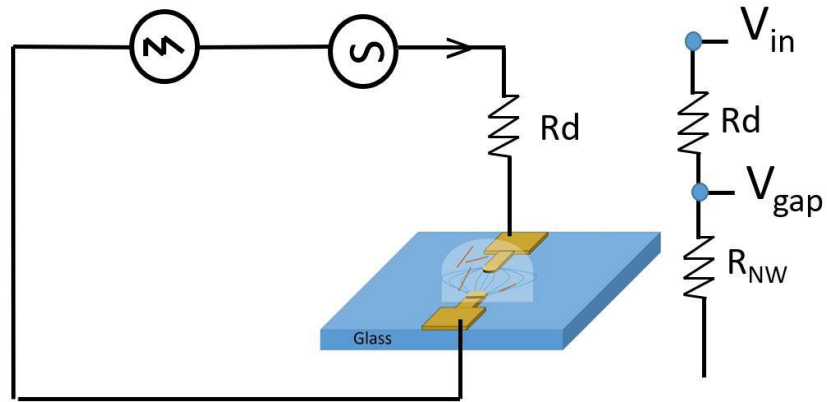


Figure 4.1: Voltage divider system with DEP circuit topology.

To test that idea, a series of devices were fabricated using the parameters previously studied, i.e. AC voltage at $8 V_{peak-to-peak}$ and frequencies of 1 and 10 MHz with no DC offset. A new batch of Ge NWs in anisole was prepared by sonication. For each device and frequency, the DEP process was coupled with the voltage divider system and was set with a resistor R_d of 0Ω , $16 \text{ k}\Omega$, $22 \text{ k}\Omega$ and then $33 \text{ k}\Omega$. The samples were analysed by optical and SEM microscopy and the images at 10 MHz are presented in Figures 4.2 and 4.3. The devices' images fabricated at 1 MHz were not shown as they performed the same collection trend as at 10 MHz.

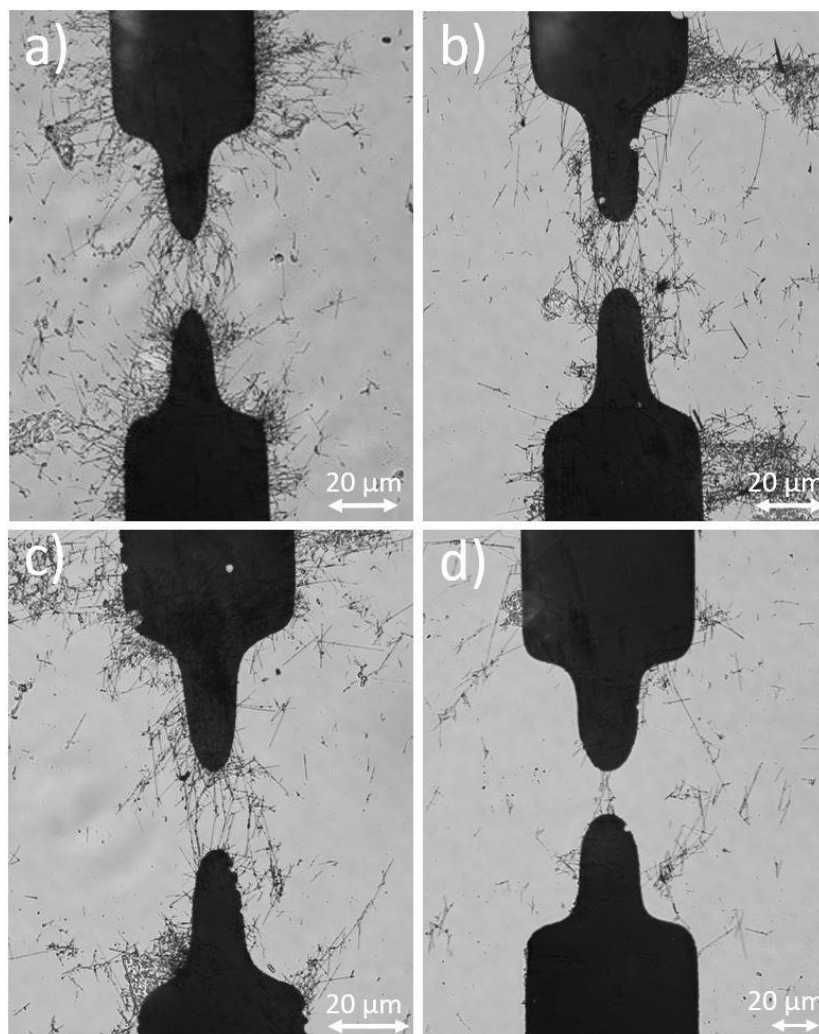


Figure 4.2: Images obtained by optical microscopy of devices fabricated at a DEP voltage of $8 V_{peak-to-peak}$ and frequency of 10 MHz. The voltage divider system was set with $Rd =$ a) $0 k\Omega$, b) $16 k\Omega$, c) $22 k\Omega$ and d) $33 k\Omega$.

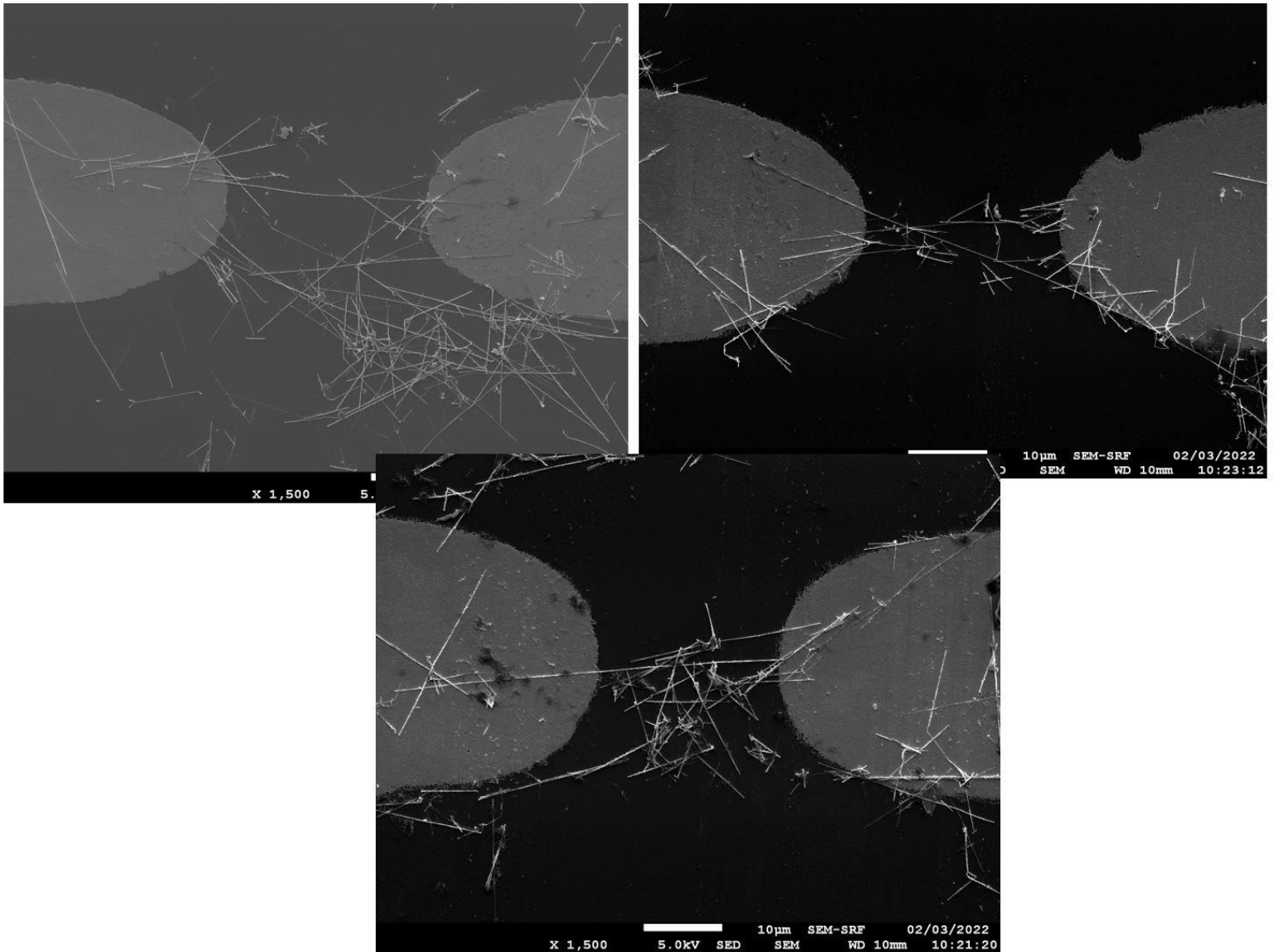


Figure 4.3: SEM images of ≈ 1 NW in devices fabricated at a DEP voltage of $8 V_{peak-to-peak}$, frequency of 10 MHz and with a voltage divider resistor of 33 k Ω .

A limiting resistor value was considered at the point where 2 to 1 NWs seemed to be aligned as suggested by a quick check using optical microscopy. At 1 MHz the limiting resistor was found to be at 16k Ω , while at 10 MHz the limiting resistor was found to be at 33 k Ω . Analogous alignment yield was obtained for 1 MHz and 10 MHz with a similar progression than with increasing frequency observed in Chapter 3 where here the number of aligned NWs decreased with increasing R_d . As R_d is increased, the necessary resistance R_{NW} (before $V_{gap} \approx 0$) decreases, which is why fewer NWs are collected until only a couple or one NW is collected.

From the SEM images at 10 MHz with $R_d = 33 \text{ k}\Omega$ Figure 5.3 1 NW seems to be aligned although it is also surrounded by other entangled NWs. It is possible that those entangled NWs were dragged by the more conductive one by branched NWs or that smaller NWs and particles were collected by residual electrophoresis created by the function generator at high frequency (DC offset artefact at high frequency) [270]. A method that could have been used to reduce entangled NWs was to reduce the NWs concentration risking chances to collect any NWs and quality NWs.

5.1 Current response

The $I(V)$ responses were measured using the set-up described in the previous Chapter 2 and used in Chapter 3. The electrical measurements of the devices were put in Figure 4.4 for the device fabricated at 1 MHz with a limiting resistor of $16 \text{ k}\Omega$ and Figure 4.5 for the devices fabricated at 10 MHz with a limiting resistor of $33 \text{ k}\Omega$.

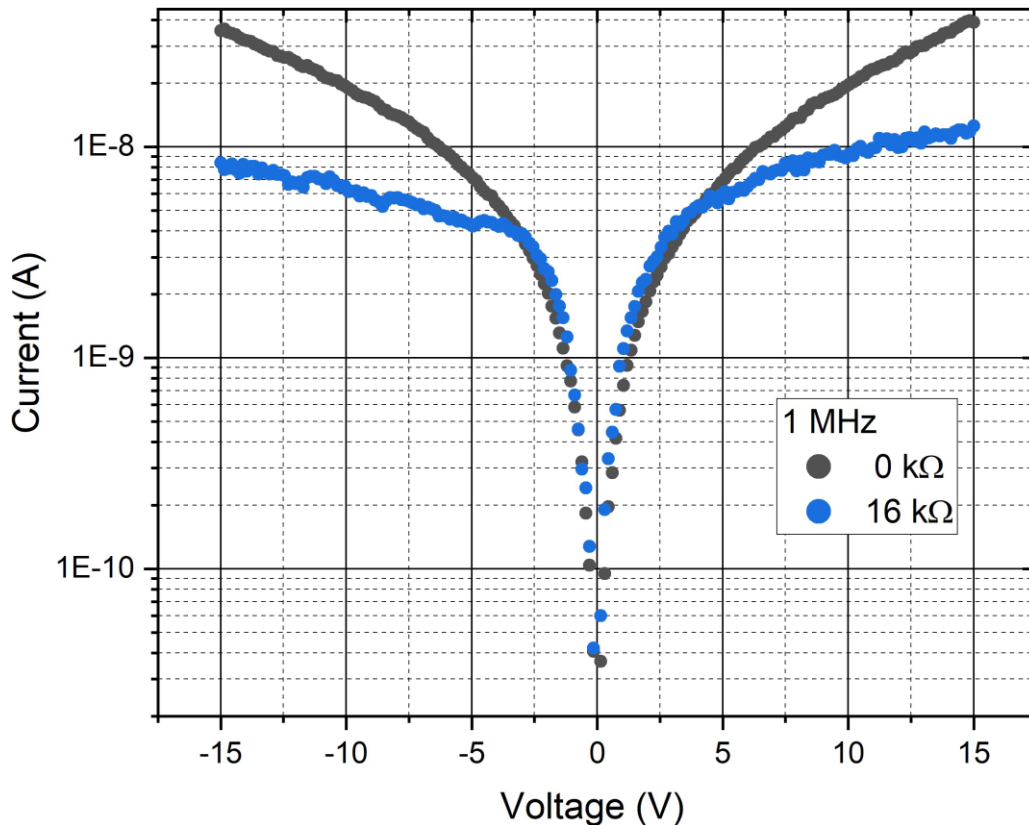


Figure 4.4: $I(V)$ characteristics of the aligned NWs at 1 MHz and AC field of $8 V_{peak-to-peak}$, with a voltage divider resistor $R_d = 0 \text{ k}\Omega$ and $16 \text{ k}\Omega$.

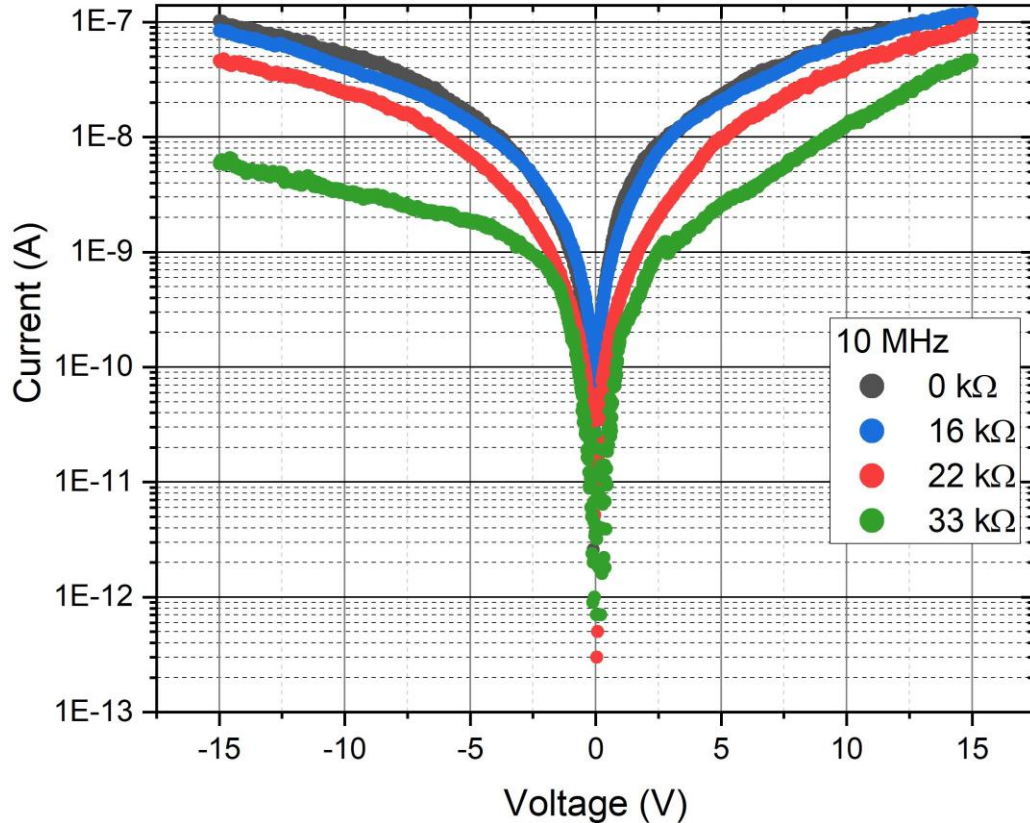


Figure 4.5: $I(V)$ characteristics of the aligned NWs at 10 MHz and AC field of $8 V_{peak-to-peak}$, with a voltage divider resistor $R_d = 0 \text{ k}\Omega$, $16 \text{ k}\Omega$, $22 \text{ k}\Omega$ and $33 \text{ k}\Omega$.

For all the responses obtained using $R_d = 0 \text{ k}\Omega$, symmetrical transistor-like performances are observed at 1 and 10 MHz frequencies. As expected and with no DC offset applied during DEP (and thus no EP), transistor-like performances are obtained as the collected NWs have no preferential alignment. This further confirms the possibility to build NW-based devices with a certain control on the desired performances.

At 10 MHz and with increasing R_d , the increasing asymmetry suggests devices that head toward one NW alignment (heterojunction). As the collection rate decreases the device performances are dominated by the heterostructured NWs. It implies that for heterostructured NWs with no preferential alignment on the electrodes, transistor performances can be reached if enough NWs are aligned in the gap to counterbalance heterogeneity at the junctions which would otherwise result in asymmetrical response as explained in Chapter 3. The resistance of the resulting devices fabricated at 1 and 10 MHz was investigated as a function of the increasing R_d and put in Figure 4.6.

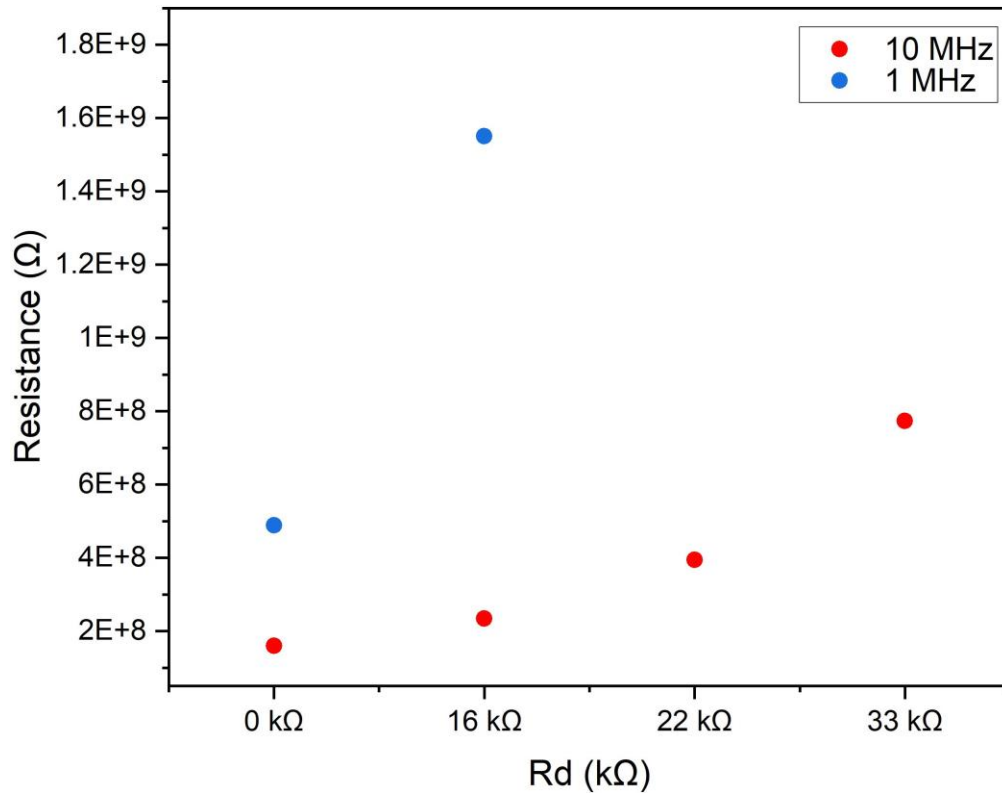


Figure 4.6: Resistance of the device measured between 10-11 V as a function of the voltage divider set-up resistor R_d .

As fewer and fewer NWs bridge the gap, the electrical resistance at the contacts increases due to increase electron scattering at the contact as equivalently observed with decreasing NWs size [10]. For ≈ 1 contacted NW, the resistance at 10-11 V is lower for devices with NW aligned at 10 MHz than at 1 MHz. It also implies that for $R_d = 16 \text{ k}\Omega$, ≈ 1 NW-based device aligned at 1 MHz is less conductive than say a couple of higher quality NWs-based devices aligned at 10 MHz. In the similar voltage range, by considering the resistance of ≈ 1 NW-based device at 10 and 1 MHz, it is possible to extract an approximate number of aligned NWs at 0 kΩ, 22 kΩ and 16 kΩ. At 10 MHz the estimated numbers of NWs are; 16 NWs aligned at 0 kΩ, 12 NWs at 16 kΩ, and 8 NWs at 22 kΩ for ≈ 1 NW aligned at 33 kΩ. At 1 MHz the estimated number of NWs aligned with 16 kΩ is 7 NWs. Those number of NWs are consistent with the optical microscopy images in Figure 4.2.

Additionally, the resistivity ($\Omega\cdot\text{cm}$) of ≈ 1 NW-based device (with the resistivity of the contact) has been calculated for NWs collected at 1 MHz and 10 MHz in order to compare them to the resistivity obtained by Sarah Beretta *et al.*.

In their study, using the same Ge NWs growth process, the NWs resistivity was measured using Focused Ion Beam Induced Deposition (FIBID) to contact a randomly chosen Ge NW to platinum and gold electrodes. They found resistivity values of 0.18-0.21 $\Omega\cdot\text{cm}$ ($476.19 - 555.56 \text{ S m}^{-1}$) for 1 single Ge NW [233]. As shown in the graph Figure 4.6, the obtained resistance for 1 NW-based device at 10 MHz is $7.73 \times 10^8 \Omega$ which corresponds to a resistivity (obtained from Ohm's law) of $8.7 \Omega\cdot\text{cm}$. At 1 MHz the measured resistance for 1 NW was $1.55 \times 10^9 \Omega$ which corresponds to a resistivity of $17 \Omega\cdot\text{cm}$. Such a difference can be explained by the measurement technique. Focused Ion Beam induced deposition (FIBID) of Platinum to connect NWs to the gold electrodes allows locale deposition and high-resolution nanopatterning thus resulting in ultra-low contact resistivity [271]. Table A.3.1 placed in the appendix reports the resistivity of single Ge NWs found in the literature from different growth techniques and device fabrications. Compared to resistivity obtained from other techniques the Ge NWs aligned and contacted by DEP at 1 and 10 MHz have promising resistivity. Current response measurements at different temperatures would have allowed investigation of the contact resistance and barrier heights enabling more accurate extraction of the Ge NW resistivity without contact resistivity. Moreover, a second layer of electrodes deposited on top of the current electrodes would have improved contact and reduced resistivity further.

5.2 Optical properties; photocurrent spectroscopy

The photoresponse characteristic of an array and of approximately a single NW device were investigated. Using the spectroscopy setup described in Chapter 2 the device was placed on a stage to receive the incident light beam. The optical chopper was set to rotate at 330 Hz and placed between the monochromator light source output and the device. Illumination was performed with a wavelength from 400 to 1100 nm and a bias voltage of 100 mV was applied. The illumination spot diameter was 1 mm and illuminated the entire device as well as part of the Au electrodes which can not be avoided. The light was shone onto the device perpendicular to the NWs axis alignment and the photocurrent was measured as a function of the photon excitation wavelength giving the spectrum presented in the following graphs. Figure 4.7 presents the photoresponse of an array of Ge NWs aligned with no resistor $R_d = 0 \text{ k}\Omega$.

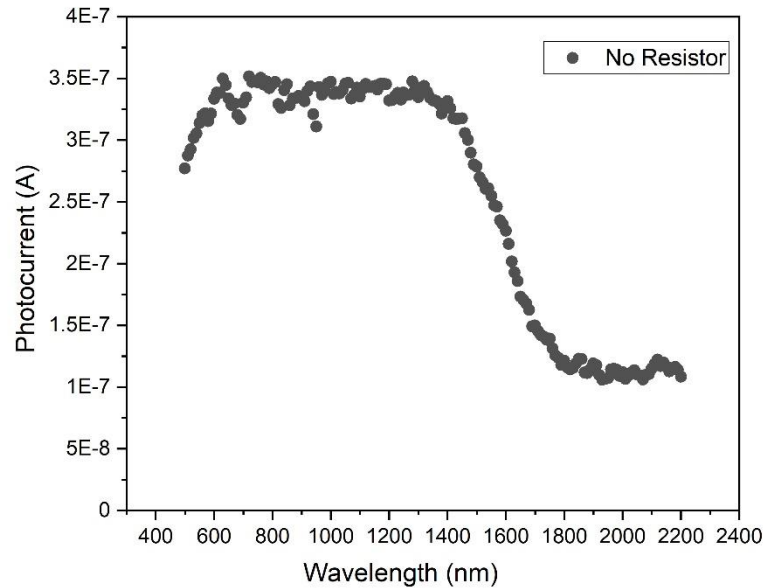


Figure 4.7: Spectral response spectroscopy at room temperature of an array (**black curve**) at a DEP frequency of 10 MHz with a resistor of 0 k Ω (**black curve**).

The photoresponse of an array of NWs was found to dominate under illumination between 600 and 1400 nm in the visible and infrared wavelength with a maximum photocurrent measured at 0.34 μA . For a wavelength converted in increasing energy (eV), the onset photocurrent is from 1550 nm corresponding to 0.8 eV which is the Ge energy band gap. Previously measured Ge-based devices presented in the literature show results that are in correlation with optical results obtained in this study [272]. However, there is a slight difference; for a reference germanium photodetector, as presented in reference [273], the photocurrent dominates over a wavelength of 900 nm to 1550 nm while in this study the photocurrent has an onset from 500 nm. Such broad photoresponse has been observed for Ge material either doped [274], with a Schottky barrier [275], multilayered [276] or strained heterostructure [277].

When the incident light energy is greater than the band-gap of a p-type NWs there is a positive photoresponse (in contrast with a negative photocurrent response for n-type material [6]). Upon illumination, photoexcited free carriers result in the observed photocurrent. As mentioned further enhancement of the photocurrent can either be from impurities at the interface, doping or lowering of the Schottky barrier. For Ge NWs, intensity increases at a wavelength onset of 1550 nm with more carriers released at higher energy until a drop at ≈ 600 nm.

Illumination upon the device and contacts has been largely investigated for NWs and has particularly shown a lowering of the Schottky barrier and an increase in photocurrent [278]. The photoresponse current obtained from ≈ 1 NW is shown below in Figure 4.8.

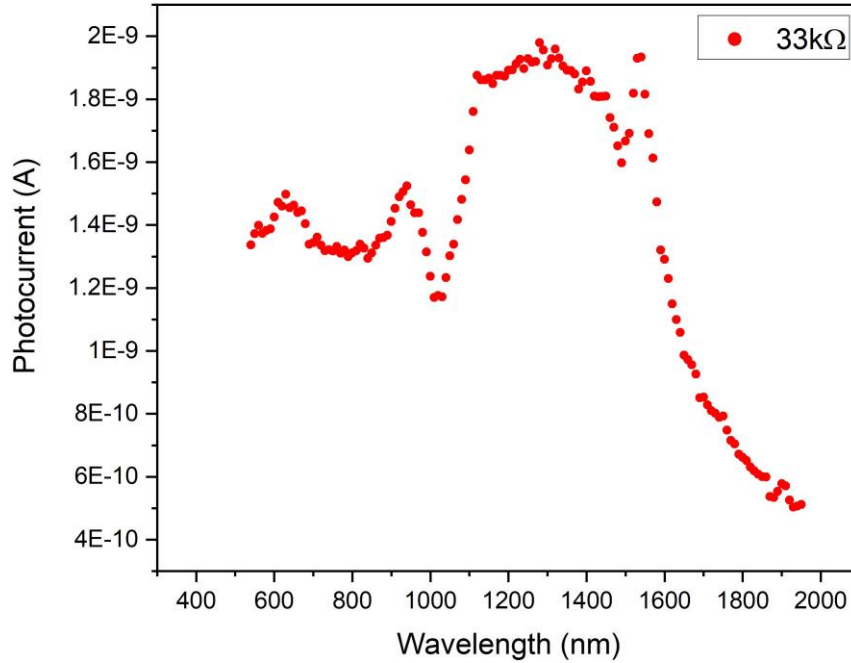


Figure 4.8: Spectral response spectroscopy at room temperature of ≈ 1 Ge NW. The device is fabricated with NWs aligned at a DEP frequency of 10 MHz with a resistor of 33 k Ω .

The photoresponse of a single Ge NW was found to dominate between 1110 and 1540 nm with a maximum photoresponse of 1.9 nA. The spectrum shows a first distinctive valley response between 500-900 nm and a second valley between 1120-1540 nm. A couple of peaks are present with one at 600 nm, a second at 900 nm and a last distinctive shoulder at 1550 nm. The device response suggests higher sensitivity near-infrared. Wavelengths between 780 and 850 nm, 1300 and 1550 nm, are the essential wavelengths of communication with minimum losses and attenuation through glass and fibres, resulting in higher quality, better signal-to-noise ratio and longer potential link distance compared to other wavelengths [279].

Compared to an array of Ge NWs presented in Figure 4.7, the single Ge NW photoresponse Figure 4.8 is in two parts; a region between 500-900 nm with a response of 1.3 nA and at higher photocurrent a region between 1000-1550 nm with 1.9 nA.

Overall the photoresponse is about two magnitudes lower than for an array of NWs but most probably that ≈ 1 NW device is more sensitive. Previous studies on single Ge NW have demonstrated similar high photoresponse in the wavelength range of 1000-1600 nm where it is also shown that it was due to the Schottky barrier between Ge NW and Au electrode [278]. Their photocurrent response for a single Ge NW (NW of 2 μm long and 60 nm diameter) in contact with Au electrodes is consistent with what was measured in this study and suggests that 1 Ge NW is measured. Sett *et al.* [278] highlighted that asymmetrical contact induces increasing carrier conduction because of the barrier separation of carriers avoiding recombination. This characteristic has been observed for metal-semiconductor Schottky contact of ZnO NWs (collected by DEP) between Pt electrodes [280], and single GaAs NW between Au electrodes [281]. As demonstrated, for an array of NWs (with EP shown in Chapter 3) or for ≈ 1 Ge NW aligned, the asymmetrical current response comes from the heterojunction of the device with a graded chemical junction within the NW. Ge(Au)alloy/Ge(core) creates an ohmic contact (or "less Schottky") on one side and an abrupt junction Ge(core)/Au(electrode) resulting in a Schottky contact on the other side. At the Schottky contact and at equilibrium (as shown in Figure 1.19 b) in Chapter 1) builds a layer of negative carriers (electrons) in the semiconductor and positive carriers (holes) in the metal interface forming the energy barrier (in abrupt interface red line). The Schottky barrier height is sensitive to carrier generation and transport. Hence, under illumination generation of electron and hole carriers, and under forward voltage, the applied electric field is opposite to the built-in and lowers the Schottky barrier. This type of asymmetric structure has demonstrated enhanced sensitivity [282] where photocurrent can be produced with no applied bias while symmetric structures have photocarriers in a built-in potential well until external bias is high enough to pass through the barrier [283]. It would have been interesting to measure the photocurrent response of devices fabricated with DEP at lower frequencies in order to analyse how lower-quality NWs would perform under illumination.

The performance of a photodetector is measured by the responsivity that also reflects its sensitivity. The spectral responsivity can be determined by evaluating the incident light power using two different reference diodes of known responsivity. Using Si and InGaAs commercial photodiodes, the responsivity of an array and of ≈ 1 Ge NW has been plotted in the following Figure 4.9. The light spot being larger than the detection area, it is difficult to accurately calculate the incident optical power. The graph Figure 4.9 indicates for ≈ 1 Ge NW (in the red curve) high responsivity of 6.2×10^5 A/W at 700 nm and 5.2×10^5 A/W at 1550 nm. To the best of our knowledge, this is one of the highest responsivity measured for photodetector based on semiconductor NWs.

Such high responsivity for the selected wavelengths of 650-700 nm and 1550 nm have great potential for application within red visible light and optical communication wavelength respectively [284, 285]. Table 5 compares responsivity performances from a couple of studies on single NW for photodetection.

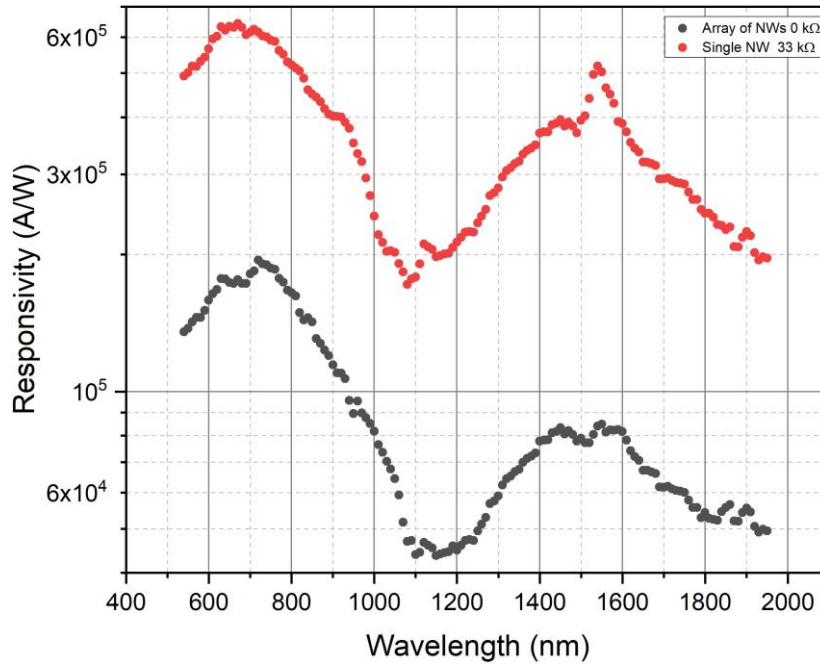


Figure 4.9: Optical responsivity of an array of Ge NWs (in black) and 1 NW (in red). Both devices have NWs aligned by DEP at 10 MHz with no resistor and with a resistor of 33 kΩ in the voltage divider system.

Table 5: Photodetector nanowire-based responsivities found in the literature.

References (doi)	NWs	Synthesis	Dimensions	Contact Method	Responsivity A/W	Wavelength (nm)
This work	Single Ge	MOVPE	$\Theta = 60 \text{ nm}$ $L = 20 \text{ }\mu\text{m}$	DEP	6.2×10^5	700
					5.2×10^5	1550
	Array Ge				2×10^5 8×10^4	700 1550
Sett et al. [332] [278]	Single Ge	MOVPE	$\Theta = 30 \text{ nm}$ $L = 1.2 \text{ }\mu\text{m}$	EBL + top metallisation/random selection	3.6×10^5 3.7×10^7	650 850
Das et al. [333]	Single Si	Etching top-down	$\Theta = 80 \text{ nm}$ $L = 1 \text{ }\mu\text{m}$	EBL + top metallisation/random selection	1.5×10^4	450-1000
Kuo et al. [334]	Single InSb	Electrochemical	$\Theta = 200 \text{ nm}$ $L = 10 \text{ }\mu\text{m}$	EBL/FIB random selection	8.4×10^4	500
Guo et al. [335]	Single InAs	MBE	$\Theta = 40 \text{ nm}$ $L = 10 \text{ }\mu\text{m}$	EBL + top metallisation/random selection	1.9×10^3	1500

Notes; MOVPE=Metalorganic Vapor-Phase Epitaxy, MBE= Molecular Beam Epitaxy, DEP= Dielectrophoresis, EBL=Electron Beam Lithography, FIB=Focused Ion Beam.

The array of Ge NWs (in the black curve) shows less sensitivity with 2×10^5 A/W at 700 nm and 8×10^4 A/W at 1550 nm. This difference with ≈ 1 Ge NW could be due to more scattering from the array of NWs or shadowing from overlapping NWs.

In this study, the high responsivity is most likely originating from multiple physical mechanisms occurring at the NW. Enhanced carrier collection can arise from Schottky barrier lowering (in heterojunction) [278], surface traps at the interface of NWs (for p-type NWs) [275] and optical resonance can originate from spectral selectivity or internal reflection antenna [286]. Control on the chemical composition and morphology of NWs have shown to lead to possible absorption of light leading to optical resonance. Cao *et al.* [227] measured optical resonance from individual Ge NWs of 50 and 200 nm diameter (60 nm diameter in this study). They highlighted spectral selectivity and optical resonance of the NWs at wavelengths of 700, 900 and 1250 nm where they also measured maximum response. Using the photocurrent response Figure 4.8 and responsivity Figure 4.9 one can speculate that the devices feature optical resonance. A possible way to confirm the latter would have been to measure the NWs horizontally and vertically with a reflectance system in cross-polarisation in order to determine the absorption of the NWs as a function of the wavelength [287].

It was explained that the Schottky contact at the junction Ge(core)/Au(electrode) was an asset due to the carriers' separation and lowering of the barrier by the photogenerated carriers.

During the photogeneration of carriers, and under forward bias with negative electrodes at the Schottky contact, possible recombination of the carriers is reduced by the oxide layer at the Ge/GeO₂ interface.

Indeed, the shallow trap states highlighted by SCLC in Chapter 3 capture photogenerated electrons separating and prolonging free holes' lifetime to reach electrodes resulting in an increase of photocurrent. As a consequence, it is possible that the photodetector NW device can perform photocurrent response without the need for external bias voltage [288].

Conclusion

In summary, the possibility of a single NW alignment has been demonstrated, based on a voltage divider coupled with DEP alignment. Although the system could have been improved with further filtration and concentrations investigation of the NWs solution to avoid entangling, reaching 1 single NW between electrodes by DEP is shown to be easier than for most of the existing techniques. Such NWs entanglement could come from branched NWs that are formed during growth upon seeds disturbances like sudden temperature variations [289]. Moreover, coupled with the selectivity performances of DEP, it is possible to select the length and crystal quality from a batch of NWs. With increasing resistance (Rd) in the voltage divider setup and without EP, aligned NWs in the device lead toward a heterojunction system, asymmetric diode-like behaviour. Using optimum DEP parameters, it was estimated that at the highest frequency of 10 MHz and with a voltage of 8 V_{peak-to-peak}, ≈ 1 Ge NW device has a resistivity of 8.7 Ω.cm against 0.18 Ω.cm obtained from the same growth but with a device fabricated with a randomly chosen NW contacted by Focused Ion Beam Induced Deposition. Although Ge NWs have been very scarcely studied via DEP the obtained resistivity is promising and shows DEP considerable interest in nanotechnology implementation.

Photodetection performances of an array and ≈ 1 Ge NW are investigated. It was shown that ≈ 1 Ge devices have high responsivity of 6.2 x 10⁵ A/W at a wavelength of 700 nm and 5.2 x 10⁵ A/W at 1550 nm against 4 to 7 magnitude lower for an array of Ge NWs and more than 10 orders of magnitude lower for bulk Ge photodetector [290]. Arising from the Schottky heterojunction of the NWs structure and traps, such responsivity in a photodetector is of great interest for photonic and telecommunication applications where specific radiations need to be detected. Moreover, single NW has potential in applications like single photon detectors and single molecule chemical sensing. This highlights the potential of DEP coupled with a voltage divider system. While keeping DEP selection properties the possibility to further control the alignment rate has promising development over the future collection and entailing performances.

Chapter 5

Germanium nanowires-based biosensor device

Introduction

It was confirmed in the previous chapters that the use of DEP enables the self-alignment of NWs across a pre-defined electrode gap and also offers the possibility to select ensembles of NWs with desired properties for a given application. Moreover, it is low-cost and permits the rapid fabrication of devices [2]. The selection of NWs properties from within the ensemble results in devices having much more reproducible performance from batch to batch. This is of particular importance when looking to use such devices as the active element for bio-sensing as it removes the requirement for calibration for individual sensors, reducing the cost and complexity of the final sensor system. In the previous chapter, aligned NWs at high frequency were showing increasing carrier mobility. Additional devices fabricated with optimum parameters validated their repeatability.

While biosensor FETs have previously been demonstrated from NWs, in this work 3 distinct changes have been made. Firstly, nearly all previous NW-based immuno-FETs have used Si, however, in this work, Ge NWs are used. Compared to Si, the high carrier mobility of Ge NWs and smaller band gap are anticipated to result in enhanced sensitivity to protein binding events. Other advantages of Ge in comparison with Si include higher carrier injection velocity and lower temperature growth and processing, making its choice attractive for the development of CMOS-compatible devices [291]. Secondly, the use of DEP offers the possibility of rapid fabrication, while maintaining reliable and repeatable performance between devices. The third difference is in the use of smaller aptamers rather than antibodies to attach the target protein, as previously discussed in Chapter 1 this should result in the protein being located closer to the surface of the NWs and hence in a larger variation in the channel conductivity. In summary, the following chapter establishes the feasibility of the application of DEP used as an easy and reliable way to fabricate nanowire devices that can be used for biosensing. Functionalised Ge NWs directed towards selective detection of the protein of SARS-CoV2 as an example target of rapidly emerging threat is envisaged as a principle that can be extended to any protein.

The sensor devices were fabricated using the alignment parameters investigated in the previous Chapter 1. Based on these results, a DEP frequency of 10 MHz was used for all subsequent devices fabrication with no offset applied (no EP) and investigation for the potential use of these devices as biosensors.

5.1 Characterisation of the functionalisation layers by Raman spectroscopy

Once the optimum DEP parameters had been determined, a series of fresh devices were fabricated to investigate their functioning as potential biosensors. After the DEP process, the aligned NWs were functionalised in order to attach the binding element to their surface. The aptamer probe molecule was attached to the Ge surface using a silanisation method detailed in Chapter 2 and also described in reference [212].

To verify that the functionalisation had been successful and that the aptamer layer is attached to the NWs, Raman spectroscopy scans were performed on the NWs. After each deposited layer, a scan was performed. To qualitatively characterise the step-by-step functionalisation of the Ge NWs device, Raman spectroscopy has been used (technically described in Chapter 2). The main issue encountered with this kind of spectroscopy is the interference of inherent fluorescence caused by certain types of molecules which can influence the measurement process and, in turn, the interpretation of the ensuing bands. The analysis was carried out after each step of the functionalisation process using an inVia Reflex Qontor Confocal Raman Spectroscope (Renishaw, UK). The analysis of the NWs was performed using a 532 nm laser with 3 mW power and 10 s exposure time with a 100X objective. Each spectrum consisted of 7 scans in the range of 150 to 3500 cm^{-1} . The glass signal was automatically and systematically removed using WIRE-5 software (Renishaw, UK). As a guide, molecular schematics have been added to the spectras and are represented in the appendix from Figure A.4.1 to Figure A.4.3.

More details on Raman spectroscopy can be found in Chapter 2. The presented graphs are the resulting analysis of the step-by-step functionalisation.

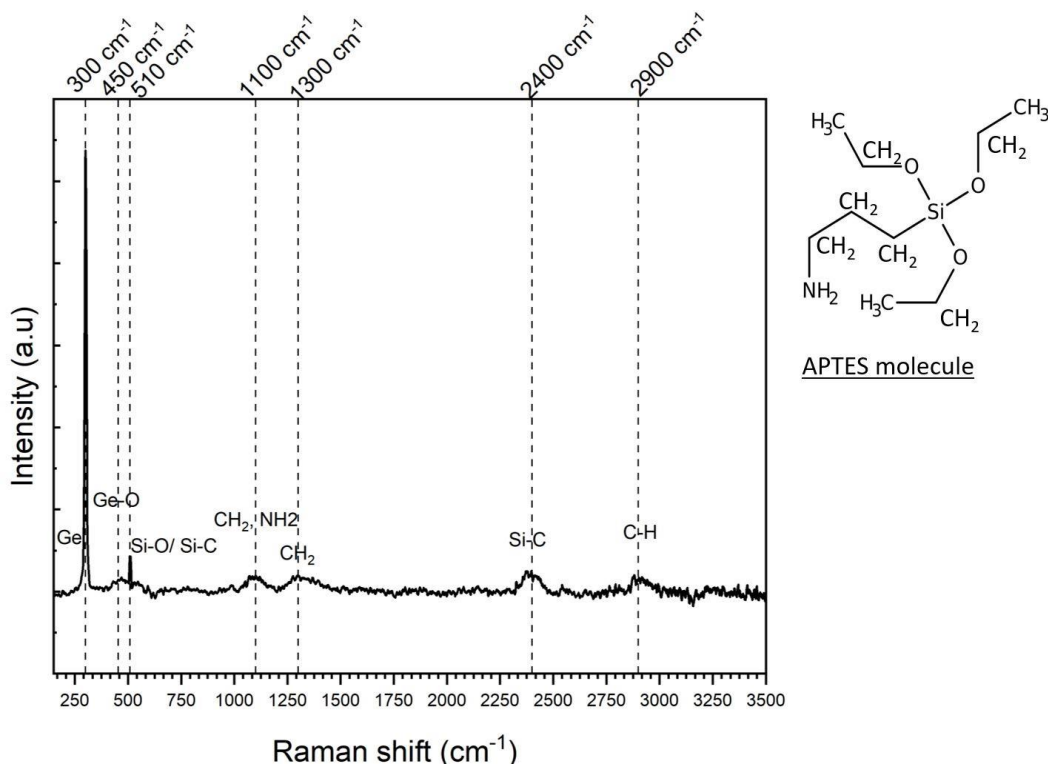


Figure 5.1: Raman spectra of the aligned Ge NWs after silanisation and a chemical representation of the 3-aminopropyl-triethoxysilane molecule.

Figure 5.1 shows the Raman spectra of the first step of functionalisation; Ge NWs with silanisation layer (APTES molecules) in the same conditions mentioned above in the 150-3500 cm⁻¹ range. The vibrational band observed at 300 cm⁻¹ is attributed to crystalline Ge and 450 cm⁻¹ corresponds to Ge-O from silane bound to the oxide of Ge.

The band observed at 510 cm⁻¹ can be attributed to the stretching mode of Si-O and Si-C ($\nu(\text{SiO})$, $\nu(\text{SiC})$) and at 1100 cm⁻¹ the band corresponds to the CH₂ ($\gamma(\text{CH}_2)$) twisting and rocking of NH₂ ($\delta(\text{NH}_2)$). Lastly, at 1300 cm⁻¹ the vibration mode is the specific scissoring of CH₂. Above 2000 cm⁻¹ the two bands reveal stretching modes of Si-C and C-H bonds at 2400 cm⁻¹ and 2900 cm⁻¹ respectively [292]. After silanisation, a layer of glutaraldehyde (GA) is deposited and acts as a linker that binds with the amine-terminated silane and provides an aldehyde binding group for the amine-terminated aptamer sequence.

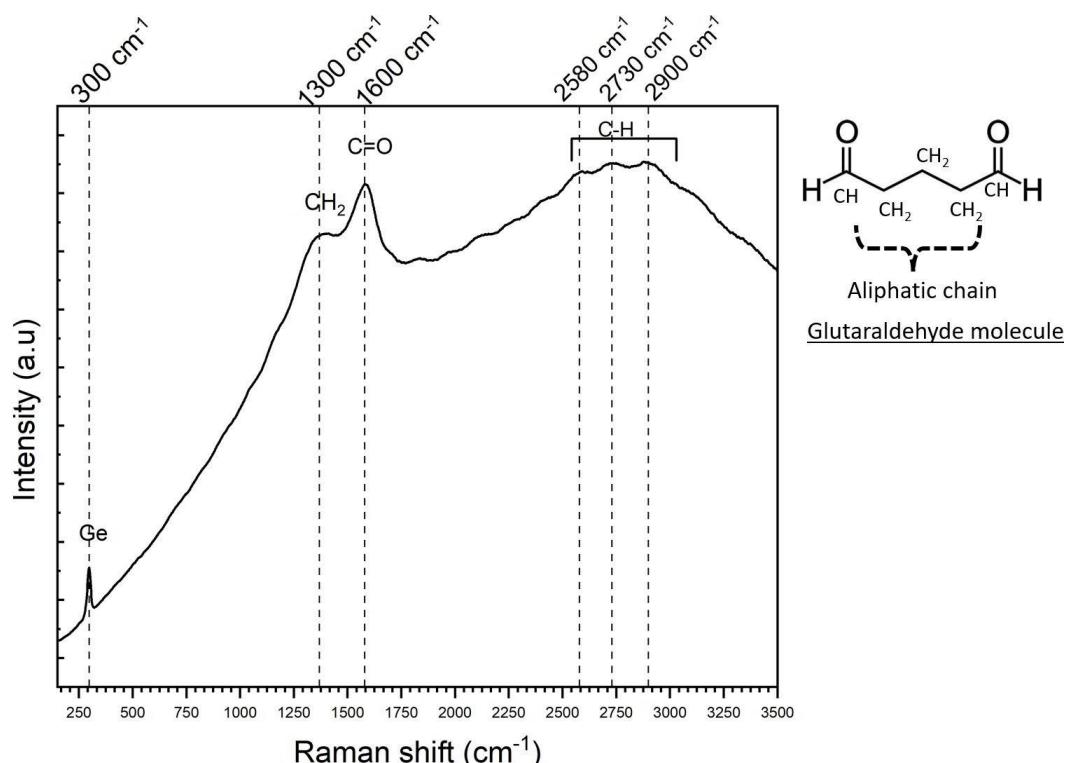


Figure 5.2: Raman spectra of the aligned Ge NWs after silanisation and glutaraldehyde mono-layer. On the right is a chemical representation of the glutaraldehyde molecule.

The obtained Raman signal presented in Figure 5.2 shows several bands that can be attributed to the GA layer. The Ge band at 300 cm^{-1} is still present. CH₂ stretching band at 1300 cm^{-1} and the 3 bands at 2580 , 2730 and 2900 cm^{-1} from the aliphatic chain have been detected despite the signal deformation. The deformation of the signal is due to the presence of fluorescence that prevents discerning clearly APTES and GA. Nevertheless, the newly observed C=O vibration at 1600 cm^{-1} is a characteristic band from the GA. Impurities from the sample or the free aldehyde group (C=O) can be the cause of the significant fluorescence background which visibly overlaps Raman bands. Nonetheless, it was still possible to detect specific bands and it is further proof of the presence of GA [293].

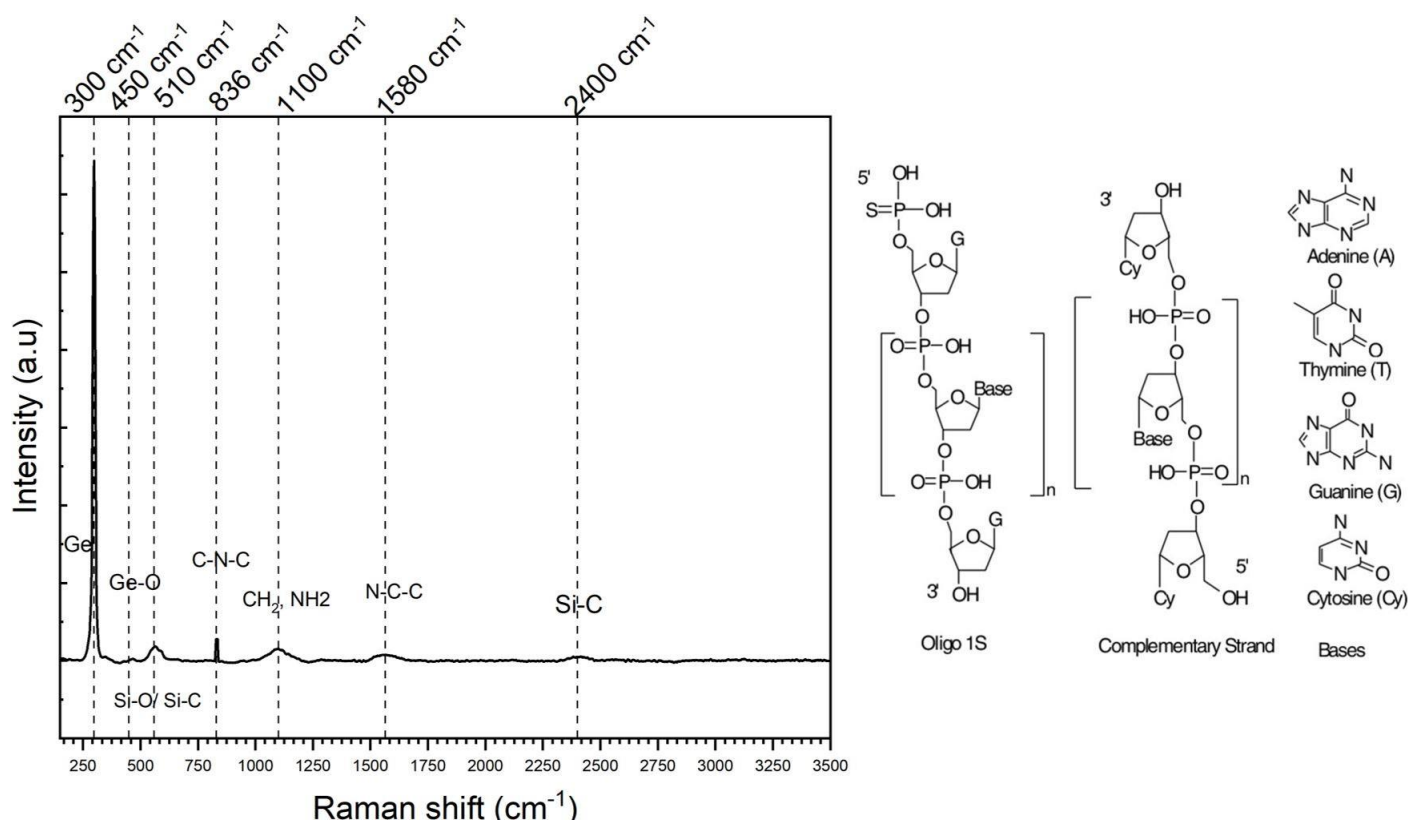


Figure 5.3: Raman spectra of the aligned Ge NWs after complete functionalisation; silanisation, glutaraldehyde and aptamerisation final monolayer. On the right are the chemical representations of protein molecules and their bases.

Because of their complex nature and size, DNA, proteins and aptamers are usually analysed using Surface Enhanced Raman Spectroscopy (SERS) with which detection and recognition are more sensitive and accurate for those particular molecules. Nevertheless, using standard Raman spectroscopy, identification of the aptamer layer and thus the complete functionalisation was possible to evidence. Several of the previous bands detected from the silane layer are again revealed by spectroscopy. The symmetrical stretching mode C-N-C of the amino acids (bases) is observed at 836 cm^{-1} (strong vibrational signal) and the weak band observed at 1580 cm^{-1} is also a fingerprint for aptamer and corresponds to the N-C-C bending, it can also be associated to aromatic ring band vibration of amino acids [224]. A table put in Appendix A.4.4 summarises the functionalisation molecules and their band vibration positions. Once the bio-functionalisation layers were highlighted the devices were tested for their responsivity to increasing concentration of spike protein of SARS-Cov2.

5.2 I(V) with increasing spike protein concentration

To investigate the biosensor properties, increasing concentrations from 1 μM to 1 nM (with $M = \text{mole.L}^{-1}$) of spike protein (Cambridge BioScience spike protein) dispersed in PBS were drop-casted onto the sample and the current-voltage response was measured after each exposure. For all concentrations, a droplet of 4 μL was deposited on the functionalised NWs and left for 15 minutes, the sample was then washed using PBS to remove any unbound protein and gently blow-dried with nitrogen prior to measurement. Until complete functionalisation, and after exposure to the spike protein concentration the NWs are exposed to water from the functionalisation and PBS solution. As observed in the previous Chapter 3, water had a negative effect on the Ge NWs; a detrimental reaction cycle of oxidation and dissolution that leads to the destruction of the NWs. However, it was shown that silanisation (APTES) on semiconductors provides a protective barrier to water [145] resulting in a passivating shell. Hence, to determine that the functionalised NWs were stable and did not suffer dissolution, a functionalised device was exposed to PBS for increasing lengths of time and the current-voltage response was collected using a probe station system at room temperature in air, with no change in the electrical performance being detected (see appendix Figure A.4.5). A further 4 devices were fabricated using the same procedure, IV curves were taken after functionalisation and upon exposure to increasing concentration of spike protein. Figure 5.4 shows the resultant IV curves of one device for each concentration, along with a functionalised device without spike protein exposure used as a reference (black curve).

After the device is functionalised, a significant reduction is observed in the current response at all biases compared to the non-functionalised device from $5 \times 10^{-8}\text{A}$ down to $1.50 \times 10^{-10}\text{A}$ as observed in Figure A.4.6 placed in the appendix. The presence of the aptamer layer on the NWs has introduced a positive charge distribution across the nanowire surface, which resulted in the attraction of electrons (to reach equilibrium) and induce charge depletion within the NWs and the observed current reduction. Positive surface charge on the NWs results in the depletion of charge carriers (holes) in the p-type Ge NWs, leading to a reduction of the current response. As known, additional charges at the surface induce opposite charges within the semiconductor channel. Hence, conversely, for attachment of negatively charged molecules, there is an accumulation of charge carriers (holes) in the p-type channel leading to an increasing current response [3]. It was mentioned in previous research showed in Chapter 1 that APTES and GA layers are negatively charged, which supports that the final aptamer layer is positively charged and dominates the surface charge.

Depletion from positive charges has previously been modelled by adding p-type charges (positively charged) to the surface of the Ge NWs [88] and as such supports that the overall net charge from the functionalisation layer used here is positive. Despite a final rinse having taken place after the functionalisation step, there may be still some residual trapped salt from the PBS near the surface of the NWs causing increased noise. That is why the presented curves have been smoothed using standard polynomial regression.

An increase in the measured current is observed at all biases upon exposure to the spike protein. This is due to the binding of the spike protein to the aptamer, resulting in a change in the charge distribution at the surface of the NWs reducing the initial depletion. The relative noise in the current measurements reduces as the spike protein concentration is increased. The spike protein binding to the aptamer results in negative potential at the surface and results in the accumulation of carriers (holes) within the NWs ensuing in an increase in the current response [294]. As explained the functionalisation layers act similarly to a gate electrode in a conventional FET device; with negative gate voltage in the case of the spike protein.

To further examine and quantify the changes in current with the concentration of the spike protein, the relative change in source-drain current at a fixed bias point (2 V) is plotted as a function of the concentration in Figure 5.4 b). The parameter ΔI is used to analysing the relative change in the current and is given in equation (5.1) below.

$$\Delta I = \frac{I - I_0}{I_0} \quad (5.1)$$

Where I is the measured current and I_0 is that measured at the same voltage in the $I(V)$ characteristic without the presence of the target spike protein. While a bias of 2 V is used here, a similar effect is seen for all bias points measured (positive and negative). Figure 5.4 b) gives the mean value for four devices at the same bias of ± 2 V, with the error given as one standard deviation. Three regimes can be identified across the concentration range. Between concentrations of 1 aM (10^{-18}) to 100 fM (10^{-13}), there is a clear increase in the measured current as the spike protein concentration is increased, with an increasing gradient of 5.1 ± 0.9 for the +2 V points and 6.3 ± 0.8 for the -2 V points across this range.

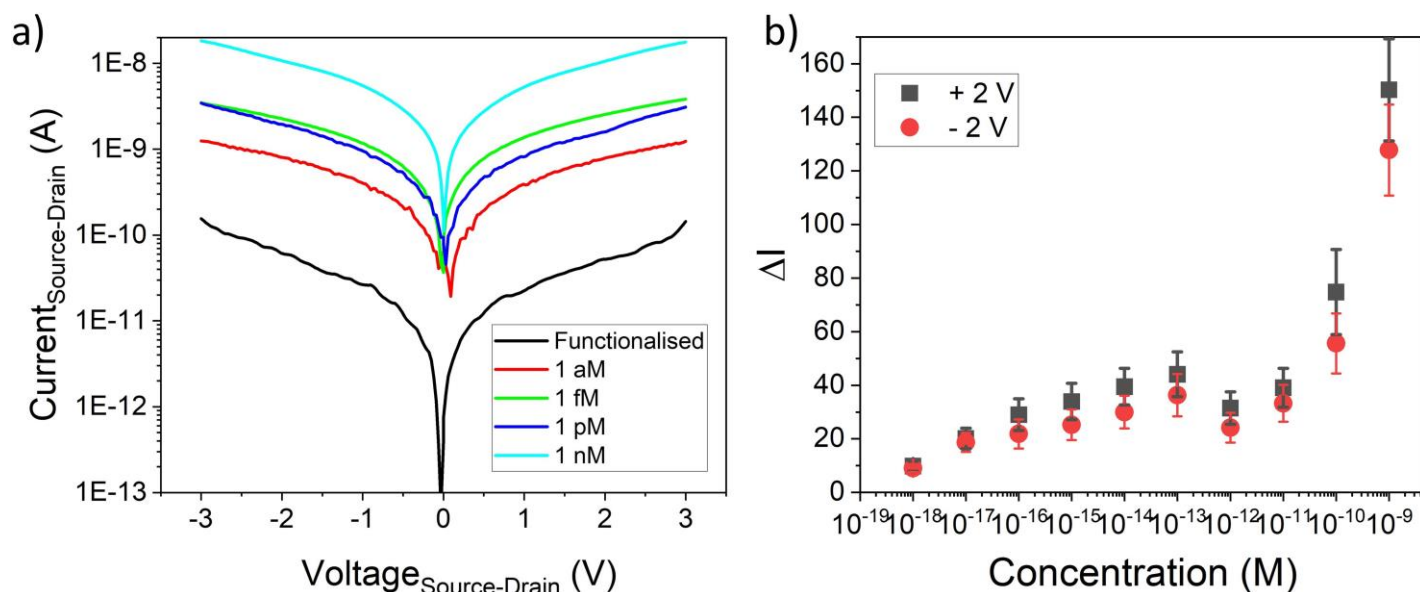


Figure 5.4: (a) IV characteristics of as fabricated Ge Nanowire FETs, after functionalisation and exposure to increasing concentrations of the spike protein from 1 aM to 1 nM. All devices were fabricated with a DEP frequency of 10 MHz. (b) shows the relative increase in the source-drain current, relative to a functionalised device at a bias of $V_{DS} = 2$ V. Response has been measured from 0 to 3V and in reverse from 0 to -3 V.

This indicates that over this range the amount of protein binding to the aptamers is increasing, resulting in a changed surface potential and hence a change in the measured current. Between a concentration of 100 fM (10^{-13}) and 10 pM (10^{-11}) a saturation region is observed, this seems to indicate that once a concentration of 100 fM (10^{-13}) has been reached all the aptamers bound to the NWs have now also bound to a protein and as such, no further change occurs in the surface potential. For concentrations above 10 pM (10^{-11}), a very sharp and sudden increase in the current is then observed, the origin of this mechanism is not clear. However, it may be that at such high concentrations, current can travel directly through the protein layer itself. An alternative explanation may be that as the entire substrate is functionalised (glass and NWs) a conduction path has now been formed around the NWs by the protein/aptamer layers, or that charges transfer through proteins allowing NWs to transfer charge between themselves.

To ensure the changes in the IV response are due to the protein binding and are repeatable, two reference control devices were made. As for Figure 5.4 b) the relative changes in source-drain current at a fixed bias point (2 V) are plotted as a function of the concentration for the two references. Firstly, a reference with no NWs and just functionalised electrode gap is used to verify that the current measured is due to the NWs and not charge transport through the functionalisation layers. The first reference plot Figure 5.5 a) exhibits no measurable changes at increasing spike protein concentration.

It demonstrates that the gap is not being bridged by the functionalisation layer bound with spike protein. The response strongly increases where the current travels directly through the functionalisation and protein layers from a concentration of 1 nM (10^{-9} M) similar to the functionalised NWs that have a much higher relative increase as they are more sensitive devices. Secondly, to determine the specificity of the aptamer functionalisation on the NWs, reference devices were tested in Bovine Serum Albumin (BSA) instead of the spike protein of the SARS-CoV2 and put Figure 5.5 b). BSA is a standard non-targeted protein commonly employed as a negative control for antibodies or aptamer selectivity. The NWs device fabrication and functionalisation steps were exactly the same only the protein was changed.

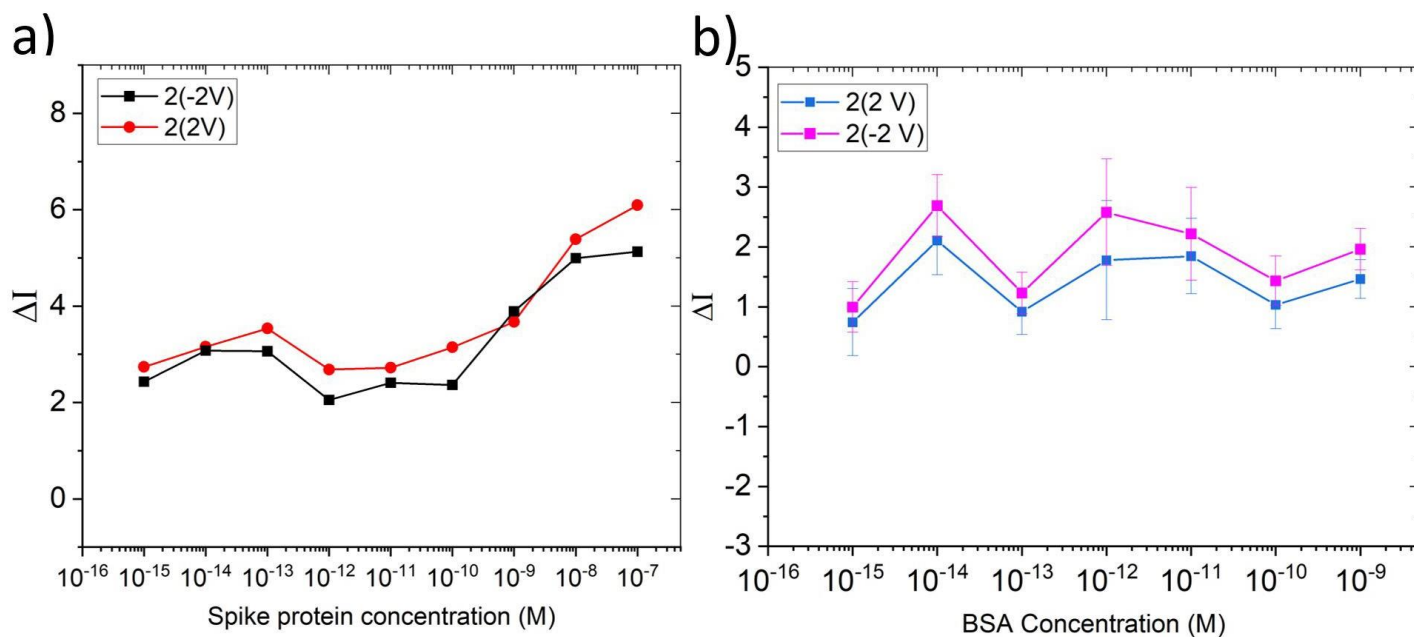


Figure 5.5: Control reference devices showing the relative variation in the source-drain current to a functionalised device with a) no NWs at a bias of $V_{DS} = 2$ V and b) functionalised NWs and increasing concentration of BSA protein at a bias of $V_{DS} = 2$ V.

The signal response obtained from the devices tested with BSA exposure (b) highlights the selectivity of the aptamer towards its binding with the spike protein of SARS-Cov2. Indeed the devices showed negligible response with increasing BSA concentration attesting to no bonding event. To push further verification on the selectivity it would have been interesting to test the functionalised NWs with a real solution of the SARS-CoV-2 virus as well as a reference virus.

As a deduction, the current measured here in Figure 6.4 is due to conduction through the NWs and the changes with spike protein concentration caused by the variation in the surface potential.

Previous simulations on Ge NWs have shown that molecular charge transfer can occur from the surface of the nanowire, resulting in an enhancement of around 300% in the current [88]. The results suggest that a similar transfer of charge may be occurring from the proteins to the nanowires.

Conclusion

It was demonstrated that it was possible to extend the functionality of NWs aligned by DEP to the domain of bio functionalisation with a very encouraging outcome. Following a step-by-step functionalisation using aptamers as the recognition element, the different layers were qualitatively characterised by Raman Spectroscopy. Exposure to increasing concentrations of spike protein resulted in a distinct increasing signal with a LoD of at least 1 aM in a working range of 1 aM to 100 fM. Moreover, the performance of the functionalisation was testified by references; with no NWs but with a functionalised gap and references with functionalised NWs exposed to a negative control protein. From previous biosensing work using such spike protein, the following limits of detection have been found; 0.220 pM with a working range of 0.1 pM to 1 μ M using functionalised gold nanoislands [295], 2.06 aM [296] with a working range of 2.06 aM to 20.6 fM using functionalised graphene as a channel in FET, and 51.44 fM using functionalised thin film as the FET channel [297].

While most of the studies have been working with silicon NWs for biosensing, in general, [298], this work brings out the possibilities that Ge offers without the need for oxide removal. Coupled with DEP it allows the selection of high-quality NWs with the possibility of fabricating heterojunction for heterostructured NWs. There have been several other reports recently looking at FET-based biosensors for the detection and monitoring of COVID-19 [296, 299]. These have all shown similar responses in terms of sensitivity to spike protein concentrations. Our previous work [300] is the most similar to the results reported here, in terms of using aptamers rather than antibodies and performing the measurements in the air rather than in liquid.

The key difference in this work is in the use of Ge NWs as the active channel rather than bulk silicon. Compared to our previous results the use of NWs has resulted in an enhanced sensitivity with an increased current being observed at 2 orders of magnitude lower concentration here. The likely reason for this improved sensitivity is due to the smaller surface area of the NWs compared to a large FET area. A single-bound protein represents a larger relative charge on the device. By extrapolating this, one could anticipate that a single nanowire device would provide the ultimate limit in terms of sensitivity. It would have been interesting to functionalise a single Ge NW using the voltage divider system presented in Chapter 4.

This analysis could have been insightful on the optimum limits of detection per NWs as a function of the concentration. Moreover, functionalised Ge NWs aligned at a lower frequency than 10 MHz would have provided more information on the detection capability with NWs of lower conductivity and higher numbers.

In the previous chapter, the potential of DEP for NWs-based device fabrication was established. DEP could i) select NWs length relative to chosen electrode gap, ii) place NWs on predefined electrode designs and most of all iii) DEP could select enhanced electrical properties of NWs. It was found that it was possible to take further nanoparticle manipulation by combining DEP and EP. As discussed earlier, nanowire-based bio-FETs that have been reported to date have either used drop-casting of dispersed NWs between contacts or expensive nano-fabrication to realise devices. Here, it has been demonstrated that DEP offers viable advantages of label-free, noninvasive and low-cost alternative approach to fabricated nanowire bio-FETs yielding reproducible and reliable device performance. Considering biosensors more generally, this work demonstrates that aptamers have the potential to act as specific binding elements, which could potentially be extrapolated to a large number of possible target proteins and molecules. The upshot, combining these with NWs offers the possibility to achieve nano-scale sensors with high sensitivity and the possibility of improving nanoscale building blocks of integrated electronics.

Chapter 6

Dielectrophoresis implementation for GaAsBi nanowires-based device

Introduction

GaAsBi is one of the compound materials that has attracted great interest due to their potential for optoelectronic device integration. Because of its considerable band gap engineering and reduction [204]. Bi incorporation in GaAs allows such alteration of band structure where Bi level situated below GaAs valence band rises the valence band to an upwards bowing. Bi % band gap reduction allows the reduction of Auger recombination (non-radiative energy loss recombination that increases threshold voltage) [301]. As the gap is smaller, the excess energy from the electron-hole recombination is easier transferred to electrons or holes from the valence gap. Yet, the large lattice mismatch between GaAs and Bi makes epitaxial growth difficult with defects affecting the surface quality of films for instance [302]. As known, nanowires during growth have the capacity to adapt to strains thanks to elastic dilatation properties and so NWs are a good structural fit for GaAsBi [303]. Fabricated for the first time by Molecular Beam Epitaxy (MBE), GaAsBi NWs were synthesised by the group of Dr Robert Richards (Sheffield) in Japan. Different parameters such as Bismuth flux pressure and synthesis temperature resulted in three different batches of NWs. It was explained that NWs, because of their 1D geometry feature significant advantages for nanotechnology. It has been shown in the previous chapters that dielectrophoresis (DEP) enables precise control of NWs as well as unique properties of selectivity. Interestingly, NWs present different morphology and chemical structure according to their growth parameters like an increasing amount of chemical material within the growth chamber. It was shown in Chapter 3 that the chemical structure and surface of the NWs played an important role in their contact configuration with the electrodes but also with the final electrical properties. Although it is an understudied area, NWs surface is a key factor when it comes to any kind of science applications and electrical devices integration. Therefore, this chapter presents the uncommon GaAsBi NWs grown with different parameters resulting in surface morphology. The application of DEP on different surface morphology NWs is investigated with the aim of exploring for the first time the properties of the resulting devices.

6.1 Characterisation of the nanowires

6.1.1 Morphological and chemical characterisation of the nanowires

Scanning and Transmitted Electron microscopy analysis

Following the synthesis by MBE (detailed in Chapter 1), three batches of NWs were characterised by Scanning Electron Microscopy (SEM) and Energy Dispersive X-ray Spectroscopy (EDX) in order to define their dimensions, morphology and chemical nature. Small pieces of the synthesised NWs directly on substrates were placed in the SEM chamber for analysis. The analyses have been summarised in the following figures; the obtained SEM images are presented in Figure 6.1 and the EDX chemical mapping is in Figure 6.2. On the upper right of the figures, a table summarising the batch growth parameters has been put as an indicator.

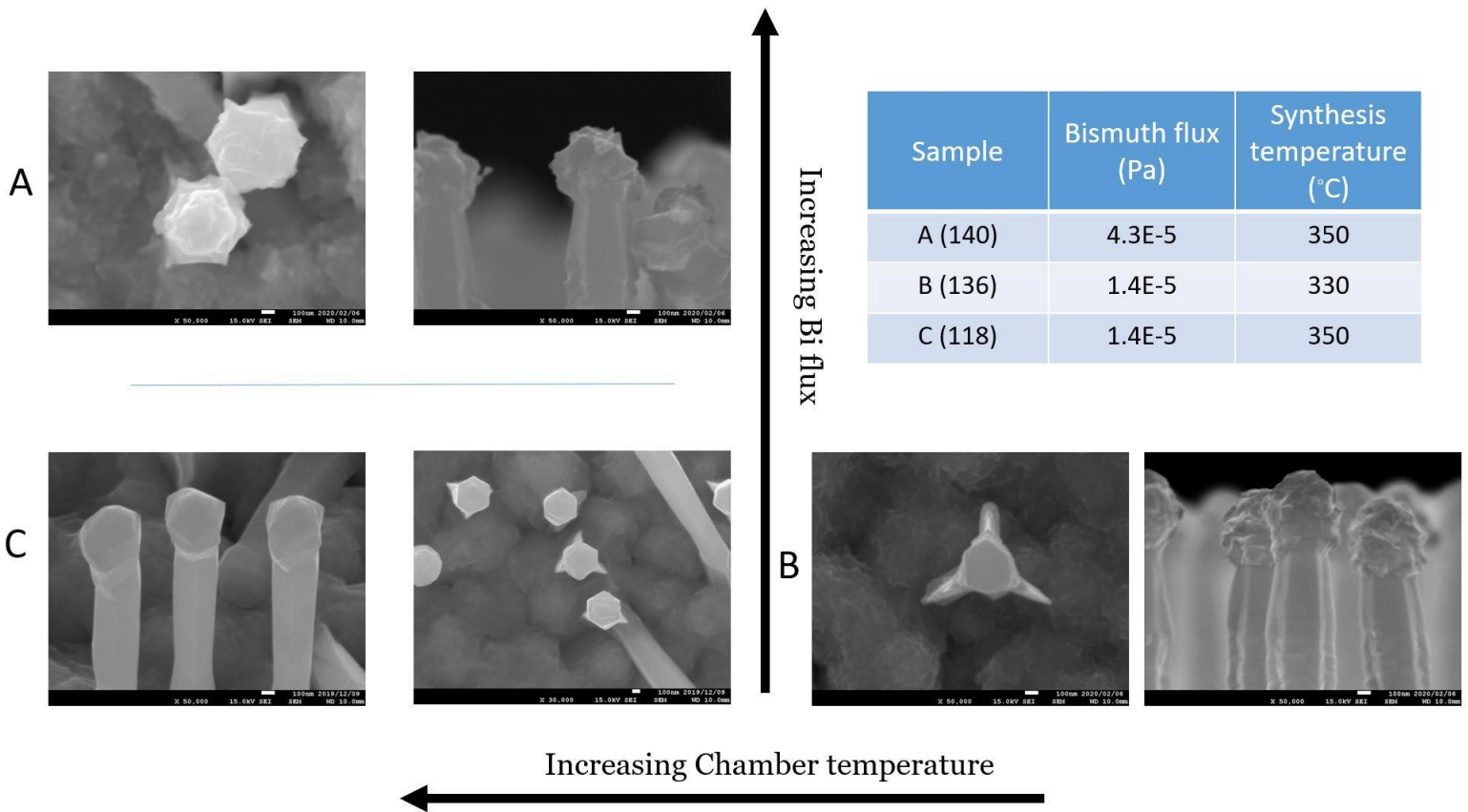


Figure 6.1: SEM images of the three different GaAsBi NWs morphology A) NWs fabricated with a Bi flux of 4.3×10^{-5} Pa and synthesis temperature of 350°C B) NWs fabricated with a Bi flux of 1.4×10^{-5} Pa and synthesis temperature of 330°C , C) NWs fabricated with a Bi flux of 1.4×10^{-5} Pa and synthesis temperature of 350°C .

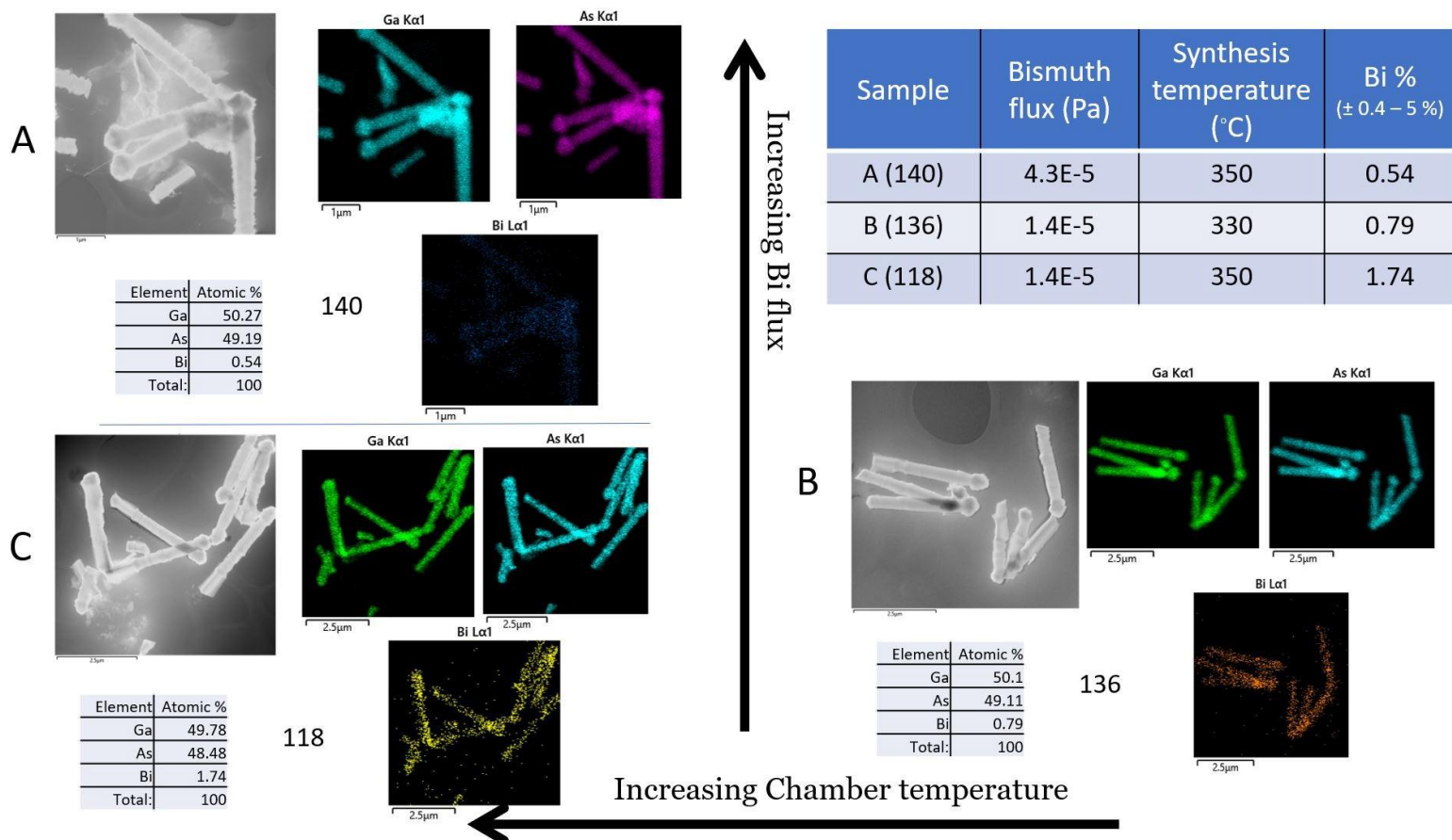


Figure 6.2: EDX chemical mapping of the three different batches of GaAsBi NWs.

All the NWs are measured by SEM to be of $L = 3-4 \pm 0.5 \mu\text{m}$ long with an average diameter of $\varnothing = 450 \pm 5 \text{ nm}$. As synthesised the NWs presented no oxide layer. GaAsBi NWs were synthesised using Ga nanoclusters/seeds and presented a tip of a well-mixed GaAsBi compound according to the EDX mapping Figure 6.2. Batch C with low Bi flux demonstrated the highest amount of Bi % with 1.74 % conforming to EDX analysis shown in Figure 6.2. However, it should be stressed that the EDX chemical analysis accuracy has a percentage error of $\pm 0.4 - 5 \%$.

Interestingly, all three batches have very different surface morphology than the Ge NWs that had a more "needle" shape morphology. Batch A, B and C have in common a protuberance round shape at the tip probably originating from the nanoclusters/seeds. Batch A and B have generally similar morphology with a noticeable coarse triangular core along the NWs of B (Figure 6.1). More details on the morphology can be seen in the appendix on SEM images A.5.1 to A.5.3. At equal Bi pressure but higher temperature than B, C presents overall a more smoothed core morphology with fewer asperities as seen in appendix Figures A.5.2 to A.5.3. Although quite like B, C also presents a coarse triangular shape at the base.

One could argue that in the growth system of GaAsBi NWs a lower Bi flux and increased temperature most probably would lead to smoother surface morphology but can also lead to a triangular base [119]. Essouda *et al.* [194] grew by MOVPE GaAs NWs with a GaAsBi shell that exhibited similar corrugated surface morphology.

Raman Spectroscopy Characterisation

The chemical nature of the GaAsBi NWs was also confirmed by Raman Spectroscopy. The sample consisted of the as-grown GaAsBi NWs transferred on a glass substrate by gentle scrubbing. The experiment was carried out using an inVia Reflex Qontor Confocal Raman Spectroscope (Renishaw, UK). The analysis of the NWs was performed using a 532 nm laser with 3 mW power and 5 s exposure time with a 100X objective. The 532 nm laser provides a circular analysing spotlight of 0.8 μm diameter. Each spectrum consisted of 5 scans in the range of 150 to 1100 cm^{-1} . The glass signal was automatically removed using WIRE-5 software (Renishaw, UK). More details on Raman spectroscopy are given in Chapter 2. All three batches presented the same Raman spectra and the resulting scan has been put in Figure 6.3.

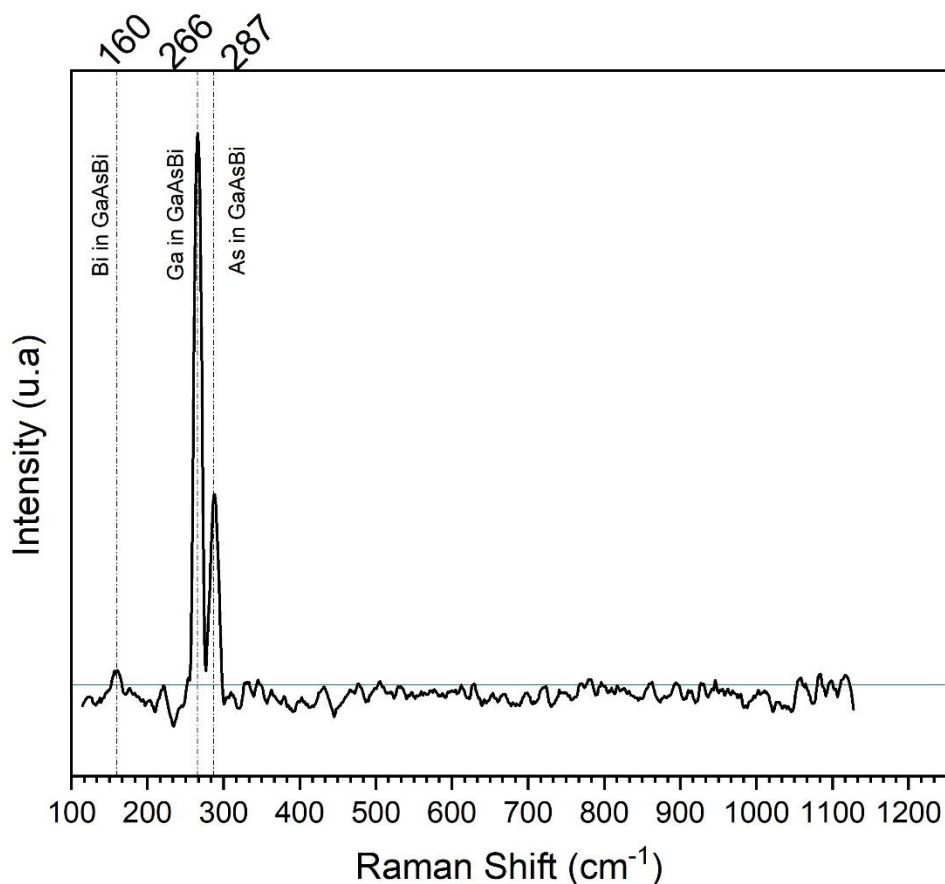



Figure 6.3: Raman Spectroscopy of the GaAsBi NWs.

Taken separately, the signature peaks of Ga, As and Bi measured by Raman spectroscopy at RT are reported at 246 cm^{-1} (Ga), 290 cm^{-1} (As) and 96 cm^{-1} (Bi) [304, 305, 306]. As a compound, GaAs peaks have been measured at 268 cm^{-1} and 292 cm^{-1} [307, 308]. With the introduction of Bi in GaAs, more distortion of the lattice occurs with modification of the electronic cloud and modification of the vibrational peak response. Hence, chemical characterisation of GaAsBi by Raman spectroscopy has shown signature peaks at 180 cm^{-1} , 269 cm^{-1} and 288 cm^{-1} attributed to Bi bond with either to Ga or As, and the two last peaks ($266\text{-}287\text{ cm}^{-1}$) are attributed to GaAs also shifted by the introduction of Bi [309, 310, 311]. Therefore, in the spectrum obtained in Figure 6.3, the peaks obtained at 160 , 266 and 287 cm^{-1} can be associated with the presence of GaAsBi also supporting EDX analysis.

The response at 160 cm^{-1} is a little above the general noise signal and it is probably due to the small amount of Bi% incorporation. The following table 6 summarises the Raman peaks from the literature compared to the peaks obtained from the present work.

Table 6: Raman vibrational peaks from the literature cited above and from the present work.

	Bi (cm^{-1})	Ga (cm^{-1})	As (cm^{-1})
Literature	96	246	290
		GaAs (cm^{-1})	
		268	292
		GaAsBi (cm^{-1})	
	180	269	288
Thesis work	160	266	287


 Raman shift cm^{-1}

6.2 Characterisation of the nanowires in different mediums for dielectrophoresis

6.2.1 Characterisation of the nanowires in anisole

In the same way, as with the Ge NWS, the GaAsBi NWs were tested in anisole for their chemical inertia. In Chapter 3, anisole demonstrated ideal wettability to perform DEP on electrodes microfabricated on glass. Besides, Ge NWs were shown to be in good inertia with anisole after 2 months in solution, their morphology and chemical nature remained unchanged compared to other mediums like deionised water or DMF. Therefore, the same medium was used, and, prepared in anisole the GaAsBi NWs were analysed by TEM to evaluate their inertia and confirm their compatibility. The NWs solution was transferred onto a carbon-coated copper grid using a micropipette. The GaAsBi NWs were not showing morphological changes after 2 weeks and so the analysis was also pushed further to 2 months and the resulting images were put in the following Figure 6.4.

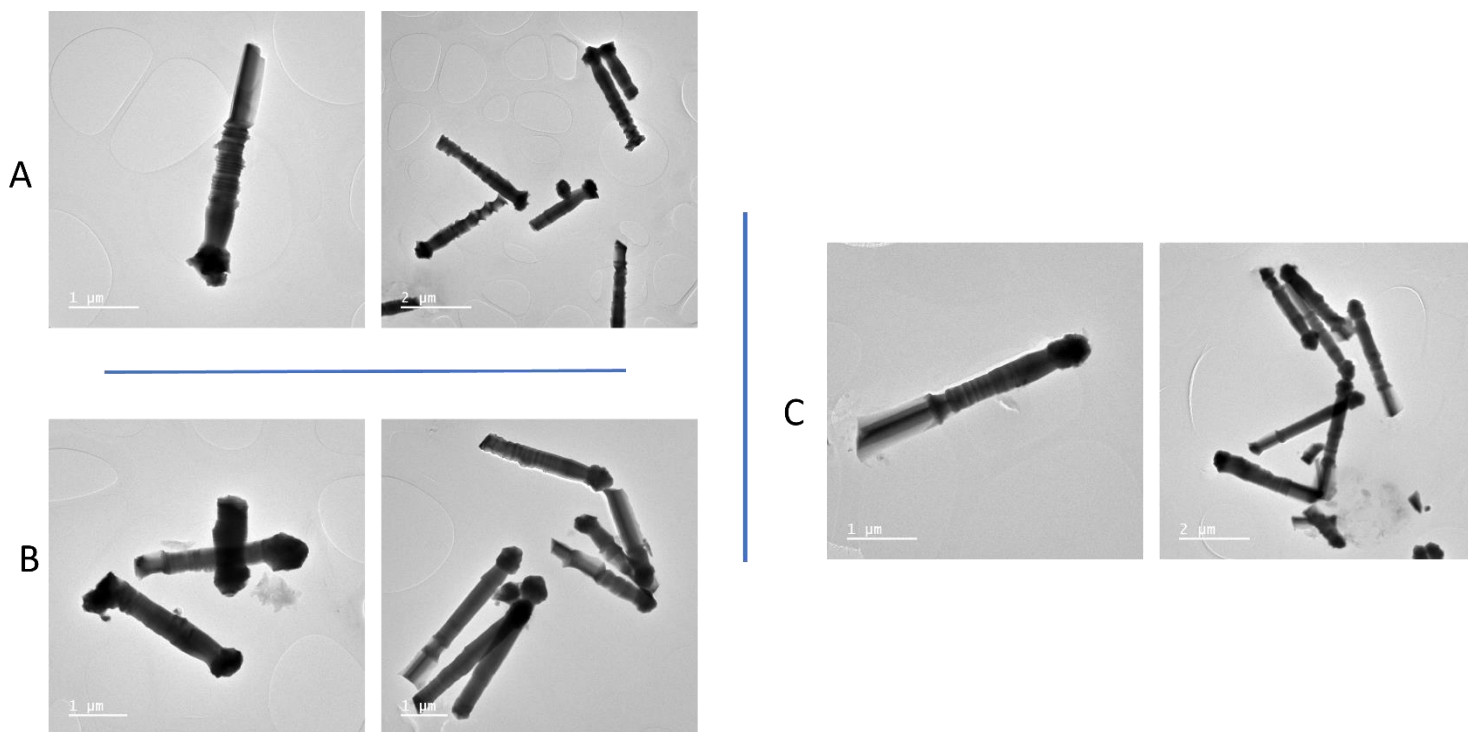


Figure 6.4: Bright field TEM images of the three different GaAsBi NWs batches in anisole after two months in solution. NWs from batches A, B and C are still intact after long storage in anisole.

After two months in anisole, GaAsBi NWs appear to be in good inertia, morphology and chemical state were unchanged if for a grown oxide layer of 2-3 nm presented in the appendix in images Figure A.5.4. Anisole can thus be used as a medium for GaAsBi NWs for DEP. Additionally, a diffraction pattern was performed to evaluate the crystallinity characteristic of the NWs. As they all presented the same trend one image representing the diffraction pattern results was put in the appendix Figure A.5.5. The diffraction pattern indicated that the NWs are crystalline, although the crystal phase could not be found.

6.2.2 Dielectrophoresis force and Clausius-Mossotti factor calculations

In this section, DEP simulation was performed on the GaAsBi NWs in order to investigate the CMF and DEP force theoretically exerted on the NWs. This gives a first evaluation of the NWs collection. The same previous Matlab code was used, as well as parameters of 8 $V_{peak-to-peak}$ applied on a set of round end tip electrodes with a 5 μm gap for GaAsBi NWs of 3-4 μm long. A gap of 5 μm was used as it was the smallest feature of microfabrication available in our facilities. To the best of our knowledge and as a new NW material, literature on the electrical properties of GaAsBi NWs is scarce. Thus, as an experimental start, a theoretical resistivity of 50 $\text{k}\Omega \text{ cm}^{-1}$ (20 S m^{-1}) was used from the work presented in reference [312] on GaAs NWs of closest dimensions ($\varnothing=100 \text{ nm}$, Length=2-3 μm). Those parameters were chosen by the similarity of dimensions and chemical nature. Table 7 summarises the characteristics of the materials used for the simulation, Ge is shown for comparison.

Table 7: Materials characteristics.

	Dielectric constant ϵ	Electrical Conductivity (S m^{-1})
Germanium	16	476.19 - 555.56
Gallium-Arsenide	12.8	20
Anisole	2E-6	4.33

The graphs Figure 6.5 shows the simulated DEP force on the GaAsBi NWs. More details on the CMF and DEP force graphs have been put in the appendix Figure A.5.6 to Figure A.5.8.

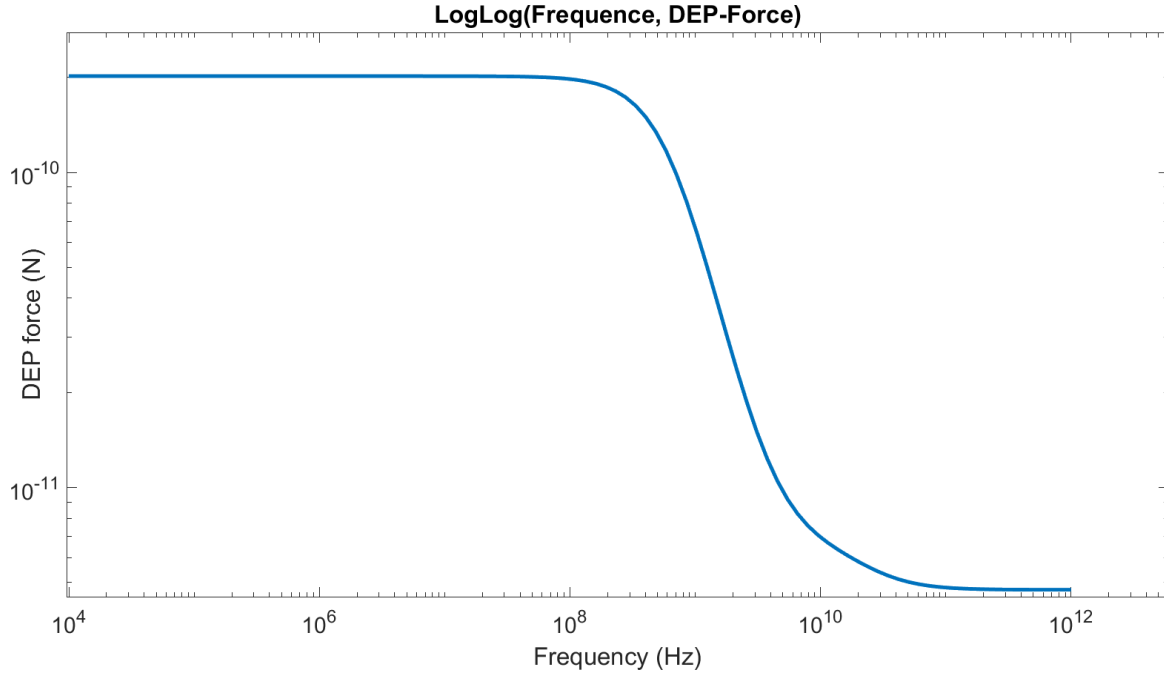


Figure 6.5: Calculated DEP force as a function of the frequency for GaAsBi NWs aligned at a voltage of $8 V_{peak-to-peak}$ on a $5 \mu\text{m}$ electrode gap in anisole.

As equivalently observed with the Ge NWs, the DEP force and CMF decrease with frequency. The calculation code was designed so that the NWs are not doped. In the case of the GaAsBi NWs, it is most probable that the NWs are more or less conductive and the simulation curves would present a shift to the right or the left. From 500 kHz to 10 MHz, the simulation curves show a DEP force and CMF on a plateau and start decreasing at a higher frequency than 100 MHz. Compared to the previously studied Ge NWs, the calculated DEP force, from 500 kHz to 10 MHz presented a plateau and a decrease at 10 MHz, although experimental results featured a different DEP force curve shifted to the left. For the same frequency of 10 MHz the DEP force is estimated at 2×10^{-10} N for GaAs and 4×10^{-10} N for the Ge NWs using the same voltage.

The differences lie in the conductivity, structural and quality properties as well as in the volume. Ge NWs are potentially more conductive than the GaAsBi NWs and have higher structural order (if referring to the diffraction pattern Figure 3.1 Chapter 4 Vs GaAsBi Figure A.5.5 in the appendix). However, DEP force is generally more important on bigger volumes, and the GaAsBi NWs are bigger ($6.36 \times 10^{-10} \text{ mm}^3$) than the Ge NWs ($5.65 \times 10^{-11} \text{ mm}^3$) [70]. Experimental results will help answer this question and give more insight into the DEP forces, collection properties and electrical performances.

6.2.3 Real-time resistance monitoring

In order to be able to detect NWs collection over time as the DEP process starts, the electrode gap was monitored by following the subsequent changes in resistance. The real-time resistance changes were recorded using the coded Matlab calculation command connected to the Tektronix Digital Oscilloscope, a function generator and the fabricated transimpedance amplifier (TIA illustrated Figure A.2.10 in the appendix and explained in Chapter 3). Additionally, optical microscopy was used to follow the NWs collection with the frequency. The anisole solution of GaAsBi NWs was prepared by using the same protocol as with the Ge NWs presented in Chapter 4. The DEP setup was the same. Using the parallel electrode bars with round tips as previously studied, a sinusoidal signal with amplitude $8 V_{peak-to-peak}$ (and a left artefact offset of 100 mV creating electrophoresis) and a frequency from 500 kHz to 10 MHz was applied using a function generator. An electrode gap of 5 μm was used as it was the smallest gap feature that could be fabricated in our facilities. The recording of the resistance started prior to the GaAsBi NWs solution placement on the DUT and was stopped after ≈ 12 minutes when the droplet completely dried. It was specified that both electrodes are affected by each other's electric field and behave like a capacitor (intensifies at high frequency). The previous electrode gap of 20 μm was leading to an insufficient signal-to-noise ratio because of the parasitic capacitance that overlaps any changes in dropping resistance. The parasitic capacitance tends to increase with smaller electrode separation and becomes important especially when the devices are electrically characterised [253]. As a consequence of using a smaller gap for smaller nano-particles, the obtained curves were automatically smoothed for more visibility with the same minimum degree to avoid misinterpretation. Figure A.2.10 in the appendix presents the circuit schematic and Figure A.2.11 shows the computational code details for the real-time monitoring of the resistance that has to be considered with GaAsBi NWs parameters. Figure 6.6 shows a typical example of the obtained resistance plot over time at a voltage of $8 V_{peak-to-peak}$ and frequency of 500 kHz applied for all three different batches of GaAsBi NWs.

The electrodes being closer to each other the electric field reaches quickly the opposite contact electrode and the start resistance is lower than for electrodes separated by 20 μm (170 k Ω at time 0 s for 20 μm gap VS 17 k Ω at time 0 s for 5 μm).

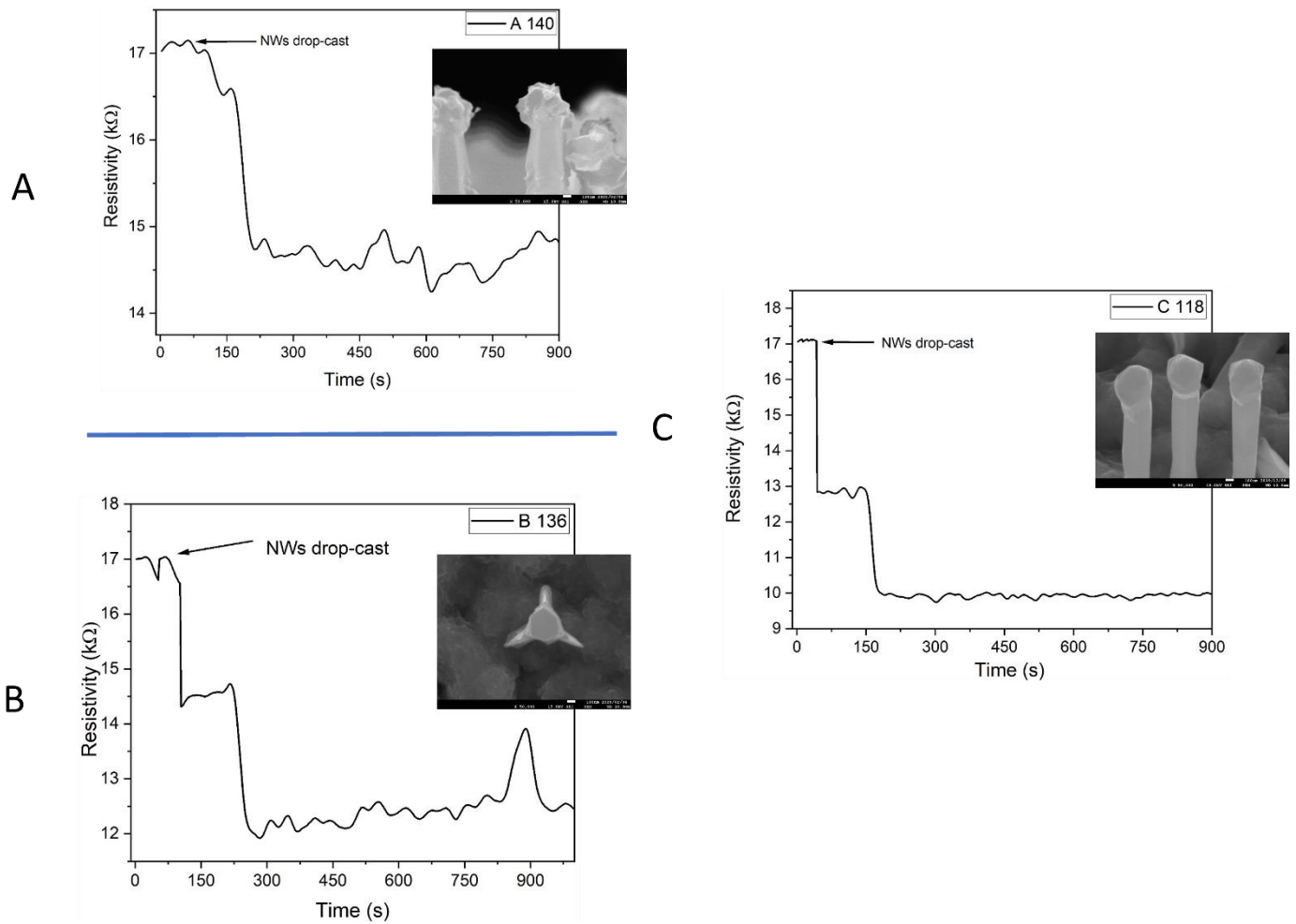


Figure 6.6: Resistance as a function of time during DEP at a signal of $8 V_{peak-to-peak}$ and frequency of 500 kHz. The graphs are obtained by resistance approximation using a Matlab code calculation. The insets are SEM images of the respective NWs on the substrate.

Quite resembling behaviour to the monitoring of DEP with Ge NWs, batches **A**, **B** and **C** have a common trend where, following the placement of the solution (≈ 90 seconds), a fast drop of resistance is recorded. In Figure 6.6 the general drop is in two steps. This trend could be because once collected, the aligning structure needs to stabilise and move a little before settling. Images of the collections were obtained by optical microscopy using the Olympus BX53 and are put in Figure 6.7. At 500 kHz in Figure 6.7 a), it is not clear why the NWs would feature two steps of resistance drops. However, in the appendix Figure A.5.9 a different focus was used on the device fabricated at 5 MHz c) Figure 6.7. As there are fewer NWs aligned, it is possible to see that the GaAsBi NWs align with very interesting behaviour and a similar behaviour was observed for the other frequencies. Liu *et al.* [236] determined that the ideal ratio gap size/NWs length was about 0.85 - 1 for an optimised DEP force. The NWs, measured by SEM have a length of 3-4 μm . As a consequence, in the case of the GaAsBi devices, the ratio gap size/NWs is 1.25 - 1.6 and results in a weaker DEP force than for a smaller gap size closer to the NWs length.

The chaining behaviour observed from the NWs indicates an attitude of adaptation to weak DEP force. Liu *et al.* [236] also demonstrated through simulation the "pearl chain" assembly of NWs. As the NWs start to orientate parallel to the electric field between the electrodes and in the vicinity of the electrodes, NWs are attracted to the electrode tips where the gradient is high (see COMSOL simulation Figure 3.19 Chapter 3). The NWs then move together by dipole-dipole interaction with the neighbouring NWs and create a longer chain as the NWs move parallel to the field. Between the NWs, this is an effect of "local-DEP" that creates this changing of electrostatic interaction [313]. Once a chain is completed and bridges the gap the first drop of resistance appears and, as the structure stabilises a second drop is recorded [314].

Similar behaviour has been observed with spherical particles [315] but also on rhodium (Rh) NWs [316] although in general resulting electrical and optical characteristics of chained NWs haven't been explored. Consequently, below a critical length, NWs can adapt to weak DEP force (mutual DEP force). The measured NWs were smaller than the 5 μm electrode gap size, so it would have been interesting to have longer NWs or smaller gaps to analyse the effect of directly aligning NWs against chaining NWs and question the length selectivity mechanisms and conditions. As no NWs were directly bridging the gap, this example shows a very interesting behaviour of adaptability that small NWs have by forming longer entities. As observed with the previous calculations the decreasing number of collected NWs is the result of a decreasing DEP force with frequency but also a result of the number of quality NWs within batches. This suggests that the DEP force curve is also shifted to the left towards lower frequencies where experimentally the plateau is instead situated before 500 kHz (plot Figure 6.5).

Interestingly, conforming to the results from monitoring the resistance, it seems that either the shape or other synthesis parameters like Bi % content are influencing the DEP and placement of the NWs aligning in the gap. An equivalent behaviour was observed for DEP at higher frequency (not shown) with fewer sharp drops of resistance because of the decreasing signal-to-noise ratio.

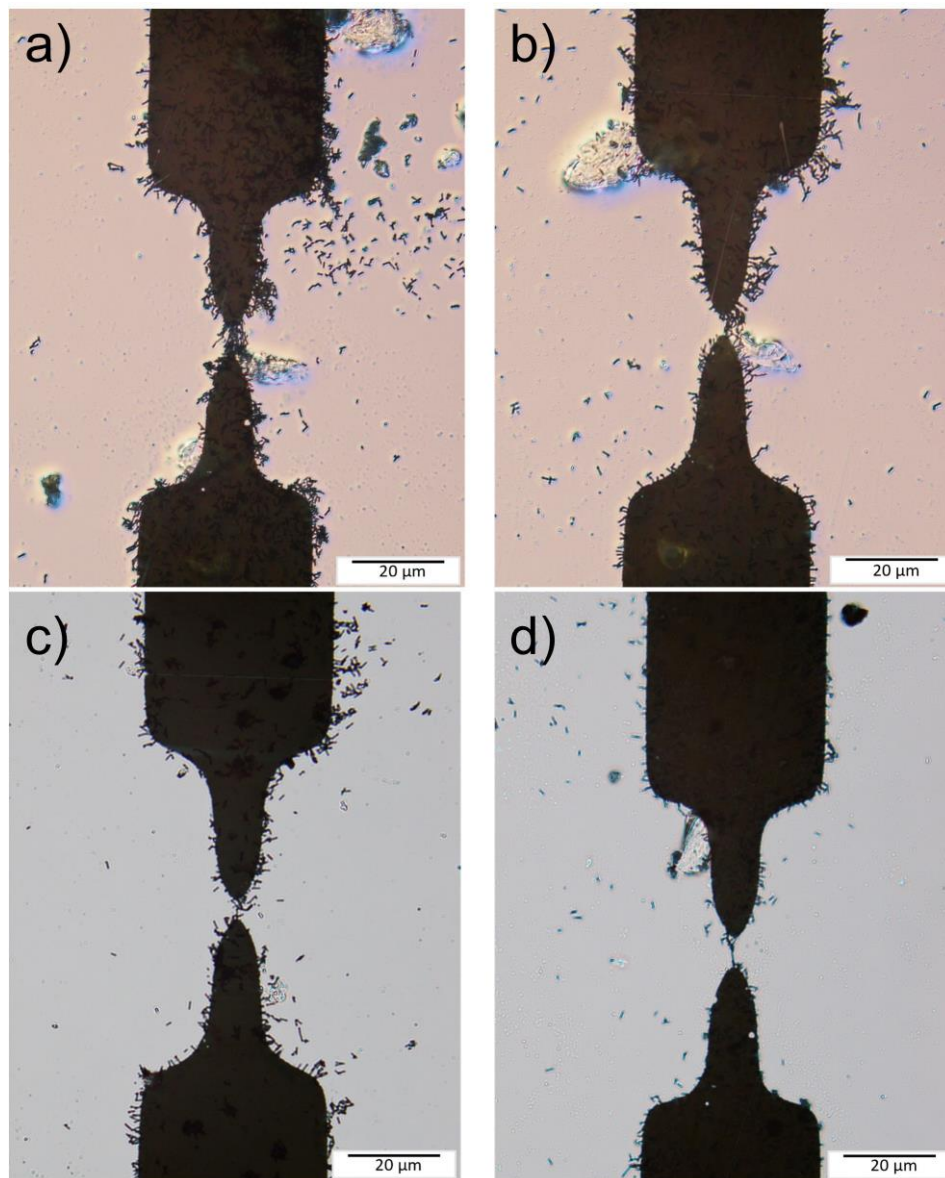


Figure 6.7: Example of dielectrophoresis collection of GaAsBi nanowires; a) 500 kHz, b) 1 MHz, c) 5 MHz, d) 10 MHz. This typical example is obtained from batch A.

DEP magnitude

The time constant τ showed in Chapter 3 and below equation 6.1 has been investigated using the obtained monitored resistance in the subsection above [254].

$$\tau = \frac{-t}{\ln(Z(t)_{NWs})} \tag{6.1}$$

t represents the time at which change of resistance $Z(t)_{NWs}$ is obtained via the Matlab code A.2.11 shown in the appendix. Figure 6.8 shows the resulting plot of the inverse of the time constant expressing the DEP magnitude over frequencies from 500 kHz to 10 MHz of the three different batches of GaAsBi NWs. The $Z(t)_{NWs}$ values were consistently chosen at the same time of 570 s generally in the middle of the experiment where the resistance was already decreasing by bridging NWs. As explained the time constant τ of the NWs collection expresses the DEP force magnitude over frequency.

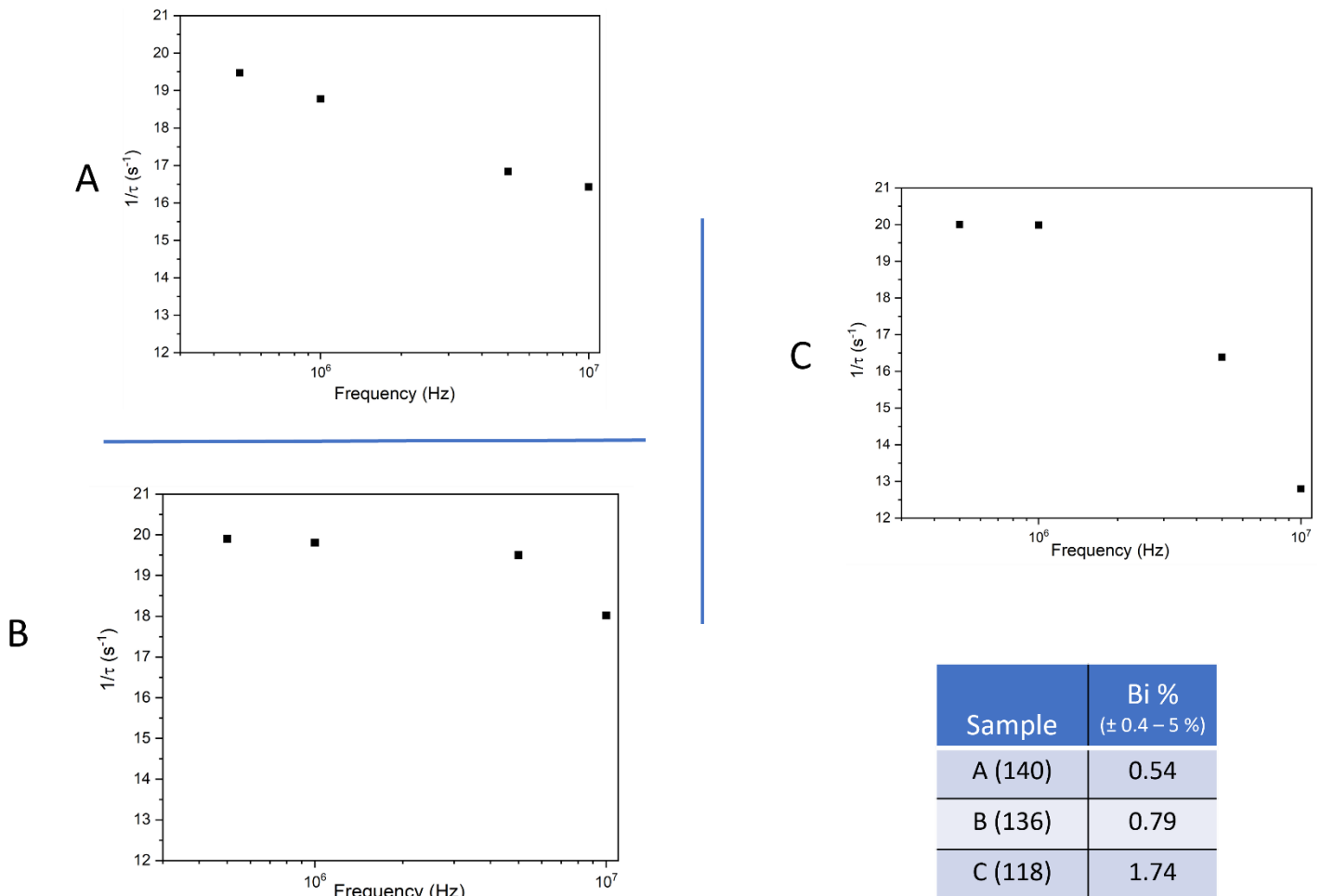


Figure 6.8: Inverse of time constant τ , describing the magnitude of the DEP force as a function of DEP signal frequency.

At low frequency, according to plots in Figure 6.8, the DEP magnitude is the highest and as a consequence attracts more NWs than at high frequency. All the samples were analysed by optical microscopy presented above in Figure 6.7 and were having a similar trend to Ge NWs where fewer NWs were aligned with increasing frequency. The decreasing magnitude and decreasing NWs aligned in the gap were as expected complimentary.

Batch **B** showed a generally smaller DEP magnitude decrease from 20 s^{-1} to 18 s^{-1} while batch **A** and **C** showed a DEP magnitude decreases from 20 s^{-1} to 16 s^{-1} . For batch **C**, 5 MHz was the maximum frequency before getting difficulties collecting any NWs after several trials. Above that parameter, it implies that there were very few NWs of better quality in batch **C** than the ones collected at 5 MHz. The experimental results obtained in Figure 6.8 have been correlated to the theoretical DEP and CMF equations simulated via the Matlab calculation code. The DEP magnitudes in Figure 6.8 show a general decreasing trend specifically for batch **C** while batch **B** only starts to decrease at 10 MHz. At this point, it is difficult to estimate whether the Bi % of the NWs or their morphology is responsible for the DEP magnitude variations and NWs alignment. In general, and as also observed with the Ge NWs in Chapter 3, the Matlab code gives an approximate idea of the CMF and DEP force trend. Plots in Figure 6.8 denote a decrease of the DEP force from $\approx 5 \text{ MHz}$ which would make the theoretical DEP force curve shift to the left either because of more conductive NWs than the theoretical value or additional parameters like surface morphology or because the DEP equations (3.2) need to be further refined because of the difference between the approximated prolate ellipsoid and the real shape of the GaAsBi NWs.

In the objective of manipulating GaAsBi for the first time using DEP, the first steps to determine the feasibility of the use of DEP were studied. In these experiments, tests were performed for preparing DEP-like medium/particle inertia, and calculations of CMF and DEP to have primary insight into the relationship of DEP with the GaAsBi NWs alignment. Images of the aligned NWs revealed an interesting behaviour of chaining in order to adapt to a large electrode gap and weak DEP force experienced by the NWs. This behaviour, already demonstrated in previous studies highlights the possibility to use bigger electrode gap sizes for small synthesised NWs and investigating NWs structures [313]. Moreover, based on calculated DEP force, CMF, measured resistance and optical microscopy images, increasing frequency features decreasing CMF and DEP force ensuing decreasing the collection of NWs. However, it was also seen that for differing Bi % and surface morphology, predictions over DEP polarisation and collection are more complex.

6.3 Influence of the dielectrophoresis frequency

6.3.1 Electrical properties; IV response

Following DEP performed to fabricate devices with differing Bi % in GaAsBi NWs, the resultant current-voltage (IV) responses were measured for each device using the measurement setup described in Chapter 2. To evidence the electrical response characteristic a reference was fabricated where the NWs were drop-casted between the electrodes without applying any DEP signal. Once fabricated, the electrical properties of the NWs devices aligned at different frequencies were investigated. For each frequency, at least 2 devices were fabricated. A voltage of 10 V forward (0 to 10 V) and then reverse (0 to -10 V) was applied through the device as a first test voltage. The devices fabricated with batch **A** were able to take a DC voltage of a maximum of 10 V before breaking down while devices fabricated with batch **B** and **C** could take a maximum of 3 V before breaking down. Accordingly, all the devices for batches **A**, **B** and **C** were measured with an applied DC voltage of 3 V for comparison.

Figure 6.9 shows the typical IV responses for each device at different DEP frequencies. The device IVs in a brown colour highlight that without any applied DEP, there is a negligible increase in the current as the potential is increased. This is most likely due to residual surface contaminants, residing in the channel, from either drop casting the NWs or the subsequent isopropanol rinse forming a conduction channel. The current without any DEP signal being applied is at least an order of magnitude smaller than that observed once a DEP voltage is applied, indicating that any NW or current flow from just drop casting the NWs is insignificant. Batch **B** showed no current response for frequencies higher than 500 kHz. It was observed that most of the NWs were gone either from washing with ethanol or sample transportation after alignment. Only devices with more NWs fabricated at low frequency and higher DEP force were able to display a current path through the NWs bridging the gap. Batch **B** has a very distinct morphology and thus it is most likely that the triangular core of the NWs stopped them from placing and adhering well to the electrodes and surface as hypothesised in the previous section. More studies on the adhesive and molecular interaction between NWs electrodes/surfaces could help in the future to answer that issue (for instance investigate surface interaction using high-power optical microscopy [317]).

The complexity of molecular interactions between nanoparticles and surfaces like electrostatic surface charges, non-covalent interactions and hydrophobic forces make it an understudied area in particular for irregular particle morphology. A solution worth investigating could have been to deposit a conductive layer on the top of the electrodes to assure contact with the NWs after DEP.

In the case of batches **A** and **C**, the NWs stayed in contact with the electrodes even after washing and transportation indicating good adherence with the surfaces. In batch **C**, at 5 MHz the current response is the highest of all batches with a maximum current response of 0.01 A at 3V. This result was obtained only once and is unrealistic and won't be considered for the rest of the study. It could be due to impurities or metallic layer remains from electrode fabrication. At lower frequencies of 500 kHz, the device shows asymmetry and even seems to feature SCLC in the forward voltage response. All the IV measurements at all frequencies could be taken for batch **A** 140. It indicates that the NWs were stable and adhering well to the electrodes and glass surface even after washing and transportation.

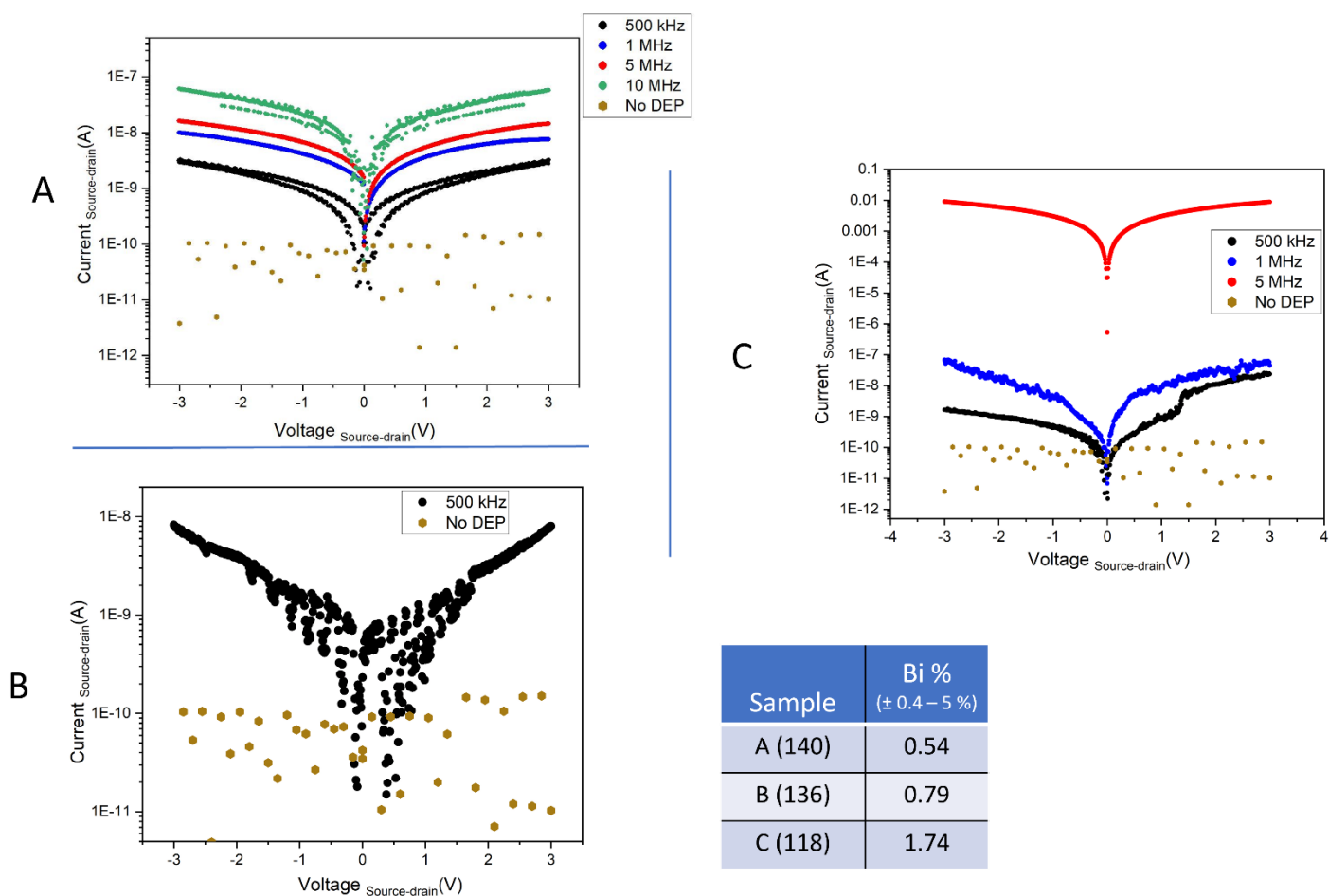


Figure 6.9: IV characteristics of as fabricated GaAsBi nanowire devices at differing DEP frequencies and differing Bi % with a floating gate potential. The table shows the different Bi % for batches A, B and C.

All frequencies display devices with transistor-like behaviour with symmetry in forward and reverse voltage. For most of the different batches and frequencies, the devices show transistor-like behaviour with symmetric responses. It was observed in the case of the Ge NWs that the asymmetric diode response was due to the heterostructure of the NWs given by the Ge(Au)alloy tip/ Ge core. Here, the GaAsBi NWs have a tip and core that feature a homogeneous chemical structure (as demonstrated in EDX analysis Figure 6.2) and as a consequence symmetric response. However, in this chapter, besides the different chemical nature, size and surface morphology are also quite different from the previously studied Ge NWs.

To detail the performance of the devices fabricated at different frequencies, the IV characteristics are re-plotted on log-log scales in forward and reverse voltage from Figure 6.10 to Figure 6.12. The gradients measured in batch A presented in Figure 6.10 demonstrate symmetric devices that behave like transistors, especially for low and high frequencies with gradients closer to 1 in both biases.

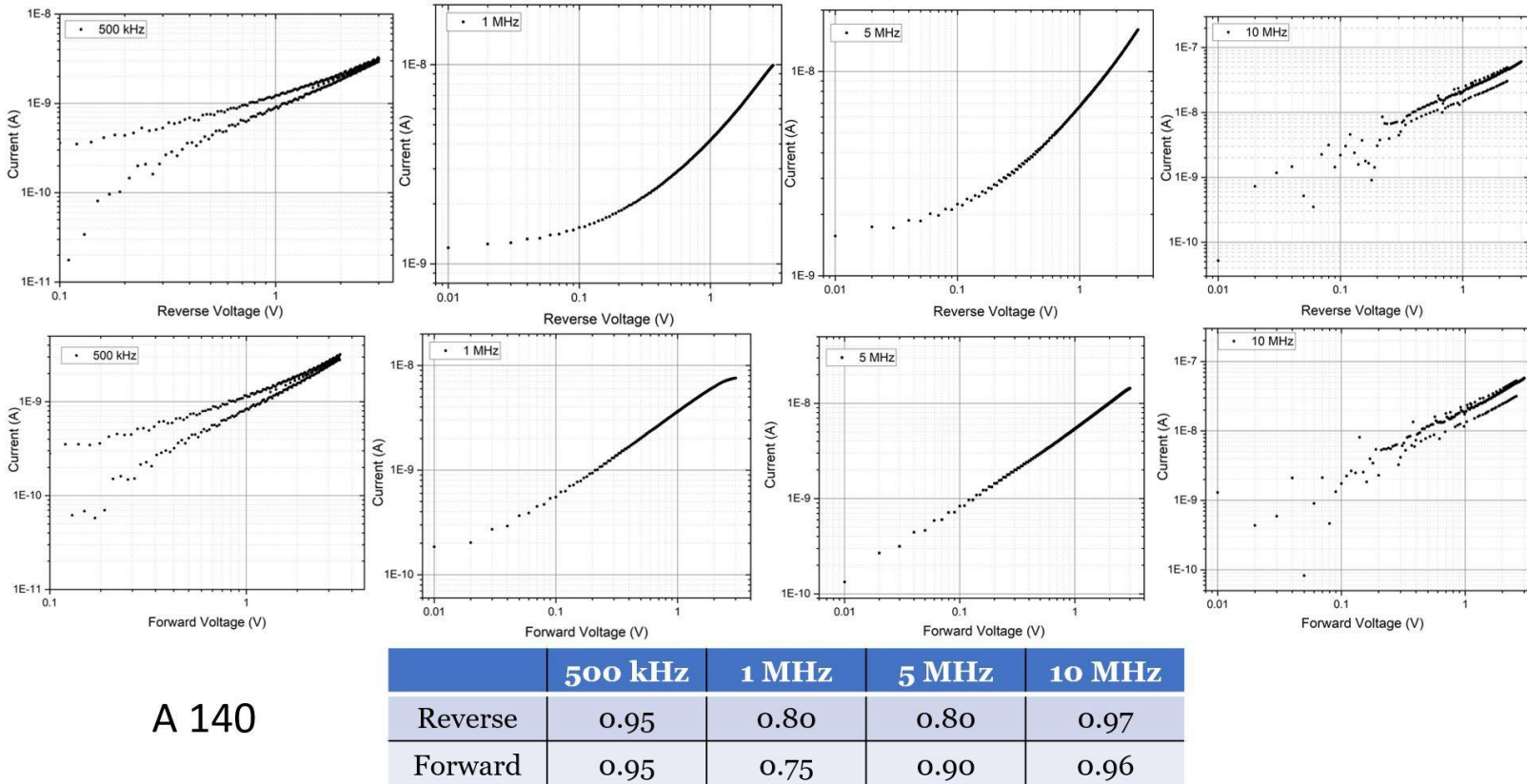


Figure 6.10: Reverse (top) and forward (bottom) voltage IV characteristics of GaAsBi NWs with Bi % 0.54 (batch A 140). DEP frequencies of 500 kHz, 1 MHz and 10 MHz with a voltage of $8 V_{peak-to-peak}$. Below is a table of the gradients in reverse and forward voltage at differing frequencies.

At frequencies of 500 kHz and 10 MHz, the devices have a current response that is noisier than for intermediate frequencies of 1 MHz and 5 MHz. The reasons could be due to low-quality NWs attracted at low frequency and or discontinuity in the structural connection from the NWs chain heighten with fewer NWs. Both devices fabricated at 1 and 5 MHz show comparable results where in reverse voltage, the ohmic gradient appears roughly from 0.5 V after a slower increase of the current. In forward voltage, both frequencies have a linear response with gradients of 0.75 at 1 MHz and 0.90 at 5 MHz as summarised in the table below in Figure 6.10. Overall, the conduction mechanism of the devices' contact with batch A NWs shows ohmic tendencies with gradients close to 1. Contrary to what was observed with the Ge NWs, the current response behaviour of GaAsBi NWs with increasing frequency is more complex because of the different surface morphology and Bi% of the NWs.

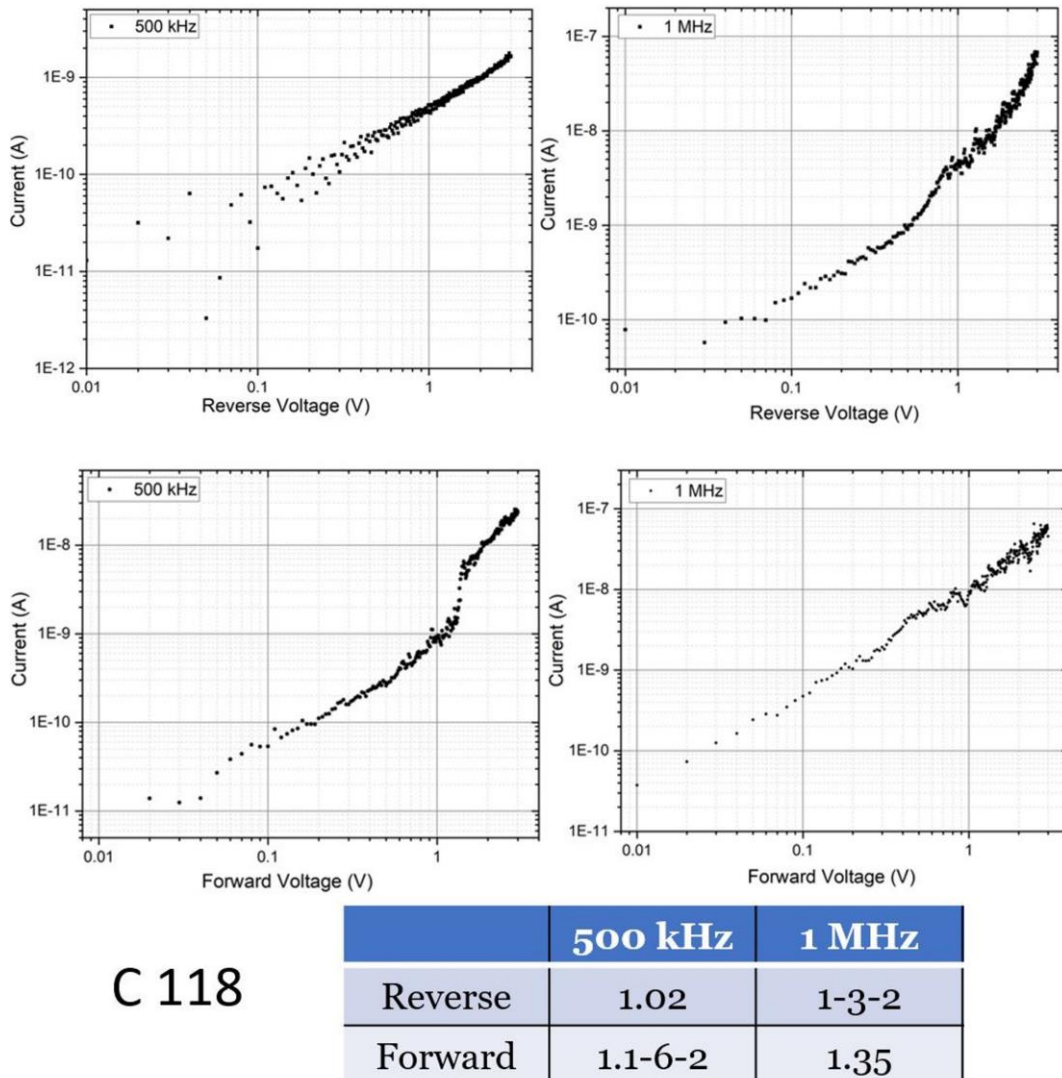


Figure 6.11: Reverse (top) and forward (bottom) IV characteristics of GaAsBi NWs with Bi % 1.74 (batch C 118). DEP frequencies of 500 kHz and 1 MHz fabricated with a voltage of 8 $V_{peak-to-peak}$. Below is a table of the gradients in reverse and forward voltage at differing frequencies.

- As previously observed, batch **C** shows 500 kHz asymmetric responses. In forward bias (bottom graphs), an ohmic gradient of 1.1 is observed at low voltage followed by SCLS gradient > 2 indicating low carrier concentration resulting from the depletion of injected electrons trapped by defect states [261]. Then trap-free SCLC with a gradient of 2 at 1.5 V suggests that the trap states are being filled [126]. Similarly, at 1 MHz in forward bias, a less pronounced SCLC can be observed between 0.4 and 1 V with more symmetry between both bias responses. At 5 MHz the current response was unreliable and removed from the experiments.
- In reverse bias, at 500 kHz (top graphs), a single gradient of 1.02 is measured indicating leakage current coming from crystal defect as it could be expected from NWs collected at low frequency and also observed in the case of the Ge NWs. At low frequencies, the asymmetric aspect of the responses couldn't be explained at the time of the device fabrication. It was found, in order to perform SEM imaging analysis that metallisation (by plasma deposition) of the device surface crushed the NWs down flattening them rendering difficult any morphological examination at differing frequencies which most probably is the origin of the asymmetry since the chemical nature of the NWs is homogeneous. Nevertheless, electrophoresis (EP) created by a DC offset artefact of 100 mV was kept in the experiment and the resulting asymmetric device response could originate from differences in the morphology of the NWs **C** as visible in the appendix on image A.5.3 in the red circles. Indeed, such structure differences will have one side more sensitive than the other due to an increased surface-to-volume ratio, increasing in return surface charges, polarisation and sensitivity to the environment [17]. This reveals DEP manipulation, has the potential to manipulate different particles' surface morphology in addition to NWs with different chemical heterostructures. Although the detailed influence of increasing frequency on collected particle morphology is still unknown.

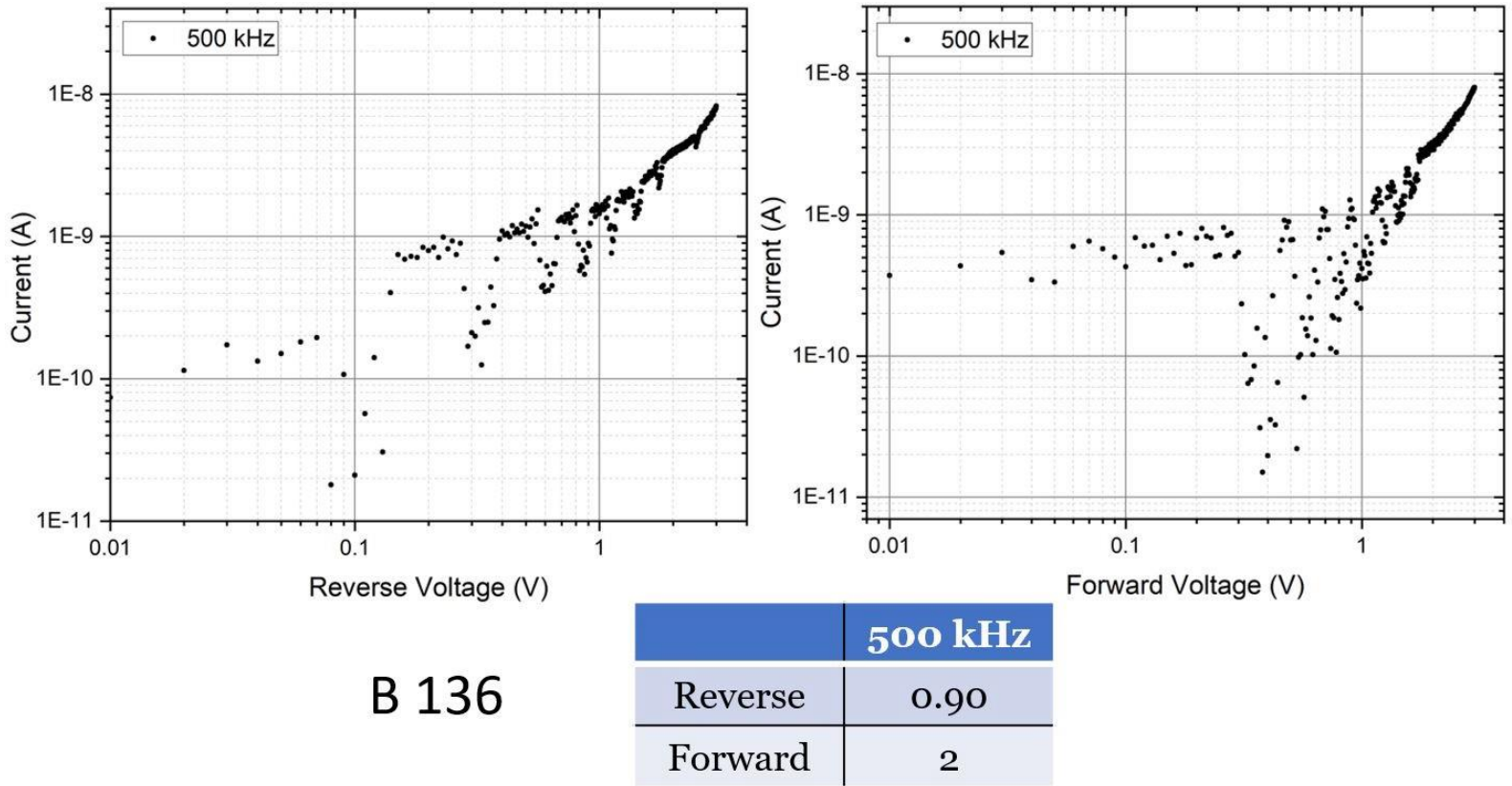


Figure 6.12: Forward and reverse IV characteristics of GaAsBi NWs with Bi % 0.79 (batch B 136). DEP frequency of 500 kHz fabricated with a voltage of 8 V_{peak-to-peak}. Below is a table of the gradients in reverse and forward voltage at differing frequencies.

Similarly to batch C at low frequency, batch B features devices with a slight asymmetric current response with SCLC in forward bias with a gradient of 2 and leakage current with a gradient close to 1 in reverse bias. The obtained signals are noisy until an applied voltage of 2 V, implying power-dependent devices.

Previously, comparable results have been presented on NWs with surface roughness. Indeed, a characteristic called Interface or Surface Roughness Scattering (SRS) has been investigated and is described in Chapter 1. It establishes that surface roughness greatly influences electron transport and sensitivity of NWs [17]. SRS also causes a reduction of electron mobility; indeed surface roughness can locally change the electronic band structure of the material reducing the mobility [318]. The rougher the surface is the less mobile carriers are. Thus, directly affiliated with the mobility and scattering properties, it has also been determined that SRS, acting as a perturbation of the surface potential [319] reduces the density of states [123]. Carriers in nanostructure with rough surfaces will scatter and will be confined in the surface/interface region; the density of states mostly found at the surface or interface of NWs (surface states) will be occupied by those scattered carriers.

This would explain the transition with increasing frequency that seems to be, besides regarding the quality of the material, also influenced by surface morphology and chaining NWs compared to chemical structure as seen with the Ge NWs. Additionally, surface roughness inevitably increases the surface-to-volume ratio of NWs and so potentially increases surface defect states and depletion because of their interaction with the surrounding environment as they are more sensitive. As a consequence, there is competition between increasing surface sensitivity and reduction of electron mobility and density of states.

It was previously seen with the Ge NWs in Chapter 4 that, increasing frequency aligns NWs that featured higher conductivity. Hence, it is interesting to investigate higher conductivity properties with increasing frequency and with different NWs morphology and Bi%. To do so, the Fermi-velocity law previously demonstrated for silicon transistor NWs devices [320] was applied to the resultant IV curves of the GaAsBi NWs devices to determine the carrier mobility.

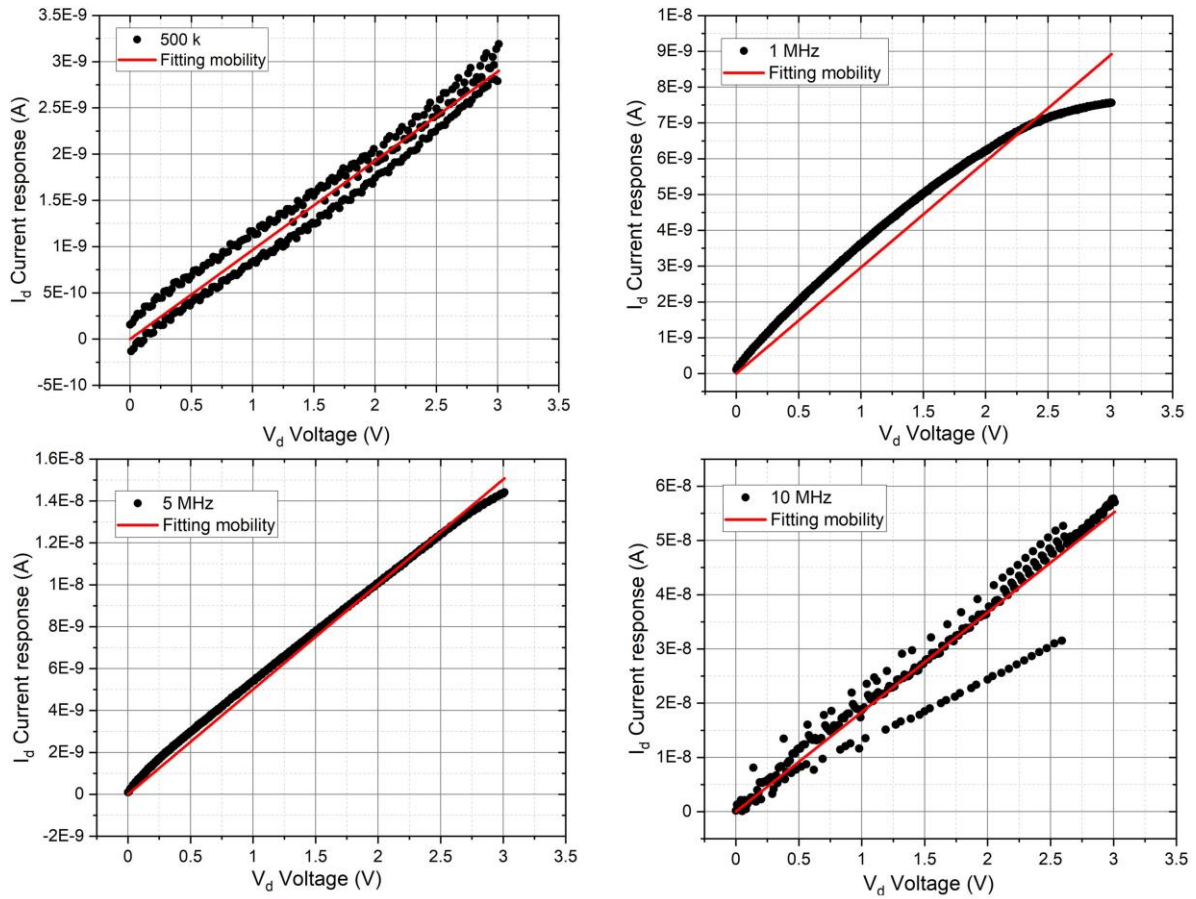
The Fermi-velocity law is written as follows;

$$I_d = \frac{\mu_l C_g}{2L} * \frac{V_d^2}{1 + \frac{V_d}{V_c}} \quad (6.2)$$

with,
$$V_c = \frac{v_{sat}}{\mu_0} \quad (6.3)$$

and,
$$C_g = \frac{2\pi\epsilon_{ox}}{\ln \left[\frac{2R_{ox} + 2R_{NW}}{2R_{NW}} \right]} \quad (6.4)$$

Where V_c is the critical voltage, $\mu_0 = 0.86 \text{ m}^2\text{V}^{-1}\text{s}^{-1}$ is the intrinsic mobility of carriers in bulk GaAs [321] and v_{sat} is the thermal velocity. V_d is the applied DC voltage, L is the distance between the electrodes and C_g is the gate capacitance related to the oxide layer. By fitting the Fermi-velocity law to experimental data using linear fit in Origin, carriers' mobility at increasing frequency has been extracted for different Bi % NWs devices. The fitting was performed at the IVs Ohmic regions and the mobility values are presented in the tables below the graphs Figures 6.13 and 6.14. The transistor behaviour can be evaluated in conjunction with adapted mobility. An increase in carrier mobility can be seen as improving the quality of the NWs in the device although it has to be considered that the obtained mobility accounts for the chaining NWs. With one single measure obtained at 500 kHz for batch **B**, the carrier mobility couldn't be investigated further and was discarded. Nevertheless, batch **B** presented a fitting carriers mobility of $9.71 \pm 0.17 \text{ cm}^2\text{V}^{-1}\text{s}^{-1}$ at 500 kHz.



A (140)

Frequency	Fitting Mobility ($\text{cm}^2\text{V}^{-1}\text{s}^{-1}$)
500 kHz	5.29 ± 0.027
1 MHz	16.3 ± 0.10
5 MHz	27.5 ± 0.059
10 MHz	100.9 ± 0.70

Figure 6.13: Fitting mobility based on the Fermi-velocity law on forward IV response of batch A. The table below summarises the obtained fitting mobility.

By fitting the Fermi-velocity law on the devices fabricated with batch A from 500 kHz to 10 MHz DEP frequency, carriers mobility of 5.29 ± 0.03 to $100.90 \pm 0.70 \text{ cm}^2\text{V}^{-1}\text{s}^{-1}$ were determined. Despite chaining NWs, decreasing DEP force and aligned NWs, the fitting mobility shows an increase in carrier mobility translating that more conductive NWs are aligned at high frequency.

The fitting analysis on batch C at 500 kHz was performed on the ohmic regions situated from 0 to 0.75 V and from 0 to 1.2 V at 1 MHz and the rest (SCLC) was removed. The Fermi-velocity law on the devices fabricated with batch C from 500 kHz to 1 MHz DEP frequency demonstrates fitting mobility of 3.48 ± 0.03 to $51.70 \pm 0.60 \text{ cm}^2\text{V}^{-1}\text{s}^{-1}$ respectively.

As an additional note, at 5 MHz that presented unreliable I(V) response Figure 6.9 resulted in fitting mobility of $16.36 \times 10^5 \pm 9 \times 10^3 \text{ cm}^2 \text{ V}^{-1} \text{ s}^{-1}$ supporting that this data was invalid and discarded.

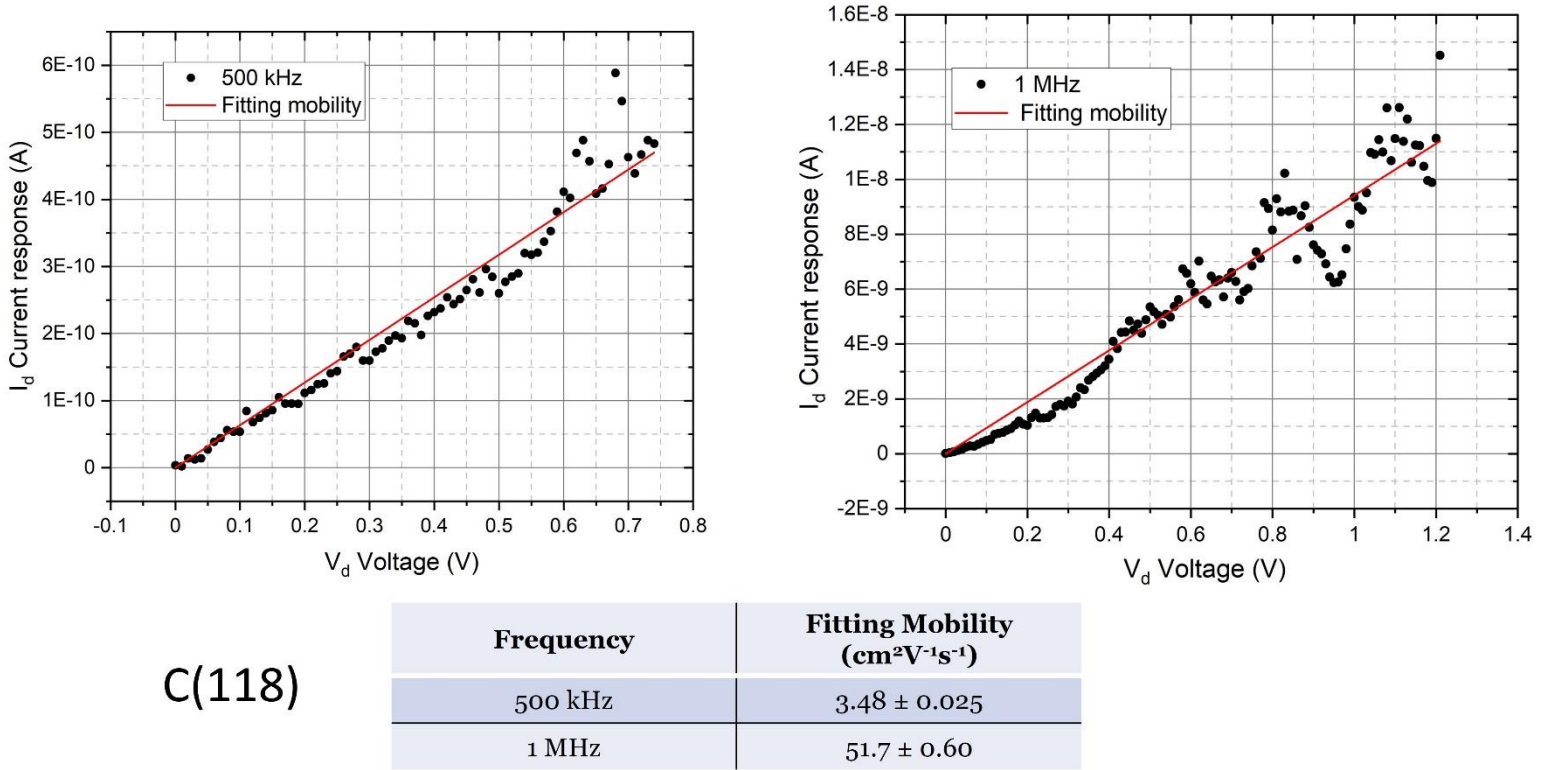


Figure 6.14: Fitting mobility based on the Fermi-velocity law on forward IV response of batch C. The table below summarises the obtained fitting mobility.

All the devices fabricated with the different batches show a similar trend where the mobility μ_l increases. SRS reduces the carrier’s mobility, despite the latter, the mobility still increases within the NWs with increasing frequency, suggesting that the carriers are still able to travel from NW to NW (and follow the pace of the changing polarity during DEP). Nevertheless, with more chains of NWs at a low frequency of 500 kHz for example, the reduced mobility of carriers could be due to the discontinuous channels formed by several NWs instead of longer single crystals bridging the gap. The results show more likely that increasing the DEP frequency results in better quality selected aligned NWs. Although it was not possible to verify whether DEP could also select specific NWs surface morphology with increasing frequency it is evident that the morphology of the NWs plays an important role in DEP and devices performance, opening possibilities for NWs synthesis.

Carrier mobility in bulk GaAsBi has been measured going from $1371 \text{ cm}^2 \text{ V}^{-1} \text{ s}^{-1}$ (Bi% 2.5 %) to $2116 \text{ cm}^2 \text{ V}^{-1} \text{ s}^{-1}$ (Bi% 1.2 %) [207]. While smooth surface GaAs NWs have been reported with carriers mobility from 31 to $1040 \text{ cm}^2 \text{ V}^{-1} \text{ s}^{-1}$ [322, 323].

In the case of this study, GaAsBi NWs range of mobility from 3.48 to 51.7 $cm^2V^{-1}s^{-1}$ has been estimated. As known, the lower carrier mobility at lower scale materials like nanostructure is attributed to crystal defects, surface dangling bonds, and carrier scattering. Despite attempts to eliminate crystallographic defects (e.g passivations) to improve carriers' mobility, bulk-like mobility remains elusive [206]. An understanding of carrier mobility and scattering in rough nanoparticles is needed to improve NW devices based performances. In the following section, the photoresponse of the GaAsBi NWs devices was investigated to further understand the properties of such NWs aligned by DEP.

6.4 Optical properties; photocurrent spectroscopy

In the interest of the photoresponse sensitivity and characteristics of GaAsBi devices based on differing Bi % content, the fabricated devices of batches **A** and **C** were illuminated under a calibrated Horiba iHR320 monochromator system. The optical chopper was set to rotate at 330 Hz and placed between the monochromator light source output and the device. Illumination was performed with a wavelength from 400 to 1100 nm and a bias voltage of 100 mV was applied. The illumination spot was 1 mm in diameter and illuminated the entire gap device as well as part of the Au electrodes which can not be avoided. The light was shone onto the device perpendicular to the NWs axis and the photocurrent was measured as a function of the photon excitation wavelength giving the spectrum presented in the graph below. The photocurrent spectroscopy measurement set-up has been detailed in Chapter 2 to measure the NWs photoresponse.

Figure 6.15 shows the normalised spectral current responses obtained from the GaAsBi devices fabricated at a DEP frequency of 1 MHz and with differing Bi % of **A** and **C**. Photoresponse from devices fabricated with batch **B** at 500 kHz (not shown) featured unreliable and noisy photoresponse suggesting that the NWs had too low conductivity and could not induce photocurrent under illumination. The obtained spectra in Figure 6.15 reveal that a photocurrent could be induced under light stimulation. Upon illumination, photoexcited free carriers result in the observed photocurrent. The spectrum shows that the photoresponses of the devices dominated over the energy of ≈ 1.4 to 1.8 eV corresponding to wavelengths of 660 to 850 nm in the visible red and near-infrared respectively. Below the GaAs energy gap (in pink dotted line), photocurrent response drops as no photons with lower energy are absorbed. Figure A.5.10 in the appendix shows the normalised photoresponse as a function of the wavelength. In the literature, photoresponse from GaAs NWs has been largely studied and shows peak responses between 1.42-1.54 eV at wavelength 800-870 nm [178], while GaAsBi thin films have shown a response between 1.37-1.45 eV at wavelength 850-900 nm (with Bi% $\approx 3\%$) and 1.23-1.37 eV at 900-1000 nm (with Bi% $\approx 1.5\%$) [324, 325].

A spectral shift can be observed between the two differing Bi % batches. From that, estimation of the Bi % content was undertaken using the photocurrent. Maximum cut-off energies have been selected at 20, 30, 35 and 40 % intensity of photocurrent. As indicated in Figure 6.15 (in pink) the electronic band gap of GaAs defines the limit above which energy domain belongs to GaAs, thus 35 % to 40 % are the less reliable.

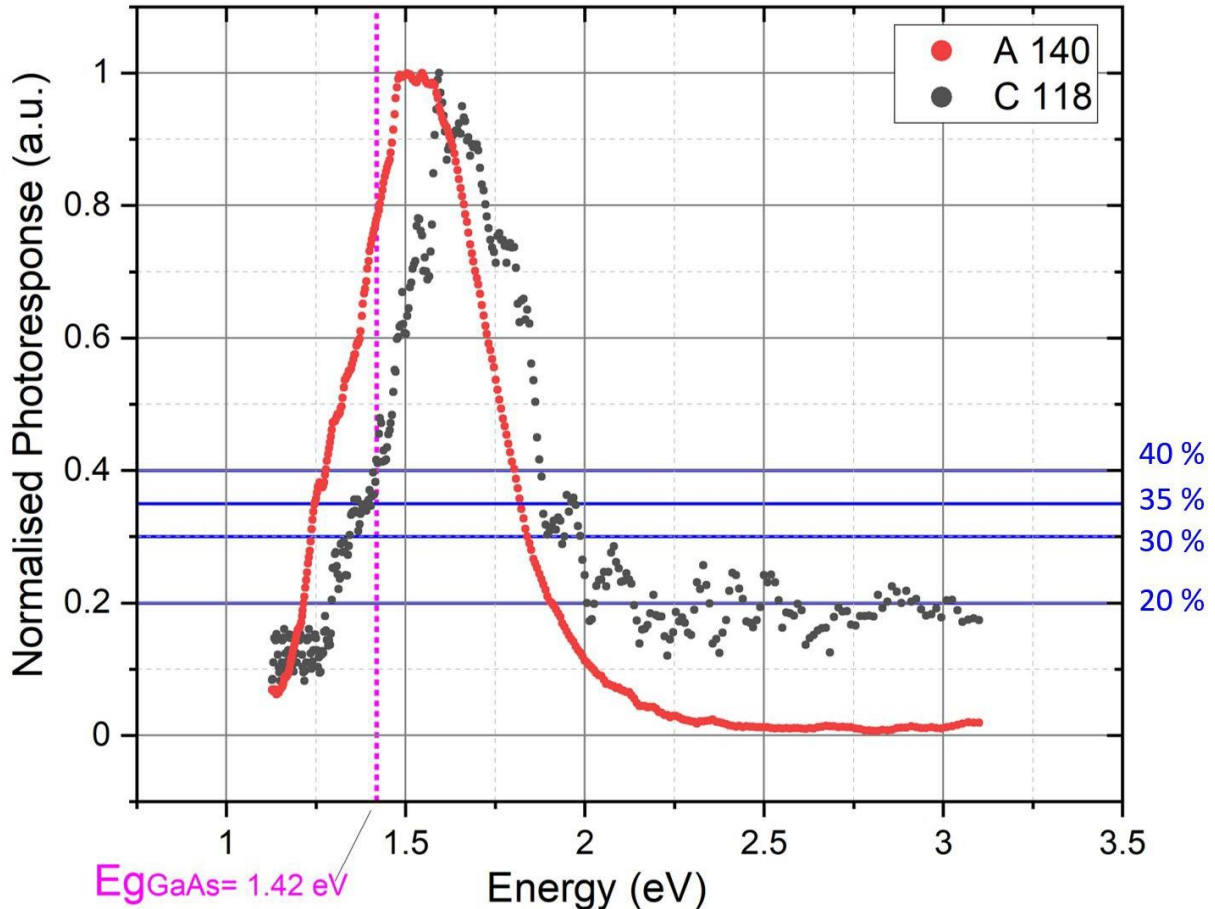


Figure 6.15: Normalised spectral responses as a function of the energy measured at room temperature. Devices fabricated with NWs aligned at a DEP frequency of 1 MHz. The pink line shows the GaAs band gap at 1.42 eV.

The extended cut-off energy of A (red curve) is sensitive to composition and it can be interpreted as a reduction of the band gap by Bi % incorporation. In previous work, photoresponse was largely investigated for bulk GaAs incorporated with Bi %, particularly for the band-gap shifts caused by Bi %. A band-gap reduction of 83 meV/Bi% was mostly reported by photoresponse analysis for GaAs with the incorporation of $0.1 < \text{Bi} (\%) < 6$ [188], although a reduction of 42 meV/Bi% has also been communicated [184].

In this work, 83 meV/Bi% was used as a reference to estimate the Bi% of the batches by photoresponse analysis. The following table summarises the measured cut-off energies and the corresponding calculated Bi %.

Table 6.3: Measured cut-off energies and corresponding incorporated Bi %.

Normalised Photocurrent (%)	Cut-off Energy (eV)		83 meV /Bi%	
	A	C	A . Bi %	C . Bi %
20	1.21	1.29	2.5 %	1.56 %
30	1.23	1.36	2.28 %	0.72 %
35	1.24	1.39	2.16 %	0.36 %
40	1.27	1.40	1.80 %	0.24 %

At 20 % of the maximum photocurrent intensity the Bi% has been estimated at 2.5 % in **A** NWs and 1.56 % for **C** NWs. Those results contradict the previous EDX chemical analysis measurement indicating **A** Bi=0.54 % and **C** Bi=1.74 %. EDX accuracy of $\pm 0.4 - 5$ % could be at the origin of the contradiction knowing moreover that **A** NWs were synthesised with a maximum Bi flux (4.3×10^{-5} Pa Vs 1.4×10^{-5} Pa for **B** and **C**).

Between 500 kHz and 1 MHz, the carrier mobility estimated by plotting the Fermi-velocity Figure 6.13 is much lower for **A** than for **C** (e.g. 16.3 ± 0.10 VS 51.7 ± 0.60 $cm^2V^{-1}.s^{-1}$ at 1 MHz). Now, if one asserts that **A** has higher Bi % than **C** by 1% (at 20 % of the maximum photocurrent intensity) one can assume that Bi% does not affect the carriers' mobility. The latter is consistent with what has already been observed in several studies on unchanged carriers' mobility with differing Bi % in bulk GaAs [207] but also shows a decrease in carrier mobility in films with Bi % > 4% [326]. Previous studies on GaAs NWs have suggested carrier mobility ranging from 31 to 1040 $cm^2V^{-1}.s^{-1}$ for NWs generally thinner with smooth surface morphology. Bulk GaAsBi studies have referenced carrier mobility ranging from 1370 to 2800 $cm^2V^{-1}.s^{-1}$ for Bi % of 1.6 % and 0.84 % respectively. Table A.5.11 in the appendix shows values extracted from literature presenting carrier mobility obtained on bulk and semiconductor NWs. As such, if Bi% does not influence carriers' mobility it tends to support that the surface morphology is at the origin of the carrier mobility discrepancy. However, more analyses are necessary to confirm that outcome. Figure 6.1 showed that the morphology of **A** and **B** was rougher than the core morphology of **C** despite a star-like shape base. Ideally, the surface roughness of the NWs could have been measured by Atomic Force Microscopy but this experiment was unsuccessful. GaAsBi thin film surface roughness has been shown to be greatly influenced by increasing Bi% incorporation [327].

There are several methods to obtain smooth NWs surface morphology. The growth of GaAsBi NWs by MBE is a recent material of study, more investigation on synthesis parameters is needed to understand the influence of temperature, Bi flux and time on the final NWs morphology.

Ptak *et al.* studied GaAsBi thin film surface roughness and demonstrated that smooth surface morphology can be obtained with optimum growth rate; however electrical, optical and structural properties were not established [328]. It is also possible to obtain smooth surface NWs by post-treatment using for instance surface coating that showed increased saturation voltage and carrier mobility of the NWs compared to high surface roughness NWs before coating [38].

The performance of a photodetector is measured by the responsivity that also reflects its sensitivity. It is the photocurrent through the photodetector per active surface per unit power of light. The spectral responsivity can be determined by evaluating the incident light power using two different reference diodes of known responsivity. Using a Si commercial photodiode, the responsivity of an array of GaAsBi NWs aligned at 1 MHz for different Bi % of A and C were analysed and plotted in the following Figure 7.16. The light spot being larger than the detection area, it is difficult to accurately calculate the incident optical power. The graph Figure 6.16 indicates that both devices have responsivity that dominates over a wavelength from 660 to 850 nm reaching responsivity of 1.3×10^4 A/W for C and 5.6×10^4 A/W for A. Such results are consistent with GaAs array of NWs that have shown a responsivity of 4.5×10^4 A/W between 450-800 nm and 6.4×10^5 A/W at 520 nm for passivated and doped GaAs NWs [178].

According to Figure 6.16, differing Bi% incorporation of +1% results in a responsivity that increases 5 times. Nanotexturing or surface roughness on GaAs and Ge nanoparticles have been used to reduce broadband reflectance and enhance light confinement [329] resulting in higher detection and responsivity. The high responsivity obtained from the GaAsBi NWs can originate from light scattering [329], surface traps at the interface of NWs (for p-type NWs) [275] and optical resonance can originate from spectral selectivity or internal reflection [286]. Moreover, for NWs thicker than 200 nm in diameter, internal reflection provides efficient light trapping [286].

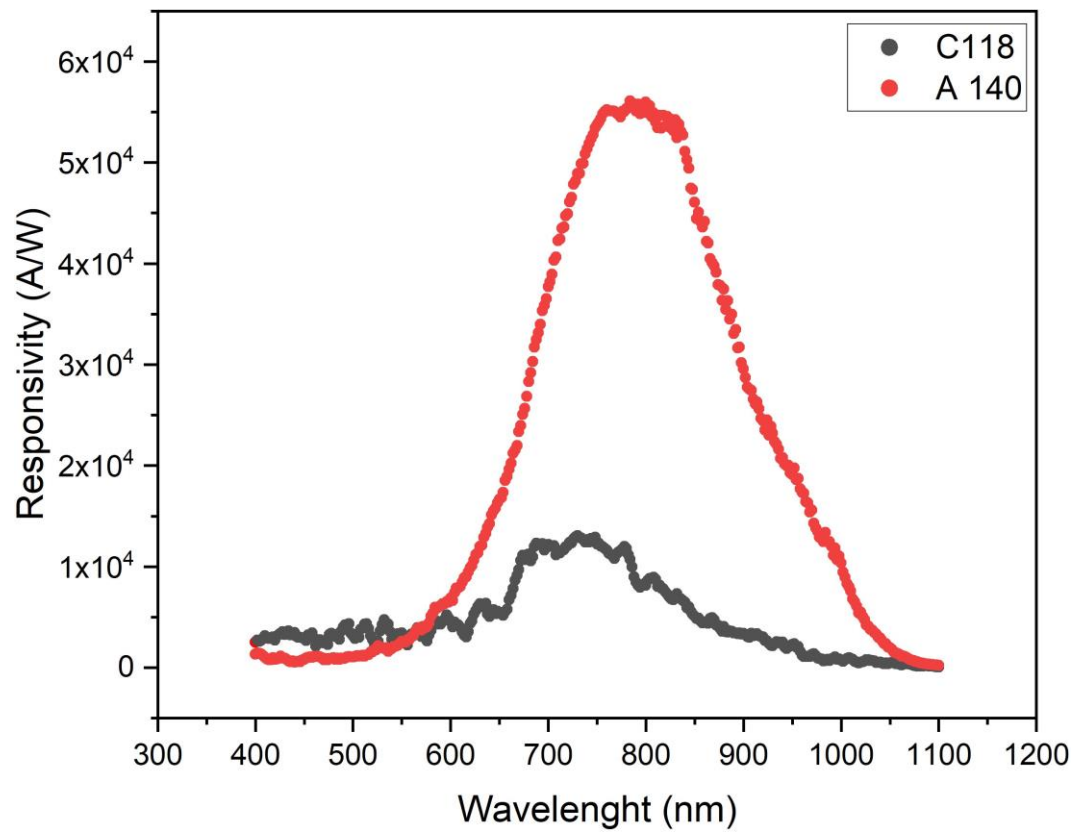


Figure 6.16: Optical responsivity of an array of GaAsBi NWs aligned at 1 MHz with a Bi % of 2.5 % in A (red curve) and 1.5 % in C (black curve).

Conclusion

In conclusion, this chapter focused on the first electrical and optical characteristic studies of GaAsBi NWS synthesised for the first time by MBE. The nature and morphology of the NWs were confirmed and examined by SEM, TEM and Raman spectroscopy. The three different batches of differing growth parameters showed surface roughness and distinctive morphology. It was established that anisole was a suitable medium to be used as a matrix for DEP manipulation in order to fabricate GaAsBi devices. Initial analysis of DEP using approximated calculations with available GaAs information revealed an expected trend of decreasing DEP force with increasing frequencies. The electrical characteristics of the resulting devices were established. Most of the responses featured transistor-like behaviour (with EP from DC offset) with symmetric responses supporting the homogeneous chemical structure demonstrated by EDX. However, few asymmetrical responses brought out that DEP coupled with EP also has the potential to influence the alignment of NWs with different morphology in addition to chemical heterostructure. Chaining of NWs was observed by means of optical microscopy revealing the adaptability of the NWs to weak DEP force. Despite chaining GaAsBi NWs increasing carrier mobility was obtained by Fermi-velocity law implying improved conductivity even with chaining and SRS effect. Electric current through the devices gives information on carrier mobility and sensing properties. It was demonstrated from photocurrent response that batches **A** and **C** that Bi % does not influence carrier mobility (until a certain Bi% decrease of mobility [326]) but reduces the band-gap energy from 1.29 eV to 1.21 eV with $\approx +1$ % of Bi. A possible explanation for carrier mobility degradation is that dislocations occur at high Bi concentrations where the relaxation of the NWs crystal starts to be limited. A second explanation comes from the ensuing SRS. In general, at the limit of the mean free path and surface, carriers experience more scattering; scattering that is enhanced by surface roughness. Thus, carriers' mobility and device performances are strongly affected by the NWs' surface conditions and doping. The high responsivity of batches **A** and **C** revealed potential applications from visible red to near-infrared light detectors and solar cells [330]. It would have been interesting to get photoresponses from NWs aligned at increasing DEP frequencies, it is most probable that the increasing electron mobility would have featured increasing photocurrent responses and responsivity. Scientific research of NWs surface and electrical transport properties of semiconductors provides knowledge to improve NWs conductivity for advanced integrated circuits and sensors.

Chapter 7

Conclusions and Further Work

In conclusion, Ge and GaAsBi NWs have been demonstrated to be great building blocks for future technology such as photodetectors and biosensors with unique advantages when controlled, selected and orientated by DEP. The properties of the NWs-based devices were investigated in detail via current responses, DEP magnitude (through an automated setup) and photo-spectroscopy with a focus on the effect of DEP frequencies on the devices' performances. Gained knowledge was applied to demonstrate successful sensing applications as proof of concept corroborating DEP and NWs functionality. In Chapter 3, anisole was found to be an ideal medium to prepare Ge and GaAsBi NWs solution because of its low volatility, good chemical inertia and high contact angle on the electrodes' surface. COMSOL simulations and optical microscopy showed that parallel electrodes with round tips had ideal and more precise collection features than interdigitated electrodes or square tip designs. These optimum experimental parameters were subsequently used throughout the thesis. The current response analyses showed asymmetry resulting from the axial-graded chemical heterostructure of the Ge NWs. It was exposed that an unintended EP force induced a specific orientation of the gold-Ge-alloy NWs' tips toward one electrode creating an ohmic contact on one side and Schottky contact on the other. Such versatility of manipulation and orientation of structure has never been presented before. Currently, heterostructured NWs, either axial or radial are grown for their band-gap engineering and superior properties than planar geometries and are only implemented as single NW devices, mostly without selection and by a top-down approach [331]. Hence, EP combined with DEP makes it possible to collect more than one NW between electrodes with one common orientation. Unfortunately, the nature of the electrodes and gold tips of the NWs prevented chemical analysis by SEM that could have accurately yielded all the NWs' orientations. The detailed electrical and optical characterisation of Ge NWs-based devices fabricated with a frequency range of 500 kHz to 10 MHz confirmed theoretical speculations.

With increasing frequency and despite a decreasing DEP force collecting fewer NWs, they were of better conductivity; from a factor of 2θ at 500 kHz to 4.38θ at 10 MHz as proved by the Mott-Gurney plot showing increasing carrier mobility.

Additionally, a decrease of SCLC was observed in forward voltage with increasing frequency; with fewer defects in the NWs, charges are more likely to follow the pace of the changing polarity through the NW and hence generate movement resulting in aligned NWs of higher quality. The NWs collection with increasing conductivity can be regarded as NWs that tend towards ideal semiconductor crystals. It would have been also very interesting to investigate increasing conductivity by using conductivity mapping by AFM giving even information on individual NW conductivity [75]. In addition, determining the evolution of the electronic energy states in the NWs with increasing DEP frequency would have been very instructive. It can be measured using Kelvin probe force microscopy (KPFM) where the tip acting as a probe measures the resulting current response as a function of the rising temperature (energy) and the energy diagram can be found. The Ge NWs-based devices also revealed an increasing rectification ratio of 0.9 at 500 kHz to 500 at 10 MHz and a turn-on voltage decrease from 1.3 V to 0.2 V close to the expected turn-on for a Ge diode (0.3 V). NWs-based devices collected at high frequency showed to be repeatable performances highlighting the additional capabilities of DEP.

Then, for the first time, a voltage divider system coupled with DEP was demonstrated in Chapter 4. This simple setup used an increasing resistance Rd to reduce aligned NWs with a fixed frequency. In this way, a high-frequency selectivity of 10 MHz for high conductivity NWs was kept and combined with the possibility of reaching one single Ge NW aligned. It was observed that the ideal alignment of one single NW was prevented by entanglements of NWs, hence, here filtration and NWs growth branching improvement would be interesting for further work. As an extra investigation, the functionalisation of ≈ 1 Ge NW would have been of great interest in order to explore the ultimate limit of detection in terms of sensitivity. The electrical characterisation showed that without EP applied, the obtained signals were symmetric with a transistor-like behaviour for arrays of NWs. With decreasing number of NWs, and increasing resistance Rd current responses tended toward asymmetric diode-like behaviour confirming previous results seen in Chapter 3. The resistivity of ≈ 1 Ge NW aligned at 1 and 10 MHz was approximated at 1.55×10^9 and $7.73 \times 10^8 \Omega$ corresponding to 17 Ω .cm and 8.7 Ω .cm respectively. The resistivity measured using FIBID to contact a randomly chosen Ge NW (from the same source) to platinum and gold electrodes was 0.18-0.21 Ω .cm [233]. Such a difference can be explained by the contact electrode technique of FIBID allowing local deposition and high-resolution nanopatterning and thus, resulting in ultra-low contact resistivity [271].

More excitingly, the photodetection characteristics of an array and ≈ 1 Ge NW were compared by photo-spectroscopy. Both results were analogous to what was obtained in the literature [278].

For ≈ 1 Ge NW, photodetection featured specific peaks responses near-infrared and telecommunication wavelength with a responsivity of 6.2×10^5 A/W at 700 nm and 5.2×10^5 A/W at 1550 nm, they are one of the highest responsivity observed for single semiconductor NW-based photodetectors. Such high responses can also be explained by the Schottky barrier lowering or optical resonance. Nevertheless, a high responsivity is more desirable for photodetection, and near-infrared has the potential for photovoltaic cells.

In Chapter 6, sensing devices' fabrication capabilities were pushed further and a biosensor for the spike protein of the SARS-CoV-2 was fabricated. Using a silanisation method an aptamer probe molecule was attached to arrays of Ge NWs surface aligned at 10 MHz by DEP. Although the Ge NWs were exposed to water, the stable passivating shell provided by the silanisation had a two-fold effect; protection against dissolution (proved by water exposition tests) and functionalisation layer. This highlighted that although Ge has been disregarded because of its surface oxide it is still misunderstood and can be an advantage. Furthermore, upon exposure to increasing concentration of the spike protein, the sensor current response transduced an increasing signal as a direct result of the attachment of the negatively charged protein. The biosensor was proved to have a limit of detection of at least 1 aM with a working range of 1 aM to 100 fM. The specificity of the aptamer to detect the spike protein has been confirmed using bovine serum albumin (BSA) protein as a negative control. With a maximum current response of $\Delta I=3$ with the BSA compared to a minimum of $\Delta I=10$ with the spike protein, the attached aptamer confirmed its selectivity to the spike protein. The realisation of such NWs-based biosensors by DEP reveals a great prospective for biological detection. DEP has provided NW selection, reliability, selectivity, low power consumption, high surface area, and high carrier mobility that open the doors to a wide genetic field of detection with easily integrated nanomaterials. A future challenge for commercialisation can be the non-specific binding of other proteins or species from complex environments like blood and saliva. In the case of this thesis, it would have been insightful to test saliva from sick patients or to test a complete virus.

To further demonstrate the potential of DEP for NWs and their sensing properties, GaAsBi NWs were for the first time implemented in devices using DEP and later characterised for their potential characteristic as photodetectors. First of all, SEM images revealed that for differing Bi content and growth parameters of 3 different batches, the NWs presented distinct morphology amongst the batches. It was also revealed that during DEP, NWs could adapt to a bigger electrode gap environment by forming chains as a direct result of weaker DEP force.

Electric performances of chaining NWs are still not well known and hence, it would have been interesting to compare the performances with smaller electrode gap devices to obtain whole aligning NWs. Such rough morphology showed to strongly influenced DEP because of unstable attachment and alignment between the electrodes. More studies are necessary to understand the adhesive and molecular interaction between nanoparticles and surfaces like electrostatic surface charges, non-covalent interactions and hydrophobic forces. Nevertheless, for other batches and morphology NWs, the measured current response from the devices was symmetric as the NWs presented no chemical heterostructure. However, some asymmetry was observed for NWs presenting strong physical heterostructure and roughness including a triangular base and, some SCLC indicated defect states and possible scattering of the carriers by surface roughness. This showed the possibility that EP can not only influence the orientation of chemical heterostructure but also physical heterostructure. With increasing DEP frequency, the Fermi-velocity law exposed increasing carrier mobility of 5.29 ± 0.03 to $100 \pm 0.70 \text{ cm}^2\text{V}^{-1}\cdot\text{s}^{-1}$ at 500 kHz and 10 MHz despite chaining NWs (NWs from A) confirming DEP conductivity selection. Here, it would have been interesting to investigate the NW-NW contact by electron microscopy and AFM would have provided information on whether all the chained NWs are of similar increasing conductivity. The optical characteristics of the devices were investigated by photocurrent spectroscopy. For two differing Bi % content NWs a spectral shift was observed and, photocurrent peaks were measured at the energy of 1.4 to 1.8 eV wavelengths of 660 to 850 nm in the visible red and near-infrared respectively. Thanks to previous work on band-gap reduction with Bi % incorporation in bulk, a difference of 1 % in Bi incorporation was found in two different batches at 20 % of the maximum photocurrent intensity. With Bi % incorporation of 2.50 % and 1.56 % in GaAs, it was also found that the Bi % does not affect carrier mobility as similarly observed in the literature [207]. The performances of the obtained photodetectors were asserted by responsivity of $1.3 \times 10^4 \text{ A/W}$ with 1.56 % of Bi and $5.6 \times 10^4 \text{ A/W}$ with 2.50 % of Bi in GaAs at a wavelength of 660 to 850 nm. Such responsivity is ideal for applications from red to near-infrared light detectors and solar cells [330]. As a first investigation of GaAsBi NWs-based devices, the suggested further work is to investigate the growth parameters in order to obtain NWs with less surface roughness and disparity in morphology. This chapter highlighted the importance of surface morphology as more investigation on synthesis parameters is needed.

The novelty that presents this thesis relies on the usage of DEP for nanowires manipulation with extensive scientific input on the performances of the resulting device for sensing technology. For any nanoparticle, morphology or chemical nature, the surface plays a crucial role in the collection and alignment by DEP but also they are the foundation of the final device sensing characteristics. This suggests careful consideration of the NWs' dimensions and morphology in complement with implementation conditions when designing devices.

Bibliography

- [1] Igor L. Markov. Limits on fundamental limits to computation. *Nature*, 512(7513):147–154, 2014.
- [2] Siriny Laumier, Thomas Farrow, Harm van Zalinge, Luca Seravalli, Matteo Bosi, and Ian Sandall. Selection and Functionalization of Germanium Nanowires for Bio-Sensing. *ACS Omega*, 7(39):35288–35296, oct 2022.
- [3] Siti Fatimah Abd Rahman, Nor Azah, and Md Arshad. Fabrication of Silicon Nanowire Sensors for Highly Sensitive pH and DNA Hybridization Detection. *Nanomaterials*, 12(15):2652, 2022.
- [4] Yonatan Calahorra, Anke Husmann, Alice Bourdelain, Wonjong Kim, Jelena Vukajlovic-Plestina, Chess Boughey, Qingshen Jing, Anna Fontcuberta i Morral, and Sohini Kar-Narayan. Highly sensitive piezotronic pressure sensors based on undoped GaAs nanowire ensembles. *Journal of Physics D: Applied Physics*, 52(29):294002, jun 2019.
- [5] A. H. Reshak. Bismuth-containing semiconductors GaAs_{1-x}Bi_x for energy conversion: Thermoelectric properties. *Materials Science in Semiconductor Processing*, 148(June):106850, 2022.
- [6] Veerendra Dhyani and Samaresh Das. High speed MSM photodetector based on Ge nanowires network. *Semiconductor Science and Technology*, 32(5), apr 2017.
- [7] Mart Graef. More than moore white waper. In *2021 IEEE International Roadmap for Devices and Systems Outbriefs*, pages 1–47, 2021.
- [8] Tim Fryer. Life after silicon. *Engineering and Technology*, 13(9):62–65, 2018.
- [9] Abhimanyu Tharayil, R. Rajakumari, Amresh Kumar, Manabendra Dutta Choudhary, Parth Palit, and Sabu Thomas. New insights into application of nanoparticles in the diagnosis and screening of novel coronavirus (SARS-CoV-2). *Emergent Materials*, 4(1):101–117, 2021.
- [10] Min-Seung Jo, Hyeon-Joo Song, Beom-Jun Kim, Yoo-Kyum Shin, Sung-Ho Kim, Xu Tian, Sang-Min Kim, Min-Ho Seo, and Jun-Bo Yoon. Aligned CuO nanowire array for a high performance visible light photodetector. *Scientific Reports*, 12(1):2284, feb 2022.
- [11] Jim Kling. Moving diagnostics from the bench to the bedside. *Nature Biotechnology*, 24(8):891–893, aug 2006.

- [12] A. M. Sanchez, J. A. Gott, H. A. Fonseca, Y. Zhang, H. Liu, and R. Beanland. Stable Defects in Semiconductor Nanowires. *Nano Letters*, 18(5):3081–3087, 2018.
- [13] Fernando Patolsky and Charles M. Lieber. Nanowire nanosensors. *Materials Today*, 8(4):20–28, 2005.
- [14] Zhiming M Wang. *Nanoscale Sensors*, volume 19 of *Lecture Notes in Nanoscale Science and Technology*. Springer International Publishing, Cham, 2013.
- [15] Charles M Lieber. Nanoscale Science and Technology: Building a Big Future from Small Things. *MRS Bulletin*, 28(7):486–491, jul 2003.
- [16] Zhe Jiang, Quan Qing, Ping Xie, Ruixuan Gao, and Charles M. Lieber. Kinked p-n junction nanowire probes for high spatial resolution sensing and intracellular recording. *Nano Letters*, 12(3):1711–1716, 2012.
- [17] Zhiyang Li, Calvin Leung, Fan Gao, and Zhiyong Gu. Effects of nanowire length and surface roughness on the electrochemical sensor properties of nafion-free, Vertically aligned Pt nanowire array electrodes. *Sensors (Switzerland)*, 15(9):22473–22489, 2015.
- [18] Marios Constantinou, Kai F. Hoettges, Sergiy Krylyuk, Michael B. Katz, Albert Davydov, Grigorios Panagiotis Rigas, Vlad Stolojan, Michael P. Hughes, and Maxim Shkunov. Rapid determination of nanowires' electrical properties using a dielectrophoresis-well-based system. *Applied Physics Letters*, 110(13), 2017.
- [19] David G Grier. A revolution in optical manipulation. *Nature*, 424(6950):810–816, Aug 2003.
- [20] Kristian Mølhave, Thomas Wich, Axel Kortschack, and Peter Bøggild. Pick-and-place nanomanipulation using microfabricated grippers. *Nanotechnology*, 17(10):2434–2441, May 2006.
- [21] S. Yngman, F. Lenrick, Y.-P. Liu, Z. Ren, M. Khalilian, B. J. Ohlsson, D. Hessman, L. Samuelson, R. Timm, and A. Mikkelsen. GaN nanowires as probes for high-resolution atomic force and scanning tunneling microscopy. *Review of Scientific Instruments*, 90(10):103703, Oct 2019.
- [22] Michael C.P. P Wang and Byron D. Gates. Directed assembly of nanowires. *Materials Today*, 12(5):34–43, May 2009.
- [23] Sze. *Physics of Semiconductor Devices*, volume 10 of *Environmental Science and Engineering*. Springer International Publishing, Cham, 2007.
- [24] Erik P A M Bakkers, Magnus T Borgström, and Marcel A Verheijen. Epitaxial Growth of III-V Nanowires on Group IV Substrates. *MRS Bulletin*, 32(2):117–122, 2007.
- [25] Thomas Martensson, C Patrik T Svensson, Brent A Wacaser, Magnus W Larsson, Werner Seifert, Knut Deppert, Anders Gustafsson, L Reine Wallenberg, and Lars Samuelson. Epitaxial iii-v nanowires on silicon. *Nano Letters*, 4(10):1987,1990, Oct 2004.

- [26] Maria F Pantano and Irma Kuljanishvili. Advances in mechanical characterization of 1D and 2D nanomaterials: progress and prospects. *Nano Express*, 1(2):022001, Sep 2020.
- [27] Mostafa A El-Sayed. Some Interesting Properties of Metals Confined in Time and Nanometer Space of Different Shapes. *Accounts of Chemical Research*, 34(4):257–264, Apr 2001.
- [28] Martin Foldyna, Linwei Yu, Soumyadeep Misra, and Pere Roca i Cabarrocas Roca i Cabarrocas. Using nanowires to enhance light trapping in solar cells. *SPIE Newsroom*, (November):2–5, 2013.
- [29] Carlos Garcia Nunez Anastasios Vilouras, William Taube Navaraj, Fengyuan Liu, and Ravinder Dahiya. Zno nanowires-based flexible uv photodetector system for wearable dosimetry. *IEEE Sensors Journal*, 18(19):7881–7888, 2018.
- [30] R Könenkamp, Robert C Word, and C Schlegel. Vertical nanowire light-emitting diode. *Applied Physics Letters*, 85(24):6004–6006, Dec 2004.
- [31] P Agarwal, M N Vijayaraghavan, F Neuilly, E Hijzen, and G A M Hurkx. Breakdown Enhancement in Silicon Nanowire p-n Junctions. *Nano Letters*, 7(4):896–899, Apr 2007.
- [32] C Thelander, M T Björk, M W Larsson, A E Hansen, L R Wallenberg, and L Samuelson. Electron transport in InAs nanowires and heterostructure nanowire devices. *Solid State Communications*, 131(9):573–579, 2004.
- [33] Mikael T. Björk, Jonas Ohlsson, Torsten Sass, Ann I Persson, Claes Thelander, Martin H. Magnusson, Knut Deppert, Reine Wallenberg, and Lars Samuelson. One-dimensional steeplechase for electrons realized. *Nano Letters*, 2:87–89, 2002.
- [34] Michele Amato and Riccardo Ruruli. Surface physics of semiconducting nanowires Progress in Surface Science. *Progress in Surface Science*, 91(1):1–28, 2016.
- [35] John T. Fourkas. Nanoscale photolithography with visible light. *Journal of Physical Chemistry Letters*, 1(8):1221–1227, 2010.
- [36] S. Bangsaruntip, G. M. Cohen, A. Majumdar, Y. Zhang, S. U. Engelmann, N. C.M. Fuller, L. M. Gignac, S. Mittal, J. S. Newbury, M. Guillorn, T. Barwicz, L. Sekaric, M. M. Frank, and J. W. Sleight. High performance and highly uniform gate-all-around silicon nanowire MOSFETs with wire size dependent scaling. *Technical Digest- International Electron Devices Meeting, IEDM*, (April 2014):1–5, 2009.
- [37] Richard G. Hobbs, Nikolay Petkov, and Justin D. Holmes. Semiconductor nanowire fabrication by bottom-up and top-down paradigms. *Chemistry of Materials*, 24(11):1975–1991, Jun 2012.
- [38] Woong Ki Hong, Sunghoon Song, Dae Kue Hwang, Soon Shin Kwon, Gunho Jo, Seong Ju Park, and Takhee Lee. Effects of surface roughness on the electrical characteristics of ZnO nanowire field effect transistors. *Applied Surface Science*, 254(23):7559–7564, 2008.

- [39] R S Wagner and W C Ellis. Vapor, liquid, solid; mechanism of single crystal growth. *Applied Physics Letters*, 4:89–90, 1964.
- [40] Yi Cui, Lincoln J Lauhon, Mark S Gudixsen, Jianfang Wang, and Charles M Lieber. Diameter-controlled synthesis of single-crystal silicon nanowires. *Applied Physics Letters*, 78(15):2214–2216, 2001.
- [41] Pinion Christopher William. *Understanding the Vapor-Liquid-Solid and Vapor-Solid- Solid mechanisms of Si nanowire growth to synthetically encode precise nanoscale morphology*. PhD thesis, University of North Carolina, 2017.
- [42] Hong-yi Lee, Bo-wen Huang, Yi-ci Tsai, and Jiann Shieh. Rapid, Low-Temperature Growth of Sub-10 nm Silica Nanowires through Plasma Pretreatment for Antireflection Applications. *ACS Applied Nano Materials*, 2:2836–2843, 2019.
- [43] Yi-Hsin Liu, Ho-Ying Chen, Hsiu-Fang Fan, Yu-Hsien Chen, and Fudong Wang. Unique Growth Pathway in Solution–Solid–Solid Nanowires: Cubic to Hexagonal Phase Transformation. *ACS Omega*, 5(29):18441–18448, 2020.
- [44] Matteo Bosi, Luca Seravalli, Sara Beretta, and Claudio Ferrari. Growth of germanium nanowires with isobutyl germane. *Nanotechnology*, 30(8), 2019.
- [45] Lina Zou, Yinfeng Li, Shaokui Cao, and Baoxian Ye. Gold nanoparticles/polyaniline Langmuir–Blodgett Film modified glassy carbon electrode as voltammetric sensor for detection of epinephrine and uric acid. *Talanta*, 117:333–337, 2013.
- [46] Yu Huang, Xiangfeng Duan, Qingqiao Wei, Charles M Lieber, and Charles M. Lieber Yu Huang, Xiangfeng Duan, Qingqiao Wei. Directed Assembly of One-Dimensional Nanostructures into Functional Networks. *Science*, 291(5504):630–633, 2001.
- [47] M Tanase, D M Silevitch, A Hultgren, L A Bauer, P C Searson, G J Meyer, and D H Reich. Magnetic trapping and self-assembly of multicomponent nanowires. *Journal of Applied Physics*, 91(10):8549–8551, 2002.
- [48] Jun Yao, Hao Yan, and Charles M Lieber. A nanoscale combing technique for the large-scale assembly of highly aligned nanowires. *Nature Nanotechnology*, 8(5):329–335, 2013.
- [49] Guihua Yu, Anyuan Cao, and Charles M Lieber. Large-area blown bubble films of aligned nanowires and carbon nanotubes. *Nature nanotechnology*, 2(6):372–377, jun 2007.
- [50] Guihua Yu, Xianglong Li, Charles M Lieber, and Anyuan Cao. Nanomaterial-incorporated blown bubble films for large-area, aligned nanostructures. *J. Mater. Chem.*, 18(7):728–734, 2008.
- [51] Ritesh Agarwal, Kosta Ladavac, Yael Roichman, Guihua Yu, Charles M Lieber, and David G Grier. Manipulation and assembly of nanowires with holographic optical traps. *Opt. Express*, 13(22):8906–8912, oct 2005.

- [52] Kinneret Keren, Rotem S Berman, Evgeny Buchstab, Uri Sivan, and Erez Braun. DNA-Templated Carbon Nanotube Field-Effect Transistor. *Science*, 302(5649):1380–1382, 2003.
- [53] Joun et al. Lee. DNA Assisted Assembly of Multisegmented Nanowires. *Electroanalysis*, 19(22):2287–2293, 2007.
- [54] Wei Gao, Hiroki Ota, Daisuke Kiriya, Kuniharu Takei, and Ali Javey. Flexible Electronics toward Wearable Sensing. *Accounts of Chemical Research*, 52(3):523–533, 2019.
- [55] Giwon Lee, Haena Kim, Seon Baek Lee, Daegun Kim, Eunho Lee, Seong Kyu Lee, and Seung Goo Lee. Tailored Uniaxial Alignment of Nanowires Based on Off-Center Spin-Coating for Flexible and Transparent Field-Effect Transistors. *Nanomaterials*, 12(7):1116, mar 2022.
- [56] Y Huang, X Duan, Y Cui, L J Lauhon, K H Kim, and C M Lieber. Logic gates and computation from assembled nanowire building blocks. *Science (New York, N.Y.)*, 294(5545):1313–1317, nov 2001.
- [57] Andrea Tao, Franklin Kim, Christian Hess, Joshua Goldberger, Rongrui He, Yugang Sun, Younan Xia, and Peidong Yang. Langmuir-blodgett silver nanowire monolayers for molecular sensing using surface-enhanced raman spectroscopy. *Nano Letters*, 3(9):1229– 1233, 2003.
- [58] Dongmok Whang, Song Jin, Yue Wu, and Charles M Lieber. Large-Scale Hierarchical Organization of Nanowire Arrays for Integrated Nanosystems. *Nano Letters*, 3(9):1255– 1259, 2003.
- [59] Peter A. Smith, Christopher D. Nordquist, Thomas N. Jackson, Theresa S. Mayer, Benjamin R. Martin, Jeremiah Mbindyo, and Thomas E. Mallouk. Electric-field assisted assembly and alignment of metallic nanowires. *Applied Physics Letters*, 77(9):1399–1401, 2000.
- [60] Erik M. Freer, Oleg Grachev, Xiangfeng Duan, Samuel Martin, and David P. Stumbo. High-yield self-limiting single-nanowire assembly with dielectrophoresis. *Nature Nanotechnology*, 5(7):525–530, 2010.
- [61] Ronald Pethig, Ying Huang, Xiao Bo Wang, and Julian P.H. Burt. Positive and negative dielectrophoretic collection of colloidal particles using interdigitated castellated microelectrodes. *Journal of Physics D: Applied Physics*, 25(5):881–888, 1992.
- [62] Vishal Gupta, Insiya Jafferji, Miguel Garza, Vladislava O Melnikova, David K Hasegawa, Ronald Pethig, and Darren W Davis. ApoStreamTM, a new dielectrophoretic device for antibody independent isolation and recovery of viable cancer cells from blood. *Biomicrofluidics*, 6(2):24133, jun 2012.
- [63] Panasonic’s joint research paper receives iet nanobiotechnology premium award. <https://news.panasonic.com/global/topics/4620>. Accessed: 2022-02-30.

- [64] Shimadzu, particle size analyser. <https://www.shimadzu.co.uk/particle-size-analysis>. Accessed: 2022-02-03.
- [65] Georg R. Pesch and Fei Du. A review of dielectrophoretic separation and classification of non-biological particles. *Electrophoresis*, 42(1-2):134–152, 2021.
- [66] Kunitoshi Yamamoto, Seiji Akita, and Yoshikazu Nakayama. Orientation and purification of carbon nanotubes using ac electrophoresis. *Journal of Physics D: Applied Physics*, 31(8):L34–L36, apr 1998.
- [67] K D Hermanson, S O Lumsdon, J P Williams, E W Kaler, and O D Velev. Dielectrophoretic assembly of electrically functional microwires from nanoparticle suspensions. *Science (New York, N.Y.)*, 294(5544):1082–1086, 2001.
- [68] Khashayar Khoshmanesh, Saeid Nahavandi, Sara Baratchi, Arnan Mitchell, and Kouros Kalantarzadeh. Dielectrophoretic platforms for bio-microfluidic systems. *Biosensors and Bioelectronics*, 26(5):1800–1814, 2011.
- [69] Thomas B. Jones. *Electromechanics of Particles*, volume 89. Cambridge University Press, new york, cambridge university press edition, oct 1995.
- [70] Ronald Pethig. *Dielectrophoresis Theory, Methodology and Biological Applications*. Hoboken, NJ : John Wiley and Sons, Inc, 2017.
- [71] Sourobh Raychaudhuri, Shadi A. Dayeh, Deli Wang, and Edward T. Yu. Precise semiconductor nanowire placement through dielectrophoresis. *Nano Letters*, 9(6):2260–2266, 2009.
- [72] Enis Tuncer. Structure-property relationship in dielectric mixtures: Application of the spectral density theory. *Journal of Physics D: Applied Physics*, 38(2):223–234, 2005.
- [73] Hao Zhu, Qiliang Li, Hui Yuan, Helmut Baumgart, Dimitris E. Ioannou, and Curt A. Richter. Self-aligned multi-channel silicon nanowire field-effect transistors. *Solid-State Electronics*, 78:92–96, 2012.
- [74] Breton J May, Matthew R Belz, Arshad Ahamed, A T M G Sarwar, Camelia M Selcu, and Roberto C Myers. Nanoscale Electronic Conditioning for Improvement of Nanowire Light-Emitting-Diode Efficiency. *ACS Nano*, 12(4):3551–3556, 2018.
- [75] Marios Constantinou, Grigorios Panagiotis Rigas, Fernando A. Castro, Vlad Stolojan, Kai F. Hoettges, Michael P. Hughes, Emily Adkins, Brian A. Korgel, and Maxim Shkunov. Simultaneous Tunable Selection and Self-Assembly of Si Nanowires from Heterogeneous Feedstock. *ACS Nano*, 10(4):4384–4394, apr 2016.
- [76] Grigorios Rigas Maxim Shkunov and Marios Constantinou. Solution processable nanowire field-effect transistors. *Materials Research Society Symposium Proceedings*, 1287(July):69–74, 2011.

- [77] Kai F. Hoettges, Martin B. McDonnell, and Michael P. Hughes. Use of combined dielectrophoretic/electrohydrodynamic forces for biosensor enhancement. *Journal of Physics D: Applied Physics*, 36(20), oct 2003.
- [78] North Atlantic Treaty Organization Janos H. Fendler, Imre Dekany. *Nanoparticles in Solids and Solutions*. Springer Netherlands, Dordrecht, springer netherlands edition, 1996.
- [79] Colin Boxall. The electrophoresis of semiconductor particles. *Chemical Society Reviews*, 23(2):137, 1994.
- [80] Antonio et al. Aliano. AC Electrokinetics. In *Encyclopedia of Nanotechnology*, page 17. Springer Netherlands, 2012.
- [81] Kaiyan Yu, Jingang Yi, and Jerry W. Shan. Motion control, planning and manipulation of nanowires under electric-fields in fluid suspension. *IEEE Transactions on Automation Science and Engineering*, 12(1):37–49, 2015.
- [82] Juan Wu, Xilin Li, and Kaiyan Yu. Electrophoresis-Based Adaptive Manipulation of Nanowires in Fluid Suspension. *IEEE/ASME Transactions on Mechatronics*, 25(2):638– 649, 2020.
- [83] Devon A. Brown, Jong-Hoon Hoon Kim, Hyun-Boo Boo Lee, Gareth Fotouhi, Kyong-Hoon Hoon Lee, Wing Kam Liu, and Jae-Hyun Hyun Chung. Electric field guided assembly of one-dimensional nanostructures for high performance sensors. *Sensors (Switzerland)*, 12(5):5725–5751, 2012.
- [84] Rainer Dick. Dimensional Effects on Densities of States and Interactions in Nanostructures. *Nanoscale Research Letters*, 5(10):1546–1554, oct 2010.
- [85] Anqi Zhang, Gengfeng Zheng, and Charles M. Lieber. *Nanowires*. NanoScience and Technology. Springer International Publishing, Cham, 2016.
- [86] Xudong Wang, Jun Zhou, Jinhui Song, Jin Liu, Ningsheng Xu, and Zhong L Wang. Piezoelectric Field Effect Transistor and Nanoforce Sensor Based on a Single ZnO Nanowire. *Nano Letters*, 6(12):2768–2772, dec 2006.
- [87] Umesh Kumar Bhaskar, Thomas Pardoen, Vikram Passi, and Jean Pierre Raskin. Surface states and conductivity of silicon nanowires. *Journal of Applied Physics*, 113(13), 2013.
- [88] Luca Seravalli, Claudio Ferrari, and Matteo Bosi. Germanium nanowires as sensing devices: Modelization of electrical properties. *Nanomaterials*, 11(2):1–13, 2021.
- [89] Mo-Yuan Shen, Bor-Ran Li, and Yaw-Kuen Li. Silicon nanowire field-effect-transistor based biosensors: From sensitive to ultra-sensitive. *Biosensors and Bioelectronics*, 60:101–111, 2014.
- [90] S. Y. Lee, T. H. Kim, and D. I. Suh. An electrical characterization of a hetero-junction nanowire (NW) PN diode (n-GaN NW/p-Si) formed by dielectrophoresis alignment. *Physica E: Low-Dimensional Systems and Nanostructures*, 36(2):194–198, 2007.

- [91] Carlos Garcia Núñez, Alejandro F. Braa, Nair López, Jose L. Pau, and Basilio J. Garcia. Single GaAs nanowire based photodetector fabricated by dielectrophoresis. *Nanotechnology*, 31(22), 2020.
- [92] Jinyao Tang, Ziyang Huo, Sarah Brittan, Hanwei Gao, and Peidong Yang. Solution-processed core-shell nanowires for efficient photovoltaic cells. *Nature nanotechnology*, 6(9):568–572, aug 2011.
- [93] Jianping Meng and Zhou Li. Schottky-Contacted Nanowire Sensors. *Advanced Materials*, 32(28):1–16, 2020.
- [94] Stephen J Pearton. Wet and Dry Etching of Compound Semiconductors. In Paul H Holloway and Gary E McGuire, editors, *Handbook of Compound Semiconductors*, pages 370–441. William Andrew Publishing, Park Ridge, NJ, 1995.
- [95] A. Dimoulas, P. Tsipas, A. Sotiropoulos, and E. K. Evangelou. Fermi-level pinning and charge neutrality level in germanium. *Applied Physics Letters*, 89(25):12–15, 2006.
- [96] Won Il Park, Jin Suk Kim, Gyu Chul Yi, and Hu Jong Lee. ZnO nanorod logic circuits. *Advanced Materials*, 17(11):1393–1397, 2005.
- [97] Sandro Carrara, Davide Sacchetto, Marie Agnès Doucey, Camilla Baj-Rossi, Giovanni De Micheli, and Yusuf Leblebici. Memristive-biosensors: A new detection method by using nanofabricated memristors. *Sensors and Actuators, B: Chemical*, 171-172:449–457, 2012.
- [98] Peng Yang, Guangshuo Cai, Xinzhong Wang, and Yanli Pei. Electrolyte-Gated Indium Oxide Thin Film Transistor Based Biosensor With Low Operation Voltage. *IEEE Transactions on Electron Devices*, 66(8):3554–3559, 2019.
- [99] Kyoungmin Woo, Wonkyu Kang, Kyungmin Lee, Pilwoo Lee, Yoonjae Kim, Tae-Sik Yoon, Chu-Young Cho, Kyung-Ho Park, Min-Woo Ha, and Hyun Ho Lee. Enhancement of cortisol measurement sensitivity by laser illumination for AlGaIn/GaN transistor biosensor. *Biosensors and Bioelectronics*, 159:112186, 2020.
- [100] Akanksha et al. Roberts. Graphene functionalized field-effect transistors for ultrasensitive detection of Japanese encephalitis and Avian influenza virus. *Scientific reports*, 10(1):14546, sep 2020.
- [101] Fernando Patolsky, Gengfeng Zheng, Oliver Hayden, Melike Lakadamyali, Xiaowei Zhuang, and Charles M Lieber. Electrical detection of single viruses. *Proceedings of the National Academy of Sciences*, 101(39):14017–14022, 2004.
- [102] Anran Gao, Na Lu, Yuchen Wang, Pengfei Dai, Tie Li, Xiuli Gao, Yuelin Wang, and Chunhai Fan. Enhanced Sensing of Nucleic Acids with Silicon Nanowire Field Effect Transistor Biosensors. *Nano Letters*, 12(10):5262–5268, 2012.
- [103] Pengfei et al. Song. A microfluidic field-effect transistor biosensor with rolled-up indium nitride microtubes. *Biosensors and Bioelectronics*, 190:113264, 2021.

- [104] Prashanth Kumar, Papanasam Esakki, Lucky Agarwal, PeddaKrishna, Sumit Kale, and Brinda Bhowmick. Recent Progress on Sensitivity Analysis of Schottky Field Effect transistor Based Biosensors. *Silicon*, 15(1):25–35, jan 2023.
- [105] Mohit Kumar, Vijendra Singh Bhati, Sapana Ranwa, Jitendra Singh, and Mahesh Kumar. Pd/ZnO nanorods based sensor for highly selective detection of extremely low concentration hydrogen. *Scientific Reports*, 7(1):236, mar 2017.
- [106] Karl Skucha, Zhiyong Fan, Kanghoon Jeon, Ali Javey, and Bernhard Boser. Palladium/silicon nanowire Schottky barrier-based hydrogen sensors. *Sensors and Actuators, B: Chemical*, 145(1):232–238, 2010.
- [107] Guifeng Fan, Hongwei Zhu, Kunlin Wang, Jinquan Wei, Xinming Li, Qinke Shu, Ning Guo, and Dehai Wu. Graphene/Silicon Nanowire Schottky Junction for Enhanced Light Harvesting. *ACS Applied Materials and Interfaces*, 3(3):721–725, 2011.
- [108] F. Puppò, F. L. Traversa, M. De Ventra, G. De Micheli, and S. Carrara. Surface trap mediated electronic transport in biofunctionalized silicon nanowires. *Nanotechnology*, 27(34), 2016.
- [109] Anil W Dey, Johannes Svensson, Martin Ek, Erik Lind, Claes Thelander, and Lars-Erik Wernersson. Combining Axial and Radial Nanowire Heterostructures: Radial Esaki Diodes and Tunnel Field-Effect Transistors. *Nano Letters*, 13(12):5919–5924, 2013.
- [110] M T Björk, B J Ohlsson, C Thelander, A I Persson, K Deppert, L R Wallenberg, and L Samuelson. Nanowire resonant tunneling diodes. *Applied Physics Letters*, 81(23):4458–4460, 2002.
- [111] Dmitry B. et al. Suyatin. Strong schottky barrier reduction at Au-catalyst/GaAs-nanowire interfaces by electric dipole formation and fermi-level unpinning. *Nature Communications*, 5:1–8, 2014.
- [112] C Thelander, T Mårtensson, M T Björk, B J Ohlsson, M W Larsson, L R Wallenberg, and L Samuelson. Single-electron transistors in heterostructure nanowires. *Applied Physics Letters*, 83(10):2052–2054, 2003.
- [113] Yiyang Wu, Rong Fan, and Peidong Yang. Block-by-Block Growth of Single-Crystalline Si/SiGe Superlattice Nanowires. *Nano Letters*, 2(2):83–86, 2002.
- [114] Jonas Johansson and Kimberly A Dick. Recent advances in semiconductor nanowire heterostructures. *CrystEngComm*, 13(24):7175, 2011.
- [115] Alex M Lord, Quentin M Ramasse, Despoina M Kepaptsoglou, Jonathan E Evans, Philip R Davies, Michael B Ward, and Steve P Wilks. Modifying the Interface Edge to Control the Electrical Transport Properties of Nanocontacts to Nanowires. *Nano Letters*, 17(2):687–694, feb 2017.

- [116] Francois Leonard, Alec Talin, B. S. Swartzentruber, and S. T. Picraux. Diameter-dependent electronic transport properties of Au-Catalyst/Ge-nanowire Schottky diodes. *Physical Review Letters*, 102(10):1–4, 2009.
- [117] Raymond T Tung. The physics and chemistry of the Schottky barrier height. *Applied Physics Reviews*, 1(1):011304, mar 2014.
- [118] Sharma. *Metal-Semiconductor Schottky Barrier Junctions and Their Applications*. Springer US, Boston, MA, 1984.
- [119] Jin et al. Zou. Nanowire morphology Growth Mechanism of Truncated Triangular III-V Nanowires. *small*, 3(3):389–393, 2007.
- [120] Fedja J. Wendisch, Mehri Abazari, Hossein Mahdavi, Marcel Rey, Nicolas Vogel, Maurizio Musso, Oliver Diwald, and Gilles R. Bourret. Morphology-Graded Silicon Nanowire Arrays via Chemical Etching: Engineering Optical Properties at the Nanoscale and Macroscale. *ACS Applied Materials and Interfaces*, 12(11):13140–13147, mar 2020.
- [121] Amr Hisham K. Mahmoud, Fatma M. H. Korany, Christen Tharwat, Mohamed Hussein, Mohamed A. Swillam, Salah Sabry A. Obayya, and Mohamed Farhat O. Hameed. Surface roughness effect on characteristics of Si nanowire solar cell. *Journal of Photonics for Energy*, 10(04), 2020.
- [122] Ghada Yassin Abdel-Latif, Mohamed Farhat O Hameed, Mohamed Hussein, Maher Abdel Razzak, and Salah Sabry A Obayya. Characteristics of highly efficient star-shaped nanowires solar cell. *Journal of Photonics for Energy*, 8:47001, 2018.
- [123] Jing Wang, Eric Polizzi, Avik Ghosh, Supriyo Datta, and Mark Lundstrom. Theoretical investigation of surface roughness scattering in silicon nanowire transistors. *Applied Physics Letters*, 87(4):8–11, 2005.
- [124] Fengyun Wang, Senpo Yip, Ning Han, Kitwa Fok, Hao Lin, Jared J. Hou, Guofa Dong, Takfu Hung, K. S. Chan, and Johnny C. Ho. Surface roughness induced electron mobility degradation in InAs nanowires. *Nanotechnology*, 24(37), 2013.
- [125] L. A. Kosyachenko. Active region of CdTe X-/ γ -ray detector with Schottky diode. *Semiconductor physics, quantum electronics and optoelectronics*, 8(2):45–50, 2008.
- [126] Peng Zhang, Yee Sin Ang, Allen L. Garner, agúst Valfells, J. W. Luginsland, and L. K. Ang. Space-charge limited current in nanodiodes: Ballistic, collisional, and dynamical effects. *Journal of Applied Physics*, 129(10), 2021.
- [127] Philip A Leighton. Electronic Processes in Ionic Crystals (Mott, N. F.; Gurney, R. W.). *Journal of Chemical Education*, 18:249, 1941.

- [128] Nirat Ray, Nikita Gupta, Meghadeepa Adhikary, Nikolina Nekić, Lovro Basioli, Goran Dražić, Sigrid Bernstorff, and Maja Mičetić. Influence of Structure on Electronic Charge Transport in 3D Ge Nanowire Networks in an Alumina Matrix. *Scientific Reports*, 9(1):5432, apr 2019.
- [129] S Furukawa, T Kagawa, and N Matsumoto. Estimation of localized state distribution profiles in undoped and doped a-Si:H by measuring space-charge-limited current. *Solid State Communications*, 44(6):927–930, 1982.
- [130] Anna Cavallini and Laura Polenta. 3 - Electrical characterization of nanostructures. In Carlo Lamberti, editor, *Characterization of Semiconductor Heterostructures and Nano-structures*, pages 55–91. Elsevier, Amsterdam, 2008.
- [131] X. M. Shen, D. G. Zhao, Z. S. Liu, Z. F. Hu, H. Yang, and J. W. Liang. Space-charge- limited currents in GaN Schottky diodes. *Solid-State Electronics*, 49(5):847–852, 2005.
- [132] M. A. Rafiq. Carrier transport mechanisms in semiconductor nanostructures and devices. *Journal of Semiconductors*, 39(6), 2018.
- [133] Moumin Rudra, H S Tripathi, Alo Dutta, and T P Sinha. Existence of nearest-neighbor and variable range hopping in Pr₂ZnMnO₆ oxygen-intercalated pseudocapacitor electrode. *Materials Chemistry and Physics*, 258:123907, 2021.
- [134] Dongkyun Ko. Charge transport properties in semiconductor nanowires. *Sensors and Actuators, B: Chemical*, 119(6):12759–12765, 2014.
- [135] Dong Yu, Congjun Wang, Brian L. Wehrenberg, and Philippe Guyot-Sionnest. Variable range hopping conduction in semiconductor nanocrystal solids. *Phys. Rev. Lett.*, 92:216802, May 2004.
- [136] A Lösche. Electronic Processes in Non-Crystalline Materials. *Kristall und Technik*, 7(4):K55–K56, 1972.
- [137] Ho Jin et al. Lee. Intact Crystalline Semiconducting Graphene Nanoribbons from Unzipping Nitrogen-Doped Carbon Nanotubes. *ACS Applied Materials and Interfaces*, 11(41):38006–38015, 2019.
- [138] Yan Mao, Yu Bao, Wei Wang, Zhenggang Li, Fenghua Li, and Li Niu. Development and Application of Time-Resolved Surface Plasmon Resonance Spectrometer. *American Journal of Analytical Chemistry*, 02(05):589–604, 2011.
- [139] Il-Hoon Cho, Dong Hyung Kim, and Sangsoo Park. Electrochemical biosensors: perspective on functional nanomaterials for on-site analysis. *Biomaterials Research*, 24(1):6, 2020.
- [140] Takeo Hyodo, Masahiro Yuto, Hiroaki Tanigawa, Mioko Tsuruoka, Yuki Sakamoto, Taro Ueda, Kai Kamada, and Yasuhiro Shimizu. Solid-State FET-Based Sensors Capable of Measuring Acidity of Lubricants. *ECS Meeting Abstracts*, MA2020-01(30):2291, may 2020.

- [141] Joshua M. et al. Ziegler. Sensors Based Upon Nanowires, Nanotubes, and Nanoribbons: 2016-2020. *Analytical Chemistry*, 93(1):124–166, 2021.
- [142] Jeremy A. Streifer, Heesuk Kim, Beth M. Nichols, and Robert J. Hamers. Covalent functionalization and biomolecular recognition properties of DNA-modified silicon nanowires. *Nanotechnology*, 16(9):1868–1873, 2005.
- [143] Jillian M Buriak. Organometallic Chemistry on Silicon and Germanium Surfaces. *Chemical Reviews*, 102(5):1271–1308, 2002.
- [144] F Uslu, S Ingebrandt, D Mayer, S Böcker-Meffert, M Odenthal, and A Offenhäusser. Label free fully electronic nucleic acid detection system based on a field-effect transistor device. *Biosensors and bioelectronics*, 19(12):1723–1731, jul 2004.
- [145] Martin Stutzmann, Jose Antonio Garrido, Martin Eickhoff, and Martin S. Brandt. Direct biofunctionalization of semiconductors: A survey. *Physica Status Solidi (A) Applications and Materials Science*, 203(14):3424–3437, 2006.
- [146] Paul W. Loscutoff and Stacey F. Bent. Reactivity of the germanium surface: Chemical passivation and functionalization. *Annual Review of Physical Chemistry*, 57:467–495, 2006.
- [147] Y. Cui, Q. Wei, H. Park, and C. M. Lieber. Nanowire nanosensors for highly sensitive and selective detection of biological and chemical species. *Science*, 293(5533):1289–1292, 2001.
- [148] Pooria Namdari, Hadis Daraee, and Ali Eatemadi. Recent Advances in Silicon Nanowire Biosensors: Synthesis Methods, Properties, and Applications. *Nanoscale Research Letters*, 11(1), 2016.
- [149] Yen Heng Lin, Jing Chao Wong, and Yong Sheng Peng. Characterization of the electrical properties of silicon nanowire using the dielectrophoretic assembling platform. *International Journal of Electrochemical Science*, 12(9):8651–8662, 2017.
- [150] Yogeswaran Umasankar and Shen Ming Chen. A review on the electrochemical sensors and biosensors composed of nanowires as sensing material. *Sensors*, 8(1):290–313, 2008.
- [151] Arun Kumar, Shyam Aravamudhan, Milorad Gordic, Shekhar Bhansali, and Shyam S Mohapatra. Ultrasensitive detection of cortisol with enzyme fragment complementation technology using functionalized nanowire. *Biosensors and bioelectronics*, 22(9-10):2138– 2144, apr 2007.
- [152] Nishant Chandra. Nanowire Specialty Diodes for Integrated Applications. *Angewandte Chemie International Edition*, 6(11), 951–952., (May), 2014.
- [153] Shaili Sett, K. Das, and A. K. Raychaudhuri. Investigation of factors affecting electrical contacts on single germanium nanowires. *Journal of Applied Physics*, 121(12), 2017.
- [154] Cheng Qi, Gary Goncher, Raj Solanki, and Jay Jordan. SiGe nanowire growth and characterization. *Nanotechnology*, 18(7):75302, jan 2007.
- [155] Li Z. Pei and Zheng Y. Cai. A Review on Germanium Nanowires. *Recent Patents on Nanotechnology*, 6(1):44–59, jan 2012.

- [156] Dunwei Wang, Qian Wang, Ali Javey, Ryan Tu, Hongjie Dai, Hyounsub Kim, Paul C McIntyre, Tejas Krishnamohan, and Krishna C Saraswat. Germanium nanowire field-effect transistors with SiO₂ and high- κ HfO₂ gate dielectrics. *Applied Physics Letters*, 83(12):2432–2434, 2003.
- [157] Michele Amato, Maurizia Palummo, Riccardo Rurali, and Stefano Ossicini. Silicon–Germanium Nanowires: Chemistry and Physics in Play, from Basic Principles to Advanced Applications. *Chemical Reviews*, 114(2):1371–1412, jan 2014.
- [158] Hung Yu Ye, Chia Che Chung, and C. W. Liu. Mobility Calculation of Ge Nanowire Junctionless and Inversion-Mode Nanowire NFETs With Size and Shape Dependence. *IEEE Transactions on Electron Devices*, 65(12):5295–5300, 2018.
- [159] Yann-Michel Niquet, Christophe Delerue, and Christophe Krzeminski. Effects of Strain on the Carrier Mobility in Silicon Nanowires. *Nano Letters*, 12(7):3545–3550, 2012.
- [160] G. Gu, M. Burghard, G. T. Kim, G. S. Düsberg, P. W. Chiu, V. Krstic, S. Roth, and W. Q. Han. Growth and electrical transport of germanium nanowires. *Journal of Applied Physics*, 90(11):5747–5751, 2001.
- [161] Han-Kyu Seong, Eun-Kyoung Jeon, Myoung-Ha Kim, Hwangyou Oh, Jeong-O Lee, Ju-Jin Kim, and Heon-Jin Choi. Interface Charge Induced p-Type Characteristics of Aligned Si_{1-x}Gex Nanowires. *Nano Letters*, 8(11):3656–3661, 2008.
- [162] Tobias Hanrath and Brian A. Korgel. Influence of surface states on electron transport through intrinsic Ge nanowires. *Journal of Physical Chemistry B*, 109(12):5518–5524, 2005.
- [163] H Statz, G A DeMars, L Davis, and A Adams. Surface States on Silicon and Germanium Surfaces. *Phys. Rev.*, 101(4):1272–1281, feb 1956.
- [164] J Bardeen, R E Coover, S R Morrison, J R Schrieffer, and R Sun. Surface Conductance and the Field Effect on Germanium. *Phys. Rev.*, 104(1):47–51, oct 1956.
- [165] Gillian Collins and Justin D. Holmes. Chemical functionalisation of silicon and germanium nanowires. *Journal of Materials Chemistry*, 21(30):11052, 2011.
- [166] Byungwook Yoo, Ananth Dodabalapur, Doh Lee, Tobias Hanrath, and Brian Korgel. Germanium nanowire transistors with ethylene glycol treated poly(3,4-ethylenedioxythiophene):poly(styrene sulfonate) contacts. *Applied Physics Letters*, 90:72106, 2007.
- [167] Myung Gil Kang, Dong Hoon Hwang, Byung Sung Kim, Dongmok Whang, and Sung Woo Hwang. RF characterization of germanium nanowire field effect transistors. *AIP Conference Proceedings*, 1399(December):319–320, 2011.

- [168] M. Merhej, T. Honegger, F. Bassani, T. Baron, D. Peyrade, D. Drouin, and B. Salem. Direct measurement of AC electrokinetics properties and capture frequencies of silicon and silicon-germanium nanowires. *Semiconductor Science and Technology*, 33(1), 2018.
- [169] Boris Polyakov, Brian Daly, Juris Prikulis, Vaclovas Lissauskas, Bonifacas Vengalis, Michael A. Morris, Justin D. Holmes, and Donats Erts. High-density arrays of Germanium nanowire photoresistors. *Advanced Materials*, 18(14):1812–1816, 2006.
- [170] Jan Söderkvist. A phenomenological method of predicting the performance of piezoelectric beams. *Journal of Micromechanics and Microengineering*, 1(1):16–24, 1991.
- [171] Kouros Kalantar-zadeh. *Nanotechnology Enables Sensors*. Springer New York, NY, 2008.
- [172] Xuezhe Yu, Lixia Li, Hailong Wang, Jiaying Xiao, Chao Shen, Dong Pan, and Jianhua Zhao. Two-step fabrication of self-catalyzed Ga-based semiconductor nanowires on Si by molecular-beam epitaxy. *Nanoscale*, 8(20):10615–10621, 2016.
- [173] C. Kirchner, M. George, B. Stein, W. J. Parak, H. E. Gaub, and M. Seitz. Corrosion protection and long-term chemical functionalization of gallium arsenide in an aqueous environment. *Advanced Functional Materials*, 12(4):266–276, 2002.
- [174] K Gartsman, D Cahen, A Kadyshevitch, J Libman, T Moav, R Naaman, A Shanzer, V Umansky, and A Vilan. Molecular control of a GaAs transistor. *Chemical Physics Letters*, 283(5):301–306, 1998.
- [175] Josef A Czaban, David A Thompson, and Ray R LaPierre. GaAs Core-Shell Nanowires for Photovoltaic Applications. *Nano Letters*, 9(1):148–154, 2009.
- [176] Richard D Schaller, Vladimir M Agranovich, and Victor I Klimov. High-efficiency carrier multiplication through direct photogeneration of multi-excitons via virtual single-exciton states. *Nature Physics*, 1(3):189–194, 2005.
- [177] Antonio Luque, Antonio Marti, and Arthur J Nozik. Solar Cells Based on Quantum Dots: Multiple Exciton Generation and Intermediate Bands. *MRS Bulletin*, 32(3):236–241, 2007.
- [178] Xiao Li, Xuezhe Yu, Haotian Zeng, Giorgos Boras, Kai Shen, Yunyan Zhang, Jiang Wu, Kwang Leong Choy, and Huiyun Liu. Optimizing GaAs nanowire-based visible-light photodetectors. *Applied Physics Letters*, 119(5), 2021.
- [179] A. Erlacher, M. Ambrico, V. Capozzi, V. Augelli, H. Jaeger, and B. Ullrich. X-ray, absorption and photocurrent properties of thin-film GaAs on glass formed by pulsed-laser deposition. *Semiconductor Science and Technology*, 19(11):1322–1324, 2004.
- [180] Ke Xu, Jing Hou, Jian Liu, Mengxin Li, Kuan Huang, and Yuanwei Qi. Study on assembly method for GaAs nanowires device. *Integrated Ferroelectrics*, 151(1):187–192, 2014.

- [181] Xiaoguang Sun, Shuling Wang, J S Hsu, R Sidhu, X G Zheng, Xiaowei Li, J C Campbell, and A L Holmes. GaAsSb: a novel material for near infrared photodetectors on GaAs substrates. *IEEE Journal of Selected Topics in Quantum Electronics*, 8(4):817–822, 2002.
- [182] Kohei Chiba, Akinobu Yoshida, Katsuhiro Tomioka, and Junichi Motohisa. Vertical InGaAs Nanowire Array Photodiodes on Si. *ACS Photonics*, 6(2):260–264, 2019.
- [183] Dhruv Saxena, Sudha Mokkaapati, Patrick Parkinson, Nian Jiang, Qiang Gao, Hark Hoe Tan, and Chennupati Jagadish. Optically pumped room-temperature GaAs nanowire lasers. *Nature Photonics*, 7(12):963–968, 2013.
- [184] Z. Chine, H. Fitouri, I. Zaied, A. Rebey, and B. El Jani. Photoreflectance and photoluminescence study of annealing effects on GaAsBi layers grown by metalorganic vapor phase epitaxy. *Semiconductor Science and Technology*, 25(6), 2018.
- [185] K Collar, J Li, W Jiao, Y Guan, M Losurdo, J Humlicek, and A S Brown. Determination of the impact of Bi content on the valence band energy of GaAsBi using x-ray photoelectron spectroscopy. *AIP Advances*, 7:75016, 2017.
- [186] Xing Dai, Sen Zhang, Zilong Wang, Giorgio Adamo, Hai Liu, Yizhong Huang, Christophe Couteau, and Cesare Soci. GaAs/AlGaAs Nanowire Photodetector. *Nano Letters*, 14(5):2688–2693, 2014.
- [187] Andreas Biermanns, Torsten Rieger, Genziana Bussone, Ullrich Pietsch, Detlev Grützmacher, and Mihail Ion Lepsa. Axial strain in GaAs/InAs core-shell nanowires. *Applied Physics Letters*, 102(4):43109, 2013.
- [188] B. Fluegel, S. Francoeur, A. Mascarenhas, S. Tixier, E. C. Young, and T. Tiedje. Giant spin-orbit bowing in GaAs_{1-x}Bi_x. *Physical Review Letters*, 97(6):11–14, aug 2006.
- [189] A Abdiche, H Abid, R Riane, and A Bouaza. Structural and electronic properties of zinc blend GaAs_{1-x}Bi_x solid solutions. *Physica B: Condensed Matter*, 405(9):2311–2316, 2010.
- [190] H Fitouri, I Moussa, A Rebey, and B El Jani. Study of GaAsBi MOVPE growth on (100) GaAs substrate under high Bi flow rate by high resolution X-ray diffraction. *Microelectronic Engineering*, 88(4):476–479, 2011.
- [191] S. Tixier, M. Adamcyk, T. Tiedje, S. Francoeur, A. Mascarenhas, Peng Wei, and F. Schiettekatte. Molecular beam epitaxy growth of GaAs-zBi_x. *Applied Physics Letters*, 82(14):2245–2247, apr 2003.
- [192] Wenwu Pan, Lijuan Wang, Yanchao Zhang, Wen Lei, and Shumin Wang. MBE growth strategy and optimization of GaAsBi quantum well light emitting structure beyond 1.2 μm . *Applied Physics Letters*, 114(15):152102, 2019.

- [193] Fumitaro Ishikawa, Yoshihiko Akamatsu, Kentaro Watanabe, Fumihiko Uesugi, Shunsuke Asahina, Uwe Jahn, and Satoshi Shimomura. Metamorphic GaAs/GaAsBi Hetero-structured Nanowires. *Nano Letters*, 15(11):7265–7272, 2015.
- [194] Y Essouda, H Fitouri, R Boussaha, N Elayech, A Rebey, and B El Jani. Bismuth catalyzed growth of GaAsBi nanowires by metalorganic vapor phase epitaxy. *Materials Letters*, 152:298–301, 2015.
- [195] Lu Ding, Pengfei Lu, Huawei Cao, Ningning Cai, Zhongyuan Yu, Tao Gao, and Shumin Wang. Bismuth alloying properties in GaAs nanowires. *Journal of Solid State Chemistry*, 205:44–48, 2013.
- [196] K Alberi, J Wu, W Walukiewicz, K M Yu, O D Dubon, S P Watkins, C X Wang, X Liu, Y.-J. Cho, and J Furdyna. Valence-band anticrossing in mismatched III-V semiconductor alloys. *Phys. Rev. B*, 75(4):45203, jan 2007.
- [197] Anderson Janotti, Su-Huai Wei, and S Zhang. Theoretical study of the effects of isovalent coalloying of Bi and N in GaAs. *Physical Review B*, 65:115203, 2002.
- [198] J P Petropoulos, Y Zhong, and J M O Zide. Optical and electrical characterization of InGaBiAs for use as a mid-infrared optoelectronic material. *Applied Physics Letters*, 99(3):31110, 2011.
- [199] Lijuan Wang, Liyao Zhang, Li Yue, Dan Liang, Xiren Chen, Yaoyao Li, Pengfei Lu, Jun Shao, and Shumin Wang. Novel dilute bismide, epitaxy, physical properties and device application. *Crystals*, 7(3):1–60, 2017.
- [200] Kazuma Ikeda, Han Xiuxun, Bouzazi Boussairi, and Yoshio Ohshita. GaAsN Grown by Chemical Beam Epitaxy for Solar Cell Application. In Arturo Morales-Acevedo, editor, *Solar Cells*, chapter 10. IntechOpen, Rijeka, 2013.
- [201] S Nargelas, K Jarašiūnas, K Bertulis, and V Pačebutas. Hole diffusivity in GaAsBi alloys measured by a picosecond transient grating technique. *Applied Physics Letters*, 98(8):82115, 2011.
- [202] L. Seravalli, M. Bosi, S. Beretta, F. Rossi, D. Bersani, N. Musayeva, and C. Ferrari. Extra-long and taper-free germanium nanowires: Use of an alternative Ge precursor for longer nanostructures. *Nanotechnology*, 30(41), 2019.
- [203] R. et al. Jakomin. High quality tensile-strained n-doped germanium thin films grown on InGaAs buffer layers by metal-organic chemical vapor deposition. *Applied Physics Letters*, 98(9):091901, feb 2011.
- [204] Kunishige OE and Hiroshi Okamoto. New Semiconductor Alloy GaAs_{1-x}Bi_x Grown by Metal Organic Vapor Phase Epitaxy. *Japanese Journal of Applied Physics*, 37(Part 2, No. 11A):L1283—L1285, nov 1998.
- [205] Kunishige Oe. Characteristics of Semiconductor Alloy GaAs_{1-x}Bi_x. *Japanese Journal of Applied Physics*, 41(Part 1, No. 5A):2801–2806, may 2002.

- [206] N. Erhard and A. Holleitner. Semiconductor nanowires studied by photocurrent spectroscopy. *Semiconductor Nanowires: Materials, Synthesis, Characterization and Applications*, pages 365–391, 2015.
- [207] R. N. Kini, L. Bhusal, A. J. Ptak, R. France, and A. Mascarenhas. Electron hall mobility in GaAsBi. *Journal of Applied Physics*, 106(4), 2009.
- [208] Iona Heath, John Berger, and K Alavi. Molecular Beam Epitaxy. In *Encyclopedia of Materials: Science and Technology*, volume 27, pages 5765–5780. Elsevier, nov 2001.
- [209] Horst L Stormer and Daniel C Tsui. The Quantized Hall Effect. *Science*, 220:1241–1246, 1983.
- [210] X. Lu, D. A. Beaton, R. B. Lewis, T. Tiedje, and M. B. Whitwick. Effect of molecular beam epitaxy growth conditions on the Bi content of GaAs_{1-x}Bi_x. *Applied Physics Letters*, 92(19):1–4, 2008.
- [211] S Landis. *Lithography*. ISTE. Wiley, 2013.
- [212] Luca De Stefano, Giorgia Oliviero, Jussara Amato, Nicola Borbone, Gennaro Piccialli, Luciano Mayol, Ivo Rendina, Monica Terracciano, and Ilaria Rea. Aminosilane functionalizations of mesoporous oxidized silicon for oligonucleotide synthesis and detection. *Journal of The Royal Society Interface*, 10(83):20130160, jun 2013.
- [213] Jiakun Xu, Jingjing Sun, Yuejun Wang, Jun Sheng, Fang Wang, and Mi Sun. Application of Iron Magnetic Nanoparticles in Protein Immobilization. *Molecules*, 19(8):11465–11486, 2014.
- [214] Yanling Song, Jia Song, Xinyu Wei, Mengjiao Huang, Miao Sun, Lin Zhu, Bingqian Lin, Haicong Shen, Zhi Zhu, and Chaoyong Yang. Discovery of Aptamers Targeting the Receptor-Binding Domain of the SARS-CoV-2 Spike Glycoprotein. *Analytical Chemistry*, 92(14):9895–9900, 2020.
- [215] Jean-Sebastien Lecomte. *Introduction to transmitted electron microscopy*. University of Lorraine France, January 2018.
- [216] X Zhou and G.E. Thompson. *Electron and Photon Based Spatially Resolved Techniques*. Number May 2015. Elsevier Ltd., 2017.
- [217] John Rodenburg. A record-breaking microscope news-and-views. *Nature*, 559(7714):334–335, 2018.
- [218] Yi et al. Jiang. Electron ptychography of 2D materials to deep subangström resolution. *Nature*, 559(7714):343–349, 2018.
- [219] A J Garratt-Reed, D C Bell, and Patrick Nicholson. Energy-dispersive X-ray analysis in the electron microscope. *Bios Scientific Publishers*, 25(3):162–162, 2006.

- [220] Lan Ling and Wei Xian Zhang. Mapping the reactions of hexavalent chromium [Cr(vi)] in iron nanoparticles using spherical aberration corrected scanning transmission electron microscopy (Cs-STEM). *Analytical Methods*, 6(10):3211–3214, 2014.
- [221] Prof. Leonard J. Brillson. *Surface and Interfacial Forces Introduction to Microsystem Technology*. Wiley-VCH, Berlin, 2010.
- [222] D Lin-Vien, N B Colthup, W G Fateley, and J G Grasselli. *The Handbook of Infrared and Raman Characteristic Frequencies of Organic Molecules*. Elsevier Science, 1991.
- [223] Daniel Wolverson. 8 - Raman spectroscopy. In Carlo Lamberti, editor, *Characterization of Semiconductor Heterostructures and Nanostructures*, pages 249–288. Elsevier, Amsterdam, 2008.
- [224] George Socrates. *Infrared and Raman*, volume 296. JOHN WILEY and SONS, LTD Chichester., 1994.
- [225] Kruss-scientific. Drop shape analysis. <https://www.kruss-scientific.com/>. Accessed: 2022-08-30.
- [226] Jeffrey D Clogston and Anil K Patri. *Zeta Potential Measurement*, pages 63–70. Humana Press, Totowa, NJ, 2011.
- [227] Linyou Cao, Justin S. White, Joon Shik Park, Jon A. Schuller, Bruce M. Clemens, and Mark L. Brongersma. Engineering light absorption in semiconductor nanowire devices. *Nature Materials*, 8(8):643–647, 2009.
- [228] L H Bennett. Electronic density of states. Technical report, U.S. Department of Energy Office of Scientific and Technical Information, United States, 1971.
- [229] R Paschotta. *Encyclopedia of Laser Physics and Technology 1*. Wiley VCH, 2008.
- [230] Kang L. Wang, Dongho Cha, Jianlin Liu, and Christopher Chen. Ge/Si self-assembled quantum dots and their optoelectronic device applications. *Proceedings of the IEEE*, 95(9):1866–1883, 2007.
- [231] P. K. Giri and Soumen Dhara. Freestanding Ge/GeO₂ core-shell nanocrystals with varying sizes and shell thicknesses: Microstructure and photoluminescence studies. *Journal of Nanomaterials*, 2012(May 2014), 2012.
- [232] Kaspar Snashall, Marios Constantinou, and Maxim Shkunov. Flow-assisted dielectrophoresis: A low cost method for the fabrication of high performance solution-processable nanowire devices. *Journal of Visualized Experiments*, 2017(130):1–8, 2017.
- [233] Sara Beretta, Matteo Bosi, Luca Seravalli, Paola Frigeri, Giovanna Trevisi, Enos Gombia, Francesca Rossi, Danilo Bersani, and Claudio Ferrari. Direct growth of germanium nanowires on glass. *Nanotechnology*, 31(39):394001, 2020.

- [234] A. S. Almuslem, A. N. Hanna, T. Yapici, N. Wehbe, E. M. Diallo, A. T. Kutbee, R. R. Bahabry, and M. M. Hussain. Water soluble nano-scale transient material germanium oxide for zero toxic waste based environmentally benign nano-manufacturing. *Applied Physics Letters*, 110(7), 2017.
- [235] T.B. Jones. Basic theory of dielectrophoresis and electrorotation. *IEEE Engineering in Medicine and Biology Magazine*, 22(6):33–42, nov 2003.
- [236] Yaling Liu, Jae Hyun Chung, Wing Kam Liu, and Rodney S. Ruoff. Dielectrophoretic assembly of nanowires. *Journal of Physical Chemistry B*, 110(29):14098–14106, 2006.
- [237] N. G. Green and H. Morgan. Separation of submicrometre particles using a combination of dielectrophoretic and electrohydrodynamic forces. *Journal of Physics D: Applied Physics*, 31(7):25–30, 1998.
- [238] Mingwei Li, Rustom B. Bhiladvala, Thomas J. Morrow, James A. Sioss, Kok Keong Lew, Joan M. Redwing, Christine D. Keating, and Theresa S. Mayer. Bottom-up assembly of large-area nanowire resonator arrays. *Nature Nanotechnology*, 3(2):88–92, 2008.
- [239] A. Castellanos, A. Ramos, A. Gonzalez, N. G. Green, and H. Morgan. Electrohydrodynamics and dielectrophoresis in microsystems: Scaling laws. *Journal of Physics D: Applied Physics*, 36(20):2584–2597, 2003.
- [240] J. H. Nieuwenhuis, A. Jachimowicz, P. Svasek, and M. J. Vellekoop. High-speed integrated particle sorters based on dielectrophoresis. *Proceedings of IEEE Sensors*, 1(3):64–67, 2004.
- [241] Khashayar Khoshmanesh, Chen Zhang, Saeid Nahavandi, Francisco J. Tovar-Lopez, Sara Baratchi, Zheng Hu, Arnan Mitchell, and Kouros Kalantarzadeh. Particle trapping using dielectrophoretically patterned carbon nanotubes. *Electrophoresis*, 31(8):1366–1375, 2010.
- [242] Zachary Gagnon, Jill Mazur, and Hsueh Chia Chang. Glutaraldehyde enhanced dielectrophoretic yeast cell separation. *Biomicrofluidics*, 3(4), 2009.
- [243] Nikhil Mittal, Adam Rosenthal, and Joel Voldman. nDEP microwells for single-cell patterning in physiological media. *Lab on a Chip*, 7(9):1146–1153, 2007.
- [244] Peter R.C. Gascoyne, Jody V. Vykoukal, Jon A. Schwartz, Thomas J. Anderson, Daynene M. Vykoukal, K. Wayne Current, Charles McConaghy, Frederick F. Becker, and Craig Andrews. Dielectrophoresis-based programmable fluidic processors. *Lab on a Chip*, 4(4):299–309, 2004.
- [245] J. Voldman, M. Toner, M. L. Gray, and M. A. Schmidt. Design and analysis of extruded quadrupolar dielectrophoretic traps. *Journal of Electrostatics*, 57(1):69–90, 2003.
- [246] Barbaros Çetin, Yuejun Kang, Zhemin Wu, and Dongqing Li. Continuous particle separation by size via AC-dielectrophoresis using a lab-on-a-chip device with 3-D electrodes. *Electrophoresis*, 30(5):766–772, 2009.

- [247] Nathan Swami, Chia Fu Chou, Venkatraman Ramamurthy, and Vasudha Chaurey. Enhancing DNA hybridization kinetics through constriction-based dielectrophoresis. *Lab on a Chip*, 9(22):3212–3220, 2009.
- [248] Hadi Shafiee, John L. Caldwell, Michael B. Sano, and Rafael V. Davalos. Contactless dielectrophoresis: A new technique for cell manipulation. *Biomedical Microdevices*, 11(5):997–1006, 2009.
- [249] Benjamin D. Smith, Theresa S. Mayer, and Christine D. Keating. Deterministic assembly of functional nanostructures using nonuniform electric fields. *Annual Review of Physical Chemistry*, 63:241–263, 2012.
- [250] H. Dai, T. Y. Wang, and M. C. Li. Spotlight on ultrasonic fracture behaviour of nanowires: Their size-dependent effect and prospect for controllable functional modification. *RSC Advances*, 6(76):72080–72085, 2016.
- [251] Nicolas G. Green and Hywel Morgan. Dielectrophoresis of submicrometer latex spheres. 1. Experimental results. *Journal of Physical Chemistry B*, 103(1):41–50, 1999.
- [252] Abhay K. Jain, Rajesh K. Srivastava, Manoj K. Gupta, and Suresh K. Das. A novel technique in membrane separation processes: Electroosmotic separation of benzene in ethanol solution. *Journal of Membrane Science*, 78(1-2):53–61, 1993.
- [253] Nicolas H. Beltran, Ricardo A. Finger, Jorge Santiago-Aviles, and Patricio Espinoza-Vallejos. Effect of parasitic capacitances on impedance measurements in microsensors structures: A numerical study. *Sensors and Actuators, B: Chemical*, 96(1-2):139–143, 2003.
- [254] Natacha Mureau, Ernest Mendoza, S. R.P. Silva, Kai F. Hoettges, and Michael P. Hughes. In situ and real time determination of metallic and semiconducting single-walled carbon nanotubes in suspension via dielectrophoresis. *Applied Physics Letters*, 88(24):2004–2007, 2006.
- [255] Ran Peng, Yueyue Pan, Biwu Liu, Zhi Li, Peng Pan, Shuailong Zhang, Zhen Qin, Aaron R. Wheeler, Xiaowu Tang, and Xinyu Liu. Understanding Carbon Nanotube-Based Ionic Diodes: Design and Mechanism. *Small*, 17(31):1–15, 2021.
- [256] R. B. Rakhi, K. Sethupathi, and S. Ramaprabhu. Field emission from carbon nanotubes on a graphitized carbon fabric. *Carbon*, 46(13):1656–1663, 2008.
- [257] Tobias Hanrath and Brian A. Korgel. Influence of surface states on electron transport through intrinsic Ge nanowires. *Journal of Physical Chemistry B*, 109(12):5518–5524, 2005.
- [258] James W Mayer. Gold contacts to semiconductor devices. *Gold Bulletin*, 17(1):18–26, mar 1984.
- [259] Kwan Chi Kao. 6 - Charge Carrier Injection from Electrical Contacts. In Kwan Chi Kao, editor, *Dielectric Phenomena in Solids*, pages 327–380. Academic Press, San Diego, 2004.

- [260] Munsik Oh, Won-Yong Jin, Hyeon Jun Jeong, Mun Seok Jeong, Jae-Wook Kang, and Hyunsoo Kim. Silver Nanowire Transparent Conductive Electrodes for High-Efficiency III-Nitride Light-Emitting Diodes OPEN. *Scientific Reports* /, 5:13483, 2015.
- [261] Murray A Lampert and Ronald B Schilling. Chapter 1 Current Injection in Solids: The Regional Approximation Method. In R K Willardson and Albert C Beer, editors, *Injection Phenomena*, volume 6 of *Semiconductors and Semimetals*, pages 1–96. Elsevier, 1970.
- [262] S. Alagha, A. Shik, H. E. Ruda, I. Saveliev, K. L. Kavanagh, and S. P. Watkins. Space-charge-limited current in nanowires. *Journal of Applied Physics*, 121(17), 2017.
- [263] E. J. Miller, D. M. Schaadt, E. T. Yu, C. Poblenz, C. Elsass, and J. S. Speck. Reduction of reverse-bias leakage current in Schottky diodes on GaN grown by molecular-beam epitaxy using surface modification with an atomic force microscope. *Journal of Applied Physics*, 91(12):9821–9826, 2002.
- [264] Son T. Le, P. Jannaty, A. Zaslavsky, S. A. Dayeh, and S. T. Picraux. Growth, electrical rectification, and gate control in axial in situ doped p-n junction germanium nanowires. *Applied Physics Letters*, 96(26):1–4, 2010.
- [265] Roberto Jakomin, Gregoire Beaudoin, Noelle Gogneau, Bruno Lamare, and Isabelle Sagnes. n and p-doped Germanium grown by MOVPE for solar cell applications. *Proceeding of the XIII European Workshop pn Metalorganic Vapor Phase Epitaxy Conference*, C.21(January):7–10, 2009.
- [266] Ahlem Rouis, Neila Hizem, Mohamed Hassen, and Adel Kalboussi. Electrical Properties of Silicon Nanowires Schottky Barriers Prepared by MACE at Different Etching Time. *Silicon*, 14(9):4731–4737, 2022.
- [267] S. De Cesari, A. Balocchi, E. Vitiello, P. Jahandar, E. Grilli, T. Amand, X. Marie, M. Myronov, and F. Pezzoli. Spin-coherent dynamics and carrier lifetime in strained germanium semiconductors on silicon. *Physical Review B*, 99(3):035202, jan 2019.
- [268] W. Chandra, L. K. Ang, K. L. Pey, and C. M. Ng. Two-dimensional analytical Mott-Gurney law for a trap-filled solid. *Applied Physics Letters*, 90(15):48–51, 2007.
- [269] Qiliang Li, Sang-Mo Koo, Curt A Richter, Monica D Edelstein, John E Bonevich, Joseph J Kopanski, John S Suehle, and Eric M Vogel. Precise Alignment of Single Nanowires and Fabrication of Nanoelectromechanical Switch and Other Test Structures. *IEEE Transactions on Nanotechnology*, 6(2):256–262, mar 2007.
- [270] National Grid. Voltage and Frequency Dependency. *Report*, page 6, 2018.
- [271] J J Ke, K T Tsai, Y A Dai, and J H He. Contact transport of focused ion beam-deposited Pt to Si nanowires: From measurement to understanding. *Applied Physics Letters*, 100(5):053503, jan 2012.
- [272] Jing Zhang, Shiyang Zhu, and Fei Sun. Dual-epitaxy Si/Ge broadband photodetector for application in cryogenic radiometer. *Optics Express*, 29(23):37489, nov 2021.

- [273] Emilio Fernandez Lisbona. Calibration, Testing, and Monitoring of Space Solar Cells. In *Solar Cells*, pages 501–529. Elsevier, second edition edition, 2013.
- [274] Ionel Stavarache, Valentin Serban Teodorescu, Petronela Prepelita, Constantin Logofatu, and Magdalena Lidia Ciurea. Ge nanoparticles in SiO₂ for near infrared photodetectors with high performance. *Scientific Reports*, 9(1):10286, jul 2019.
- [275] Shuo Li, Qiang Wu, Haokun Ding, Songsong Wu, Xinwei Cai, Rui Wang, Jun Xiong, Guangyang Lin, Wei Huang, Songyan Chen, and Cheng Li. High gain, broadband p-WSe₂/n-Ge van der Waals heterojunction phototransistor with a Schottky barrier collector. *Nano Research*, nov 2022.
- [276] Fan Yang, Hui Cong, Kai Yu, Lin Zhou, Nan Wang, Zhi Liu, Chuanbo Li, Qiming Wang, and Buwen Cheng. Ultrathin Broadband Germanium-Graphene Hybrid Photodetector with High Performance. *ACS Applied Materials and Interfaces*, 9(15):13422–13429, 2017.
- [277] Guangyang Lin, Dongxue Liang, Chunyu Yu, Haiyang Hong, Yichen Mao, Cheng Li, and Songyan Chen. Broadband 400-2400 nm Ge heterostructure nanowire photodetector fabricated by three-dimensional Ge condensation technique. *Optics Express*, 27(22):32801, 2019.
- [278] Shaili Sett, Ankita Ghatak, Deepak Sharma, G. V.Pavan Kumar, and A. K. Raychaudhuri. Broad Band Single Germanium Nanowire Photodetectors with Surface Oxide-Controlled High Optical Gain. *Journal of Physical Chemistry C*, 122(15):8564– 8572, apr 2018.
- [279] M Ijaz, Z Ghassemlooy, S Rajbhandari, H Le Minh, J Perez, and A Gholami. Comparison of 830 nm and 1550 nm based free space optical communications link under controlled fog conditions. In *2012 8th International Symposium on Communication Systems, Networks Digital Signal Processing (CSNDSP)*, pages 1–5. IEEE, jul 2012.
- [280] Gang Cheng, Zhaohan Li, Shujie Wang, Hechun Gong, Ke Cheng, Xiaohong Jiang, Shaomin Zhou, Zuliang Du, Tian Cui, and Guangtian Zou. The unsaturated photocurrent controlled by two-dimensional barrier geometry of a single ZnO nanowire Schottky photodiode. *Applied Physics Letters*, 93(12):123103, 2008.
- [281] Hassan et al. Ali. High-Responsivity Photodetection by a Self-Catalyzed Phase-Pure p-GaAs Nanowire. *Small*, 14(17):1704429, apr 2018.
- [282] Ziyuan Li, Jeffery Allen, Monica Allen, Hark Hoe Tan, Chennupati Jagadish, and Lan Fu. Review on III-V semiconductor single nanowire-based room temperature infrared photodetectors. *Materials*, 13(6), 2020.

- [283] Luying Li. Electron holography of nanowires – Part 1. In *Semiconductor Nanowires*, pages 221–251. Elsevier, 2015.
- [284] Malik Sulaiman, Norhana Arsad, Harry Ramza, Mohd Hazwan Harun, Hadi Guna, Farshad Nasimi, and Mohammad Syuhaimi AbRahman. Wavelength Division Multiplexing Network over Polymer Optical Fiber Using Fabricated Couplers for Informatics Communications. *Procedia Technology*, 11:1211–1217, 2013.
- [285] P. Boffi, M.C. Ubaldi, D. Piccinin, C. Frascolla, and M. Martinelli. 1550-nm volume holography for optical communication devices. *IEEE Photonics Technology Letters*, 12(10):1355–1357, 2000.
- [286] Linyou Cao, Joon Shik Park, Pengyu Fan, Bruce Clemens, and Mark L. Brongersma. Resonant germanium nanoantenna photodetectors. *Nano Letters*, 10(4):1229–1233, 2010.
- [287] Joon-Pekko Kakko, Antti Matikainen, Nicklas Anttu, Sami Kujala, Henrik Mäntynen, Vladislav Khayrudinov, Anton Autere, Zhipei Sun, and Harri Lipsanen. Measurement of Nanowire Optical Modes Using Cross-Polarization Microscopy. *Scientific Reports*, 7(1):17790, dec 2017.
- [288] Shaili Sett, Ankita Ghatak, Deepak Sharma, G. V.Pavan Kumar, and A. K. Raychaudhuri. Broad Band Single Germanium Nanowire Photodetectors with Surface Oxide-Controlled High Optical Gain. *Journal of Physical Chemistry C*, 122(15):8564– 8572, apr 2018.
- [289] Kimberly A Dick, Suneel Kodambaka, Mark C Reuter, Knut Deppert, Lars Samuelson, Werner Seifert, L Reine Wallenberg, and Frances M Ross. The Morphology of Axial and Branched Nanowire Heterostructures. *Nano Letters*, 7(6):1817–1822, jun 2007.
- [290] S Lischke, A Peczek, J S Morgan, K Sun, D Steckler, Y Yamamoto, F Korndörfer, C Mai, S Marschmeyer, M Fräschke, A Krüger, A Beling, and L Zimmermann. Ultra-fast germanium photodiode with 3-dB bandwidth of 265 GHz. *Nature Photonics*, 15(12):925–931, dec 2021.
- [291] Matteo Bosi and Giovanni Attolini. Germanium: Epitaxy and its applications. *Progress in Crystal Growth and Characterization of Materials*, 56(3):146–174, 2010.
- [292] M. Hiraoui, M. Guendouz, N. Lorrain, A. Moadhen, L. Haji, and M. Oueslati. Spectroscopy studies of functionalized oxidized porous silicon surface for biosensing applications. *Materials Chemistry and Physics*, 128(1-2):151–156, 2011.
- [293] Sungmoon Lee, Gabriel E. Choi, Chun Yang, Hai Chen Wu, and Junhua Yu. Autofluorescence generation and elimination: A lesson from glutaraldehyde. *Chemical Communications*, 49(29):3028–3030, 2013.

- [294] Hongti Zhang, Jerry Tersoff, Shang Xu, Huixin Chen, Qiaobao Zhang, Kaili Zhang, Yong Yang, Chun Sing Lee, King Ning Tu, Ju Li, and Yang Lu. Approaching the ideal elastic strain limit in silicon nanowires. *Science Advances*, 2(8):2–10, 2016.
- [295] Guangyu Qiu, Zhibo Gai, Yile Tao, Jean Schmitt, Gerd A Kullak-Ublick, and Jing Wang. Dual-Functional Plasmonic Photothermal Biosensors for Highly Accurate Severe Acute Respiratory Syndrome Coronavirus 2 Detection. *ACS Nano*, 14(5):5268–5277, 2020.
- [296] Giwan et al. Seo. Rapid Detection of COVID-19 Causative Virus (SARS-CoV-2) in Human Nasopharyngeal Swab Specimens Using Field-Effect Transistor-Based Biosensor. *ACS nano*, 14(4):5135–5142, 2020.
- [297] Parvin Fathi-Hafshejani, Nurul Azam, Lu Wang, Marcelo A Kuroda, Michael C Hamilton, Sahar Hasim, and Masoud Mahjouri-Samani. Two-Dimensional-Material-Based Field-Effect Transistor Biosensor for Detecting COVID-19 Virus (SARS-CoV-2). *ACS Nano*, 15(7):11461–11469, 2021.
- [298] Cao-An Vu and Wen-Yih Chen. Field-Effect Transistor Biosensors for Biomedical Applications: Recent Advances and Future Prospects. *Sensors (Basel, Switzerland)*, 19(19), sep 2019.
- [299] Parvin Fathi-Hafshejani, Nurul Azam, Lu Wang, Marcelo A Kuroda, Michael C Hamilton, Sahar Hasim, and Masoud Mahjouri-Samani. Two-Dimensional-Material-Based Field-Effect Transistor Biosensor for Detecting COVID-19 Virus (SARS-CoV-2). *ACS Nano*, 15(7):11461–11469, jul 2021.
- [300] Thomas Farrow, Siriny Laumier, Ian Sandall, and Harm van Zalinge. An Aptamer-Functionalised Schottky-Field Effect Transistor for the Detection of Proteins. *Bio-sensors*, 12(5), 2022.
- [301] K. Hild, Z. Batool, S. R. Jin, N. Hossain, I. P. Marko, T. J.C. Hosea, X. Lu, T. Tiedje, and S. J. Sweeney. Auger recombination suppression and band alignment in GaAs-Bi/GaAs heterostructures. In *AIP Conference Proceedings*, volume 1566, pages 488–489, 2013.
- [302] P Laukkanen, M P J Punkkinen, A Lahti, J Puustinen, M Tuominen, J Hilska, J M äkel ä, J Dahl, M Yasir, M Kuzmin, J R Osiecki, K Schulte, M Guina, and K Kokko. Local variation in Bi crystal sites of epitaxial GaAsBi studied by photoelectron spectroscopy and first-principles calculations. *Applied Surface Science*, 396:688–694, 2017.
- [303] P.C. McIntyre and A Fontcuberta i Morral. Semiconductor nanowires: to grow or not to grow? *Materials Today Nano*, 9:100058, mar 2020.
- [304] J A Creighton and R Withnall. The Raman spectrum of gallium metal. *Chemical Physics Letters*, 326(3):311–313, 2000.

- [305] Nikolas Antonatos, Vlastimil Mazanek, Petr Lazar, Jiri Sturala, and Zdenek Sofer. Acetonitrile-Assisted Exfoliation of Layered Grey and Black Arsenic: Contrasting Properties. *Nanoscale Advances*, 2, 2020.
- [306] Marco A. Zepeda, Michel Picquart, and Emmanuel Haro-Poniatowski. Laser Induced Oxidation Effects in Bismuth Thin Films. *MRS Proceedings*, 1477:imrc12–1477–s1a– p016, jan 2012.
- [307] D Spirkoska, G Abstreiter, and A Fontcuberta i Morral. Size and environment dependence of surface phonon modes of gallium arsenide nanowires as measured by Raman spectroscopy. *Nanotechnology*, 19(43):435704, sep 2008.
- [308] W.J. Choi, H Rho, J.D. Song, J.I. Lee, and Y.H. Cho. Raman scattering from InGaAs/GaAs quantum dot structures grown by atomic layer molecular beam epitaxy. *Physica E: Low-dimensional Systems and Nanostructures*, 26(1-4):115–118, feb 2005.
- [309] Renata et al. Butkute. Bismuth Quantum Dots in Annealed GaAsBi/AlAs Quantum Wells. *Nanoscale Research Letters*, 12, 2017.
- [310] A Erol, E Akalin, K Kara, M Aslan, V Bahrami-Yekta, R.B. Lewis, and T Tiedje. Raman and AFM studies on nominally undoped, p- and n-type GaAsBi alloys. *Journal of Alloys and Compounds*, 722:339–343, oct 2017.
- [311] J. A. Steele, R. A. Lewis, Mohamed Henini, O M Lemine, D Fan, Yu. I. Mazur, V. G. Dorogan, P. C. Grant, S.-Q. Yu, and G. J. Salamo. Raman scattering reveals strong LO-phonon-hole-plasmon coupling in nominally undoped GaAsBi: optical determination of carrier concentration. *Optics Express*, 22(10):11680, may 2014.
- [312] Stefan Korte, Andreas Nagelein, Matthias Steidl, Werner Prost, Vasily Cherepanov, Peter Kleinschmidt, Thomas Hannappel, and Bert Voigtlander. Charge transport in GaAs nanowires: Interplay between conductivity through the interior and surface conductivity. *Journal of Physics Condensed Matter*, 31(7), 2019.
- [313] Mahshid Sam and B.Sc. *Controlling Field-Directed Assembly of Nanowires: Towards Nanomanufacturing for Biosensors and Transparent Electrodes*. PhD thesis, University of Victoria, 2019.
- [314] Pablo Garcia-Sanchez, Juan J Arcenegui, Hywel Morgan, and Antonio Ramos. Self-assembly of metal nanowires induced by alternating current electric fields. *Applied Physics Letters*, 106(2):23110, 2015.
- [315] Robert Kretschmer and Wolfgang Fritzsche. Pearl Chain Formation of Nanoparticles in Microelectrode Gaps by Dielectrophoresis. *Langmuir*, 20(26):11797–11801, 2004.
- [316] Mahshid Sam, Nima Moghimian, and Rustom B Bhiladvala. Field-directed chaining of nanowires: towards transparent electrodes. *Materials Letters*, 163:205–208, 2016.

- [317] Benjamin R. Martin, Sarah K. St. Angelo, and Thomas E Mallouk. Interactions between suspended nanowires and patterned surfaces. *Advanced Functional Materials*, 12(11- 12):759–765, 2002.
- [318] Fengyun Wang, Guofa Dong, Johnny C. Ho, Ning Han, Zaixing Yang, SenPo Yip, Yulun Chueh, Jared J. Hou, and Ming Fang. III–V Nanowires: Synthesis, Property Manipulations, and Device Applications. *Journal of Nanomaterials*, 2014:1–14, 2014.
- [319] Pengyuan Zheng A. Electron Scattering at Surfaces and Interfaces of Transition Metals, 2015.
- [320] Mohammad Taghi Ahmadi, Hui Houg Lau, Razali Ismail, and Vijay K. Arora. Current-voltage characteristics of a silicon nanowire transistor. *Microelectronics Journal*, 40(3):547–549, 2009.
- [321] J. Wood and D.v Morgan. Gallium Arsenide and Related Compounds. *Metals forum*, 7(3):171–186, 1984.
- [322] Bernt Ketterer, Emanuele Uccelli, and Anna i Morral. Mobility and carrier density in p-type GaAs nanowires measured by transmission Raman spectroscopy. *Nanoscale*, 4(5):1789–1793, 2012.
- [323] Hannah J. Joyce, Sarwat A. Baig, Patrick Parkinson, Christopher L. Davies, Jessica L. Boland, H. Hoe Tan, Chennupati Jagadish, Laura M. Herz, and Michael B. Johnston. The influence of surfaces on the transient terahertz conductivity and electron mobility of GaAs nanowires. *Journal of Physics D: Applied Physics*, 50(22), 2017.
- [324] Robert D. Richards, Nicholas J. Bailey, Yuchen Liu, Thomas B.O. O Rockett, and Abdul R. Mohamad. GaAsBi: From Molecular Beam Epitaxy Growth to Devices. *Physica Status Solidi (B) Basic Research*, 259(2):1–14, 2022.
- [325] D A Beaton, A Mascarenhas, and K Alberi. Insight into the epitaxial growth of high optical quality GaAs $1-x$ Bi x . *Journal of Applied Physics*, 118(23):235701, dec 2015.
- [326] D A Beaton, R B Lewis, M Masnadi-Shirazi, and T Tiedje. Temperature dependence of hole mobility in GaAs $1-x$ Bi x alloys. *Journal of Applied Physics*, 108(8):083708, oct 2010.
- [327] T.B.O. Rockett, R.D. Richards, Y. Gu, F. Harun, Y. Liu, Z. Zhou, and J.P.R. David. Influence of growth conditions on the structural and opto-electronic quality of GaAsBi. *Journal of Crystal Growth*, 477:139–143, nov 2017.
- [328] A. J. Ptak, R. France, D. A. Beaton, K. Alberi, J. Simon, A. Mascarenhas, and C. S. Jiang. Kinetically limited growth of GaAsBi by molecular-beam epitaxy. *Journal of Crystal Growth*, 338(1):107–110, January 2012.
- [329] Smriti Baruah, Joyatri Bora, and Santanu Maity. High performance wide response GaAs based photo detector with nano texture on nanopillar arrays structure. *Microsystem Technologies*, 26(8):2651–2660, 2020.

- [330] T. Paulauskas, V. Pačebutas, A. Geižutis, M. Kamarauskas, M. Drazdys, M. Rudzikas, R. Kondrotas, A. Naujokaitis, I. Nevinskas, B. Šebeka, V. Strazdiene, and A. Krotkus. Performance analysis of GaAsBi/InGaAs heterostructure for III-V multi-junction solar cells. *Solar Energy Materials and Solar Cells*, 248(May):112013, dec 2022.
- [331] S Kral, C Zeiner, M StoGer-Pollach, E Bertagnolli, M I Den Hertog, M Lopez-Haro, E Robin, K El Hajraoui, and A Lugstein. Abrupt schottky junctions in al/ge nanowire heterostructures. *Nano Lett*, 15, 2015.
- [332] Shaili Sett, Subhamita Sengupta, N. Ganesh, K. S. Narayan, and A. K. Raychaudhuri. Self-powered single semiconductor nanowire photodetector. *Nanotechnology*, 29(44), 2018.
- [333] K Das, S Mukherjee, S Manna, S K Ray, and A K Raychaudhuri. Single Si nanowire (diameter ≤ 100 nm) based polarization sensitive near-infrared photodetector with ultra-high responsivity. *Nanoscale*, 6(19):11232–11239, 2014.
- [334] Cheng-Hsiang Kuo, Jyh-Ming Wu, Su-Jien Lin, and Wen-Chih Chang. High sensitivity of middle-wavelength infrared photodetectors based on an individual InSb nanowire. *Nanoscale Research Letters*, 8(1):327, 2013.
- [335] Nan Guo et al. Single InAs Nanowire Room-Temperature Near-Infrared Photodetectors. *ACS Nano*, 8(4):3628–3635, 2014.
- [336] M G Bartmann, M Sistani, S Glassner, B Salem, T Baron, P Gentile, J Smoliner, and A Lugstein. Verifying the band gap narrowing in tensile strained Ge nanowires by electrical means. *Nanotechnology*, 32(14):145711, apr 2021.
- [337] J. Greil, A. Lugstein, C. Zeiner, G. Strasser, and E. Bertagnolli. Tuning the electro-optical properties of germanium nanowires by tensile strain. *Nano Letters*, 12(12):6230–6234, 2012.
- [338] Michael S. Seifner, Masiar Sistani, Fabrizio Porrati, Giorgia Di Prima, Patrik Pertl, Michael Huth, Alois Lugstein, and Sven Barth. Direct Synthesis of Hyperdoped Germanium Nanowires. *ACS Nano*, 12(2):1236–1241, 2018.
- [339] Maria M. Kolesnik-Gray, Tarek Lutz, Gillian Collins, Subhajit Biswas, Justin D. Holmes, and Vojislav Krstic. Contact resistivity and suppression of Fermi level pinning in side-contacted germanium nanowires. *Applied Physics Letters*, 103(15):1–4, 2013.
- [340] Sabar D Hutagalung, Mohammed M Fadhali, Raed A Areshi, and Fui D Tan. Optical and Electrical Characteristics of Silicon Nanowires Prepared by Electroless Etching. *Nanoscale research letters*, 12(1):425, dec 2017.

- [341] Hannah J Joyce, Callum J Docherty, Qiang Gao, H Hoe Tan, Chennupati Jagadish, James Lloyd-Hughes, Laura M Herz, and Michael B Johnston. Electronic properties of GaAs, InAs and InP nanowires studied by terahertz spectroscopy. *Nanotechnology*, 24(21):214006, may 2013.
- [342] D.Pandey, A Bhattacharjee, and T R Lenka. Study on Temperature Dependence Scattering Mechanisms and Mobility Effects in GaN and GaAs HEMTs. In V K Jain and Abhishek Verma, editors, *Physics of Semiconductor Devices*, pages 67–70, Cham, 2014. Springer International Publishing.
- [343] D G Cooke, F A Hegmann, E C Young, and T Tiedje. Electron mobility in dilute GaAs bismide and nitride alloys measured by time-resolved terahertz spectroscopy. *Applied Physics Letters*, 89(12):122103, sep 2006.
- [344] Chun-Sheng Guo, Lin-Bao Luo, Guo-Dong Yuan, Xiao-Bao Yang, Rui-Qin Zhang, Wen-Jun Zhang, and Shuit-Tong Lee. Surface Passivation and Transfer Doping of Silicon Nanowires. *Angewandte Chemie International Edition*, 48(52):9896–9900, 2009.
- [345] Yann Michel Niquet and Christophe Delerue. Carrier mobility in strained Ge nanowires. *Journal of Applied Physics*, 112(8):0–4, 2012.
- [346] Florian Fuchs et al. Electrical Characterization of Germanium Nanowires Using a Symmetric Hall Bar Configuration: Size and Shape Dependence. *Nanomaterials*, 11(11):2917, oct 2021.
- [347] Habeeb Mousa and Kasif Teker. High-transconductance silicon carbide nanowire-based field-effect transistor (SiC-NWFET) for high-temperature applications. 2(July):78–83, 2021.

Appendix A

A.1 Semiconductor nanowires, fundamentals and previous work

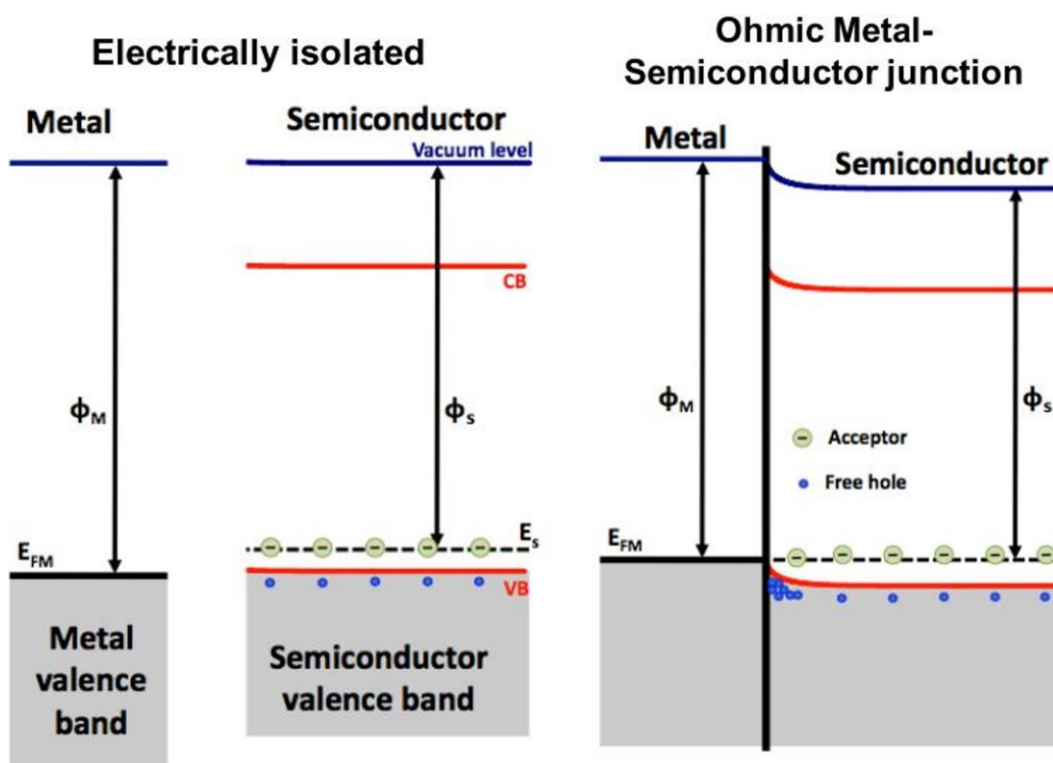


Figure A.1.1: Schematic of Ohmic contact with p-type semiconductor.

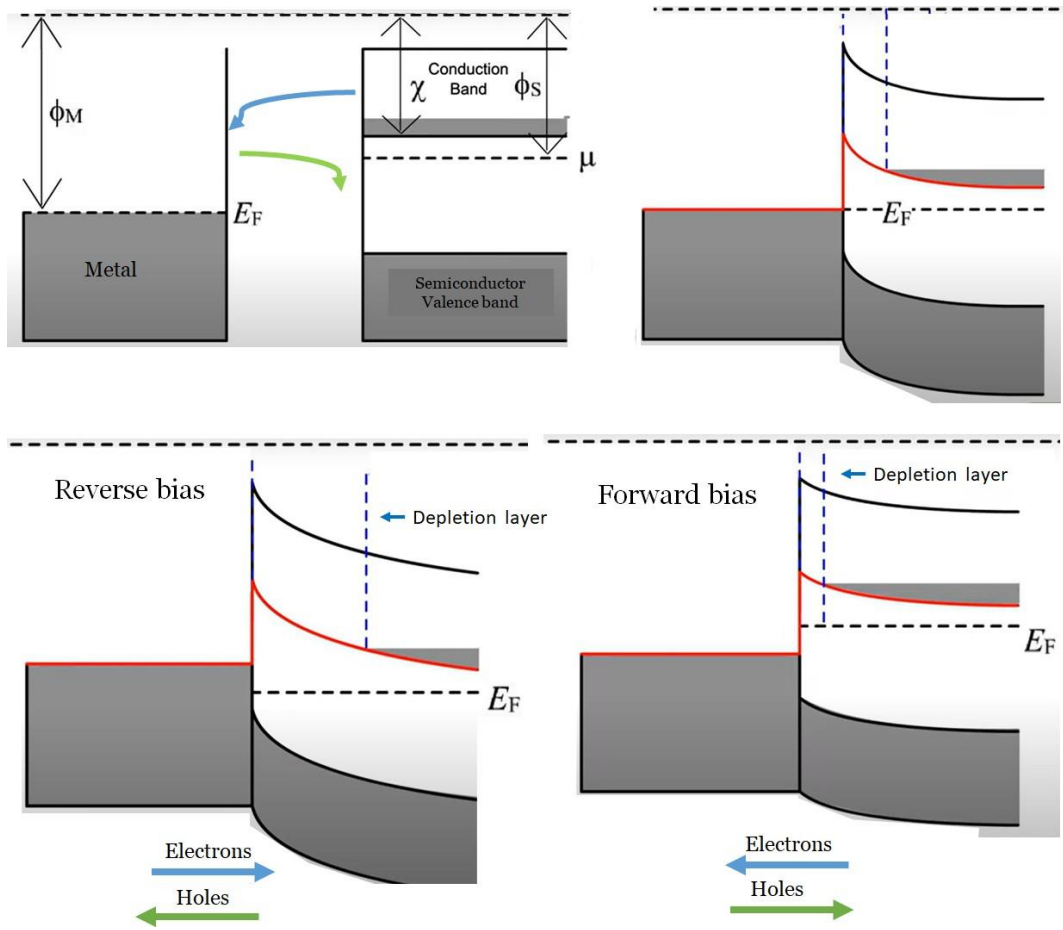


Figure A.1.2: Schematic of Schottky contact with n-type semiconductor.

A.2 Fabrication and characterisation

Photocurrent Spectroscopy; Responsivity

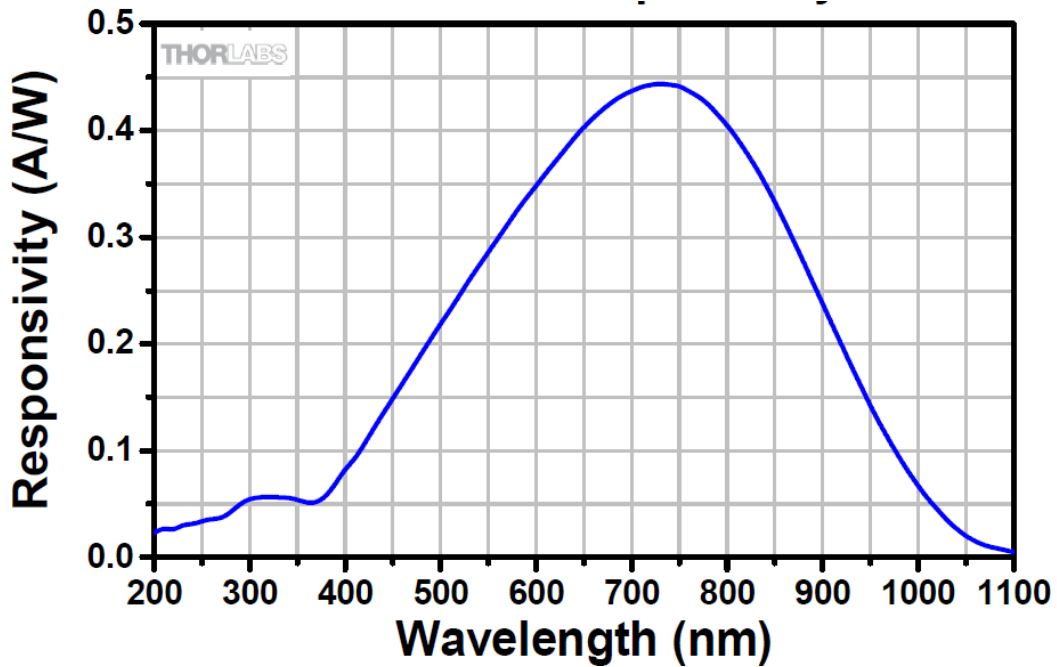


Figure A.2.1: Responsivity of commercial Silicon photodiode from Thorlabs.

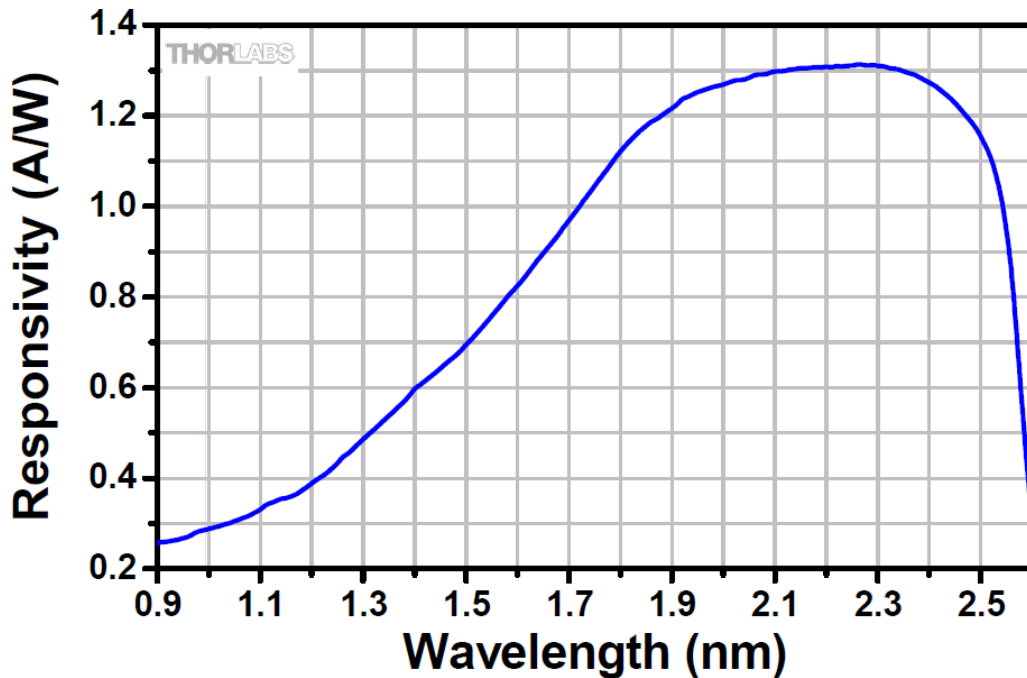


Figure A.2.2: Responsivity of commercial InGaAs photodiode from Thorlabs.

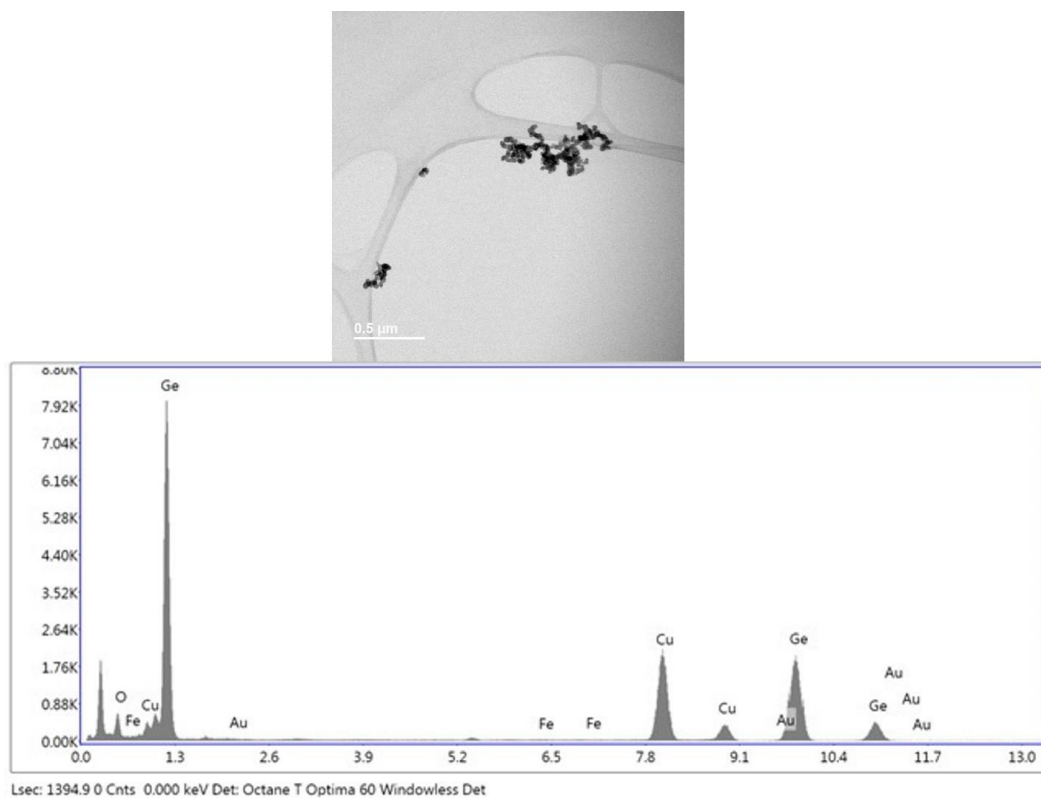
Characterisation of the Ge NWs in deionised water

Figure A.2.3: Bright field image of clustered Ge nanowires and its EDX analysis of the clusters.

A.2.4. DEP force and Clausius-Mossotti factor; Matlab calculation

In the following calculation, the Ge NWs have a permittivity $\epsilon_p = 16$ and a conductivity $\sigma_p = 476\text{-}500\text{ Sm}^{-1}$). Anisole has a permittivity of $\epsilon_m = 4.33$ and a conductivity of $\sigma_m = 2\text{E}10\text{-}6\text{ Sm}^{-1}$.

```

1
2 %% Calculating the Clausius–Mossotti factor and DEP force .
3
4
5 %% Defining parameters
6
7 l = 20e-6;           % Length of nanowire (m)
8 r = 30e-9;          % Radius of nanowire (m)
9 epsilon__0 = 8.85e-12; % Permittivity of vacuum (F/m)
10 epsilon__pr = 16;   % Relative permittivity of nanowire
11 epsilon__mr = 4.33; % Relative permittivity of medium
12 sigma__p = 476 ;    % Conductivity of nanowire (S/m)
13 sigma__m = 6e-6;    % Conductivity of medium (S/m)
14
15 % Frequency range
16 % Defines a frequency range between 10 Hz and 20 MHz with 10 numbers in a
   decade .
17
18 f = logspace (4, 10, 100);
19 omega = 2*pi*f;
20
21 % Derived parameters
22
23 % Permittivity of NW (F/m) with relative permittivity permittivity of free space
24 epsilon__p = epsilon__pr*epsilon__0;
25
26 % Permittivity of medium (F/m)
27 epsilon__m = epsilon__mr*epsilon__0;
28
29 % Complex permittivity of the particle
30 compl__epsilon__p = epsilon__p - i*sigma__p./omega;
31
32 % Complex permittivity of the medium
33 compl__epsilon__m = epsilon__m - i*sigma__m./omega;
34
35
36 % Device and measurement parameters
37
38 % Length of gap between two electrodes (m)

```

```

39 d = 20e-6;
40
41 % rms of applied voltage (V)           Vrms=Vpk/sqrt(2)
42 V = 8/sqrt(2);
43
44 % rms of electric field (V/m)
45 E = V/d;
46
47 % Root Mean Square of electric field to power of two (V/m)^2
48 E__squared = E^2;
49
50 % Gradient of field squared assuming 10% change in micrometer
51 gradient = 0.1 * E__squared/1e-6;
52
53
54 %% Clausius-Mossotti factor
55
56 %Eccentricity e
57 e=sqrt(1-(r/d)^2);
58
59 %Depolarisation factor A for prolate ellipsoid shape along x long axis
of NW
60 Ax=((1-e^2)/(2*e^3))*(log((1+e)/(1-e))-2*e);
61
62 %Depolarisation factor A for prolate ellipsoid shape along y short axis
of NW
63 Ay=(1-Ax)/2;
64
65 %Clausius Mossotti factor along the long axis
66 CMFlongaxis=(1/3)*(compl__epsilon__p - compl__epsilon__m)./(
compl__epsilon__m + Ax*(compl__epsilon__p - compl__epsilon__m));
67
68 %Clausius Mossotti factor along the short axis
69 CMFshortaxis=(1/3)*(compl__epsilon__p - compl__epsilon__m)./(
compl__epsilon__m + Ay*(compl__epsilon__p - compl__epsilon__m));
70
71 %CMF total
72 CMF=(CMFlongaxis+CMFshortaxis) / 2;
73
74
75
76 %% Calculating a factor proportional to DEP force
77
78 %DEP force (N)
79 F = (pi*2*1*r^2)*epsilon__m*real(CMF)*gradient;
80
81 %DEP force magnitude along the long axis

```

```

82 Flongaxis=(pi*2* l*r^2)*epsilon__m*real ( CMFlongaxis ) *gradient ;
83 %DEP force magnitude along the short axis
84 Fshortaxis=(pi*2* l*r^2)*epsilon__m*real ( CMFshortaxis ) *gradient
85
86
87 %% Plots
88
89 figure (1);
90 semilogx (f , real (CMFlongaxis));
91 title('SemiLogx (Frequence , Re(CMFlongaxis)');
92
93
94 figure (2);
95 semilogx (f , real (CMFshortaxis));
96 title('SemiLogx (Frequence , Re(CMFshortaxis)');
97
98 figure (3);
99 loglog (f , real (CMF));
100 title('LogLog (Frequence , Re(CMF))');
101
102 %figure(4);
103 %semilogx (f , 180*angle (K)/pi);
104
105 figure (5);
106 loglog (f , F);
107 title('LogLog (Frequence , DEP-Force)');
108
109
110 figure (6);
111 loglog (f , Flongaxis);
112 title('LogLog (Frequence , DEP-Force (longaxis)');
113
114 figure (7);
115 loglog (f , Fshortaxis);
116 title('LogLog (Frequence , DEP-Force (shortaxis)');

```


DEP force along the long and short axis as a function of the frequency

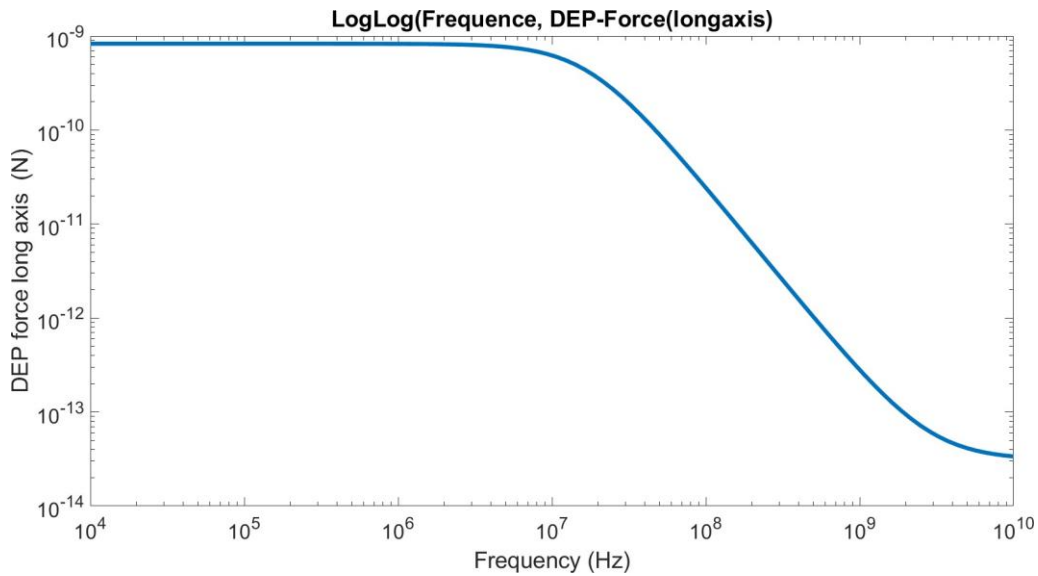


Figure A.2.5: Calculated DEP force along the long axis as a function of the frequency for Ge NWs aligned at a voltage of $8 V_{peak-to-peak}$ on a $20 \mu\text{m}$ electrode gap in anisole.

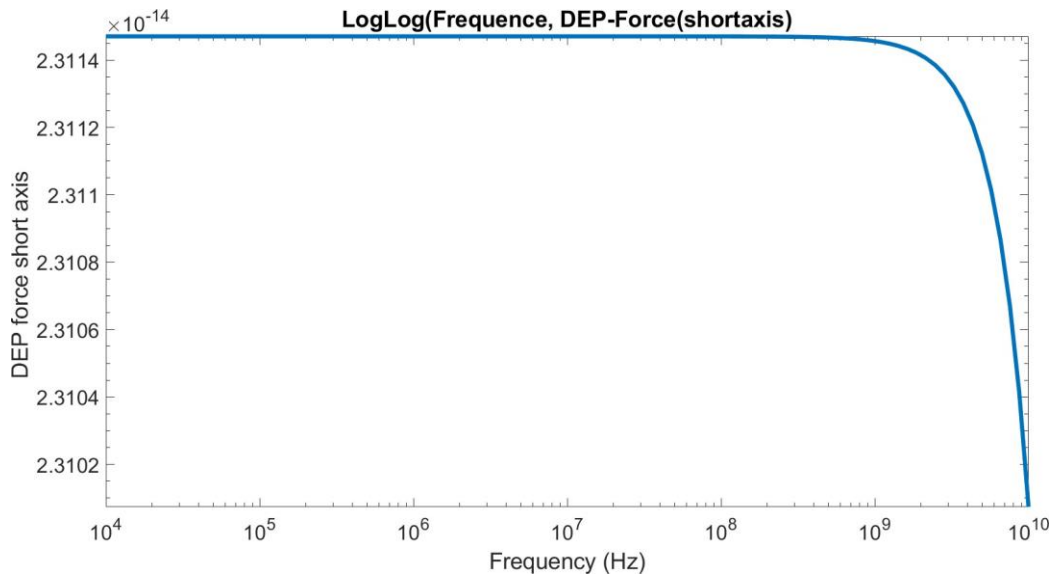


Figure A.2.6: Calculated DEP force along the short axis as a function of the frequency for Ge NWs aligned at a voltage of $8 V_{peak-to-peak}$ on a $20 \mu\text{m}$ electrode gap in anisole.

Design of the electrodes for NWs collection by DEP

Interdigitated Electrodes

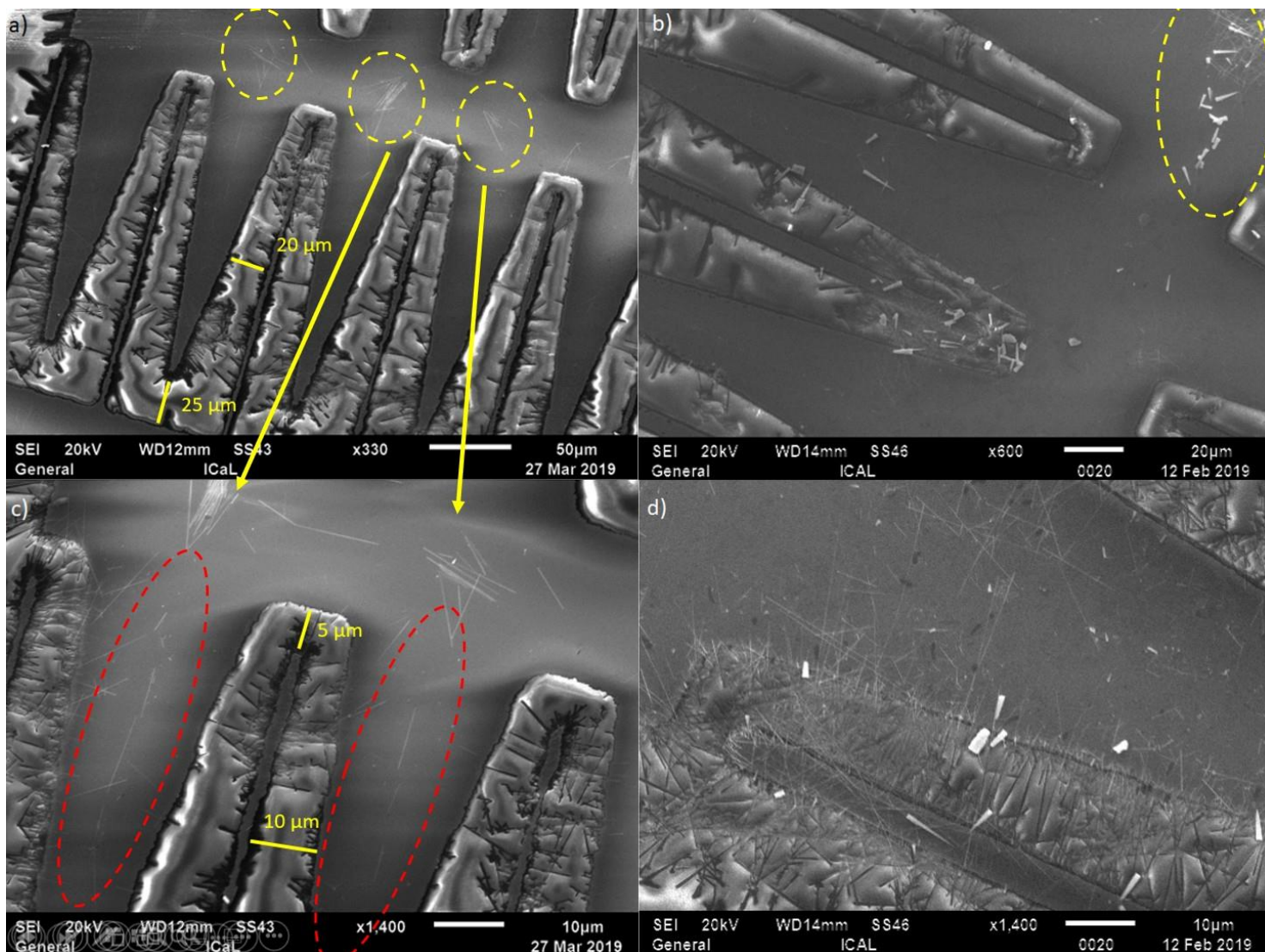


Figure A.2.7: SEM images of collected Ge NWs at a voltage of $8 V_{peak-to-peak}$ and frequency of 500 kHz a)-c) and b)-d) are groups from the same device.

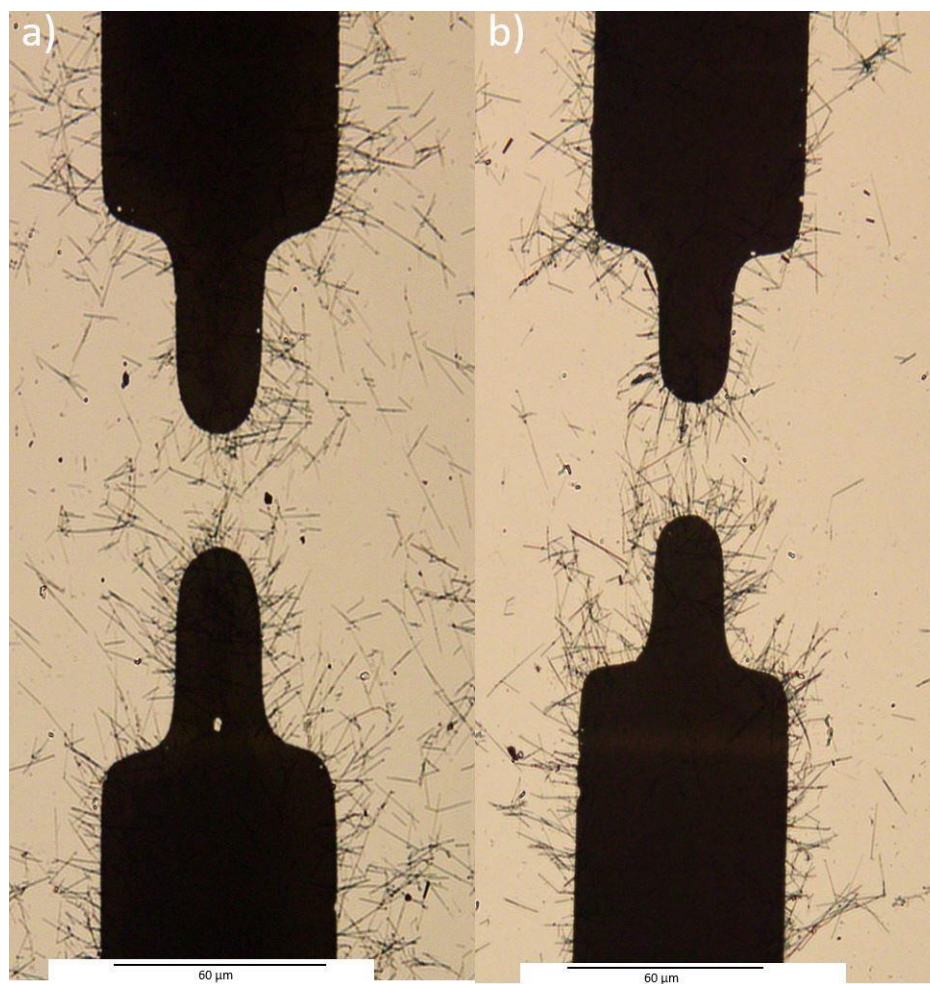
Parallel electrodes; voltage study

Figure A.2.8: Images obtained by optical microscopy of burned-off Ge NWs aligned at a) $10 V_{peak-to-peak}$ and b) $16 V_{peak-to-peak}$.

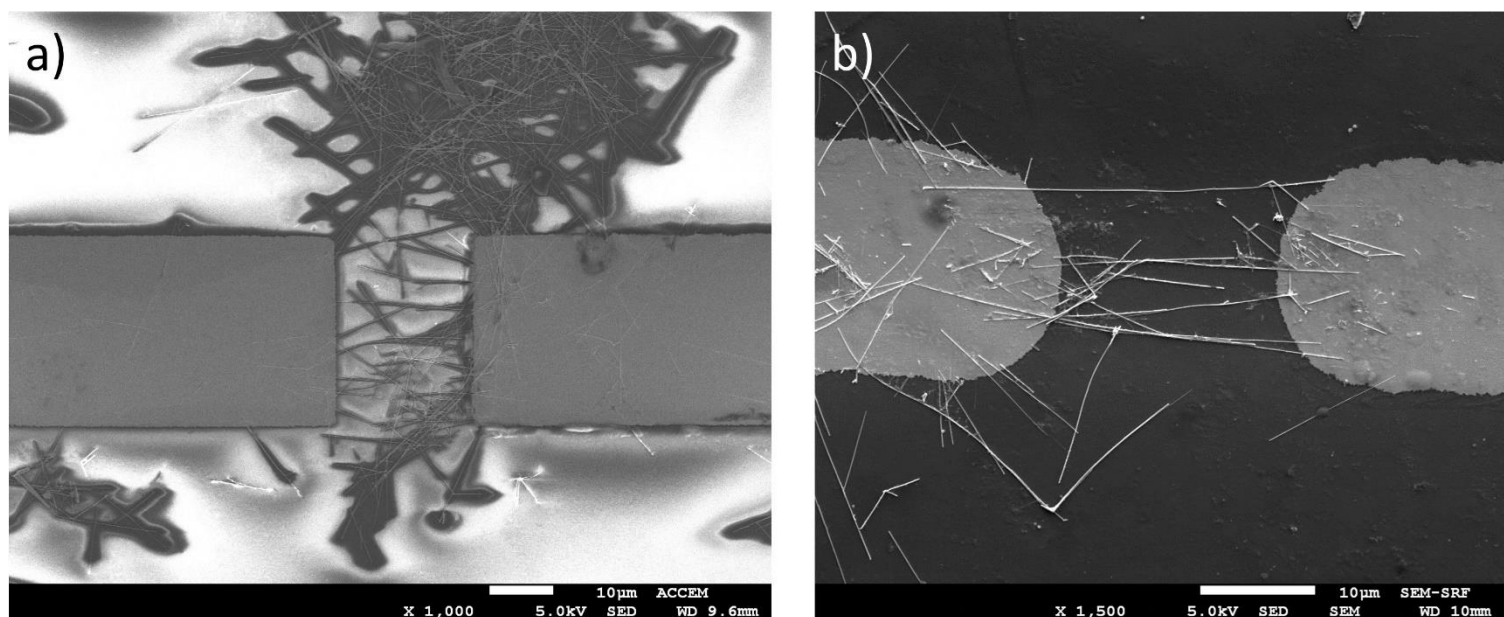
Parallel electrodes study; square and round tip

Figure A.2.9: Images obtained by SEM of aligned Ge NWs in a) rectangular and b) round end tip gap electrodes.

DEP set up and topology

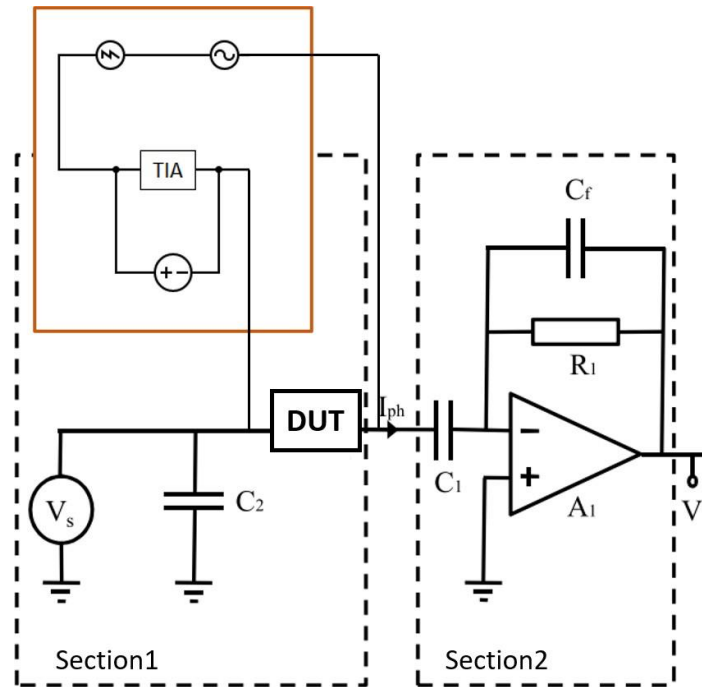


Figure A.2.10: TIA circuit topology, with the main DEP set in the brown box and TIA in the dashed box.

A.2.11 Real-time resistance monitoring code; Matlab computation

```

1 %% The user sets the parameters used for Dielectrophoresis in order to obtain the c
   alculated resistance of the DUT.
2
3
4 amp=input( ' Amplitude ? ' );           % That command ask the user what
   amplitude to apply
5 freq=input( ' Frequency ?? ' );       % That command ask the user what f
   requency to apply
6 nomeas=input( ' Measurement Number? ' ); %That command ask the user what
   time or how many measurements the programme as to do
7
8
9
10
11 %% Set TIMER
12 T = timer( ' TimerFcn ', @(~,~) disp( ' NEXT. ' ), ' Start Delay ', 1);
13
14
15
16 %% Calling for equipment
17
18 %Oscillator
19 % Creating USB Object
20 vOSC = visa( ' AGILENT ', ' USB0::0 x0699 :: 0 x03A3 :: C010904 :: 0 :: INSTR ' );
21 % Set the buffer      size
22 set(vOSC, ' Input Buffer Size ', 300000); %dont know about this size
   anymore
23 % Set the timeout value
24 vOsc.Timeout = 2;
25 % Set the Byte order
26 vOsc.ByteOrder = ' littleEndian ';
27 % Open USB Object
28 fopen (vOSC);
29
30 % Function Generator
31 interfaceObj = visa( ' AGILENT ', ' USB0::0 x0957 :: 0 x0407 :: MY43003346
   :: 0 :: INSTR ' );
32 % Create USB object.
33 fgen = icdevice( ' agilent__33220a.mdd ', interfaceObj);
34 % Connect device object to hardware.
35 connect(fgen);
36
37
38 %% Setup both Devices at the same time
39

```



```

40 %SETUP OSCILLOSCOPE
41 % Waveform Data Format (Least Significant Byte First, Signed Integer)
42 fprintf (vOSC, ' :DAT:ENC SRI ' );
43 % Specify Number of Bytes/Y Data Points (256)
44 fprintf (vOSC, ' :WFM:BYT 1 ' );
45 % Specify Data Starting Point
46 fprintf (vOSC, ' :DAT:STAR 1 ' );
47
48 % Set Waveform to Sine
49 set (fgen, ' Waveform ', ' sin ' );
50 % Set the Voltage Amplitude to 10 V
51 set (fgen, ' Amplitude ', amp );
52 % Set the F.G. Frequency to x Hz
53 set (fgen, ' Frequency ', freq );
54
55
56
57
58 %% Readout RMS (Root Mean Square of signal) from Oscilloscope
59 tic
60
61 % Input Value RMS
62 disp ( ' Getting Input RMS Voltage ' );
63 for i=1:2
64     % Readout RMS from Oscilloscope 1 input
65     fprintf (vOSC, ' MEASU:IMM:SOU1 CH1 ' );
66     fprintf (vOSC, ' MEASU:IMM:TYP AMP ' );
67     fprintf (vOSC, ' MEASU:IMM:VAL? ' );
68     WForm.RMSCh1raw= fscanf (vOSC);
69     WForm.RMSCh1=str2double (WForm.RMSCh1raw);
70     disp ( ' Value : ' );
71     disp (WForm.RMSCh1);
72 end
73
74
75 % Readout RMS from Oscilloscope 2 output
76 fprintf (vOSC, ' MEASU:IMM:SOU1 CH2 ' );
77 fprintf (vOSC, ' MEASU:IMM:TYP AMP ' );
78 fprintf (vOSC, ' MEASU:IMM:VAL? ' );
79 WForm.RMSCh2raw= fscanf (vOSC);
80 WForm.RMSCh2=str2double (WForm.RMSCh2raw);
81
82 % Readout RMS from Oscilloscope 3
83 fprintf (vOSC, ' MEASU:IMM:SOU1 CH3 ' );
84 fprintf (vOSC, ' MEASU:IMM:TYP AMP ' );
85 fprintf (vOSC, ' MEASU:IMM:VAL? ' );

```

```

86   WForm.RMSCh3raw= fscanf (vOSC) ;
87   WForm.RMSCh3=str 2 d o u b l e (WForm.RMSCh3raw) ;
88
89   % Readout phase
90   fprintf (vOSC, 'MEASU:IMM:SOU1 CH1 ' ) ;
91   fprintf (vOSC, 'MEASU:IMM:SOU2 CH2 ' ) ;
92   fprintf (vOSC, 'MEASU:IMM:TYPE PHA ' ) ;
93   fprintf (vOSC, 'MEASU:IMM:VAL? ' ) ;
94   Phase Shiftraw= fscanf (vOSC) ;
95   Phase Shift 0=str 2 d o u b l e ( Phase Shiftraw ) ;
96
97   R1=10000;          % Ohm
98   R2=1000;          % Ohm
99   R3=100000;        % Ohm
100  C1=200*10^-6;     %Farad
101  Cf=68*10^-12;
102
103  %I0=WForm.RMSCh3(1,1)*((1+j*freq*R1*Cf)/(j*freq*R1*C1))
104
105  x11=(freq*R1*C1)^2;
106  x1=sqrt(x11);
107  x22=1^2+(freq*R1*Cf)^2;
108  x2=sqrt(x22);
109
110  tic;
111  % Output Value RMS & subsequent calcs
112  disp ( 'Getting Output RMS Voltages ' ) ;
113  for j=1:10000 %loop number #number of measurements
114
115      Ztotal=0;
116      for i=1:10 %loop for the mean
117
118          % Readout RMS from Oscilloscope 2
119          fprintf (vOSC, 'MEASU:IMM:SOU1 CH2 ' ) ;
120          fprintf (vOSC, 'MEASU:IMM:TYP AMP' ) ;
121          fprintf (vOSC, 'MEASU:IMM:VAL? ' ) ;
122          WForm.RMSCh2raw= fscanf (vOSC) ;
123          WForm.RMSCh2=str 2 d o u b l e (WForm.RMSCh2raw) ;
124
125
126          % Readout RMS from Oscilloscope 3
127          fprintf (vOSC, 'MEASU:IMM:SOU1 CH3 ' ) ;

```



```

128     fprintf (vOSC, 'MEASU:IMM:TYP AMP' );
129     fprintf (vOSC, 'MEASU:IMM:VAL? ');
130     WForm.RMSCh3raw= fscanf (vOSC);
131     WForm.RMSCh3=str 2 double (WForm.RMSCh3raw);
132
133
134     z1=1+R1*Cf*2* pi * f r e q ;
135     z2=R1*C1*2* pi * f r e q ;
136     Z=(z1/z2) * 492.32;
137
138     disp (Z);
139     I0(i,1)=WForm.RMSCh2*(Z);
140     disp(I0);
141
142     Zi(i,1)=((WForm.RMSCh1/2)/I0(i,1));
143
144     Ztotal=Ztotal + Zi(i,:);
145     end
146     Zti(j,1)=(Ztotal/10);
147
148
149     Phase Shiftmean =0;
150     for i=1:10 %loop for the mean
151         fprintf (vOSC, 'MEASU:IMM: SOU1 CH1 '); %phase
152         fprintf (vOSC, 'MEASU:IMM: SOU2 CH2 ');
153         fprintf (vOSC, 'MEASU:IMM: TYPE PHA '); %take out the phase
154         fprintf (vOSC, 'MEASU:IMM:VAL? ');

155     Phase Shiftraw=fscanf (vOSC);
156     Phase Shift Tot (i,1)=str 2 double ( Phase Shiftraw );
157     Phai (i,1)=Phase Shift 0(1,1)/Phase Shift Tot (i,1);
158     Phase Shiftmean=Phase Shiftmean+Phai (i,1);
159     end
160     Phase Shift (j,1)=Phase Shiftmean / 10;
161
162     DATA.time (j,:)=toc;
163     disp ( ' Measurement Number ');
164
165
166     figure (1);set (gcf, ' WindowState ', ' maximized ');
167     x = linspace (0,3*pi,200);
168     y = cos (x) + rand (1,200);

```

```
169     sz = linspace(1,100,200);
170
171     DATA.Zti = smoothdata(Zti,'gaussian',20);
172
173     %legend('RMS Voltage OUTPUT','RMS Voltage INPUT','Current(A)')
174     yyaxis left
175     xlabel('Time (s)')
176     ylabel('Resistivity (Ohm)')
177     scatter(DATA.time(j,1),Zti(j,1),20);
178     hold on
179 end
180 fclose(instrfind);
```

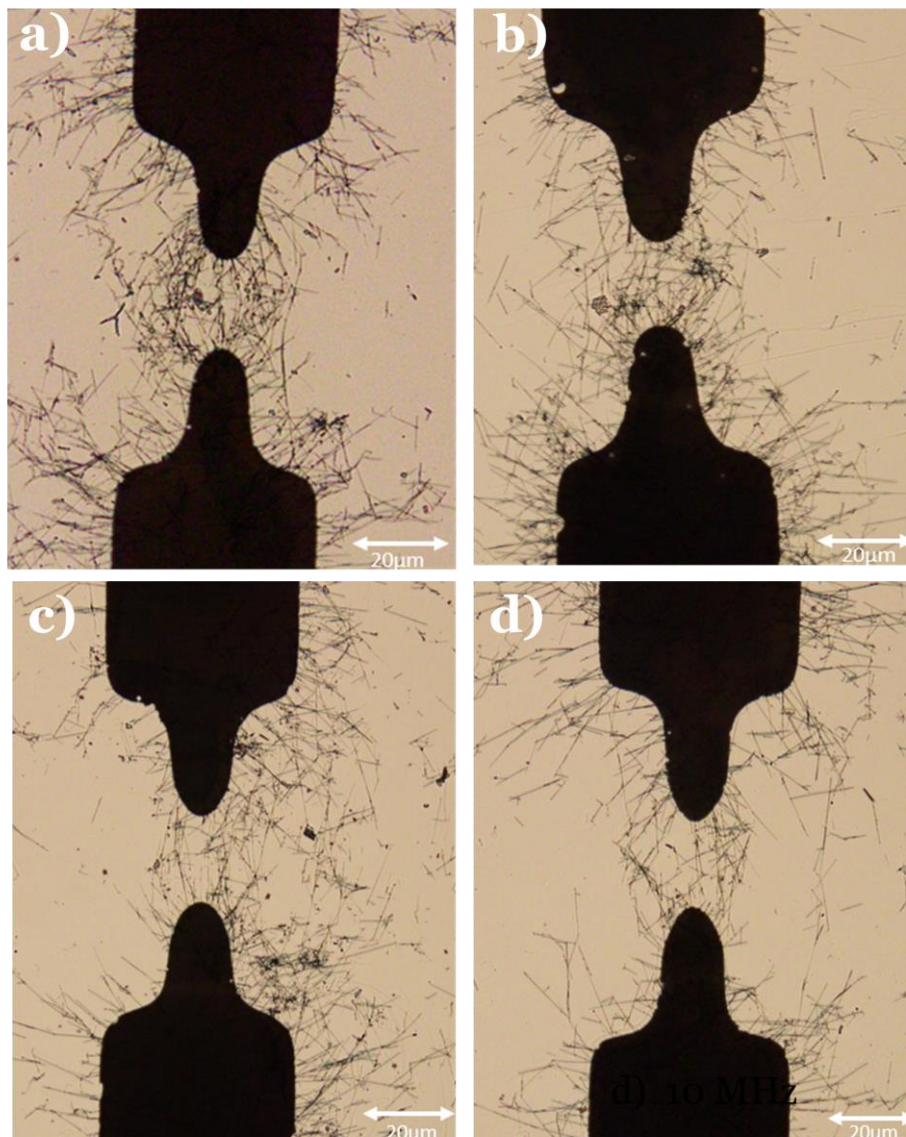
DEP collection

Figure A.2.12: Images obtained by optical microscopy of NWs aligned on devices fabricated at frequencies of ; a) 500 kHz, b) 1 MHz, c) 5 MHz, d) 10 MHz.

A.3 Fabrication and characterisation of single Ge NW alignment

Table A.3.1: Table of single NWs resistivity found in the literature.

References (doi)	NWs	Resistivity ($\Omega\cdot\text{cm}$)	Conductivity (Sm^{-1})	Synthesis	Contact/ selection
Sarah beretta et al. [233]	Germanium Single	ρ_{NW} 0.18 0.21	476.19 555.56	MOVPE	FIBID/ random by SEM
S.Sett et al. [153]	Germanium Single	$\rho_{\text{NW}} = 46$	2.17	VLS	EBL + top metallisation/random
D. Erts et al. [169]	Germanium Single	ρ_{device} 14E3 3E5	7.14E-3 3.33E-4	SFLS through Porous AAO membranes	Metal coating and AFM/random
M G Bartmann et al. [336]	Germanium Single	$\rho_{\text{device}} = 5.5$	18.20	VLS	Sputter deposited/random
J. Greil [337]	Germanium Single	ρ_{NW} 1E3 1E4	0.1 0.01	VLS	Monolithically integrated/random
M. Seifner [338]	Germanium Single	$\rho_{\text{NW}} = 11$	9.09	Electro-chemical	EBL/random
M. Kolesnik-Gray [339]	Germanium Single	ρ_{NW} 3 410	33.3 0.24	SFLS	EBL/random
This work	Germanium Single	ρ_{device} 8.7 17	5.88 11.4	MOVPE	DEP
	Array	ρ_{device} 1.5 5.7	15.5 66.6	MOVPE	DEP
S. Hutagalung [340]	Silicon Single	$\rho_{\text{device}} = 33.94$	2.95	MAEE	AFM/random

Notes: ρ_{NW} = resistivity of the NW accounted without the contact resistivity, ρ_{device} = resistivity of NW + contact resistivity, AFM= Atomic Force, AAO= Anodic Aluminium Oxide, DEP= Dielectrophoresis, EBL= Electron Beam Lithography, FIBID= Focused Ion Beam Induced Deposition, MAEE= Metal Assisted Electroless Etching, MOVPE= Metal-Organic Vapour Epitaxy, SFLS= Super-Critical Fluid-Liquid- Solid, VLS= Vapour-Liquid-Solid.

A.4 Germanium nanowires-based biosensor device

Raman spectroscopy characterisation

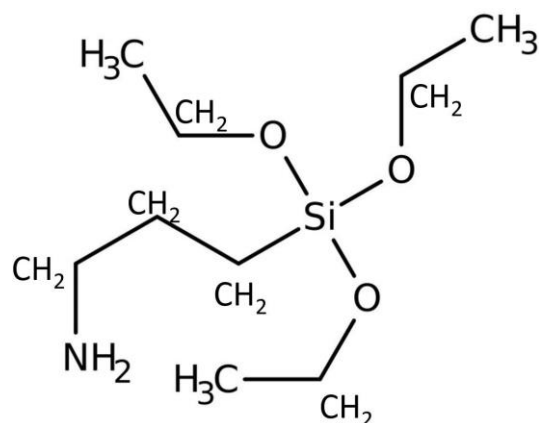


Figure A.4.1: 3-Aminopropyl-triethoxysilane (APTES) molecule with amine (NH₂) group.

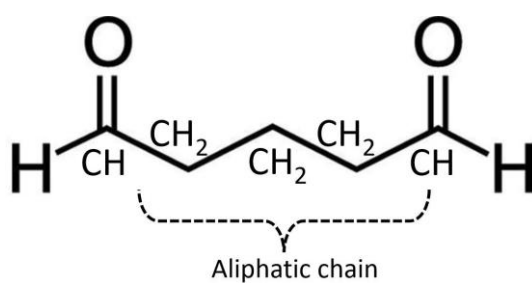


Figure A.4.2: Glutaraldehyde molecule.

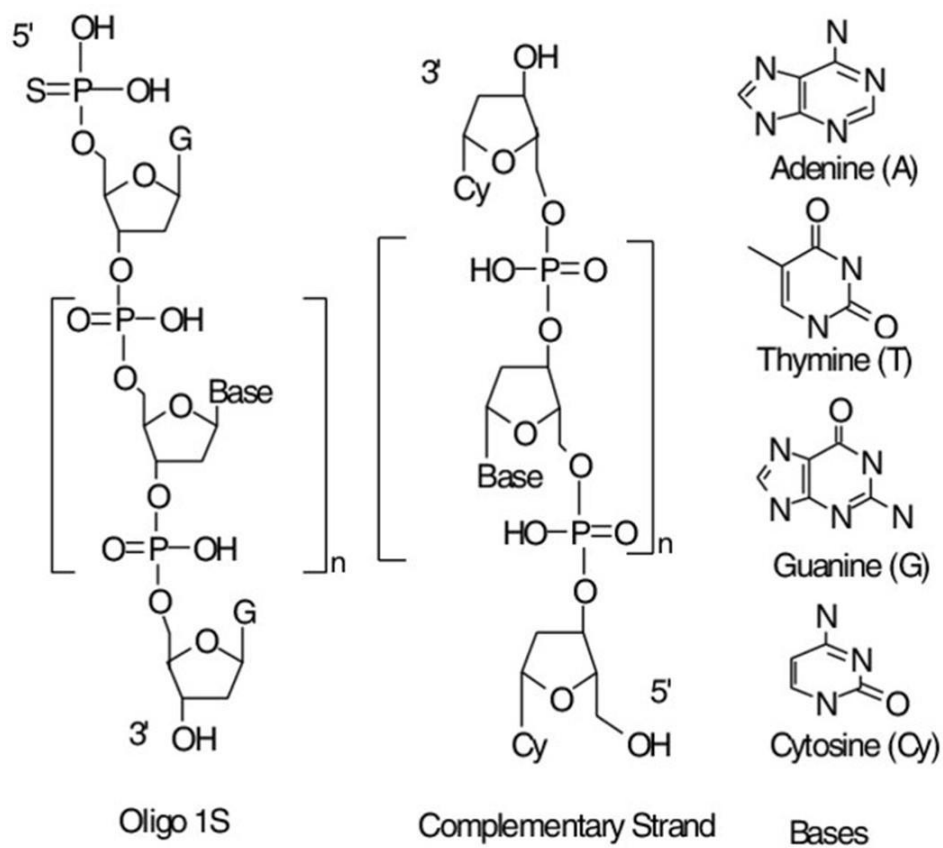


Figure A.4.3: Protein Molecule; Oligomers and their Amino acids (Bases).

Table A.4.4: Vibration bands overview.

Functional Group	Position (cm ⁻¹)	Silanisation	Glutaraldehyde	Aptamerisation
Ge	300 (Ge-Ge stretching)	✓	✓	✓
Ge-O	450 (Ge-O stretching)	✓	-	✓
Si-O	510 (Si-O stretching)	✓	-	✓
Si-C	510 (Si-C stretching)	✓	-	✓
	2400 (Si-C stretching)	✓	-	✓
C-N-C	836 (amino ring)	-	-	✓
N-H	1100 (NH ₂ rocking)	✓	-	✓
C-H	1100 (CH ₂ twisting)	✓	-	✓
	1300 (CH ₂ scissoring)	✓	✓	-
	2500-3000 (C-H aliphatic stretching)	✓	✓	-
N-H	1580 (amino ring)	-	-	✓
C=O	1600 (aldehyde)	-	✓	-

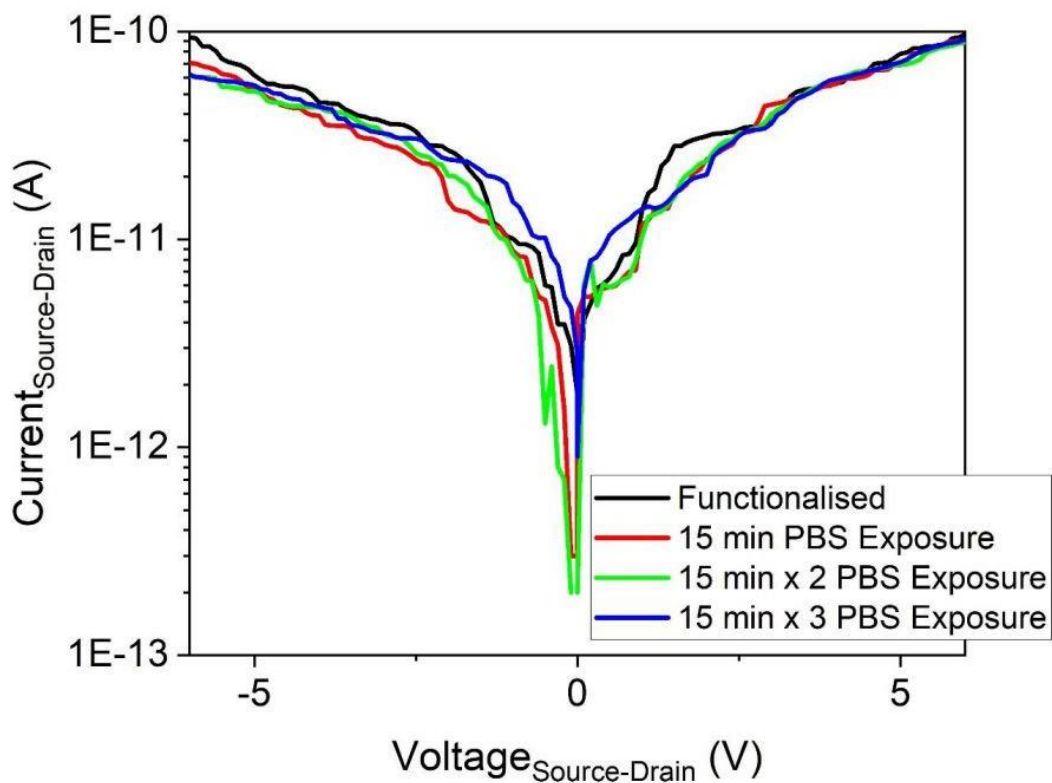
Functionalised nanowires exposed to PBS

Figure A.4.5: Control test current-voltage curves from a functionalised device fabricated with a DEP frequency of 10 MHz, after multiple exposures to PBS solution (with no spike protein), the sample was rinsed and dried between each exposure.

Current response of the non-functionalised and functionalised NWs device

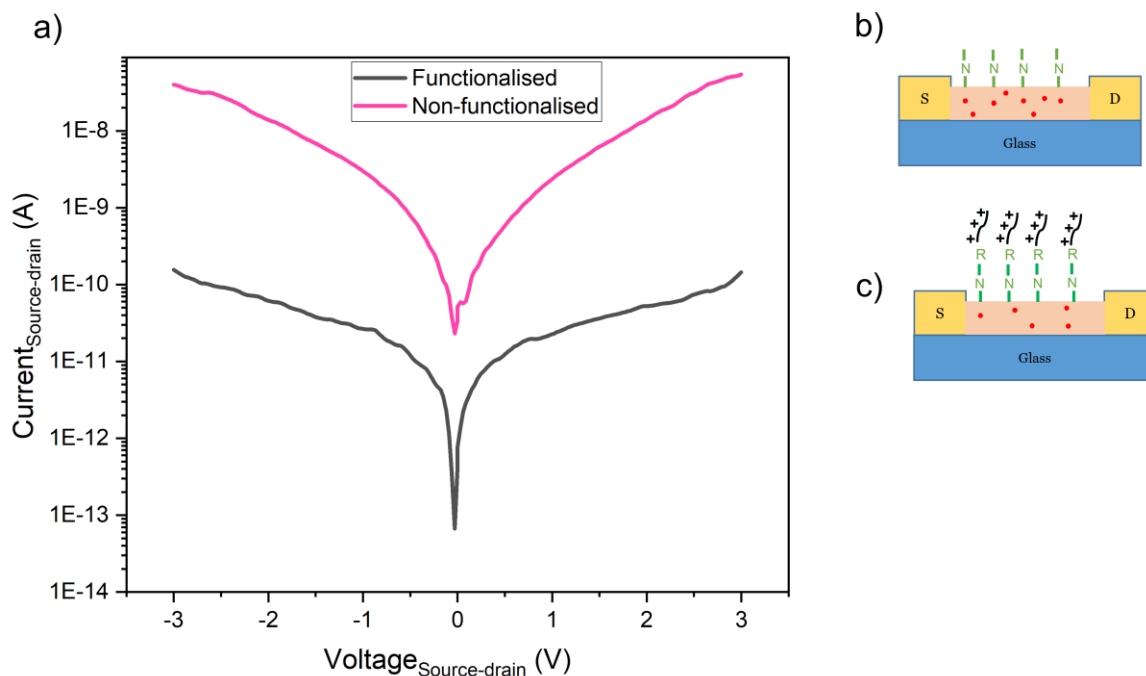


Figure A.4.6: a) is the I(V) response of the Ge NWs device before and after functionalisation, b) is a schematic of the underlying mechanism before the aptamer layer with holes carriers in the p-type Ge NWs (represented in red dots) and c) after deposition of the positively charged aptamer layer and depletion of holes.

A.5 Dielectrophoresis implementation technique for GaAsBi nanowires- based device

SEM images of the as-synthesised NWs

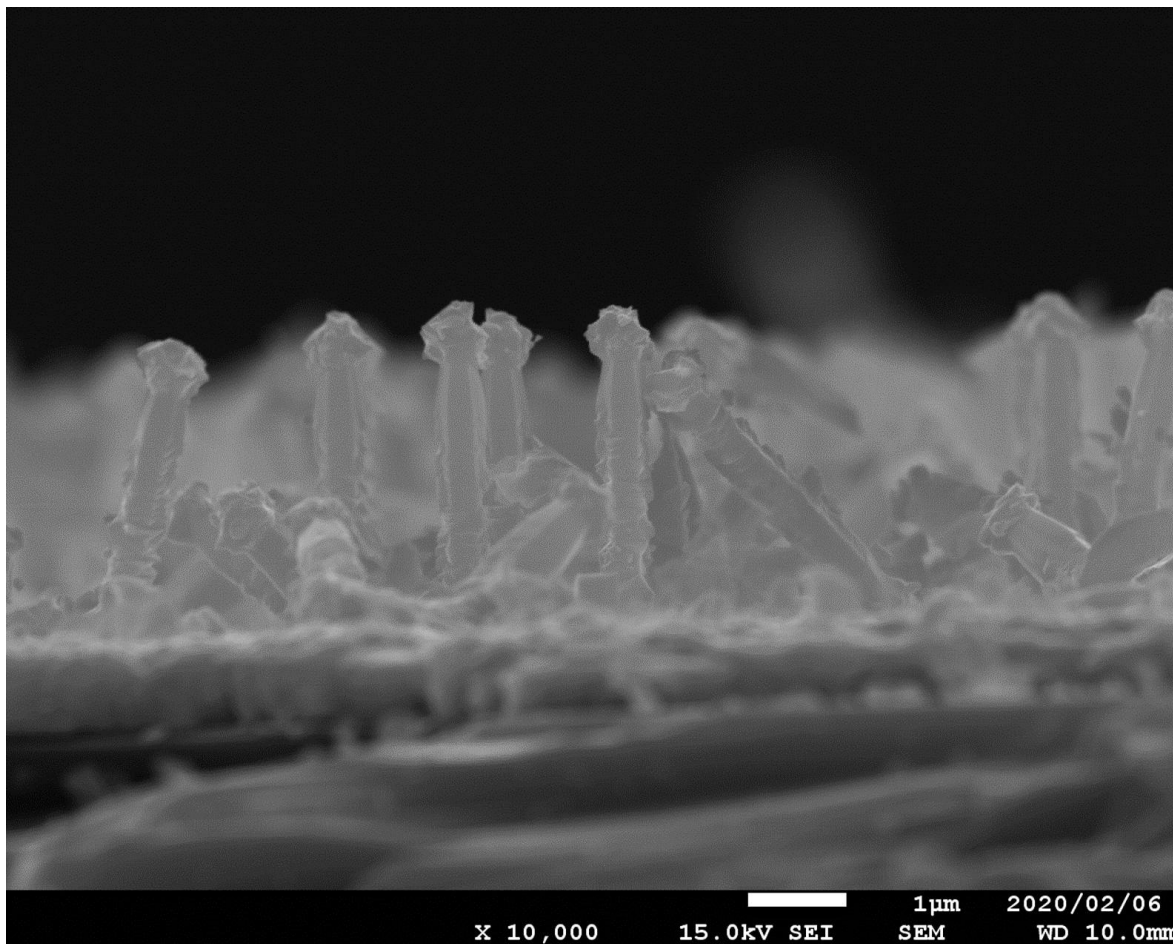


Figure A.5.1: Dark field SEM image of the NWs from batch A 140.

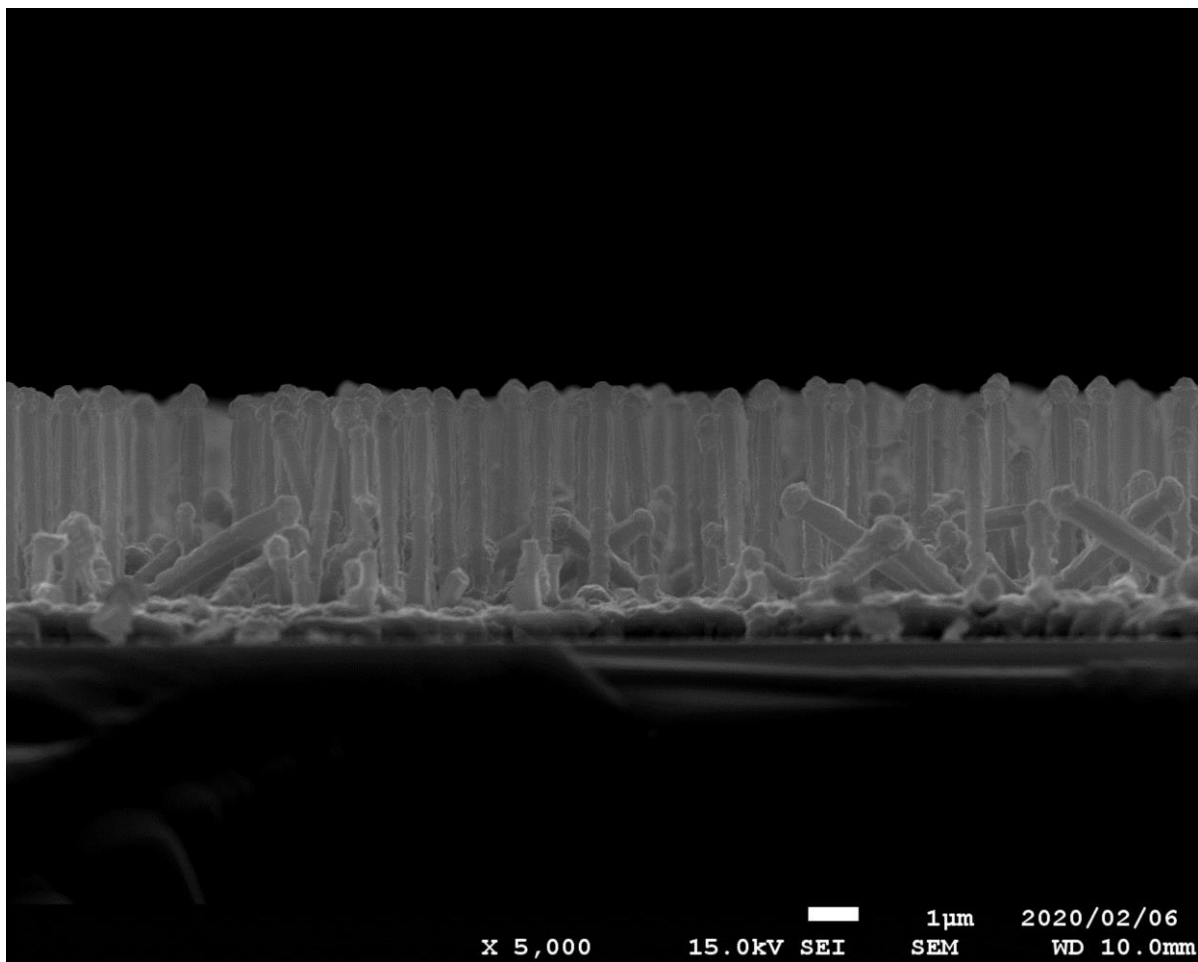


Figure A.5.2: Dark field SEM image of the NWs from batch B 136.

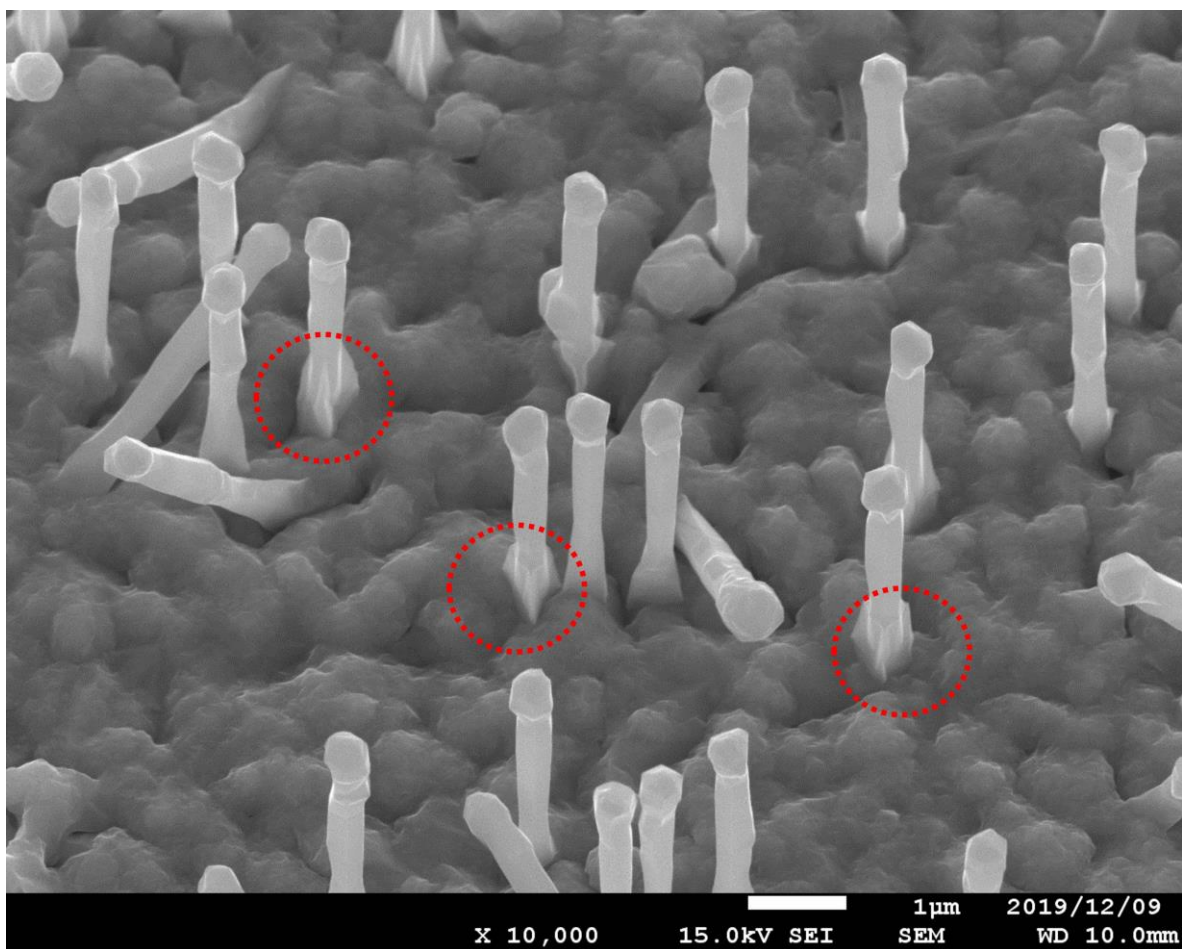


Figure A.5.3: Dark field SEM image of the NWs from batch C 118.

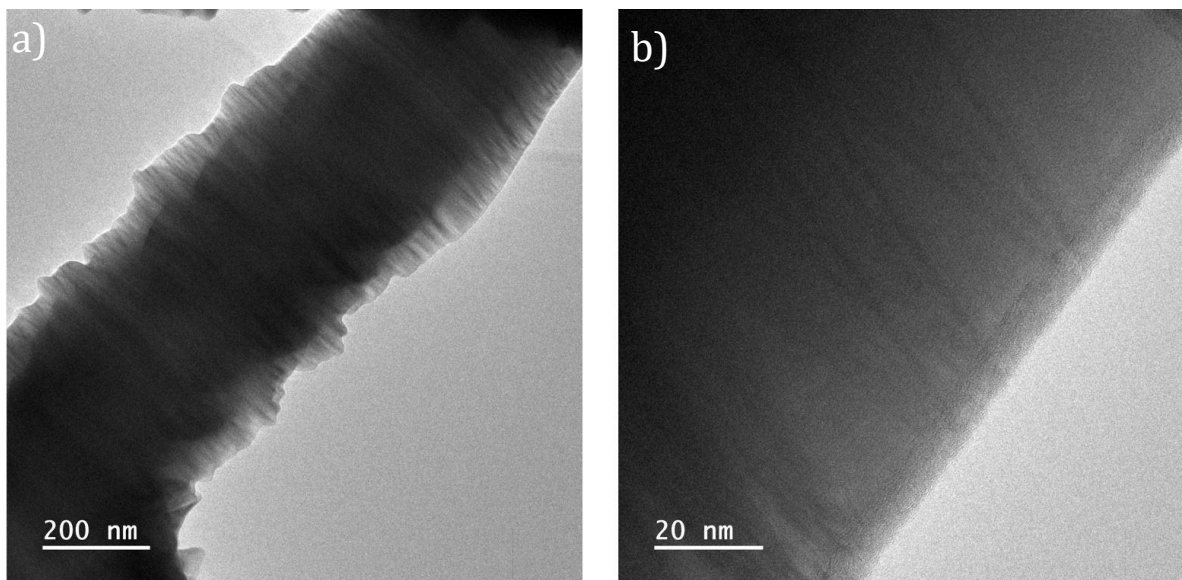
Characterisation of the NWs for DEP in Anisole

Figure A.5.4: Bright-field images obtained by TEM of the oxide layer measured to be 3 nm thick on the GaAsBi NWs after two months in anisole a) core of a NW, b) close up of a NW surface.

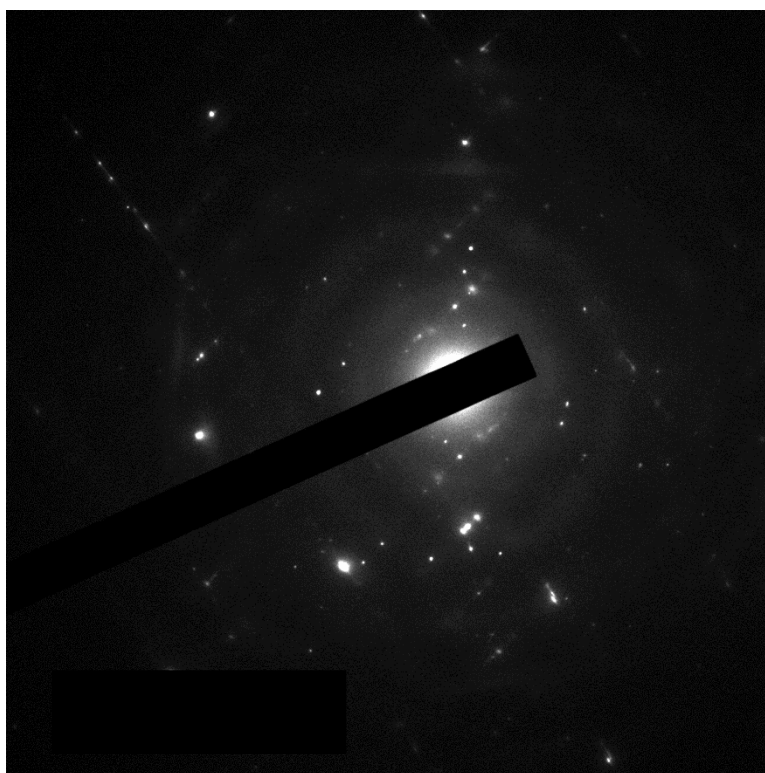


Figure A.5.5: Diffraction pattern of a GaAsBi NWs.

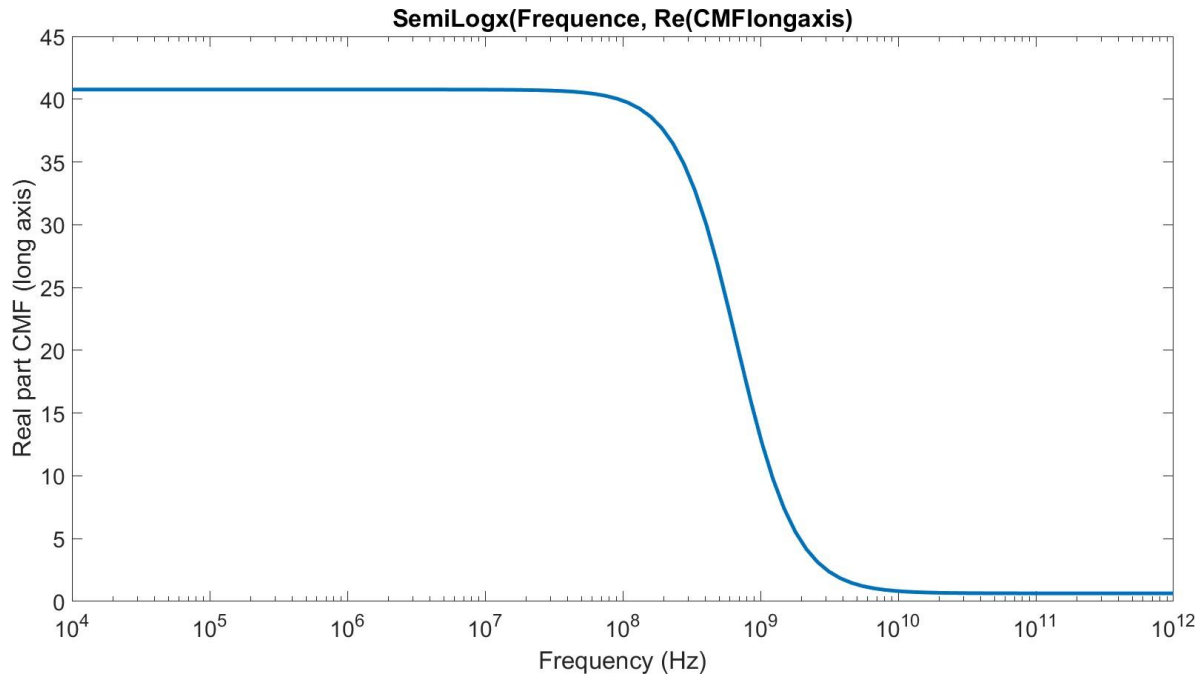
Clausius Mossotti factor and DEP force calculation

Figure A.5.6: Calculated real part of the CMF along the long axis as a function of the frequency for GaAsBi NWs aligned at a voltage of $8V_{peak-to-peak}$ on a $5\mu\text{m}$ electrode gap in anisole.

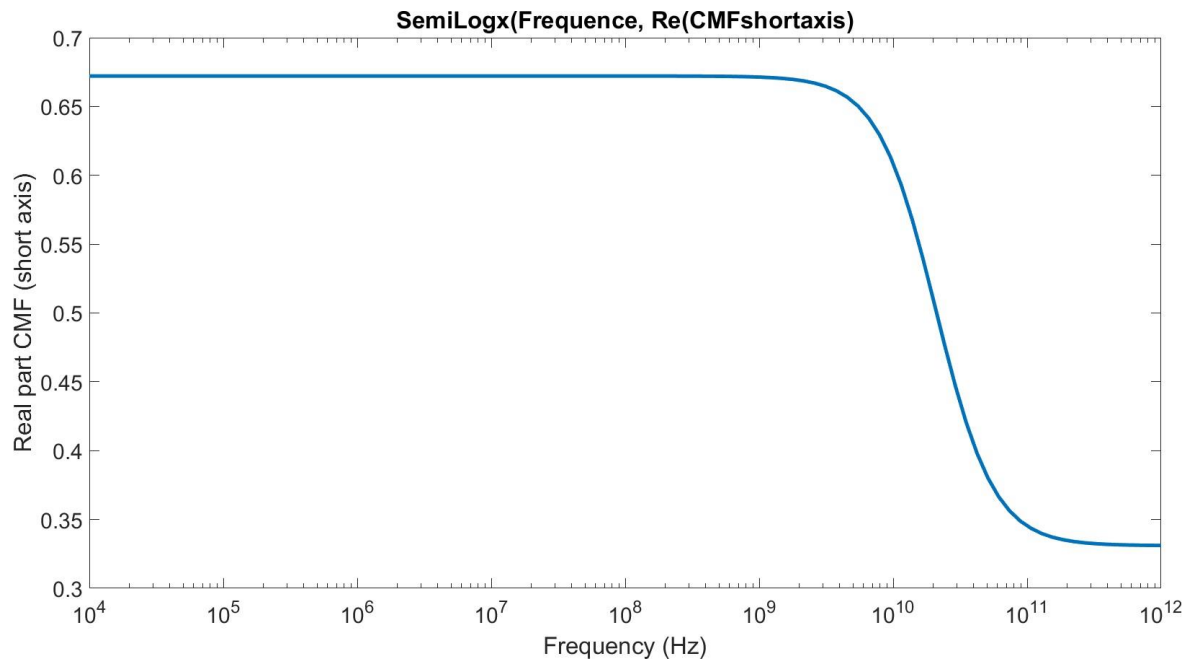


Figure A.5.7: Calculated real part of the CMF along the short axis as a function of the frequency for GaAsBi NWs aligned at a voltage of $8V_{peak-to-peak}$ on a $5\mu\text{m}$ electrode gap in anisole.

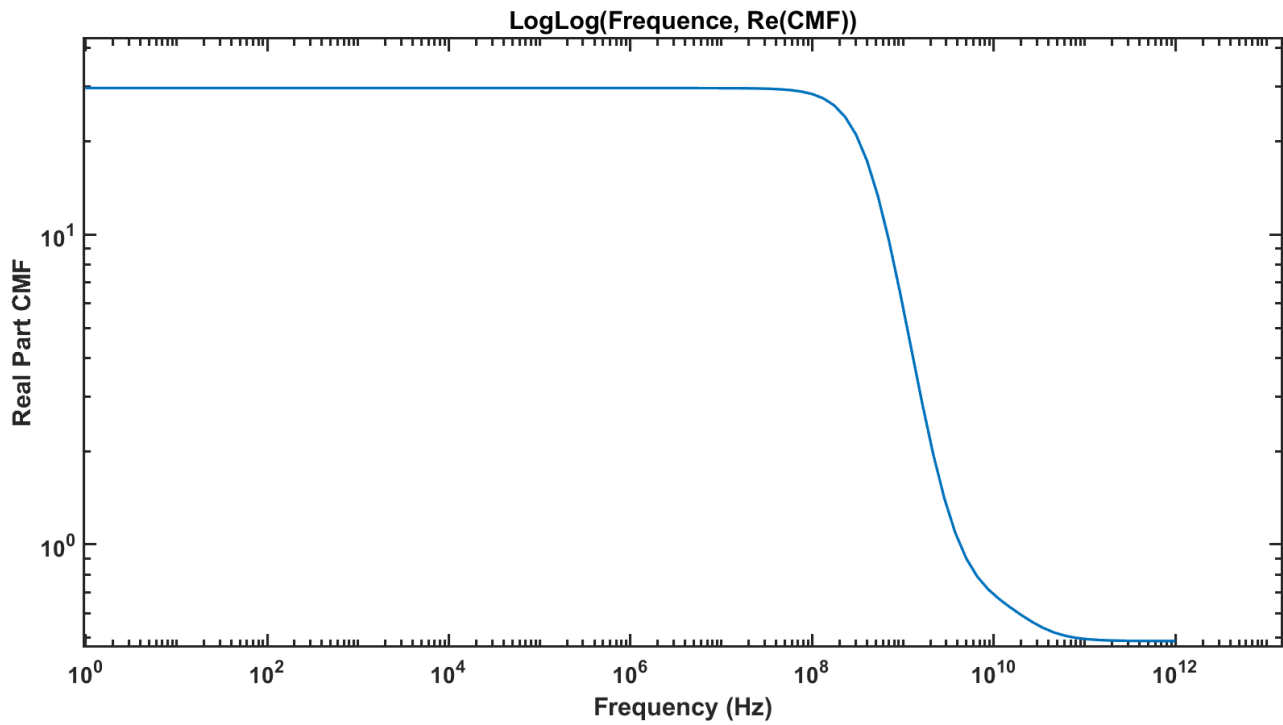


Figure A.5.8: Calculated real part of the Clausius Mossotti factor as a function of the frequency for GaAsBi NWs aligned at a voltage of $8 V_{peak-to-peak}$ on a $5 \mu\text{m}$ electrode gap in anisole.

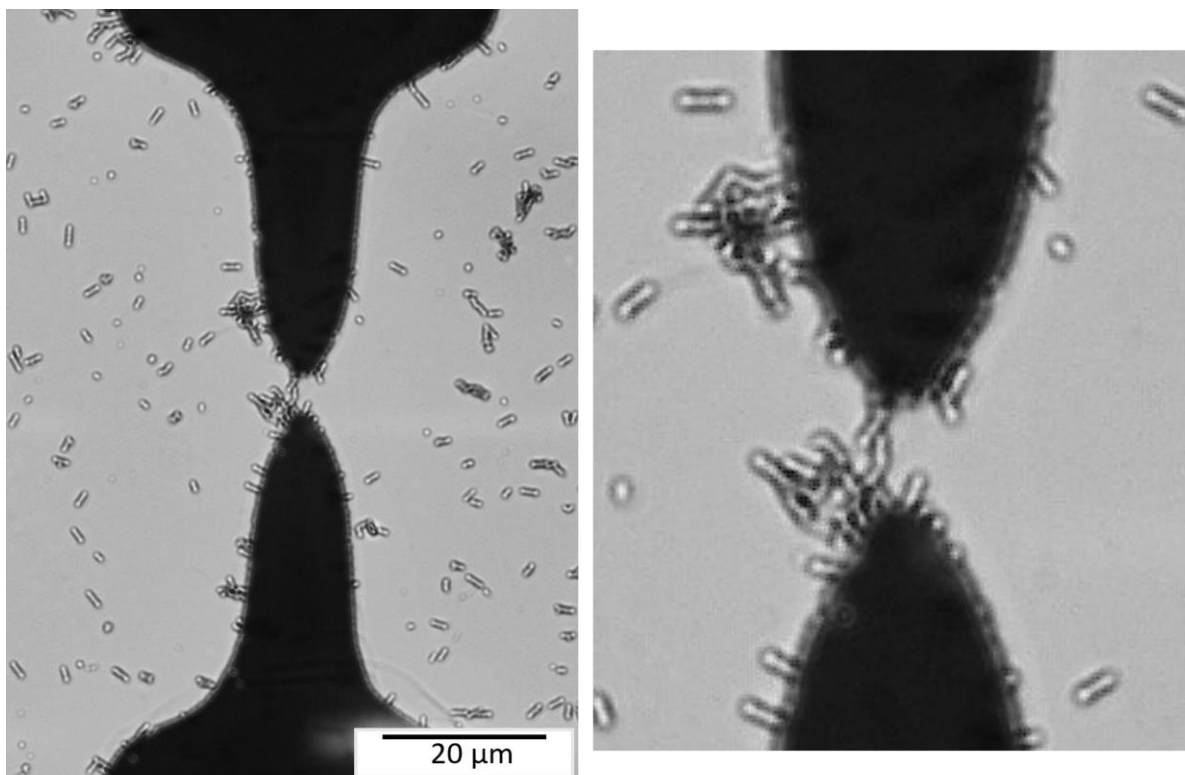
Dielectrophoresis alignment of GaAsBi

Figure A.5.9: Optical microscopy images of dielectrophoresis alignment of GaAsBi NWs aligned at a voltage of $8 V_{peak-to-peak}$ and frequency of 5 MHz on 5 μm electrode gap.

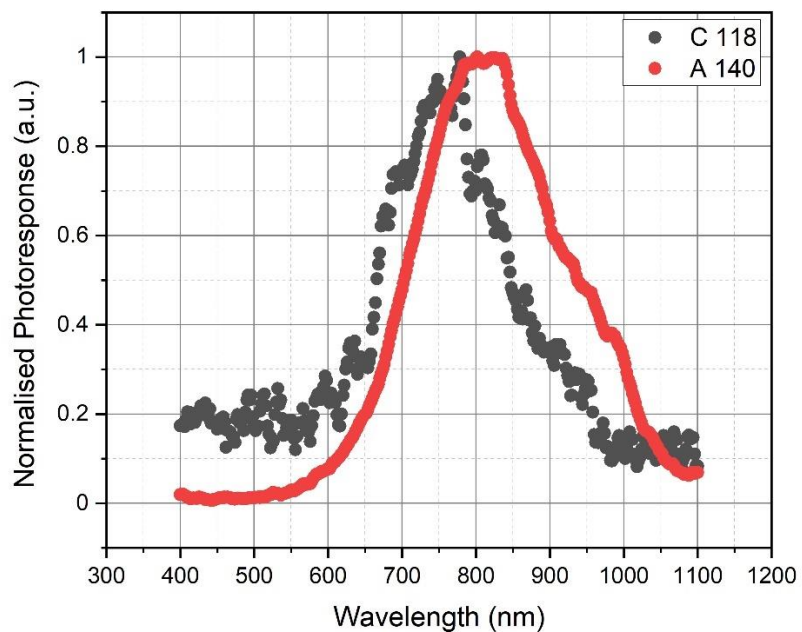
Electrical and optical characterisation

Figure A.5.10: Normalised spectral response as a function of the wavelength at room temperature. Devices fabricated with NWs from batch A (red plot) and batch C (black plot) aligned at a DEP frequency of 1 MHz.

Table A.5.11: Comparison of bulk and semiconductor nanowires mobility as a function of the apparent surface morphology.

Material	Dimensions	Mobility (cm ² (V.s) ⁻¹)	Apparent surface morphology	References
GaAs NWs	L=15 μm Ø= 150 nm	31	Smooth	[322]
	L=10 μm Ø= 90 nm	10.3 - 67.5	Smooth	[206]
	L= 1-2 μm Ø= 80 nm	1040	Smooth	[323]
	L=1-2 μm Ø= 50 nm	1000	Smooth	[342]
GaAs bulk	NA	1000 6000	NA	[342]
GaAsBi bulk	NA	1371 (2.5 %) 2116 (1.2 %) 2800 (0.84 %)	NA	[330] [343]
GaAsBi NWs	L= 4-5 μm Ø= 450 nm	(≈2.5 %) 500 kHz 5.29 1 MHz 16.3 5 MHz 27.5 10 MHz 100.9	(≈1.5 %) 3.48 51.7	SRS This work
InAs NWs	L= 10 μm Ø= 30 nm	300	SRS	[124]
Si NWs	L= 2 μm Ø= 80 nm	4.67	SRS	[344]
Ge bulk	NA	3900 1900	NA	[347]
Ge NWs	L= X μm Ø= 8 nm	3000 (strained)	smooth	[345]
	L= 4 μm Ø= 90 nm	64	smooth	[346]
	L= 20 μm Ø= 60 nm	3.5 * X	smooth	This work